Mathematical Modeling of Wave Energy Converter Devices in Real Sea Conditions

THESIS

Submitted in partial fulfillment
of the requirements for the degree of
DOCTOR OF PHILOSOPHY

by

KSHMA TRIVEDI
ID No. 2019PHXF0439H

Under the Supervision of

Prof. Santanu Koley

BITS Pilani
Pilani | Dubai | Goa | Hyderabad

BIRLA INSTITUTE OF TECHNOLOGY AND SCIENCE, PILANI
2023

BIRLA INSTITUTE OF TECHNOLOGY AND SCIENCE, PILANI

CERTIFICATE

This is to certify that the thesis entitled "*Mathematical Modeling of Wave Energy Converter Devices in Real Sea Conditions*" submitted by **KSHMA TRIVEDI**, ID No. 2019PHXF0439H in partial fulfillment of the requirements for the degree of DOCTOR OF PHILOSOPHY embodies original work done by her under my supervision.

Supervisor
PROF. SANTANU KOLEY
Associate Professor,
BITS-Pilani, Hyderabad Campus
Date: 19.12.2023

Declaration of Authorship

I, **KSHMA TRIVEDI**, declare that this thesis titled, 'Mathematical Modeling of Wave Energy Converter Devices in Real Sea Conditions' and the work presented in it are my own. I confirm that:

- This work was done wholly or mainly while in candidature for a research degree at this University.
- No portion of this work referred to in this thesis has been submitted in support of an application for another degree or qualification of this or any other university or other institution of learning.
- Where I have consulted the published work of others, this is always clearly attributed.
- Where I have quoted from the work of others, the source is always given. With the exception of such quotations, this thesis is entirely my own work.
- Where the thesis is based on work done by myself jointly with others, I have made clear exactly what was done by others and what I have contributed myself.

Signed: Kshma Trivedi

Date: **19/12/2023**

To

my grand father Shri Narayan Trivedi

&

my father Satish Chandra Trivedi

&

my mother Neeta Trivedi

and teachers

for their endless love, support and encouragement

Acknowledgements

Undertaking this research work has been a truly life-changing experience for me and it would not have been possible to do without the support and guidance that I have received from many people.

With immense pleasure and profound sense of gratitude, I take this opportunity to express my sincere indebtedness to my supervisor **Prof. Santanu Koley**. He has been a pillar of strength for me. His affectionate nature and patience throughout the duration of the research work is something I shall cherish throughout my life. It has been a humbling experience and a wonderful honor to be his student. I could not have imagined having a better advisor and mentor for my Ph.D.

I would also like to extend my gratitude to my DAC members, **Prof. Jonnalagadda Jagan Mohan** and **Dr. Nirman Ganguly**, for their helpful questions, comments, and constant feedback during this research work.

My sincere thanks to the present Head of the Department, **Prof. Pradyumn Kumar Sahoo** and former Head of the Department **Prof. Dipak K Satpathi**, DRC convener, **Prof. Sharan Gopal**, and each faculty member of the Department of Mathematics, BITS-Pilani, Hyderabad Campus, for their help, support, and encouragement to carry out my research work.

With a deep sense of gratitude, I express my sincere indebtedness to **Prof. Trilochan Sahoo**, Professor, Dept. of Ocean Engineering and Naval Architecture, IIT Kharagpur, **Prof. Subramaniam Neelamani**, Senior Research Scientist, Kuwait Institute for Scientific Research, Kuwait, **Prof. Subash Chandra Martha**, Associate Professor, Dept. of Mathematics, IIT Ropar, **Prof. Rodolfo Silva**, Professor, Instituto EPOMEX, Universidad Autónoma de Campeche, **Dr. Ayrton Alfonso Medina Rodríguez**, Postdoctoral researcher, Instituto de Ingeniería, Universidad Nacional Autónoma de México, **Dr. KG Vijay**, Assistant Professor, Department of Ocean Engineering, IIT Madras for their precious suggestions and guidance during my research work.

I would also like to convey my gratitude to my co authors Dr. Itxaso Oderiz Martinez, Dr. Edgar Mendoza, Dr. Gregorio Posada Vanegas, Dr. Chandra Shekhar Nishad, Dr. Arun Choudhary, Dr. Kottala Panduranga for their contributions and support during my research work.

I express my sincere thanks to Department of Science and Technology for providing necessary financial support through INSPIRE Faculty Fellowship Project (Project No: DST/INSPIRE/04/2017/002460) in terms of Project Associate I and II Fellowships.

I gratefully acknowledge BITS-Pilani, Hyderabad Campus, for providing me with the necessary facilities to carry out my research work.

I would also like to convey special thanks to my Chillers “Vipin, Amya, Santanu, and Rahul” and my very close friends Monica, Vinod, Anjusree, Sunita, Susam, Amar, Pankaj, Shravani, Shivangi, Amrutha, Tapaswini, Anannya, Astha, Ankita, Ankur, Sakshi, Diksha, Ruchi, Hiren, Amit, Amritanshu who were with me in both happy and difficult moments during my PhD life.

A special thanks to all my department research scholars for their endless help, companionship, and for making my life more enjoyable and happier in these years.

Most importantly, I would like to thank my father, mother and sister-in-law, and all my family members for their love, care, and support for my personal life.

A very special thanks to my brother Vishnu Kant Trivedi for always support me financially.

I am very much thankful to Dr. Prashant Patel. He acted as the constant motivator for me through out my PhD life.

Above all, I sincerely pray to my dear Lord Hanuman for his blessings and kindness on me during every phase of my entire life.

Abstract

The thesis focuses on a class of problems associated with the hydrodynamics of oscillating water column and piezoelectric wave energy converter devices with particular emphasis on

- developing boundary element method based numerical tools to deal with the wave scattering and radiation problems associated with the wave energy converter devices under the assumption of linearized wave-structure interaction theory, and
- examining the devices' performance and efficiency with a focus on identifying resonant frequencies to increase the power output and efficiency of the devices.

The class of physical problems analyzed in the present study are handled for solutions using the coupled eigenfunction expansion-boundary element method, and constant and linear boundary element methods. These solution methodologies are very effective and efficient to deal with wave energy converter devices having complex structural shapes and configurations. Further, the effect of bottom undulations on the performance of the devices is analyzed. For all the cases, major emphasis is given to analyze the occurrences of resonances due to matching frequencies of the water column motion within the oscillating water column (OWC) device chamber with the frequency of the incident waves and sloshing phenomena. The effect of structural shapes, turbine control parameters, seabed parameters, and incident wave characteristics on the power generation and efficiency of the devices is analyzed. For standalone OWC devices and breakwater-integrated OWC devices, major parameters of interest such as radiation susceptance coefficient, radiation conductance coefficient, volume flux, and hydrodynamic efficiency of the devices are analyzed to investigate the performance of OWC devices in regular incident waves. Further, for irregular incident waves, the local wave climate at the OWC plant site Pico, Portugal is considered, and the performance of the OWC devices is analyzed based on the variation of annual-averaged efficiency parameters as functions of turbine characteristics and device geometry. For hybrid OWC and piezoelectric plate devices, the study is carried out in both frequency and time domains. Efforts are put to determine the largest bandwidth around the most probable incident wave frequencies for which multiple resonances occur to maximize the power extraction process. In the two-layer fluid case, the occurrences of interconnecting resonances due to the surface and internal wave modes to maximize the power generation by OWC devices are investigated in a detailed manner. In all the problems, numerical convergence of the BEM-based solutions is provided, and certain computational results are validated with experimental and analytical results available in the literature.

Keywords: Boundary element method; Fredholm integral equations; Surface gravity waves; Oscillating water column; Piezoelectricity; Wave radiation; Wave scattering; Resonance.

Contents

CERTIFICATE i

Declaration of Authorship ii

Acknowledgements

Abstract

Contents

List of Tables

List of Figures

List of Symbols

Abbreviations

1 Introduction 1

1.1 Preamble . . . 1

1.2 State of the art . . . 5

1.2.1 Classification of wave energy converter devices . . . 5

1.2.2 Oscillating water column wave energy converter device . . . 6

1.2.3 Piezoelectric wave energy converter device . . . 8

1.2.4 Hydrodynamics of the oscillating water column device in the presence of regular incident waves . . . 9

1.2.5 Hydrodynamics of the breakwater integrated oscillating water column device 11

1.2.6 Hydrodynamics of the oscillating water column device in the presence of irregular incident waves . . . 13

1.2.7 Hydrodynamics of the piezoelectric wave energy converter device . . . 13

1.2.8 Water wave interaction with the costal structures in the presence of the two-layer fluid model . . . 14

1.2.9 Optimization of parameters associated with the wave energy converter devices . . . 16
1.3 Motivation and outline of the thesis . . . 16
1.4 Mathematical description of waves and structures . . . 20
1.4.1 Basic equations for water wave propagation in homogeneous fluid . . . 20
1.4.2 Basic equations of water wave in stratified fluid . . . 24
1.4.3 Basic equations associated with the hydrodynamics of oscillating water column wave energy converter device . . . 27
1.4.4 Basic equations and edge conditions for flexible structures . . . 29
1.4.4.1 Basic equations and boundary conditions associated with the piezoelectric wave energy converter device . . . 31
1.5 Fundamentals of integral equations . . . 32
1.6 Boundary Element Method (BEM) . . . 34
1.6.1 Fundamental solution of the Laplace equation . . . 35
1.6.2 Boundary integral equations formulation . . . 36
1.6.3 Boundary element method based on constant element approach . . . 37
1.6.4 Boundary element method based on linear element approach . . . 40

2 Mathematical modeling of oscillating water column wave energy converter devices placed over undulated sea bed 43
2.1 General introduction . . . 44
2.2 Mathematical formulation . . . 44
2.3 Solution methodology . . . 47
2.3.1 Eigenfunction expansion in region R_1 . . . 47
2.3.2 Boundary element formulation in region R_2 . . . 48
2.4 Various quantities associated with OWC devices . . . 51
2.5 Results . . . 54
2.5.1 Convergence study . . . 56
2.5.2 Validation . . . 57
2.5.3 Resonance mechanism . . . 58
2.5.4 Type I bed profile . . . 59
2.5.5 Type II bed profile: . . . 64
2.6 Conclusions . . . 66

3 Mathematical modeling of breakwater-integrated oscillating water column wave energy converter devices under irregular incident waves 68
3.1 General introduction . . . 69
3.2 Mathematical Formulation . . . 69
3.3 Solution methodology based on BEM . . . 72
3.4 Parameters associated with the performance of OWC devices in regular waves . . . 74
3.5 Parameters associated with the performance of OWC devices in irregular waves . . . 76
3.6 Results and Discussions . . . 79
3.6.1 Numerical convergence of the BEM based solution . . . 79
3.6.2 Comparison with existing results . . . 81
3.6.3 Results for regular incident waves . . . 82
3.6.4 Results for irregular incident waves . . . 86
3.7 Conclusions . . . 91

4 Performance of a hybrid wave energy converter device consisting of a piezoelectric plate and oscillating water column device placed over an undulated seabed 93
4.1 General introduction . . . 94
4.2 Mathematical formulation . . . 94
4.3 Solution methodology based on BEM . . . 97
4.3.1 Formulation of the integral equations . . . 98
4.4 Parameters associated with the hybrid wave energy converter device . . . 101
4.4.1 Wave power extraction by the OWC device . . . 101
4.4.2 Wave power extraction by the piezoelectric plate . . . 102
4.4.3 Wave power extracted by the wave energy converter device consists of piezoelectric plate and OWC device . . . 102
4.5 Results . . . 102
4.5.1 Validation . . . 103
4.5.2 Results associated with the hydrodynamic performance of the standalone OWC device . . . 106
4.5.3 Results associated with the hydrodynamic performance of the standalone piezoelectric plate having fixed edges . . . 108
4.5.4 Results associated with the hydrodynamic performance of hybrid wave energy converter device consists of piezoelectric plate (fixed edges) and OWC device . . . 111
4.5.5 Results associated with the hydrodynamic performance of the piezoelectric plate having seaside free edge and shore side fixed edge . . . 115
4.5.6 Results associated with the hydrodynamic performance of hybrid wave energy converter device consists of piezoelectric plate (fixed edge near to the OWC device and seaside free edge) and OWC device . . . 117
4.5.7 Summary comparison among standalone OWC, piezoelectric plate and the hybrid device . . . 119
4.6 Time-dependent simulations . . . 120
4.7 Optimization of various parameters associated with the hybrid wave energy converter device and seabed . . . 123
4.8 Shortcomings of the present study . . . 125
4.9 Conclusions . . . 125

5 Mathematical modeling of oscillating water column wave energy converter devices placed over an undulated seabed in a two-layer fluid system 129
5.1 General introduction . . . 130
5.2 Mathematical Formulation . . . 130
5.3 Solution methodology based on BEM . . . 134
5.4 Mathematical formulation and solution methodology for interface piercing (IP) OWC device . . . 137
5.5 Various parameters associated with the hydrodynamic performance of the OWC device . . . 139
5.6 Results and discussions . . . 143
5.6.1 Numerical convergence . . . 144
5.6.2 Comparison with existing results . . . 144
5.6.3 Results associated with INP OWC device . . . 145
5.6.4 Results associated with the IP OWC device . . . 150

5.7 Time-dependent simulations 154
5.8 Effect of air compressibility on the hydrodynamic performance of the OWC devices 157
5.9 Conclusions 160

6 Summary **164**
6.1 Major Research Developments and Findings 166
6.2 Applications 169
6.3 Scope of possible extensions for the future work 170

References **172**

List of Publications **184**

Conclusions **188**

Biography **191**

List of Tables

2.1 Comparative study of μ, ν and η_{max} for the OWC device placed on bottom of type II with $a_1 = 0.5$ and $m = 3$. Here $N = 5$ is considered. 56
2.2 Comparative study of μ, ν and η_{max} for the OWC device placed on bottom of type II with $a_1 = 0.5$ and $m = 3$. Here $\kappa = 60$ is considered. 57

3.1 Set of nine sea states represent the local wave climate at the OWC plant site Pico, Azores, Portugal. Here, the units of $\overline{P}_a/L_w$, N_{op} and $\overline{W}_a$ are kW/m, rad/sec and kW respectively. Further, $V_0 = 1050m^3$, $\gamma = 1.4$, $\rho_a = 1.25kg/m^3$, $p_a = 1.013 \times 10^5 Pa$. 78
3.2 Comparative study of η_{max} for type I and type II OWC devices with $a/h = 0.5$, $y_0/h = -0.72$ and $Kh = 0.5$. 80
3.3 Comparative study of η_{max} for type I and type II OWC devices with $b/h = 1.0$, $r/h = 2.5$ and $Kh = 0.5$. 80

4.1 Taguchi method parameters. 123
4.2 Taguchi method L8 matrix. 123
4.3 Output performance attributes of the 8 systems. 124

5.1 Comparative study of $\eta_{max,I}$ for INP and IP OWC devices. 145
5.2 Comparative study of $\eta_{max,II}$ for INP and IP OWC devices. 145
5.3 Resonating frequencies in $\eta_{max,I}$ curve for INP OWC device (corresponding to Fig. 5.4(a)). 147

List of Figures

1.1 Global wave resource map. Image courtesy of Gunn and Stock-Williams [1] . . . 2
1.2 Schematic diagram of discretized domains in various numerical methods. 3
1.3 Classification of wave energy converters based on their working mechanisms Antonio [2]. 7
1.4 The working principle of OWC caisson device subjected to (a) wave crest, and (b) wave trough. 7
1.5 The OWC wave power pilot plant on the island of Pico, Azores, Portugal (Falcão et al. [3]). 8
1.6 Illustration of the piezoelectric bimorph (Renzi [4]). 9
1.7 Structure of two-dimensional boundary value problems in open water region. . . 20
1.8 Structure of two-dimensional boundary value problems in a two-layered fluid system. 25
1.9 Schematic diagram of side cross-section of the oscillating water column device. . 27
1.10 Schematic of the side cross-section of the piezoelectric device. 31
1.11 Different routes for solving the real engineering problems. 34
1.12 Cross-section of the domain D bounded by Γ 36
1.13 Discretization of boundary using constant elements. 38
1.14 Discretization of boundary using linear elements. 40

2.1 Vertical cross-section of the OWC device. 45
2.2 Contour in region R_j for $j = 1, 2$. 52
2.3 Computational boundaries of region R_2 for (a) $\alpha = -3.0$, (b) $\alpha = -1.0$, (c) $\alpha = 0$ and (d) $\alpha = 3.0$. 55
2.4 Computational boundaries of region R_2 for (a) $a_1 = 1.0$, $m = 3.0$, (b) $a_1 = 1.0$, $m = 5.0$. 56
2.5 Variation of η_{max} vs Kh_1 for different (a) b/h_1 and (b) a/h_1. Lines represent the solutions obtained by the present coupled eigenfunction expansion - boundary element method and symbols represent the solutions provided in Evans and Porter [5]. 58
2.6 Variation of η vs Kh_1 for different bottom slopes $\beta = 16°$ and $\beta = 26°$. Lines represent the solutions obtained by the present coupled eigenfunction expansion - boundary element method and symbols represent the solutions provided in Ning et al. [6]. 58
2.7 Variation of (a) μ, (b) ν, (c) $|\frac{q^S}{q^I}|$ and (d) η_{max} vs Kh_1 for different b/h_1 with $\alpha = -3$. 60
2.8 Variation of (a) μ, (b), ν, (c) $|\frac{q^S}{q^I}|$ and (d) η_{max} vs Kh_1 for different a/h_1 with $\alpha = -3$. 61
2.9 Surface plot of η_{max} as a function of a/h_1 and (b) b/h_1 with $\alpha = -3$ and $T = 10$sec. 62

2.10 Variation of (a) μ, (b) ν, (c) $|\frac{q^S}{q^I}|$ vs Kh_1 for different θ, and (d) variation of η_{max} vs Kh_1 and θ with $\alpha = -3$. 63
2.11 Variation of (a) ν and (b) η_{max} vs Kh_1 for different α. 64
2.12 Variation of (a) μ, (b) ν, (c) $|\frac{q^S}{q^I}|$ and (d) η_{max} vs Kh_1 for different ripple amplitude a_1 with $m = 3.0$. 65
2.13 Variation of (a) μ, (b) ν, (c) $|\frac{q^S}{q^I}|$ and (d) η_{max} vs Kh_1 for different number of ripples m with $a_1 = 4.0$. 66

3.1 Vertical cross sections of (a) type I OWC device, and (b) type II OWC device. . 70
3.2 Variation of η_{max} vs Kh for different a/h for type I OWC device placed over uniform bottom with $\theta = 90°$. Lines represent the solutions obtained by the present boundary element method and symbols represent the solutions provided in Evans and Porter [5]. 82
3.3 Variation of η_{max} vs Kh for different (a) b/h and (b) a/h for type I OWC device. 82
3.4 Variation of η_{max} vs Kh for different (a) r/h and (b) y_0/h for type II OWC device. 83
3.5 Variation of (a) F_h for different b/h, (b) F_h for different a/h, (c) F_v for different b/h and (d) F_v for different a/h as a function of Kh for type I OWC device. . . 84
3.6 Variation of (a) F_h for different r/h, (b) F_h for different y_0/h, (c) F_v for different r/h and (d) F_v for different y_0/h as a function of Kh for type II OWC device. . 85
3.7 Variation of σ_p vs $\wedge$ for different (a) b/h and (b) a/h for the annual wave spectral density $S_{I,ann}$ and for type I OWC device. 86
3.8 Variation of σ_p vs $\wedge$ for different (a) r/h and (b) y_0/h for the annual wave spectral density $S_{I,ann}$ and for type II OWC device. 87
3.9 Variation of $\overline{\eta}_{a,ann}$ vs $\wedge$ for different (a) b/h and (b) a/h for type I OWC device. 88
3.10 Variation of $\overline{\eta}_{a,ann}$ vs $\wedge$ for different (a) r/h and (b) y_0/h for type II OWC device. 88
3.11 Surface plot of $\overline{\eta}_{a,ann}$ as a function of (a) a/h and b/h with $\wedge = 0.01$ and (b) N and D with $K_a = 0.375$. 89
3.12 Surface plot of $\overline{\eta}_{a,ann}$ as a function of (a) r/h and y_0/h with $\wedge = 0.01$ and (b) N and D with $K_a = 0.375$. 90

4.1 Vertical cross section of wave energy converter device. 95
4.2 Variation of (a) power extraction P_{plate} by the piezoelectric plate as a function of incident wave period T, (b) η as a function wavenumber Kh_1 for sloping seabed with sloping angle $\beta = 16°$, and (c) η as function of Kh_1 in the presence of uniform seabed. 104
4.3 Time series of (a) free surface elevation outside the chamber, (b) free surface elevation at the chamber center, and (c) air pressure inside the OWC device chamber. 105
4.4 (a) variation of P_{OWC} vs Kh_1 for various b/h_1, and (b) contour plot of P_{OWC} as a function of Kh_1 and b/h_1. 106
4.5 (a) variation of P_{OWC} vs Kh_1 for various d_2/h_1, and (b) contour plot of P_{OWC} as a function of Kh_1 and d_2/h_1. 106
4.6 Variation of P_{OWC} vs Kh_1 for various (a) m, and (b) a_1/h_1. 107
4.7 Variation of (a) P_{plate} vs Kh_1 for various l_1/h_1, and (b) contour plot of P_{plate} as a function of Kh_1 and l_1/h_1. 108
4.8 (a) variation of P_{plate} vs Kh_1 for various d_1/h_1, and (b) contour plot of P_{plate} as a function of Kh_1 and d_1/h_1. 109
4.9 Variation of P_{plate} vs Kh_1 for various (a) m, and (b) a_1/h_1. 109

4.10 (a) variation of P_{Total} vs Kh_1 for various b/h_1, and (b) contour plot of P_{Total} as a function of Kh_1 and b/h_1. 111
4.11 (a) variation of P_{Total} vs Kh_1 for various d_2/h_1, and (b) contour plot of P_{Total} as a function of Kh_1 and d_2/h_1. 111
4.12 Variation of P_{Total} vs Kh_1 for various (a) m, and (b) a_1/h_1. 112
4.13 (a) variation of P_{Total} vs Kh_1 for various l_1/h_1, and (b) contour plot of P_{Total} as a function of Kh_1 and l_1/h_1. 112
4.14 (a) variation of P_{Total} vs Kh_1 for various d_1/h_1, and (b) contour plot of P_{Total} as a function of Kh_1 and d_1/h_1. 114
4.15 (a) variation of P_{Total} vs Kh_1 for various gp/h_1, and (b) contour plot of P_{Total} as a function of Kh_1 and gp/h_1. 115
4.16 (a) variation of P_{plate} vs Kh_1 for various l_1/h_1, and (b) contour plot of P_{plate} as a function of Kh_1 and l_1/h_1. 116
4.17 (a) variation of P_{plate} vs Kh_1 for various d_1/h_1, and (b) contour plot of P_{plate} as a function of Kh_1 and d_1/h_1. 116
4.18 (a) variation of P_{Total} vs Kh_1 for various b/h_1, and (b) contour plot of P_{Total} as a function of Kh_1 and b/h_1. 117
4.19 (a) variation of P_{Total} vs Kh_1 for various d_2/h_1, and (b) contour plot of P_{Total} as a function of Kh_1 and d_2/h_1. 118
4.20 (a) variation of P_{Total} vs Kh_1 for various (a) l_1/h_1, and (b) contour plot of P_{Total} as a function of Kh_1 and l_1/h_1. 118
4.21 (a) variation of P_{Total} vs Kh_1 for various (a) d_1/h_1, and (b) contour plot of P_{Total} as a function of Kh_1 and l_1/h_1. 119
4.22 (a) variation of P_{Total} vs Kh_1 for various (a) gp/h_1, and (b) contour plot of P_{Total} as a function of Kh_1 and gp/h_1. 119
4.23 Variation of the free surface displacement $\tilde{\zeta}(x,t)$ (blue lines) and plate displacement $\tilde{\zeta}(x,t)$ (red lines) versus x at various time t (a) $t = 2$ s, (b) $t = 5$ s, (c) $t = 10$ s, and (d) $t = 15$ s . Here the phase angle is taken zero. The evolution is also shown as an animation in the Multimedia file (Fig_15.mp4). Multimedia view: `https://github.com/santanukoley/Movie-Files.git` 121
4.24 Variation of the free surface displacement $\tilde{\zeta}(x,t)$ (blue lines) and plate displacement $\tilde{\zeta}(x,t)$ (red lines) versus x at various time t (a) $t = 2$ s, (b) $t = 5$ s, (c) $t = 10$ s, and (d) $t = 15$ s . Here the phase angle is varied according to Eq. (4.40). The evolution is also shown as an animation in the Multimedia file (Fig_16.mp4). Multimedia view: `https://github.com/santanukoley/Movie-Files.git` . . . 122
4.25 Variation of the instantaneous reflection coefficient K_r for the case when (a) phase angle is taken zero, and (b) phase angle is varied according to Eq. (4.40). 123
4.26 Variation of the instantaneous power extraction P_{Total} for (a) $b/h_1 = 1.0$, (b) $b/h_1 = 1.5$, (c) $b/h_1 = 2.0$, and (d) $b/h_1 = 2.5$. 127
4.27 Optimized systems' power extraction P_{Total} vs frequency ω based on Eq. (4.38). 128

5.1 Vertical cross section of the INP OWC device. 131
5.2 Vertical cross-section of the IP OWC device. 138
5.3 Comparison of present numerical results with the results of (a) Evans and Porter [5] for η_{max} vs KH_1 for different b/H_1, and (b) Rezanejad et al. [7] for η_{max} vs KH_1 for different H_2/H_1 with $s = 1$. 146
5.4 Variation of (a) $\eta_{max,I}$, and (b) $\eta_{max,II}$ vs KH_1 for different chamber length b/H_1. 146
5.5 Variation of (a) $\eta_{max,I}$, and (b) $\eta_{max,II}$ vs KH_1 for different submergence depth a/H_1. 148

5.6 Variation of (a) $\eta_{max,I}$, and (b) $\eta_{max,II}$ vs KH_1 for various ripples m. 148
5.7 Variation of (a) $\eta_{max,I}$, and (b) $\eta_{max,II}$ vs KH_1 for various ripple amplitude a_1 . 149
5.8 Variation of (a) $\eta_{max,I}$, and (b) $\eta_{max,II}$ vs KH_1 for various density ratio s. . . . 150
5.9 Variation of (a) $\eta_{max,I}$, and (b) $\eta_{max,II}$ vs KH_1 for different chamber length b/H_1. 150
5.10 Variation of (a) $\eta_{max,I}$, and (b) $\eta_{max,II}$ vs KH_1 for different chamber length a/H_1. 151
5.11 Variation of (a) $\eta_{max,I}$, and (b) $\eta_{max,II}$ vs KH_1 for various number of ripples m. 152
5.12 Variation of (a) $\eta_{max,I}$, and (b) $\eta_{max,II}$ vs KH_1 for various ripple amplitudes a_1/H_1. 153
5.13 Variation of (a) $\eta_{max,I}$, and (b) $\eta_{max,II}$ vs KH_1 for various density s. 153
5.14 Variation of free surface elevation $\zeta_c(x,t)$ vs x associated with the wavenumber k_I in presence of INP device for different time (a) $t = 0$, (b) $t = 10$, (c) $t = 20$, and (d) $t = 30$. 155
5.15 Variation of free surface elevation $\zeta_c(x,t)$ vs x associated with the wavenumber k_{II} in presence of INP device for different time (a) $t = 0$, (b) $t = 10$, (c) $t = 20$, and (d) $t = 30$. 156
5.16 Variation of interface elevation $\zeta_c(x,t)$ vs x associated with the wavenumber k_I in presence of INP device for different time (a) $t = 0$, (b) $t = 10$, (c) $t = 20$, and (d) $t = 30$. 157
5.17 Variation of interface elevation $\zeta_c(x,t)$ vs x associated with the wavenumber k_{II} in presence of INP device for different time (a) $t = 0$, (b) $t = 10$, (c) $t = 20$, and (d) $t = 30$. 158
5.18 Variation of free surface elevation $\zeta_c(x,t)$ vs x associated with the wavenumber k_I in presence of IP device for different time (a) $t = 0$, (b) $t = 10$, (c) $t = 20$, and (d) $t = 30$. 159
5.19 Variation of free surface elevation $\zeta_c(x,t)$ vs x associated with the wavenumber k_{II} in presence of IP device for different time (a) $t = 0$, (b) $t = 10$, (c) $t = 20$, and (d) $t = 30$. 160
5.20 Variation of interface elevation $\zeta_c(x,t)$ vs x associated with the wavenumber k_I in presence of IP device for different time(a) $t = 0$, (b) $t = 10$, (c) $t = 20$, and (d) $t = 30$. 161
5.21 Variation of interface elevation $\zeta_c(x,t)$ vs x associated with the wavenumber k_{II} in presence of IP device for different time (a) $t = 0$, (b) $t = 10$, (c) $t = 20$, and (d) $t = 30$. 162
5.22 Variation of (a) $\eta_{max,I}$, and (b) $\eta_{max,II}$ vs T_0 for INP OWC device without and with air compressibility. 163
5.23 Variation of (a) $\eta_{max,I}$, and (b) $\eta_{max,II}$ vs T_0 for IP OWC device without and with air compressibility. 163

List of Symbols

x, y, z:	Cartesian coordinates
u, v, w:	Velocity components
h:	Water depth
k_0:	Wavenumber associated with incident wave
c:	Phase velocity of wave
c_g:	Group velocity of wave
ω:	Angular frequency
λ:	Wavelength associated with incident wave
∇^2:	$\left(= \frac{\partial^2}{\partial x^2} + \frac{\partial^2}{\partial z^2}\right)$ Laplacian operator
δ_{ij}:	Kronecker delta
A:	Amplitude of the incident wave
g:	Acceleration due to gravity
G:	Fundamental solution
(x_0, z_0):	Source point
(x, z):	Field point
H_{ij}, G_{ij}:	Influence coefficients
ν:	Poisson ratio
ρ:	Density of the fluid
ρ_p:	Density of the plate
E:	Young's modulus
Φ:	Velocity potential (function of both space and time)
ϕ:	Spatial velocity potential
ϕ^I:	Incident velocity potential
b_h:	Height of the bottom foundation
h:	water depth

a: Submergence depth of the front wall of the OWC device

b: Chamber length of the OWC device

l: Distance from the origin to the LHS far-field boundary

L_w: Chamber width of the OWC device

r: Radius of the quarter circle

d: Thickness of the front wall of the OWC device

A: Amplitude of the incident wave

$\wedge$: Turbine control parameter

V_0: Air volume above the internal free surface

γ: Specific heat ratio

p_a : Atmospheric air pressure

ρ_a: Density of the air

$\dot{m}$: Mass flow rate of air across the Wells turbine

N: Rotational speed of the Wells turbine

D: Turbine rotor diameter of the Wells turbine

p: Air pressure across the turbine

q^S, q^R: Volume fluxes associated with the scattering and radiation problems

$\tilde{A}, \tilde{B}$: Radiation susceptance parameter, radiation conductance parameter

P_w: Mean energy flow rate per unit length across a vertical cross-section normal to the incident wave direction

W : Turbine power output

ω: Angular frequency of the incident wave

H_s : Significant wave height

T_e: Energy period

$T_{1/3}$: Significant wave period

S_I : Incident wave spectrum

$\overline{P}_a$: Average incident wave energy flux for the irregular waves

$\overline{W}_a$: Averaged available power to the turbine

$\overline{\eta}_a$: Average efficiency of the OWC device in irregular waves

$\overline{P}_{a,ann}$: Annual averaged incident wave energy flux in irregular waves

$\overline{\eta}_{a,ann}$: Annual averaged plant efficiency in irregular waves

$S_{I,ann}$: Annual spectral density

η : Efficiency of the OWC device in regular incident waves

F_h : Horizontal wave force acting on the front wall of the OWC device

F_v: Vertical wave force acting on the front wall of the OWC device

$\wedge_{opt}$: Optimum value of the control parameter

y_0: y-coordinate of the center of the quarter circle

E: Energy associated with the incident wave per wave period

η_{max}: Maximum efficiency of the OWC device in regular waves

W_a: Instantaneous power available to the Wells turbine

σ_p: Variance of the air pressure fluctuations

ψ: Frequency of occurrences of sea state

A_i: Incident wave amplitude for each regular wave component

ω_i^{av}: Average frequency of each regular wave component

ζ: Free surface elevation and plate deflection

l_1 : Plate length

k_I: Surface-wave mode

k_{II}: Internal-wave mode

$\eta_{max,I}$: Maximum efficiency due to the surface-wave mode

$\eta_{max,II}$: Maximum efficiency due to the internal-wave mode

s: Density ratio

$\mathcal{Q}$: Uniform compressive force

Abbreviations

KFBC: **K**inematic **F**ree **S**urface **B**oundary **C**ondition

DFBC: **D**ynamic **F**ree **S**urface **B**oundary **C**ondition

BVP: **B**oundary **V**alue **P**roblem

BC: **B**oundary **C**ondition

PTO: **P**ower **T**ake **O**ff

LIMPET: **L**and **I**nstalled **M**arine **P**ower **E**nergy **T**ransmitter

SWL: **S**till **W**ater **L**evel

BEM: **B**oundary **E**lement **M**ethod

WEC: **W**ave **E**nergy **C**onverter

OWC: **O**scillating **W**ater **C**olumn

PWEC: **P**iezoelectric **W**ave **E**nergy **C**onverter

Chapter 1

Introduction

1.1 Preamble

Global energy requirements are gradually rising as a result of population growth and industrialization. It is significant to remember that developing nations have significantly contributed to the population growth, which has increased by 2 billion in just one generation. The prevention of energy crises is one of the most overlooked problems of the modern era (see Kannan and Vakeesan [8]). As a result, the demand for energy is rising rapidly in order to fulfill the demands of the expanding population in the world. According to the World Energy Outlook (WEO) 2007, non-conventional energy sources such as crude oil, coal, and gas are the leading resources for the world energy supply and are projected to fulfill approximately 84% of energy demand in 2030 (Shafiee and Topal [9]). Accessible energy is inadequate for the people due to numerous factors such as the advancements profile of a country, the financial circumstances of people, and the nature of technological development of the country. The environment is severely contaminated as a consequence of the emissions of various gases, especially CO_2 emissions produced by the combustion of fossil fuels, which have been considered the dominant cause of the observed change in the global climate. Moreover, implementing non-renewable energy sources would not meet energy demand since these non-renewable energy sources are exhaustible and limited. In addition, the uneven distribution of non-renewables around the world gives rise to conflicts in terms of price fluctuations in the fossil fuel markets and concerns regarding supply security. It can be only assumed that this trend will get worse as fossil fuels become scarcer. As a result, most nations are keen to reduce their reliance on foreign fuel supplies in order to maintain their sovereignty and political stability.

In the present scenario, it is expected that with minimal environmental impact, renewables such as solar, wind, and hydropower, etc., will offer "greener" alternatives in place of non-renewable systems like hydrocarbon combustion engines and coal-powered co-generation power plants in

the foreseeable future. Furthermore, renewable energy has numerous advantages over fossil fuels: (i) renewable energy can provide consistent eco-friendly electricity that addresses climate change issues and helps preserve our planet, and (ii) renewable energy can reduce the over-reliance on fossil fuel suppliers and help oil-importing countries to expand their roles in global markets by establishing a new economic sector (see Mengi-Dinçer et al. [10]). Out of various renewable energy sources, wave energy has flourished as one of the most promising renewable energy sources due to its significant advantages, such as (i) negligible environmental impact, (ii) high energy density (about 2–3 kW/m^2, whereas solar and wind energy typically range from 0.1 to 0.5 kW/m^2). Nevertheless, the levelized-cost of wave energy is still very high (ranges from 90MWh to 490MWh) as compared to the conventional coal-powered power plant (about 44.40MWh)(see Cheng et al. [11]), (iii) high availability (around 90%) and natural seasonal variations of the wave energy, which accomplish the demand for electricity in a moderate climate. In addition, ocean waves have the ability to traverse long distances with minimal energy waste. A wave contains kinetic as well as gravitational potential energy, and the total energy of ocean waves is relevant to the two factors, such as wave height and wave period. Moreover, the power carried by ocean waves is usually expressed in Watt per meter of incident wavefront, and it is proportional to the square of wave height and period. A significant portion of the world's wave energy resource, with an average order of magnitude of a few tens of kW/m, can be found in the polar regions of the northern and southern hemispheres, respectively (see Fig. 1.1 by Gunn and Stock-Williams [1]).

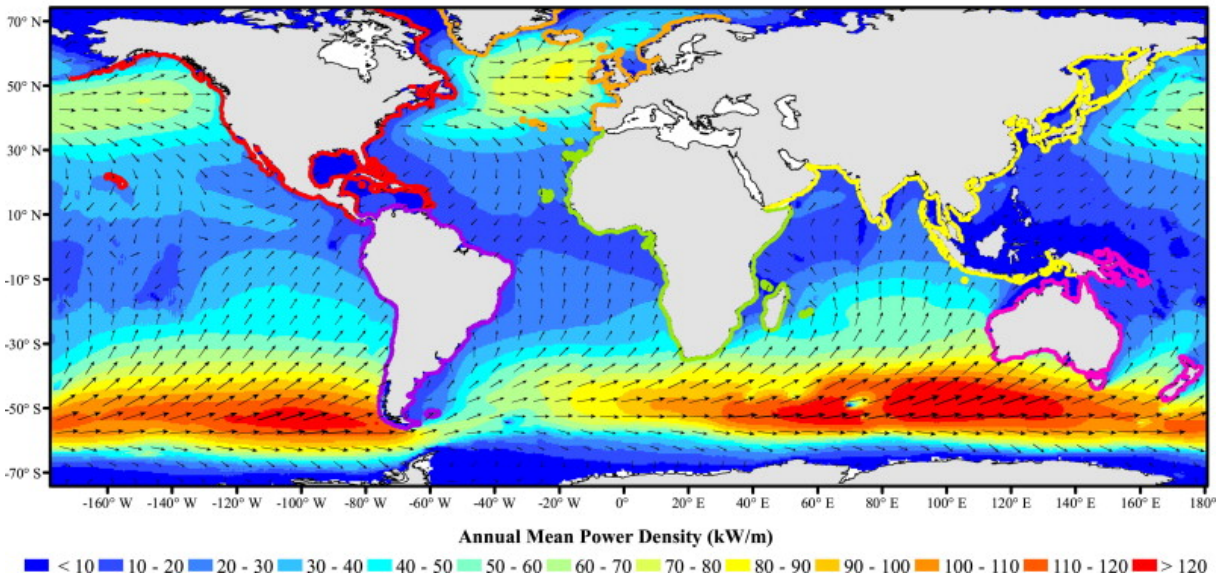

FIGURE 1.1: Global wave resource map. Image courtesy of Gunn and Stock-Williams [1]

According to an engineering perspective, the wave characteristics are mainly based on the four physical quantities: wave height, wave direction, wave period, and phase lag. Further, various physical phenomena related to these parameters are listed as (i) refraction, (ii) diffraction, (iii) reflection, (iv) shoaling and breaking, and (v) friction and large-scale vortex formation and

shedding, etc. In this circumstance, since 1950s, there has been a substantial advancement in understanding the appropriate hydrodynamics associated with various types of structures. Before the 1970s, physical problems were primarily handled theoretically or via the help of physical model tests, and most of the research was based on rigid structures. Furthermore, the physical problem becomes more complicated with the addition of structural permeability and flexibility, and it becomes quite challenging to analyze the wave-structure interaction problems analytically. Nevertheless, due to the development of high-speed computers, there has been substantial progress in the numerical modeling of wave-structure interaction problems over the past three decades. In this regard, the boundary element method (BEM) is one of the most extensively used techniques. In earlier days, this BEM technique was widely applied to handle the water wave interaction with rigid and impermeable structures. Some advantages of the present BEM-based numerical method over the other analytical and numerical solution techniques are the following.

- The eigenfunction expansion method is the most frequently used analytical solution technique in wave structure interaction problems. To use the eigenfunction expansion method, the domain of the physical problem has to be in regular shape like rectangular, circular, etc. However, the eigenfunction expansion method is not applicable to the problems having undulated seabed. To handle these irregular shaped domains, the boundary element method is a very effective tool that can provide the solution with sufficient accuracy.

- In the finite element method and finite difference method, the total domain of the physical problem needs to be discretized. However, in BEM, only the boundary of the domain needs to be discretized. Thus, in BEM, the dimension of the solution space is reduced by one unit with respect to the physical space. Consequently, the computational time is significantly reduced. A schematic diagram of discretized domains based on various numerical methods is provided in Fig. 1.2 for better clarity.

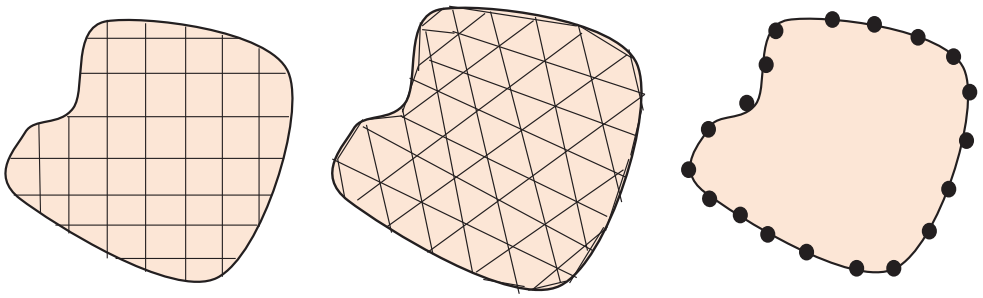

(a) FDM (b) FEM (c) BEM

FIGURE 1.2: Schematic diagram of discretized domain based on (a) finite difference method, (b) finite element method, and (c) boundary element method.

In the context of the present thesis, major emphasis is given in developing mathematical modeling and associated boundary element method-based solutions to deal with surface gravity wave interaction with various types of wave energy converter devices, such as the oscillating water column device and the piezoelectric wave energy converter device in the framework of linearized wave-structure interaction theory. The hydrodynamic performance and efficiency of the oscillating water column wave energy converter device are investigated in the presence of regular and irregular incident waves using the boundary element method. Further, for problems in finite water depth, bottom undulation is considered. Moreover, to analyze the annual average efficiency of the OWC devices in real sea conditions, the incident wave spectrum, along with the sea states representing the local wave climate at the OWC plant site in Pico, Portugal, is considered. The hydrodynamics of the hybrid wave energy converter device consisting of a piezoelectric plate and the OWC device is analyzed in the frequency domain as well as in the time domain. A multi-parameter optimization based on the Taguchi method is provided to optimize various input parameters to maximize the power output from the devices. Unlike the case of wave motion in a homogeneous fluid domain, wave motion in a two-layer fluid having an interface is very common in continental shelves and estuaries. Such waves lead to the generation of plane progressive waves in surface and internal modes. The mutual interaction of these waves with the OWC device is an interesting branch of study and is of significant importance in coastal engineering practices. For the two-layered fluid case, two types of OWC devices are considered in the present thesis: (*i*) front wall of the OWC device does not intersect the interface of the two layers (*INP OWC device*), and (*ii*) front wall of the OWC device intersects the interface of the two layers (*IP OWC device*). For most of the physical problems, the various parameters associated with the hydrodynamic efficiency of the wave energy converter devices are derived using the Green's second identity. Further, all the quantities of engineering interest, such as the average electric power in the output system per unit width, annual average, and the maximum efficiency of the OWC device are provided in a detailed manner. For a variety of physical problems and for specific parametric values, numerical convergence of the solutions is provided. The present work emphasizes the mathematical modeling of wave energy converter devices in the presence of seabed undulations under the action of regular and irregular incident waves generated in single and two-layer fluid domains. Various resonance mechanisms associated with the shapes and structural configurations of the hybrid device consisting of the piezoelectric plate and the OWC device are analyzed. The findings of various computational results are validated with known results available in the literature. In the subsequent sections, a detailed literature review of the OWC device and the piezoelectric plate is provided in the presence of regular and irregular incident waves and integration with breakwaters in both the single and two-layer fluid model cases. Further, a brief literature review associated with the parameters optimization techniques is also provided. Moreover, the basic equations associated with the linear water wave theory for water wave propagation in the homogeneous and stratified fluid medium are derived

in a detailed manner. The constant and linear boundary element approaches are also provided in detail.

1.2 State of the art

Wave structure interaction problems require an understanding of both the fluid phenomena in contact with the atmosphere and the structure's behavior in contact with the fluid, in addition to the phenomena of wave propagation. In Book II, Prop. XLV of Principia, 1687, Sir Isaac Newton first made an attempt at the development of the theory of water waves (Craik [12]). Following Newton's work, French mathematicians Laplace, Lagrange, Poisson, and Cauchy made significant theoretical advances in the linear theory of water waves (Craik [12]). Later, between 1830-1850, Russel, Green, Kelland, Airy, and Earnshaw made significant contributions to the development of linear water wave theory. Airy [13] book on "Tides and Waves" has been considered a major contribution to water wave theory. Airy's attempt on the water waves is restricted to the shallow water waves. Stokes [14] developed higher order wave theories in 1847, and following the same, Boussinesq [15] developed long wave theories in 1872, and Michell and McCowan developed wave theory for limiting wave heights in 1893 and 1894 (Craik [12]). The books of Lamb [16], Mei [17], Dean and Dalrymple [18], and Linton and McIver [19] and the literature cited therein provided the details of various phenomena associated with water waves propagation. In the last few decades, the extraction of energy from ocean waves has received a lot of attention on a worldwide basis. Over this period of time, several wave energy extraction devices have been developed, and most of them are based on the standard working mechanisms of the oscillating water column devices. The conventional OWC device consists of an open-ended, hollow structure that is partially immersed with its open end downwards, trapping a volume of air above the internal free surface. The internal free surface of the device chamber rises and falls in response to an incident wave train due to the pressure fluctuation at the open lower end. This causes a high-speed flow of air to pass through a constricted opening in the structure, which includes an air turbine and generator set that converts the energy into electricity. Masuda developed this concept in 1947 and successfully applied it to self-power navigation buoys (see Antonio [2]). In the subsequent context, a detailed literature review associated with various types of wave energy converter devices is provided.

1.2.1 Classification of wave energy converter devices

Numerous ideas and concepts have been proposed to harness the wave power from ocean waves. The wave energy extraction technologies are classified into various categories based on the wave heights, their locations (shoreline, near-shore, offshore), and working mechanisms. According to the classification based on the working mechanism of wave energy converter devices, wave

energy converters (WEC) are classified into various categories, such as oscillating water column devices, oscillating bodies, and overtopping devices. A comprehensive classification of various wave energy converter devices is provided in Fig. 1.3.

1.2.2 Oscillating water column wave energy converter device

The OWC device consists of a partly submerged collecting chamber and a PTO system that incorporates a Wells turbine positioned on top of the chamber to prevent it from coming into direct contact with salt water. In an OWC device, the wave travels through a partially submerged collector chamber with an air column above the water column. The water inside the caisson chamber oscillates due to the hydrodynamic pressures on the structure caused by the continuous impact of the wave crest and trough. The water level inside the OWC device chamber rises as a wave crest enters, compressing the air column as a result of the damping from the power take-off (PTO) device, which generates pneumatic power. The water surface falls down during the action of the wave trough and creates a vacuum that draws air into the chamber. Out of various technologies available to harness ocean wave energy, the oscillating water column (OWC) device is one such technology that has some crucial advantages over other wave energy converter technologies.

One such advantage is that OWC devices can effectively work in very low-frequency wave motion (order of 0.1 Hz) (see Evans and Porter [5] for details). Some of the other advantages of OWC devices are the following: (i) these kinds of devices have no moving parts in the ocean water, (ii) these are generally installed along the shoreline or attached to a nearshore breakwater, and, as a result, the construction and maintenance costs are low, (iii) no underwater cables are required to transfer energy (see Heath [20]). The concept and technological progress in harnessing energy from ocean waves started since 1965 when a model for a floating OWC device was built in Japan (Antonio [2]). Subsequently, the OWC device was constructed at various locations throughout the World (Luo et al. [21]) such as at Sakata, Japan (60 kW), Pico, Portugal (400 kW)(see Fig. 1.5), Limpet, Scotland (500 kW), and more lately at Mutriku, Spain (300 kW).

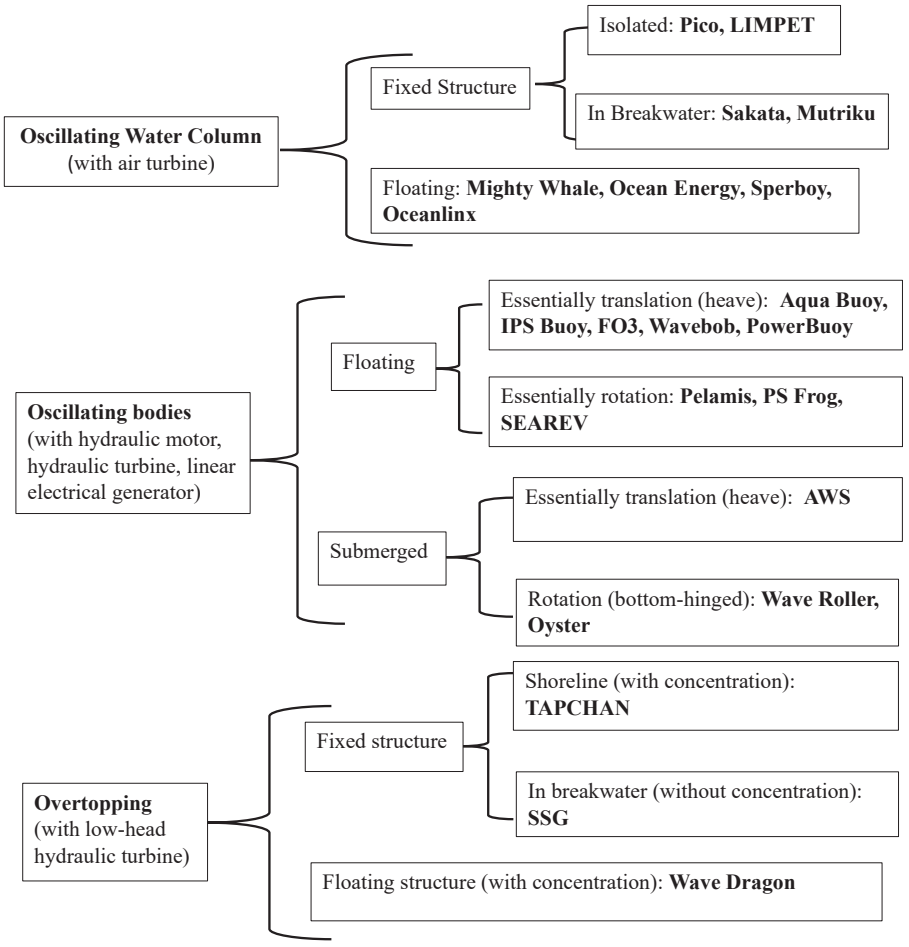

FIGURE 1.3: Classification of wave energy converters based on their working mechanisms Antonio [2].

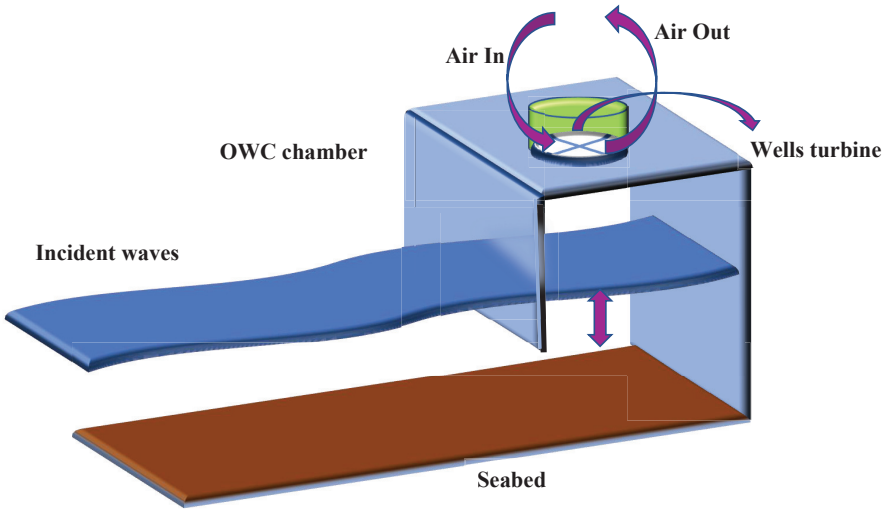

FIGURE 1.4: The working principle of OWC caisson device subjected to (a) wave crest, and (b) wave trough.

FIGURE 1.5: The OWC wave power pilot plant on the island of Pico, Azores, Portugal (Falcão et al. [3]).

1.2.3 Piezoelectric wave energy converter device

The concept of wave energy converters with flexible structures and hybrid multi-energy systems appears to be a new trend in the marine energy industry. A flexible floating structure is comprised of bio-compatible soft and flexible piezoelectric materials. Consequently, these piezoelectric materials are intriguing because they can generate electric potential when deformed by the sensor effect. Further, these piezoelectric wave energy converters (PWECs) have no limitations of shape, size, and high energy density. Although the piezoelectric wave energy converter device is used to generate electricity typically in the order of watts to kilowatts, this amount of generated electricity is enough to run low-power electronics such as LEDs, wireless routers, PCs, ocean buoys and sensors, etc. Additionally, these PWECs are environmentally sustainable, durable, inexpensive, and have no requirements for frequent maintenance. The PWECs consist of a submerged elastic plate with the attachment of piezoelectric layers on both sides of the plate, which can extract energy from the ocean waves due to the variations of tension along the plate (see Renzi [4], and Buriani [22]). A bimorph configuration of the piezoelectric plate is provided in Fig. 1.6. The piezoelectric plates can be integrated with various offshore structures like oil platforms, windmills, sea-crossing bridges, etc., not only to generate electricity but also can be used to dampen ocean wave energy to protect the offshore structures from wave loads. In general, piezoelectric materials generate electricity when the external stress is incurred. So, the relatively high kinetic energy content of ocean waves can be used to apply external stresses on the piezoelectric material, and consequently, the kinetic energy can be converted into useful

electricity. In summing up, piezoelectric wave energy converter devices in ocean waves can be considered one of the easiest and most innovative technologies to generate electricity.

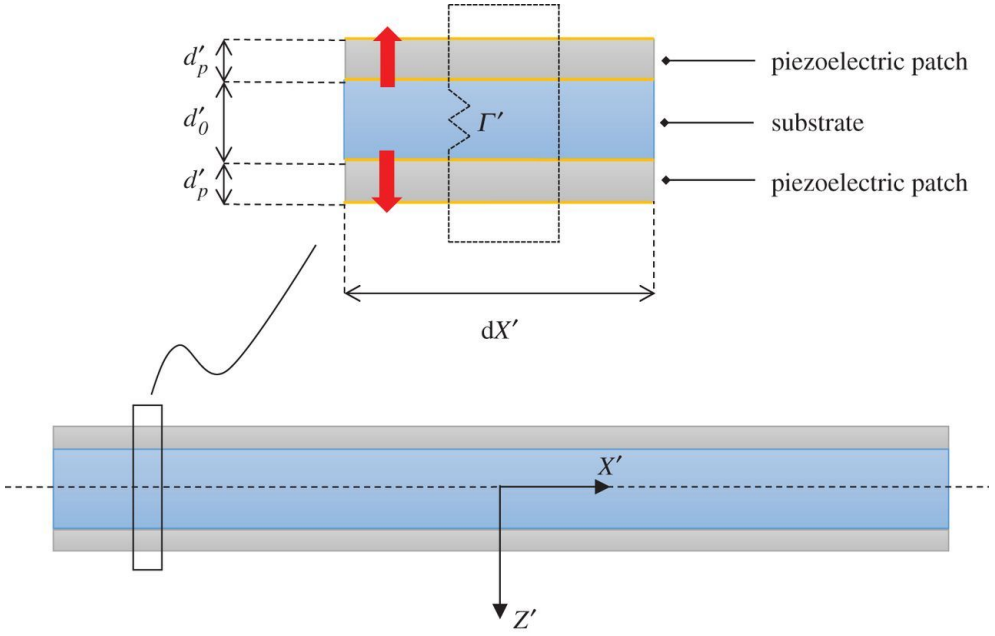

FIGURE 1.6: Illustration of the piezoelectric bimorph (Renzi [4]).

1.2.4 Hydrodynamics of the oscillating water column device in the presence of regular incident waves

Numerous theoretical and technological advances have been achieved in order to create an effective OWC device. Evans [23] and Falnes and McIver [24] carried out pioneer research on wave energy absorbers using rigid body models. The hydrodynamic performance and efficiency of the OWC device are described by oscillatory uniform surface pressure distributions in the water column for a given incident wave. The capture ratio of the OWC device is expressed as the ratio between the average air power output of the chamber and the incident wave energy flux per device length. The hydrodynamics of the OWC device is influenced by the chamber configuration and the wave energy distribution at the opening of the OWC device chamber. Further, in order to provide information about the OWC design, it is necessary to estimate the hydrodynamic performance of the OWC device under typical operating conditions, such as the motion of the oscillating water column is assumed to be a resonant piston-like motion and the water in the confined region within the OWC device chamber is excited into an antisymmetric sloshing mode (Evans and Porter [5]).

Enhancing the performance of the OWC devices is an essential consideration for industrialization, and therefore, it has been the focus of extensive studies for many researchers. In order to improve the performance and efficiency of the OWC devices, recent research interests have focused on

various modifications to the geometrical configuration of the OWC devices. In this context, some of the concepts such as various front wall geometry Kelly et al. [25], Koley and Trivedi [26], Wang and Zhang [27], Rodríguez et al. [28], chamber configuration Boccotti [29], Martins-rivas and Mei [30], Gouaud et al. [31], Malara and Arena [32], Vyzikas et al. [33], Malara and Arena [34], Trivedi et al. [35], Mayon et al. [36] and multi-chamber OWC devices Rezanejad et al. [37, 38], Wang et al. [39] are examined. These studies demonstrated that the geometrical configuration of the OWC device plays a significant role in enhancing the hydrodynamic performance and efficiency of the OWC device for a wider range of incident wave frequencies.

When ocean waves propagate toward coastline areas, the incident wave energy is constantly modified due to the bottom effects. Bottom friction causes a variety of physical phenomena such as wave refraction, shoaling and breaking, etc. Further, the undulated seabeds are created by the phenomena of sediment transport and the growth of sand bars in a wave-induced boundary layer near the sea floor. Specifically, when the incident and reflected waves combine together, a standing wave pattern forms near the boundary layer of a horizontal sea bed and promotes sediment deposition. These sinusoidal types of bed profiles are generally found in the nearshore regions. Moreover, multiple sand bars/ripples are usually found on relatively mild beach locations whose slope is less than 0.005, and the number of bars/ripples can range from 3-17 (see Mei [40]). Therefore, it is of utmost important to analyze the effect of seabed parameters on the hydrodynamic performance of the OWC device. In order to improve the capture power of the OWC device, Ning et al. [6], Rezanejad et al. [7], Koley and Trivedi [26], Vyzikas et al. [33], Rezanejad et al. [37] investigated the performance of the OWC device placed over the undulated seabed. These studies illustrated that the bottom undulation significantly modified the resonance conditions.

To study the efficiencies of OWC devices in real sea conditions and to include the nonlinearity effects, Luo et al. [41], Teixeira et al. [42] and Elhanafi et al. [43] used a computational fluid dynamics (CFD) based numerical tool. Recently, Mayon et al. [36] analyzed the impact of parabolic reflecting breakwater on the hydrodynamic efficiency of an OWC device having a cylindrical cross-section. The study demonstrated that the cylindrical OWC device placed at the parabolic focal point is able to capture more amount of incoming wave energy as compared to the open sea conditions. Wang and Zhang [44] investigated the performance of an offshore floating OWC device, which is mounted over a submerged horizontal plate. This study led to the following observations: (i) the combined OWC and plate system is more effective in harnessing ocean power as compared to the breakwater integrated OWC device, (ii) the OWC device attains maximum efficiency when the plate length is twice the length of the chamber width in short wave regime, and (iii) smaller draft of the front wall significantly enhances the effectiveness of the OWC device. Mohapatra et al. [45] studied the impact of chamber configuration and bottom slopes on the performance of the OWC device using CFD and boundary element method. A dynamic meshing strategy is developed in the solution technique to acquire the motions of

the floating OWC device for different wave features. Ning et al. [46] performed rigorous scaled model tests to design an effective OWC device. Recently, Gubesch et al. [47] demonstrated a design process to enhance the hydrodynamic performance of an asymmetrical OWC device using CFD-based numerical results and also using rigorous model test results.

1.2.5 Hydrodynamics of the breakwater integrated oscillating water column device

Traditionally, breakwaters are constructed in nearshore regions to protect the harbor from wave attacks. Nowadays, due to climate change, the sea level rises, and extreme events frequently occur (Vicinanza et al. [48]). In this scenario, only an increase in seawall height is not a fruitful solution. Moreover, the demand for renewable energies is continuously growing in every part of the world. In this context, the combination of breakwaters and wave energy converters can provide effective and efficient solutions to the aforementioned problems. These breakwater-integrated OWC devices have several advantages such as (i) this hybrid structure can effectively act as a wave barrier and can produce electricity using ocean wave energy (Falcão and Henriques [49]), (ii) the construction cost for this hybrid structure is considerably less provided that the breakwater would be built even without the inclusion of OWC device (Vicinanza et al. [48]), (iii) the maintenance and installation of the breakwater-integrated OWC device is easier compared to the stand-alone OWC device (Mustapa et al. [50]), (iv) this hybrid OWC device can effectively work and withstand during harsh wave environment, and (v) the durability of the breakwater-integrated OWC device is more compared to the stand-alone OWC device as the main components such as the turbine can be kept safely at the backside of the breakwater (Mustapa et al. [50]). Müller and Whittaker [51] used $1:36$ scale model to analyze the effect of wave forces on the inclined front wall of a nearshore OWC device. It was concluded that the impact of wave pressure on the front wall of the OWC device reduces significantly in the case of an inclined wall compared to the vertical wall. Müller and Whittaker [52] conducted model tests for $1:36$ scale model of the Islay prototype wave power station and found that large vortices developed around the thin front wall of the OWC device. These vortices dissipate wave energy, and as a result, the efficiency of the OWC device is reduced. To overcome this problem, a small thickness in the front wall of the OWC device should be considered, as suggested by Müller and Whittaker [52]. Boccotti [53] performed an experimental study on two different types of breakwater-integrated OWC devices and concluded that resonance between the random process of wind-generated waves and oscillations inside the caisson could be achieved through the regulation of air quantity. Further, it was suggested that the breakwater-integrated OWC device is more effective in protecting a port compared to the conventional caisson breakwater due to the wave energy absorption, which reduces the wave height and overtopping discharge significantly before the breakwater. Thiruvenkatasamy et al. [54] studied the wave forces on

the OWC array by conducting rigorous model tests using a 1 : 50 scale model. It was reported that (i) an air pressure release system could be incorporated to minimize the wave force, and (ii) the wave force depends on the damping of an OWC airflow. Boccotti [29] studied the performance of a breakwater-integrated OWC device, which is connected to the open sea through a small opening. It was found that the OWC device plant can absorb the total incoming wave energy when standing waves are formed. Further, it was observed that due to the swelling phenomena, the breakwater-integrated U-shaped OWC plant could absorb more incident wave energy compared to the conventional OWC device. Boccotti et al. [55] studied the performance of the breakwater-integrated U-shaped OWC device experimentally and showed that due to the small height of wind waves, the breakwater-integrated U-shaped OWC device is more stable than the conventional breakwater. The stability analysis and capture factor of the OWC caisson breakwater were discussed by Liu et al. [56] using rigorous model tests. It was concluded that under extreme sea conditions, the OWC device structure is stable, and the capture factor is also strong. Strati et al. [57] studied the performance of a breakwater-integrated U-shaped OWC device in various sea climates. It was concluded that this U-shaped OWC device acts differently in swell-dominated and wind-dominated sea states. In a wind-dominated sea state, the performance of the OWC device is enhanced due to the occurrence of resonance. On the other hand, turbine rotational speed plays a key role in enhancing the efficiency of the OWC device in a swell-dominated sea state. Malara et al. [58] performed a time-domain analysis to study the performance of a breakwater-integrated U-OWC device. They have used experimental data to calibrate various coefficients associated with the performance of the OWC device. The study was extended by Malara et al. [59] to include the three-dimensional effects on the performance and efficiency of the U-OWC device. It was shown that if the OWC device is wider enough, a two-dimensional analysis can accurately predict the performance of the OWC device. However, for a narrow OWC device, three-dimensional analysis is needed to obtain accurate results. Using model tests, Ashlin et al. [60] studied the wave forces acting on various components of the breakwater-integrated OWC device. It was concluded that (i) the wave forces acting on the front wall of the OWC device are directly proportional to the wave steepness, and (ii) vortices are formed near the front wall, which increases the wave steepness, and as a result, the wave flows into the OWC device chamber reduces. Spanos et al. [61] used a non-linear stochastic method to analyze the dynamic response of U-OWC devices equipped with linear and non-linear power take-off systems. In this work, the problem of estimating the reliability and efficiency of the OWC device is addressed for wave excitation generated by a certain power spectrum.

1.2.6 Hydrodynamics of the oscillating water column device in the presence of irregular incident waves

In real sea conditions, the incident waves are mostly irregular in nature and can be modeled as a superposition of wave components with different frequencies (Goda [62]). Therefore, it is very important to analyze the performance and efficiency of the OWC device under irregular/random waves. De O Falcão and Rodrigues [63] developed a stochastic method to analyze the performance of an OWC device in random sea waves. The random incident waves were represented using the energy spectrum, and the severity of the wave climate is represented using the concept of sea states. It was observed that the controlled rotational speed of the turbine plays an important role in enhancing the amount of produced energy compared to the control valve system. Josset and Clément [64] used the random phase method to synthesize various sea states from the Pierson–Moskowitz spectrum and performed a time-domain analysis to study the efficiency of the OWC wave power plant for each sea state. It was observed that the productivity of the power plant depends on the turbine characteristics. Sheng and Lewis [65] studied the effect of air compressibility on the hydrodynamic performance and power capture factor of floating and fixed-type OWC devices. In this study, the following results are concluded: (i) for fixed OWC devices, air compressibility significantly reduces the power conversion in the long-wave regime, and a reverse trend is observed in the short-wave regime; (ii) large air compressibility plays a key role in reducing the performance of a floating OWC device. Within the limits of linear water wave theory, Rezanejad et al. [66] analyzed the performance of an OWC device placed over a step bottom in regular and random sea waves. Further, the results associated with the efficiency of the OWC device are obtained using the model tests. It was reported that the efficiency and performance of the OWC device depend strongly on the incident wave period and damping characteristics of the turbine compared to the incident wave height. Jalón and Brennan [67] developed a physics-based simulation model to investigate the efficiency and structural durability of a fixed OWC device in random sea waves. It was reported that the hydrodynamic performance and durability of the OWC device depend on the draft of the OWC device.

1.2.7 Hydrodynamics of the piezoelectric wave energy converter device

The concept of wave energy converters with flexible structures and hybrid multi-energy systems appears to be a new trend in the marine energy industry. These piezoelectric materials are intriguing because they can generate electric potential when deformed by the sensor effect. Further, these piezoelectric wave energy converters (PWECs) have no limitations of shape, size, and high energy density. Moreover, these PWECs are environmentally sustainable, durable, inexpensive, and have no requirements for frequent maintenance. The PWECs consist of a submerged elastic plate with the attachment of piezoelectric layers on both sides of the plate,

which can extract energy from the ocean waves due to the variations of tension along the plate (see Buriani [22]). Wave power extraction by the piezoelectric materials is still at an immature stage. A novel piezoelectric wave energy harvester comprises a cantilever substrate attached by piezoelectric patches and a proof mass. The collected electric power is produced by the electromechanical coupling effect of the piezoelectric patches from the transverse wave motion of the water particles in the framework of linear water wave theory and the classical elastic beam model (see Xie et al. [68]). These studies demonstrated that the power generated by the PWECs significantly depends on the wave parameters, such as the wave height, water depth, and structural parameters, like the ratio of the width to the thickness of the cantilever and the ratio of the proof mass to the cantilever mass, etc. Further, Renzi [4] provided the fully hydroelectromechanical-coupled dynamics of a submerged piezoelectric wave energy converter device. It was demonstrated that a significant amount of energy is extracted by the PWEC device at resonance conditions, and it was found that these resonances arise due to the short crested component of the wave. Furthermore, it was demonstrated that the short-crested flexural gravity waves produced more power than the long-crested waves. Xie and Wang [69] designed a composite piezoelectric buoy energy harvester using the finite difference method. In this research, the following conclusions were drawn: (i) the root mean square of the generated power is significantly influenced by the wave height and the speed of the ocean waves, and (ii) the root mean square of the generated power increases as the wavelength and fixed end thickness of the tapered cantilever decrease. Zhou et al. [70] analyzed the dynamic responses of the PWEC device for various stoppers. It was noticed that the stopper configuration significantly enhances the performance of the PWEC device. Zheng et al. [71] and Vipin and Koley [72] demonstrated that the plate edge conditions and configurations play a significant role in altering the characteristics of resonating frequencies and, consequently, the power extraction by the breakwater-integrated PWEC device. From the aforementioned studies, it is seen that the resonating incident wave frequencies play an important role in wave power extraction by the PWEC plate. Enhancing the bandwidth of frequencies for which maximum power extraction occurs is one of the crucial aspects that need to be explored.

1.2.8 Water wave interaction with the costal structures in the presence of the two-layer fluid model

In some coastal areas, water density is not uniform throughout the water depth due to the (i) mixing of fresh river water with the saline seawater and (ii) solar heating of the upper layer water (see Manam and Sahoo [73] and Koo [74]). As a result, the two-layer fluid model is often used to study the interaction of water waves with coastal structures (Behera et al. [75]). In the two-layer fluid model, internal waves are generated and propagate along the interface between the two layers. Moreover, in the two-layer fluid system, it is standard to assume that the upper

layer fluid is lying above the denser lower layer fluid. This assumption is especially valid in the ocean, where there frequently exists a thin pycnocline with a significant variation in the density, and the water is well mixed above and below it (see Das et al. [76]). In addition, in a real ocean environment, the two-layer fluid model arises in Norway's fjords, bodies of water that consist of a layer of fresh water about 10m thick on top of an intense body of salt water (see Cadby and Linton [77]). Lamb [16] reported that the dispersion relation for the two-layer fluid model has two roots for a given frequency; one corresponds to the free surface waves, and the other corresponds to the internal waves. The mathematical model and associated formulations for the wave propagation in a two-layer fluid medium were available in the classical works of Linton and McIver [78], Cadby and Linton [77], Barthélemy et al. [79], Linton and Cadby [80], and the literature cited therein. Chamberlain and Porter [81] used a variational approach to analyze the wave scattering in a two-layer fluid having bottom undulations in a three-dimensional context using linearized water wave theory. Various results were presented to show the energy transfer between the surface and interfacial waves induced by bottom variations. Kashiwagi et al. [82] studied the wave diffraction and wave-induced motions of a freely floating body in a two-layer fluid system. It was reported that the motions of the floating body due to the effect of internal waves have relatively smaller amplitudes. However, for specific values of the density ratio, the wave-induced motions due to the internal wave are higher and are of the same order as those induced by the surface waves. Alam et al. [83] used the perturbation analysis and numerical simulation tools to analyze the Bragg resonance phenomena that occur due to the rippled seabed in a two-layer fluid medium. Behera and Sahoo [84] and Behera et al. [75] studied the water waves interaction with thick porous structures of different shapes and configurations in a two-layer fluid. The effects of density ratio, interface location, heading angle of the incident wave, and surface and internal wave modes on wave scattering are analyzed in a detailed manner. Panda and Martha [85] used the Fourier transform technique to analyze the effect of an undulated porous bed on the wave scattering in a two-layer fluid system. It was observed that the incident wave energy corresponding to the surface wave mode could be transferred to the reflected and transmitted energies corresponding to the internal mode for all possible heading angles of the incident waves. However, the transfer from the internal mode to the surface mode is only possible for smaller values of the heading angle. Medina-Rodríguez and Silva [86] studied the interaction of the obliquely incident wave with a submarine trench in a two-layer fluid system using the eigenfunction expansion method. This study showed that the reflection and transmission of wave energy corresponding to the surface wave mode are higher than those corresponding to the internal wave mode. Medina-Rodríguez and Silva [87] used the eigenfunction expansion method to investigate the efficiency of an oscillating water column device placed in the presence of an asymmetric submarine trench at the bottom in a two-layer fluid medium. It was reported that the efficiency of the OWC device depends on various factors like the density ratio, interface location, depth of the trench, and the distance of the trench from the OWC device. Islam et al. [88] studied the radiation and scattering problem in a two-layer

fluid system when a circular disc is placed in a lower-layer fluid. They found that the interface location had significant effects on the hydrodynamic force acting on the disc. Recently, Barman and Bora [89] studied the interaction of water waves by a composite breakwater located over the porous seabed in a two-layer fluid system. It was reported that the seabed characteristics have a significant impact on the wave load acting on the wall, reflection, and transmission phenomena.

1.2.9 Optimization of parameters associated with the wave energy converter devices

In recent years, the optimization of wave energy converter devices has received a lot of attention. A proper combination of the shape parameters, PTO coefficients, control algorithms, and seabed parameters is required to be optimized to enhance the performance of the wave energy converter devices in terms of maximum power extraction, resonating frequencies, and associated bandwidth. A number of research works were carried out to optimize various parameters associated with the wave energy converter devices. In this regard, a sequential optimization procedure is adopted by Bouali and Larbi [90] and Hayati et al. [91] in which the geometrical shape parameters of the OWC devices were optimized based on specific wave conditions. Differential evolution algorithm-based optimization procedure is adopted by He et al. [92] to design and optimize a square array wave energy converter device. For the sake of comprehensive multi-parameter optimization of various outputs associated with the two-body wave energy converter devices, Al Shami et al. [93] and Bao et al. [94] used the well-known Taguchi method. This particular Taguchi method was widely applied in the 1950s for process optimization of chemical industries Al Shami et al. [93]. This method is best suitable for systems in which the outputs from the systems are dependent on various input parameters, which are correlated with each other up to some extent. The Taguchi method depends on choosing orthogonal arrays, which reduces the number of simulations drastically in the optimization process (see Al Shami et al. [93] for details).

1.3 Motivation and outline of the thesis

The objectives of the present work are provided as follows:

- Developing BEM based numerical tools to deal with surface gravity wave interaction with OWC and piezoelectric plate wave energy converter devices placed over undulated seabed.
- Investigating various parameters associated with the hydrodynamics and performance of the OWC and piezoelectric plate devices for a wider range of wave, seabed and structural parameters.

- To investigate the effect of irregular incident waves on the hydrodynamics of the OWC device by considering the local wave climates with appropriate sea states and incident wave spectrum.
- To study the performance of OWC and piezoelectric plate devices in frequency as well as in time domain. Emphasis is provided to analyze the resonances to maximize the power output.
- To study the performance of OWC devices in two-layer fluid system.
- To optimize the parameters associated with seabed and the hybrid wave energy converter devices consisting OWC device and piezoelectric plate device based on the Taguchi mehtod.

The content of the thesis is divided into six chapters depending on the various types of physical problems investigated. Chapter 1 is introductory in nature. In Chapters 2 to 5, the mathematical modeling, BEM-based solution technique, and analysis of several parameters associated with the performance of OWC and PWEC devices in the presence of regular and irregular incident waves are discussed. These chapters also include the hydrodynamics of OWC devices in a two-layer fluid system and associated time-domain analysis. Finally, Chapter 6 summarizes the total work presented in the thesis and also provides the future research scope. In Chapter 1, basic introduction, detailed literature review, motivation behind the present work, outline of the thesis and mathematical preliminaries are provided. When ocean waves propagate toward the shoreline areas, the incident wave energy is significantly modified due to the bottom effects. As a result of bottom friction, several physical phenomena occur, such as wave refraction, shoaling and breaking, etc. Therefore, it is very important to take into account the undulated bottom topography to analyze the hydrodynamic performance of the OWC device, which is placed on a vertical cliff in the shoreline areas. In this background, in Chapter 2, the OWC device is considered, which consists of a wave chamber in which the rear wall is vertical rigid in nature and the front wall is sloping type. One of the advantages of using a sloping front wall OWC device is to reduce the horizontal force, and the slope causes a vertical force acting downwards, which in turn stabilizes the OWC caisson. The other advantage is that the inclined front slope increases the capture efficiency of the OWC device (see Müller and Whittaker [52] for details). Further, in the present study, the thickness of the OWC device wall is considered. This has advantages over the thin wall (i.e., the thickness is negligible) as the thin structure can induce vortex easier than the thick one. Due to this reason, there is a reduction in energy losses for an OWC device having considerable wall thickness. Moreover, to incorporate the effect of nearshore wave energy transformation, the undulated bottom is considered in this chapter. To handle the undulated bottom topography, a coupled eigenfunction expansion-boundary element method is used. The numerical convergence of the coupled eigenfunction expansion-boundary element method is presented. The effects of the width of the OWC device chamber, front wall submergence depth

and inclination with the vertical axis, and the bed undulations on the hydrodynamic efficiency of the OWC device are discussed in detail. Further, the occurrences of resonances due to the shape parameters of the OWC device are investigated.

As an extension of the mathematical modeling of the OWC device under monochromatic regular incident waves, in Chapter 3, the hydrodynamic performances and efficiencies of breakwater-integrated OWC devices are studied under unidirectional random wave environments. Two different types of OWC devices: (i) LIMPET device (sloping-face OWC device, see Heath [20] for details) and (ii) quarter-circle-shaped front wall OWC device (see Patterson et al. [95] for details) are considered for the present study. Some advantages of LIMPET type OWC device over the traditional vertical wall OWC device are the following: (i) the inclined chamber of the LIMPET OWC device offers an easier path for water entry and exit, which reduces the creation of turbulence and, as a result, there is a reduction of energy loss (Heath [20]), and (ii) the inclined front wall significantly reduces the impact of wave forces acting on the OWC device (Müller and Whittaker [52]). It is to be noted that the overtopping can occur due to the sloping wall, and therefore, a wave breaker is needed to install on the sloping front wall (Ciria [96]). During the project of developing a breakwater-integrated OWC device at Siadar, Isle of Lewis, Patterson et al. [95] emphasized the long-term stability of the OWC device against overturning and sliding, which occurs due to extreme water wave pressure. To overcome this problem, Patterson et al. [95] studied the geometrical layout of the OWC device and found that the resultant wave forces on the front wall of the quarter-circle-shaped OWC device act through the heel of the structure, which reduces the overturning moment and enhances the stability of the OWC device. Due to these advantages, a quarter-circle-shaped breakwater-integrated OWC device is considered in the present study. The associated boundary value problem is handled for the solution using the boundary element method. The annual-averaged plant efficiencies of the two aforementioned OWC devices are analyzed as a function of chamber length, submergence depth, turbine rotor diameter, and rotational speed of the Wells turbine.

The concept of wave energy converters with flexible structures and hybrid multi-energy systems appears to be a new trend in the marine energy industry. The hydrodynamic performance of the standalone OWC devices and the piezoelectric plates were studied in real ocean environments. However, there is one major shortcoming in the standalone wave energy converter devices, such as the standalone wave energy converter devices that are unable to absorb a significant amount of incident wave energy. Further, the resonating frequencies can be altered in such a manner that the same lie in close proximity to the most probable wave frequencies associated with the local wave environment. In addition, the bandwidth of the frequencies associated with the higher amount of wave power extraction can be widened to extract the maximum amount of wave power. By keeping these particular aspects in mind, the hybrid wave energy converter device consists of a piezoelectric plate, and the OWC device is proposed in Chapter 4. There are numerous advantages of the hybrid wave energy converter device over the traditional OWC

device and the piezoelectric plates, such as the power extraction by the hybrid wave energy converter device is expected to be more than the standalone OWC device and piezoelectric plate. The resonating frequencies can be altered in the presence of this proposed hybrid device. In addition, appropriate multi-parameter optimization can provide an optimized system for maximum power output in close proximity to the most probable incident wave frequencies along with wider bandwidth. These particular gaps serve as motivation for the present investigation. In the present study, the hybrid wave energy converter device is placed over the undulated seabed. Further, the influence of shape parameters associated with the OWC device and the piezoelectric plate, and parameters related to the sinusoidal seabed profiles on the power extraction by the hybrid wave energy converter device, OWC device, and the piezoelectric plate are analyzed in a detailed manner. Further, a time-domain analysis is carried out. In the time-domain analysis, the Bretschneider spectrum is taken as the incident wave spectrum, and the associated results are generated using the regular wave model.

Unlike the homogeneous water domain, in some coastal areas, water density is not uniform throughout the water depth due to the (i) mixing of fresh river water with the saline seawater, and (ii) solar heating of the upper layer water (see Manam and Sahoo [73] and Koo [74]). As a result, the two-layer fluid model is often used to study the interaction of water waves with coastal structures (Behera et al. [75]). In the two-layer fluid model, internal waves are generated and propagate along the interface between the two layers. Moreover, in the two-layer fluid system, it is standard to assume that the upper layer fluid is lying above the denser lower layer fluid. This assumption is especially valid in the ocean, where there frequently exists a thin pycnocline with a significant variation in the density, and the water is well mixed above and below it (see Das et al. [76]). Therefore, there are numerous factors that need to be analyzed while studying the hydrodynamic performance of an OWC device in a two-layer fluid system. Some of the important factors that certainly impact the efficiency of the OWC devices in a two-layer fluid system are the following: (i) the transformation of the wave energy from internal to the surface waves and vice versa, (ii) the presence of two propagating wave modes termed as surface and internal wave modes (Manam and Sahoo [73]), and (iii) internal waves, having higher wave amplitude and wave periods as compared to surface waves, contains a significantly higher amount of energy (Yuan et al. [97]). Further, bottom undulation plays an important role in the occurrences of resonance phenomena inside the device chamber. In view of these, in Chapter 5, the performance of the OWC devices placed over an undulated bottom topography is studied in a two-layer fluid system. Further, a small thickness is considered in the OWC device wall. Some of the advantages of considering this particular OWC device model are mentioned in Chapter 2. Two types of OWC devices are considered in the present work: (*i*) front wall of the OWC device does not intersect the interface of the two layers (*INP OWC device*), and (*ii*) front wall of the OWC device intersects the interface of the two layers (*IP OWC device*). The results and discussions associated with the effect of shape parameters of OWC devices and undulated

bottom, and incident wave characteristics on the efficiency of the OWC devices are given in a detailed manner. The time-dependent simulations of the free surface and interface elevations for both INP and IP OWC devices are provided. Further, the effect of air compressibility on the hydrodynamic efficiency of the OWC devices is also provided.

Finally, Chapter 6 summarizes the thesis work and discusses future research directions. This chapter highlights the major contributions of the present works. In the next section, the governing equations and boundary conditions associated with the hydrodynamics of OWC and PWEC device are provided.

1.4 Mathematical description of waves and structures

1.4.1 Basic equations for water wave propagation in homogeneous fluid

The present section yields the derivations of the basic equation corresponding to the linearized water wave theory. In the present thesis, a two-dimensional Cartesian coordinate system (x, z) is considered with the z-axis being positive in the vertical upward direction and the x-axis is aligned in the direction of incident wave propagation, unless otherwise specified. The fluid is assumed to be homogeneous, incompressible, and inviscid, and its motion is assumed to be irrotational.

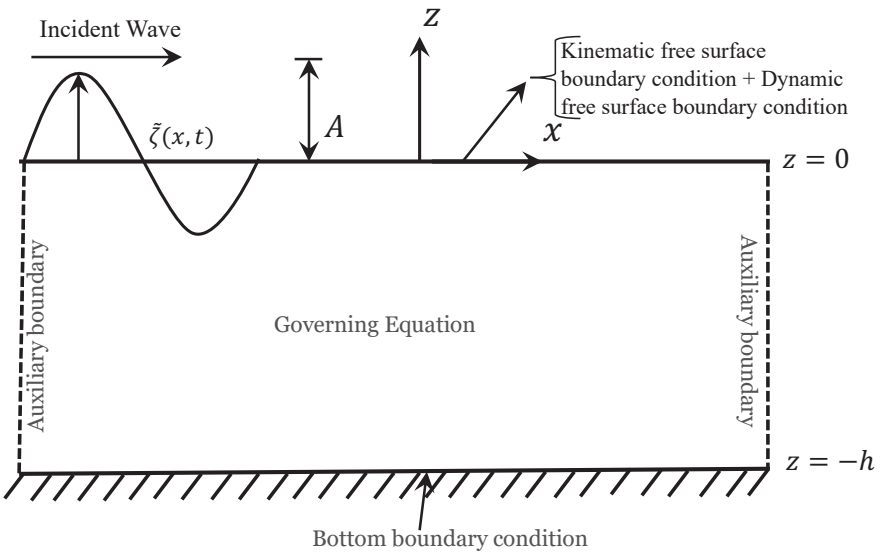

FIGURE 1.7: Structure of two-dimensional boundary value problems in open water region.

Under the assumption of the irrotational flow, the fluid velocity $\mathbf{q} = (u, w)$ can be expressed as a gradient of the velocity potential $\Phi(x, z, t)$, i.e.,

$$\mathbf{q} = \nabla\Phi. \tag{1.1}$$

In accordance with the conservation of mass, the velocity potential $\Phi(x, z, t)$ satisfies the Laplace equation in the fluid domain since the divergence of velocity vector $\mathbf{q}$ is zero.

$$\nabla^2\Phi = 0, \qquad \left(\nabla^2 = \frac{\partial^2}{\partial x^2} + \frac{\partial^2}{\partial z^2}\right), \tag{1.2}$$

The boundary conditions must be selected depending on the object's characteristics, including if it is fixed or moving, rigid or flexible, permeable or impermeable, etc. The boundary condition on the free surface is a combination of the kinematic and dynamic free surface conditions. The kinematic boundary condition relates to the motions of the water particles, while the forces acting on water particles are governed by the dynamic boundary conditions. The kinematic free surface boundary condition (KFBC) states that there must be no gap between the air-water interface. On the other hand, the dynamic free surface boundary condition (DFBC) specifies that the pressure is constant at the surface without taking into account the wind induced pressure variations. Let $F(x, z, t) = z - \tilde{\zeta}(x, t) = 0$ reflect the free surface of the water, and $\tilde{\zeta}(x, t)$ symbolises the vertical displacement of the free surface elevation. The KFBC involves that the substantial derivative of the function F must be zero at the free surface. Consequently,

$$\frac{DF}{Dt} = 0, \text{ on } z = \tilde{\zeta}(x, t). \tag{1.3}$$

Here, $\dfrac{D}{Dt} = \dfrac{\partial}{\partial t} + u\dfrac{\partial}{\partial x} + w\dfrac{\partial}{\partial z}$. Re-arranging Eq. (1.3) in terms of $\Phi(x, z, t)$, we get

$$\frac{\partial\Phi}{\partial z} = \frac{\partial\tilde{\zeta}}{\partial t} + \frac{\partial\Phi}{\partial x}\frac{\partial\tilde{\zeta}}{\partial x}, \text{ on } z = \tilde{\zeta}. \tag{1.4}$$

Now, implementing the Taylor series to Eq. (1.4) about the mean free surface $z = 0$ provides

$$\left(\frac{\partial\Phi}{\partial z} - \frac{\partial\tilde{\zeta}}{\partial t} - \frac{\partial\Phi}{\partial x}\frac{\partial\tilde{\zeta}}{\partial x}\right)\Big|_{z=\tilde{\zeta}} = \left(\frac{\partial\Phi}{\partial z} - \frac{\partial\tilde{\zeta}}{\partial t} - \frac{\partial\Phi}{\partial x}\frac{\partial\tilde{\zeta}}{\partial x}\right)\Big|_{z=0}$$
$$+\tilde{\zeta}\frac{\partial}{\partial z}\left(\frac{\partial\Phi}{\partial z} - \frac{\partial\tilde{\zeta}}{\partial t} - \frac{\partial\Phi}{\partial x}\frac{\partial\tilde{\zeta}}{\partial x}\right)\Big|_{z=0} + \ldots = 0. \tag{1.5}$$

It is supposed that the amplitude of the incident wave is small relative to its wavelength ($\lambda = 2\pi/k$, where k is the wave number), so $\tilde{\zeta} << 1$. In addition, under the assumption of linearized wave theory, fluid particle velocity, surface displacement $\tilde{\zeta}(x, t)$, and their derivatives are all small quantities. Consequently, the product and square terms of $\tilde{\zeta}(x, t)$ and Φ are infinitesimal. Hence, retaining the leading order terms, the linearized KFBC on the mean free surface $z = 0$ is expressed as

$$\frac{\partial\Phi}{\partial z} = \frac{\partial\tilde{\zeta}}{\partial t} \text{ on } z = 0. \tag{1.6}$$

On the other hand, the air-water interface, i.e., the free surface cannot tolerate variations in pressure across the interface and must respond in order to keep the pressure uniform. Therefore,

an additional boundary condition, known as dynamic free surface boundary condition is required on the free surface to specify the pressure distribution. It can be derived from the Bernoulli equation under the assumption of constant atmospheric pressure. The Bernoulli equation with the applied pressure P on the free surface $z = \tilde{\zeta}$ is given by

$$\frac{\partial \Phi}{\partial t} + \frac{1}{2}(u^2 + w^2) + \frac{P}{\rho} + gz = 0, \quad \text{on} \quad z = \tilde{\zeta}(x,t), \tag{1.7}$$

where ρ is the density of the fluid and g is the acceleration due to gravity. Due to the air's low density, its motion can be ignored and the pressure along the interface is assumed to be constant and without loss of generality, it is taken as zero. Thus, the Bernoulli's equation at the interface is given by

$$\frac{\partial \Phi}{\partial t} + \frac{1}{2}(u^2 + w^2) + g\tilde{\zeta} = 0, \quad \text{on} \quad z = \tilde{\zeta}(x,t). \tag{1.8}$$

Proceeding in the similar manner as mentioned in Eq. (1.5), we obtain the dynamic free surface boundary condition (DFBC) as

$$\begin{aligned} &\left(\frac{\partial \Phi}{\partial t} + \frac{1}{2}(u^2 + w^2) + g\tilde{\zeta}\right)\Big|_{z=\tilde{\zeta}(x,t)} = \left(\frac{\partial \Phi}{\partial t} + \frac{1}{2}(u^2 + w^2) + g\tilde{\zeta}\right)\Big|_{z=0} \\ &+\tilde{\zeta}\frac{\partial}{\partial z}\left(\frac{\partial \Phi}{\partial t} + \frac{1}{2}(u^2 + w^2) + g\tilde{\zeta}\right)\Big|_{z=0} + \ldots = 0. \end{aligned} \tag{1.9}$$

Retaining the leading order terms as discussed in Eq. (1.5), we get the DFBC as

$$\frac{\partial \Phi}{\partial t} + g\tilde{\zeta} = 0, \quad \text{on} \quad z = 0. \tag{1.10}$$

On combining Eqs. (1.6) and (1.10), the linearized boundary condition on the mean free surface is given by

$$\frac{\partial^2 \Phi}{\partial t^2} + g\frac{\partial \Phi}{\partial z} = 0, \quad \text{on} \quad z = 0. \tag{1.11}$$

Now, the seabed can be rigid, flexible, viscoelastic/poroelastic in nature. Throughout the thesis, the seabed is assumed to be rigid and impermeable unless otherwise mentioned. Therefore, the fluid cannot passes through the surface of the seabed at $z = -h$ and the same is expressed in terms of velocity potential $\Phi(x,z,t)$ as

$$\frac{\partial \Phi}{\partial z} = 0, \quad \text{on} \quad z = -h. \tag{1.12}$$

Here, $\partial/\partial n$ represents the normal derivative. It is to be noted that for the sake of simplicity, the depth h is assumed to be constant/uniform, but it could be described as a function $h = h(x)$ for the undulated seabed. Further, it is assumed that the motion of the fluid is simple harmonic in time t with angular frequency ω. Thus, the velocity potential $\Phi(x,z,t)$ and the free surface

elevation $\tilde{\zeta}(x,t)$ is expressed as

$$\Phi(x,z,t) = \Re\left\{\phi(x,z)e^{-\mathrm{i}\omega t}\right\}, \qquad \tilde{\zeta}(x,t) = \Re\left\{\zeta(x)e^{-\mathrm{i}\omega t}\right\}, \tag{1.13}$$

where $\Re$ indicates the real part of the complex-valued function, and $\phi(x,z)$ and $\zeta(x)$ represent the spatial form of the velocity potential and the free surface elevation, respectively. Substituting Eq. (1.13) into Eqs. (1.2), (1.11), and (1.12), we obtain

Governing equation:

$$\nabla^2\phi(x,z) = 0, \quad \text{in the fluid regions,} \tag{1.14}$$

Free surface BC:

$$\frac{\partial\phi}{\partial z} - \frac{\omega^2}{g}\phi = 0, \quad \text{on} \quad z = 0, \tag{1.15}$$

Bottom BC:

$$\frac{\partial\phi}{\partial z} = 0, \quad \text{at} \quad z = -h. \tag{1.16}$$

Far-field BCs:

To ensure the unique solution of the aforementioned boundary value problem (BVP), the velocity potential should satisfy the Sommerfeld radiation condition (Schot [98]) as following

$$\phi(x,z) \sim \left(A_0 e^{\mathrm{i}k_0 x} + B_0 e^{-\mathrm{i}k_0 x}\right)\frac{\cosh k_0(z+h)}{\cosh k_0 h}, \qquad \text{as} \quad x \to \pm\infty, \tag{1.17}$$

where A_0 and B_0 are the unknown coefficients need to be determined. In Eq. (1.17), the wave number k_0 is the positive real root of the dispersion relation $\omega^2 = gk\tanh kh$. It is to be noted that the vertical eigenfunction $\psi_0(z) = -\left(\frac{\mathrm{i}gA}{\omega}\right)\frac{\cosh k_0(z+h)}{\cosh k_0 h}$ satisfies the following property

$$\int_{-h}^{0}\psi_0(k_0,z)\psi_0^*(k_0,z)\,dz = \mathcal{A}, \quad \mathcal{A} = -\left(\frac{g^2A^2}{\omega^2}\right)\frac{2k_0h + \sinh(2k_0h)}{4k_0\cosh^2 k_0h}, \tag{1.18}$$

where $\psi_0^*(k_0,z)$ represents the complex conjugate of $\psi_0(k_0,z)$. Since, $k_0h = 2\pi h/\lambda$ is often refers as the depth-to-wavelength ratio, for long and shallow water waves, the dimensionless wave number is taken as $k_0h << 1$, whilst for short and deep water waves, the dimensionless wave number is taken as $k_0h >> 1$. The corresponding dispersion relations are modified as $\omega^2 = gk^2h$ for $k_0h << 1$ and $\omega^2 = gk$ for $k_0h >> 1$.

Phase velocity and group velocity

The phase velocity or wave celerity c associated with a plane progressive wave is expressed as the rate of propagation of the wave form and is given by

$$c = \frac{\lambda}{T} = \frac{\omega}{k_0} = \sqrt{\frac{g}{k_0}\tanh kh}. \tag{1.19}$$

In addition, when two progressive waves of same height H propagating in the same direction with slightly different wave frequencies and wave numbers, the resulting profile is modulated by a wave envelope that propagates with velocity c_g, which is referred as the group velocity. The group velocity is the rate at which the wave energy transfers and can be described as

$$c_g = \frac{d\omega}{dk_0} = \frac{\omega}{2k_0}\left(1 + \frac{2k_0 h}{\sinh(2k_0 h)}\right). \tag{1.20}$$

In most of the cases, under the assumption of potential flow theory, Laplace equation is the governing equation for the wave-structure interaction problems. Thus, it is worthy to study some of the basic features associated with the Laplace equation. Let ϕ satisfies the Laplace equation $\nabla^2\phi = 0$ in a particular compact domain $\Omega \subset \mathbb{R}^n$ with one of the following BCs prescribed on the boundary $\partial\Omega$

$$\phi|_{\partial\Omega} = f(x), \qquad \text{(Dirichlet)}, \tag{1.21}$$

$$\left.\frac{\partial\phi}{\partial n}\right|_{\partial\Omega} = g(x), \qquad \text{(Neumann)}, \tag{1.22}$$

$$a\phi + b\left.\frac{\partial\phi}{\partial n}\right|_{\partial\Omega} = h(x), \qquad \text{(Robin BC)}, \tag{1.23}$$

for some specific functions f, g, h and for some non-zero constants a and b. In the aforementioned cases, the value of ϕ or it's normal derivative $\partial\phi/\partial n$ are always prescribed on a co-dimension one of the boundary $\partial\Omega$, which means that one of the coordinate i.e., either time or space are kept fixed on this surface. The specification of exactly how ϕ should appear on this surface is referred to as the Cauchy data for the partial differential equation, and solving the PDE under these conditions is referred to as a Cauchy problem for the PDE. According to Hadamard, the Cauchy problem is well–posed if the following conditions are met: (i) a solution exists, (ii) the solution is unique, and (iii) the solution is dependent on the auxiliary data continuously.

Uniqueness theorem

For a smooth domain Ω, the uniqueness theorem (Folland [99]) is stated as the following

- The Dirichlet problem has at most one solution.
- If u is a solution of the Neumann problem, then any other solution is of the form $v = u + c$, for any $c \in \mathbb{R}$.
- If $\alpha \geq 0$, then the Robin problem has at most one solution.

1.4.2 Basic equations of water wave in stratified fluid

In the two-layer fluid model, internal waves are generated and propagate along the interface between the two layers. Moreover, in the two-layer fluid system, it is standard to assume that the upper layer fluid is lying above the denser lower layer fluid. A schematic diagram associated

with the two-layered fluid system is provided in Fig. 1.8. It is to be noted that the governing equation, free surface and bottom boundary conditions in the two-layered fluid system are remain same as provided in Eqs. (1.14)-(1.16) with h should be replaced by H.

Interface boundary conditions in case of two-layer fluid

Now, the case of two homogeneous superposed immiscible fluids having different densities ρ_1 and ρ_2 (with $\rho_2 > \rho_1$) is considered. The two-layers are separated by a common interface at $z = -h$ with the upper layer being open to the atmosphere and the lower layer being bounded below by the fixed rigid bottom $z = -H$. Hereafter, the subscripts 1 and 2 used for the upper and lower layer fluids, respectively.

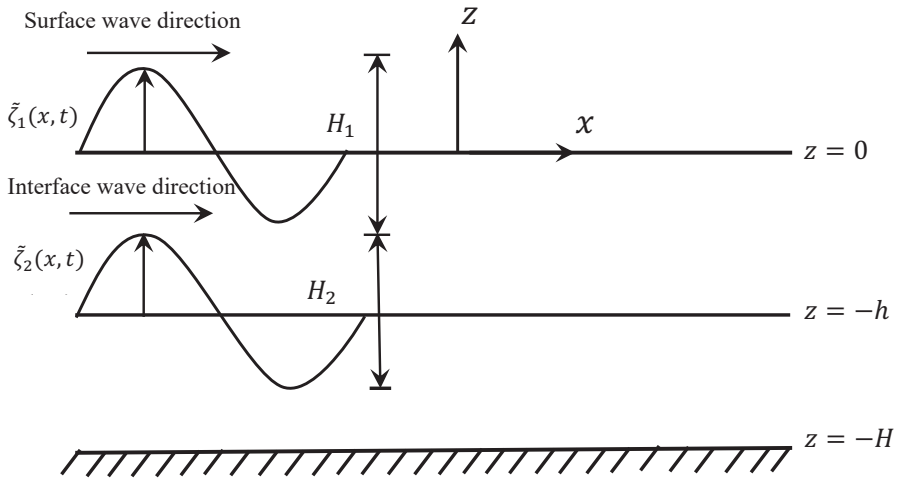

FIGURE 1.8: Structure of two-dimensional boundary value problems in a two-layered fluid system.

It is assumed that the fluid motions are irrotational, inviscid, incompressible and time harmonic as mentioned earlier, which suggests the existence of the velocity potential $\Phi_j(x,z,t) = \Re\left\{\phi_j(x,z)e^{-\mathrm{i}\omega t}\right\}$ for $j = 1, 2$, and satisfy the Laplace Eq. (1.2) in the respective fluid regions. The linearized kinematic condition in Eq. (1.6) yields

$$\frac{\partial \Phi_1}{\partial z} = \frac{\partial \Phi_2}{\partial z} = \frac{\partial \tilde{\zeta_2}}{\partial t}, \quad \text{on} \quad z = -h + \tilde{\zeta}_2(x,t), \tag{1.24}$$

where $z = \tilde{\zeta_2}(x,t)$ is the interfacial elevation. In addition to that, the Bernoulli's equation as in Eq. (1.7) is written as the following

$$\frac{\partial \Phi_j}{\partial t} + \frac{1}{2}(u_j^2 + w_j^2) + \frac{P_j}{\rho_j} + gz = 0, \quad \text{on} \quad z = -h + \tilde{\zeta}_2, \quad j = 1, 2, \tag{1.25}$$

where the fluid pressures P_1 and P_2 are acting on the interface at $z = -h + \tilde{\zeta}_2(x,t)$ from the upper and lower layers, respectively. Since the fluid pressure is continuous across the interface, using the linearized theory, the dynamic boundary condition yields

$$\rho_1\left(\frac{\partial \Phi_1}{\partial t} + g\tilde{\zeta_2}\right) = \rho_2\left(\frac{\partial \Phi_2}{\partial t} + g\tilde{\zeta_2}\right), \quad \text{on} \quad z = -h. \tag{1.26}$$

Eliminating $\tilde{\zeta_2}$ from both sides of Eq. (1.26), after using the condition (1.24), yields

$$s\left(\frac{\partial \Phi_1}{\partial z} - K\Phi_1\right) = \left(\frac{\partial \Phi_2}{\partial z} - K\Phi_2\right), \quad \text{on} \quad z = -h, \tag{1.27}$$

where $s = \rho_1/\rho_2 < 1$. When the incident wave contains the wave number k_I, the left-hand side (LHS) far-field boundary conditions is given by (Panda and Martha [85])

$$\begin{cases} \phi_j(x,z) = e^{\mathrm{i}k_I x}\psi_I(k_I,z) + A_{I,I}e^{-\mathrm{i}k_I x}\psi_I(k_I,z) + A_{II,I}e^{-\mathrm{i}k_{II}x}\psi_{II}(k_{II},z), & \text{as } x \to -\infty, \\ \phi_j(x,z) = B_{I,I}e^{\mathrm{i}k_I x}\psi_I(k_I,z) + B_{II,I}e^{\mathrm{i}k_{II}x}\psi_{II}(k_{II},z), & \text{as } x \to \infty, \end{cases} \tag{1.28}$$

where $j = 1, 2$ correspond to the regions R_1 and R_2, respectively. Further, $A_{I,I}$ and $A_{II,I}$ are the coefficients related to the amplitudes of the reflected waves for the wave modes k_I and k_{II}, respectively due to the incident wave mode k_I. Similarly, $B_{I,I}$ and $B_{II,I}$ are the coefficients related to the amplitudes of the transmitted waves containing the wave modes k_I and k_{II}, respectively due to the incident wave mode k_I. On the other hand, when the incident wave contains the wavenumber k_{II}, the LHS and RHS far-field boundary conditions are given by

$$\begin{cases} \phi_j(x,z) = e^{\mathrm{i}k_{II} x}\psi_{II}(k_{II},z) + A_{I,II}e^{-\mathrm{i}k_I x}\psi_I(k_I,z) + A_{II,II}e^{-\mathrm{i}k_{II}x}\psi_{II}(k_{II},z), & \text{as } x \to -\infty, \\ \phi_j(x,z) = B_{I,II}e^{\mathrm{i}k_I x}\psi_I(k_I,z) + B_{II,II}e^{\mathrm{i}k_{II}x}\psi_{II}(k_{II},z), & \text{as } x \to \infty. \end{cases} \tag{1.29}$$

Here, $A_{I,II}$ and $A_{II,II}$ are the coefficients associated with the amplitudes of the reflected waves for the wave modes k_I and k_{II} respectively due to the incident wave mode k_{II}. Similarly, $B_{I,II}$ and $B_{II,II}$ are the coefficients associated with the amplitudes of the transmitted waves for the wave modes k_I and k_{II}, respectively due to the incident wave mode k_{II}. In Eqs. (1.28) and (1.29), the expressions for the vertical eigenfunctions $\psi_n(k_n,z)$ for $n = I, II$ are given by

$$\psi_n(k_n,z) = \begin{cases} \dfrac{N_n^{-1}\sinh k_n(H-h)\{k_n\cosh k_n z + K\sinh k_n z\}}{K\cosh k_n h - k_n \sinh k_n h}, & \text{for} \quad -h < z < 0, \\ N_n^{-1}\cosh k_n(z+H), & \text{for} \quad -H < z < -h. \end{cases} \tag{1.30}$$

Here, k_n satisfies the dispersion relation

$$\mathcal{G}(k) \equiv (1-s)k^2 + K^2\{s + \coth k(H-h)\coth kh\} - kK\{\coth kh + \coth k(H-h)\} = 0. \tag{1.31}$$

It is to be noted that the dispersion relation in Eq. (1.31) have two positive real roots $k_n = k_I, k_{II}$ $(0 < k_I < k_{II})$, and infinite number of imaginary roots of the form ip_n for $n \geq 1$. The vertical eigenfunctions $\psi_n(k_n, z)$ for $n = I, II$ in Eq. (1.30) are orthonormal with respect to the inner product

$$\langle \psi_n, \psi_m \rangle = \int_{-H}^{-h} \psi_n(z)\psi_m(z)dz + s\int_{-h}^{0} \psi_n(z)\psi_m(z)dz = \delta_{nm}, \tag{1.32}$$

where δ_{nm} is the Kronecker delta function, and the expression for N_n^2 is given by

$$\begin{aligned} N_n^2 \;=\; & \frac{s\sinh^2 k_n(H-h)}{4k_n\left(K\cosh k_n h - k_n \sinh k_n h\right)^2} \\ & \left\{K^2\left(\sinh 2k_n h - 2k_n h\right) + k_n^2\left(2k_n h + \sinh 2k_n h\right) - 2Kk_n\left(\cosh 2k_n h - 1\right)\right\} \\ & + \frac{\left\{2(H-h)k_n + \sinh 2k_n(H-h)\right\}}{4k_n}. \end{aligned} \tag{1.33}$$

1.4.3 Basic equations associated with the hydrodynamics of oscillating water column wave energy converter device

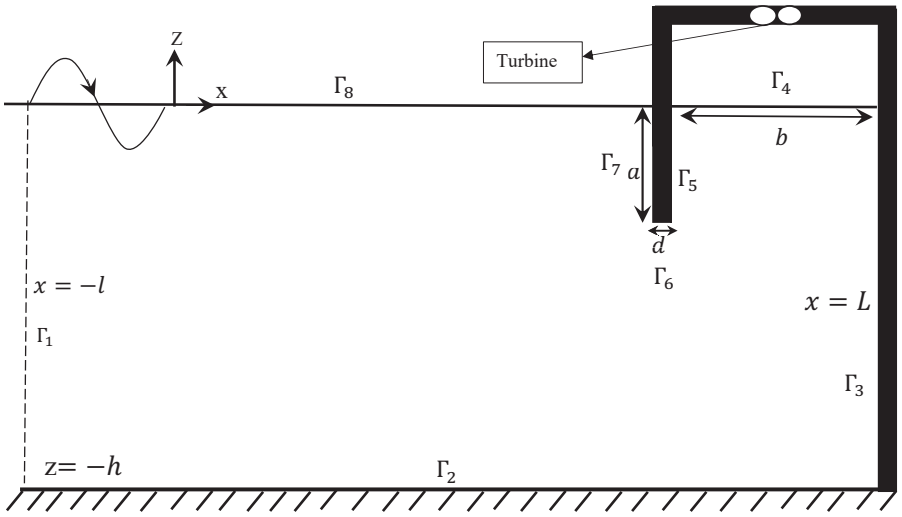

FIGURE 1.9: Schematic diagram of side cross-section of the oscillating water column device.

The oscillating water column (OWC) device consists of an open-ended, hollow structure with a downward-facing open end that is partially submerged to trap air above the internal free surface and a PTO system that incorporates a Wells turbine positioned on top of the chamber to prevent it from coming into direct contact with salt water. In the existence of incident waves, the internal free surface is compelled to oscillate with the same angular frequency ω as the incident wave, consequently establishing a uniform pressure distribution over the internal free surface Γ_4. The fluid motion is characterised by the velocity potential $\Phi(x, z, t)$, that satisfies equations (1.1),

whereas the linearized free surface condition becomes

$$\frac{\partial \Phi}{\partial t} + g\tilde{\zeta} = \begin{cases} 0, & \text{on} \quad \Gamma_8, \\ -\dfrac{P(t)}{\rho}, & \text{on} \quad \Gamma_4. \end{cases} \tag{1.34}$$

Here, $P(t)$ is termed as uniformly distributed pressure acting on the internal free surface. Further, the boundary condition on the rigid and impervious boundaries can be expressed as

$$\frac{\partial \Phi}{\partial n} = 0, \quad \text{on} \quad \Gamma_2 \cup \Gamma_3 \cup \Gamma_5 \cup \Gamma_6 \cup \Gamma_7, \tag{1.35}$$

where, $\partial/\partial n$ represents the normal derivative. Further, it is assumed that the motion of the fluid is simple harmonic in time t with angular frequency ω. Thus, the velocity potential $\Phi(x, z, t)$ is expressed as Eq. (1.13), and the pressure $P(t)$ is written as

$$P(t) = \Re\left\{pe^{-\mathrm{i}\omega t}\right\}, \tag{1.36}$$

where $\Re$ indicates the real part of the complex-valued function, and p represent the spatial form of the pressure. Substituting Eq. (1.36) into Eqs. (1.34), and using (1.6) and (1.10), we get

$$\frac{\partial \phi}{\partial z} - K\phi = \begin{cases} 0, & \text{on} \quad \Gamma_8, \\ \dfrac{\mathrm{i}\omega p}{\rho g}, & \text{on} \quad \Gamma_4. \end{cases} \tag{1.37}$$

Here, $K = \omega^2/g$. In addition, implementing Eq. (1.13) into Eq. (1.35), we obtain

$$\frac{\partial \phi}{\partial n} = 0, \quad \text{on} \quad \Gamma_2 \cup \Gamma_3 \cup \Gamma_5 \cup \Gamma_6 \cup \Gamma_7. \tag{1.38}$$

In the presence of OWC device, the velocity potential ϕ can be decomposed into the scattered and radiated velocity potentials and therefore, the total velocity potential can be written as

$$\phi = \phi^S + \left(\frac{\mathrm{i}\omega p}{\rho g}\right)\phi^R, \tag{1.39}$$

where ϕ^S and ϕ^R are signified as the scattered and radiated velocity potential, respectively. Furthermore, the scattered velocity potential is expressed as the sum of diffracted and incident velocity potentials, i.e., $\phi^S = \phi^D + \phi^I$ where ϕ^D and ϕ^I represent the diffracted and incident velocity components. In the interaction of water waves with the OWC device, the incoming waves are reflected by the rigid wall boundaries of the OWC device. Resultantly, the scattered velocity potential appears. Further, the radiated velocity potential appears due to the oscillation of the water column in the OWC device wave chamber. Here, $\phi^{S,R}$ satisfy the Eqs. (1.14), (1.37)

and (1.38). It is to be noted that substituting the expression (1.39) into Eq. (1.37), we get

$$\frac{\partial \phi^S}{\partial z} - K\phi^S = 0, \quad \text{on} \quad \Gamma_4 \cup \Gamma_8,$$

$$\frac{\partial \phi^R}{\partial z} - K\phi^R = \begin{cases} 1, & \text{on} \quad \Gamma_4, \\ 0, & \text{on} \quad \Gamma_8. \end{cases} \tag{1.40}$$

Finally, the far-field boundary conditions on Γ_1 are given by

$$\begin{cases} \phi^S(x,z) = e^{\mathrm{i}k_0 x}\psi_0(k_0,z) + A_0^S e^{-\mathrm{i}k_0 x} f_0(k_0,z), & \text{as} \;\; x \to -\infty \\ \phi^R(x,z) = A_0^R e^{-\mathrm{i}k_0 x}\psi_0(k_0,z), & \text{as} \;\; x \to -\infty. \end{cases} \tag{1.41}$$

where A_0^S and A_0^R are the coefficients associated with the reflected and radiated wave amplitudes, respectively as $x \to -\infty$. In Eq. (1.41), the expression for vertical eigenfunction $\psi_0(k_0,z)$ is given by $\psi_0(k_0,z) = -\left(\frac{\mathrm{i}gA}{\omega}\right)\frac{\cosh k_0(h+z)}{\cosh(k_0 h)}$. Here, k_0 is positive real root of the dispersion relation $\omega^2 = gk\tanh(kh)$.

1.4.4 Basic equations and edge conditions for flexible structures

The present section illustrates the governing equation and the associated edge conditions for the flexible structure modeled as a thin elastic plate in the framework of the thin elastic plate theory, also known as classical plate theory or the Kirchhoff plate theory. This Kirchhoff plate theory is a simplification of Euler-Bernoulli thin plate theory.

The displacement of the flexible elastic plate under the action of ocean waves can be written in the form $\tilde{\zeta}(x,y,t) = \Re\{\zeta(x,y)e^{-\mathrm{i}\omega t}\}$ with $\zeta(x,y)$ being spatial component of the complex deflection amplitude. The vertical deflection $\zeta(x,y,t)$ of an isotropic homogeneous thin elastic plate which is undergoing slight deformation in the presence of in-plane compressive forces $\mathcal{N}_x$ and $\mathcal{N}_y$ along the x and y-directions is given by (Sahoo [100])

$$EI\left(\frac{\partial^2\zeta}{\partial x^2} + \frac{\partial^2\zeta}{\partial y^2}\right)^2 - \mathcal{N}_x\frac{\partial^2\zeta}{\partial x^2} - \mathcal{N}_z\frac{\partial^2\zeta}{\partial y^2} + m_p\frac{\partial^2\zeta}{\partial t^2} = \mathcal{F}(x,y,t). \tag{1.42}$$

Here, EI is termed as the flexural rigidity of the plate with E being the Young's modulus. In addition, the inertia of the plate I is calculated as $I = d_p^3/12(1-\nu^2)$ in which d_p is the thickness of the plate, and ν is the Poisson ratio. Further, $m_p = \rho_p d_p$ (ρ_p is the density of the plate) is the uniform mass of the plate per unit area and $\mathcal{F}$ is the force acting on the structure. It is to be mentioned that the components of the compressive force are taken as $\mathcal{N}_x = \mathcal{N}_y = \mathcal{Q}$ for uniform compressive force. In a similar manner, $\mathcal{N}_x = \mathcal{N}_y = -\mathcal{T}$ is utilized to represent the uniform tensile force for the case of floating membrane structure.

Edge conditions

A class of edge conditions are needed to be prescribed at the ends of the flexible structures depending on the nature of the physical problem. Here, some edge conditions, which are often considered in the surface gravity wave problems are presented in the following.

Fixed edges:

For the case of fixed edges, vanishing of plate deflection and the slope of the deflection near both the edges of the plate yield (see Mohapatra et al. [101])

$$\zeta = 0, \quad \frac{\partial \zeta}{\partial x} = 0. \tag{1.43}$$

Free edges:

For the case of free edges, vanishing of bending moment and shear force near the edges of the plate are represented as

$$\frac{\partial^2 \zeta}{\partial x^2} + \nu \frac{\partial^2 \zeta}{\partial y^2} = 0, \quad EI \left\{ \frac{\partial^3 \zeta}{\partial x^3} + (2-\nu) \frac{\partial^3 \zeta}{\partial x \partial y^2} \right\} + \mathcal{Q} \frac{\partial \zeta}{\partial x} = 0. \tag{1.44}$$

Mooring edges:

If the ends of the plate are connected with the mooring chains, the following edge conditions will be considered

$$\frac{\partial^2 \zeta}{\partial x^2} + \nu \frac{\partial^2 \zeta}{\partial y^2} = 0, \quad EI \left\{ \frac{\partial^3 \zeta}{\partial x^3} + (2-\nu) \frac{\partial^3 \zeta}{\partial x \partial y^2} \right\} + \mathcal{Q} \frac{\partial \zeta}{\partial x} = q_m \frac{\partial \zeta}{\partial x}, \tag{1.45}$$

where q_m is the stiffness constant of the mooring chains (see Sahoo [100]). Here, $\mathcal{Q}$ is symbolized as uniform compressive force.

1.4.4.1 Basic equations and boundary conditions associated with the piezoelectric wave energy converter device

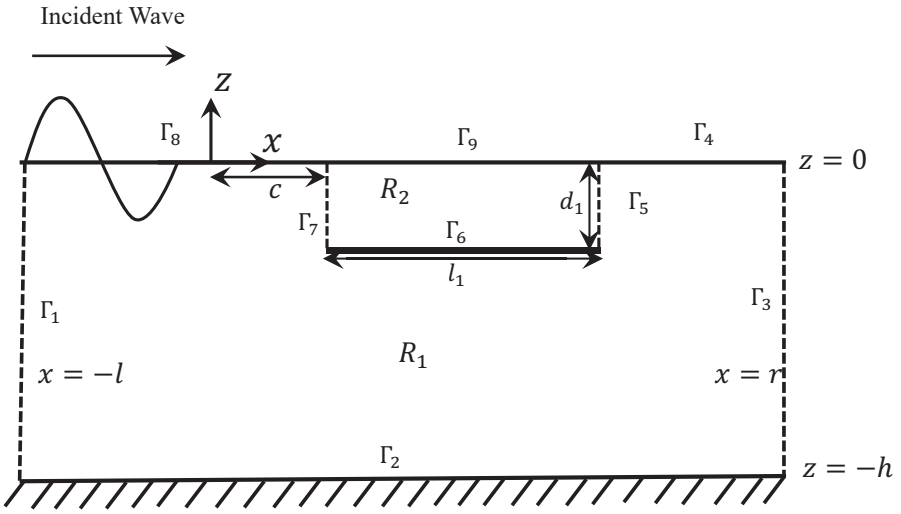

FIGURE 1.10: Schematic of the side cross-section of the piezoelectric device.

A flexible floating structure comprised of bio-compatible soft and flexible piezoelectric materials can generate electricity when deformed by the sensor effect (mechanical vibrations). The piezoelectric wave energy converter device (PWEC) consists of a submerged elastic plate with the attachment of piezoelectric layers on both sides of the plate, which can extract energy from the ocean waves due to the variations of tension along the plate. Here, the PWEC system is homogeneous, the stresses, strains, and the voltage are continuous along the plate. Hence, the wave energy converter can be modelled as a uniform composite plate based on the Kirchhoff plate theory. For modeling the piezoelectric plate, the hydroelectromechanical-coupled dynamics associated with the piezoelectric wave energy converter device is considered in the context of linear water wave theory. In the presence of a floating submerged piezoelectric plate, the fluid domain is divided into two regions R_j $(j = 1, 2)$, where $R_1 = -l < x < r, -h < z < 0$ except the region above the plate, and $R_2 = c < x < c + l_1, -d_1 < z < 0$. The velocity potentials $\Phi_j(x, z, t) = \Re\left\{\phi_j(x, z)e^{-\mathrm{i}\omega t}\right\}$ associated with regions R_j for $j = 1, 2$ satisfy the Laplace equation (1.14) along with the following boundary conditions. The boundary condition at the mean free surface $z = 0$ is given by

$$\begin{cases} \dfrac{\partial \phi_1}{\partial n} - K\phi_1 = 0, & \text{on } \Gamma_4 \cup \Gamma_8, \\ \dfrac{\partial \phi_2}{\partial n} - K\phi_2 = 0, & \text{on } \Gamma_9. \end{cases} \tag{1.46}$$

Now, the boundary condition on the impentrable bottom Γ_2 is given by

$$\frac{\partial \phi_1}{\partial z} = 0, \quad \text{on } \Gamma_2. \tag{1.47}$$

The continuity of pressure and normal velocities along the two auxiliary boundaries Γ_5 and Γ_7 placed at $x = c + l_1$ and $x = c$, respectively are given by

$$\phi_1 = \phi_2, \quad \text{and} \quad \frac{\partial \phi_1}{\partial n} = -\frac{\partial \phi_2}{\partial n} \quad \text{on} \ \ \Gamma_5 \cup \Gamma_7. \tag{1.48}$$

Now, the dynamic boundary condition on the piezoelectric plate Γ_6 is given by

$$g\chi \left(1 + \frac{\beta^2 \xi \omega}{\mathrm{i} + \xi \omega}\right) \frac{\partial^4 \zeta}{\partial x^4} - \omega^2 \gamma \zeta = \mathrm{i}\omega \left(\phi_1 - \phi_2\right), \quad \text{on} \quad z = -d_1, \quad x \in [c, c + l_1], \tag{1.49}$$

where the expressions for χ, β, ξ, and γ are given as

$$\chi = \frac{B'}{\rho g}, \ \beta = \frac{\theta'}{\sqrt{B'C'}}, \ \xi = \frac{C'}{G'}, \ \gamma = \frac{I_b}{\rho}, \tag{1.50}$$

with B', θ', C', and G' being termed as flexural rigidity of the bimorph, piezoelectric coupling factor, electric surface capacitance, and surface conductance, respectively. Further, I_b represents the surface density of the bimorph. Now, the linearized kinematic boundary condition on the plate Γ_6 is given by

$$\frac{\partial \phi_1}{\partial z} = \frac{\partial \phi_2}{\partial z} = -\mathrm{i}\omega\zeta, \quad \text{on} \quad z = -d_1, c < x < c + l_1. \tag{1.51}$$

For the plate having fixed edges, vanishing of plate displacement and the slope of the displacement near both the edges of the plate yield

$$\zeta = 0, \ \ \frac{\partial \zeta}{\partial x} = 0, \ \ \text{at} \ \ x = c, c + l_1, \ \ z = -d_1. \tag{1.52}$$

Similarly, when the plate edges are free, the edge conditions are given by

$$\frac{\partial^2 \zeta}{\partial x^2} = 0, \ \ \frac{\partial^3 \zeta}{\partial x^3} = 0, \ \ \text{at} \ \ x = c, c + l_1, \ \ z = -d_1. \tag{1.53}$$

1.5 Fundamentals of integral equations

An integral equation is an a kind of equation in which the unknown function appears under one or more integral signs. An intergral equation can be written in its most general form as

$$\alpha(x)h(x) = f(x) + \lambda \int_a \mathcal{K}(x,t)h(t)dt, \tag{1.54}$$

where the upper limit of the integration may be either fixed or a variable. The functions α, f and $\mathcal{K}$(kernel) are known functions, while h has to be calculated. λ is a non-zero real or complex parameter. Further, The classifications for integral equations are as follows

- **Fredholm integral equations :** The integral equation is known as a Fredholm integral equation if the upper limit of integration in Eq. (1.54) is a constant, say b.

  – In Eq. (1.54), if $\alpha(x) = 0$ then it is called as Fredholm integral equation of first kind. Thus,

  $$f(x) + \lambda \int_a^b \mathcal{K}(x,t)h(t)dt = 0.$$

  – In Eq. (1.54), if $\alpha(x) = 1$ then it is called as Fredholm integral equation of second kind. Thus,

  $$h(x) = f(x) + \lambda \int_a^b \mathcal{K}(x,t)h(t)dt.$$

  In the aforementioned equation, if $f(x) = 0$, it is called as the homogeneous Fredholm integral equation of second kind. Thus,

  $$h(x) = \lambda \int_a^b \mathcal{K}(x,t)h(t)dt.$$

- **Volterra integral equations :** The homogeneous, first, and second types of Volterra integral equations are defined in the same way as Fredholm integral equations with $b = x$ as the variable which is there as upper limit of integration.

  – In Eq. (1.54), if $\alpha(x) = 0$ then it is called as Volterra integral equation of first kind. Thus,

  $$f(x) + \lambda \int_a^x \mathcal{K}(x,t)h(t)dt = 0.$$

  – In Eq. (1.54), if $\alpha(x) = 1$ then it is called as Volterra integral equation of second kind. Thus,

  $$h(x) = f(x) + \lambda \int_a^x \mathcal{K}(x,t)h(t)dt.$$

  In the aforementioned equation, if $f(x) = 0$, it is called as the homogeneous Volterra integral equation of second kind. Thus,

  $$h(x) = \lambda \int_a^x \mathcal{K}(x,t)h(t)dt.$$

- **Singular integral equations :** The integral equation is said to be singular when either the upper or lower limit of integration becomes infinite, or when the kernel approaches infinity at one or more points within the range of integration. The Abel integral equation, a widely used form of singular integral equation, is stated as follows

First kind:

$$f(x) = \int_a^x \frac{h(t)}{(x-t)^\kappa} dt, \quad 0 < \kappa < 1. \tag{1.55}$$

Second kind:

$$h(x) = f(x) + \int_a^x \frac{h(t)}{(x-t)^\kappa} dt, \quad 0 < \kappa < 1. \tag{1.56}$$

The most general form of the Abel integral equation is given by

$$f(x) = \int_a^x \frac{h(t)}{(g(x)-g(t))^\kappa} dt, \quad x > a, 0 < \kappa < 1, \tag{1.57}$$

where $g(x)$ is monotonically increasing function. The particular case associated with $\kappa = 1/2$ occurs often in mathematical physics. Special numerical methods have been developed to solve these integral equations numerically. One among them is the product integration method (Weiss [102]).

1.6 Boundary Element Method (BEM)

This section provides a brief overview of the boundary element method (BEM) for solving the two-dimensional Laplace equation (see Liu [103] and Brebbia et al. [104] for details). The BEM is a useful numerical tool for dealing with initial and boundary value problems in applied sciences and engineering. The term "boundary integral equation method" is also used to describe this approach. A block diagram for brief classifications of various numerical methods applicable to different real-world engineering problems is shown in Fig. 1.11.

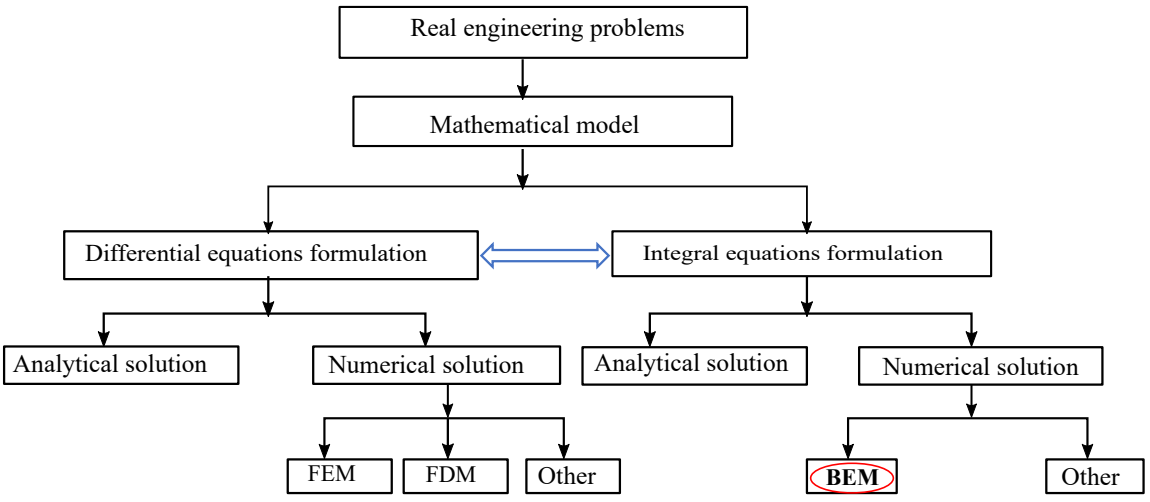

FIGURE 1.11: Different routes for solving the real engineering problems (see Liu [103] for details).

In order to transform the boundary value problem (discussed in the previous Section 1.4) into integral equations and then to solve numerically, the fundamental solution of the underlying differential operator is required.

1.6.1 Fundamental solution of the Laplace equation

The fundamental solution (also known as the free-space Green's function) $G(x, z; x_0, z_0)$ is the singular particular solution of

$$\mathcal{L}G = \delta(x - x_0, z - z_0), \tag{1.58}$$

where $\mathcal{L}$ is a termed as linear differential operator and $\delta(x - x_0, z - z_0) = \delta(x - x_0)\delta(z - z_0)$ is the two-dimensional Dirac delta function in which (x_0, z_0) is the source point. In addition, the Dirac delta function δ satisfies the subsequent characteristics

$$\int_{\Omega} \delta(x)\, d\Omega = 1, \qquad \int_a^b \delta(x - x_0) f(x)\, dx = \begin{cases} f(x_0), & \text{if } x_0 \in (a, b), \\ 0, & \text{if } x_0 \notin [a, b], \end{cases} \tag{1.59}$$

where $f(x)$ is continuous at x_0. To be specific, consider $\mathcal{L}$ is a two-dimensional Laplacian operator

$$\mathcal{L} = \nabla^2 = \frac{\partial^2}{\partial x^2} + \frac{\partial^2}{\partial z^2}.$$

Therefore, the free-space Green's function associated with the two-dimensional Laplace equation is given by (see Mei [105], Ang [106] for details)

$$G(x, z; x_0, z_0) = \frac{1}{2\pi} \ln \tilde{r}, \tag{1.60}$$

where $\tilde{r} = \sqrt{(x - x_0)^2 + (z - z_0)^2}$. Similarly, the fundamental solution associated with the three dimensional Laplace equation is given by

$$G(x, y, z; x_0, y_0, z_0) = -\frac{1}{4\pi\tilde{r}}, \tag{1.61}$$

where $\tilde{r} = \sqrt{(x - x_0)^2 + (y - y_0)^2 + (z - z_0)^2}$.

Green's identities

The Greens' identities are briefly discussed in the following.

Green's first identity

$$\int_D \nabla f . \nabla g\, dV + \int_D f \nabla^2 g\, dV = \int_S f \frac{\partial g}{\partial n}\, dS. \tag{1.62}$$

Green's second identity

$$\int_D \left(f\nabla^2 g - g\nabla^2 f\right)\, dV = \int_S \left(f\frac{\partial g}{\partial n} - g\frac{\partial f}{\partial n}\right) dS, \tag{1.63}$$

where f and g are the any two scalar functions continuous in the domain D having boundary S. Here, ∇^2 is the two dimensional Laplacian operator or harmonic operator.

1.6.2 Boundary integral equations formulation

Here, the formulation of boundary integral equation for the two-dimensional Laplace equation is discussed in brief (see Ang [106], Brebbia et al. [104] for more details). The fundamental solution as defined in Eq. (1.60) satisfies the Laplace equation everywhere in the domain D except for the point (x_0, z_0) where the singularity exists. Now, consider a circular disc centered at (x_0, z_0) having radius ϵ, the fundamental solution G is defined and satisfies the Laplace equation over the domain $D - \Gamma_\epsilon$ Applying the Green's second identity over the domain $D - \Gamma_\epsilon$, we get

$$\int_{D-\Gamma_\epsilon} \left(\phi\nabla^2 G - G\nabla^2\phi\right) dV = \int_{\Gamma+\Gamma_\epsilon} \left(\phi\frac{\partial G}{\partial n} - G\frac{\partial \phi}{\partial n}\right) d\Gamma. \tag{1.64}$$

Clearly, the left hand side of Eq. (1.64) is zero. Therefore,

$$\int_{\Gamma+\Gamma_\epsilon} \left(\phi\frac{\partial G}{\partial n} - G\frac{\partial \phi}{\partial n}\right) d\Gamma = 0. \tag{1.65}$$

Re-writing Eq. (1.65), we get

$$\int_{\Gamma} \left(\phi\frac{\partial G}{\partial n} - G\frac{\partial \phi}{\partial n}\right) d\Gamma = -\int_{\Gamma_\epsilon} \left(\phi\frac{\partial G}{\partial n} - G\frac{\partial \phi}{\partial n}\right) d\Gamma. \tag{1.66}$$

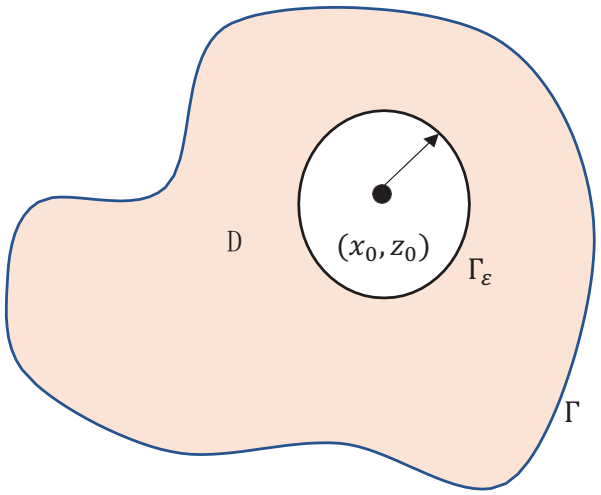

FIGURE 1.12: Cross-section of the domain D bounded by Γ

For $(x_0, z_0) \in D$, it can be derived that (Ang [107], Brebbia et al. [104])

$$\lim_{\epsilon \to 0} \int_{\Gamma_\epsilon} \phi \frac{\partial G}{\partial n} d\Gamma = -\phi(x_0, z_0), \quad \lim_{\epsilon \to 0} \int_{\Gamma_\epsilon} G \frac{\partial \phi}{\partial n} d\Gamma = 0. \tag{1.67}$$

Thus, Eq. (1.66) becomes

$$\int_{\Gamma} \left(\phi \frac{\partial G}{\partial n} - G \frac{\partial \phi}{\partial n} \right) d\Gamma = \phi(x_0, z_0) \tag{1.68}$$

Similarly, it can also be derived that (Brebbia et al. [104])

$$c(\tilde{P}) \phi(x_0, z_0) = \int_{\Gamma} \left(\phi \frac{\partial G}{\partial n} - G \frac{\partial \phi}{\partial n} \right) d\Gamma, \tag{1.69}$$

where $\tilde{P} = (x_0, z_0)$, and

$$c(\tilde{P}) = \begin{cases} 0, & \text{if } (x_0, z_0) \notin D \cup \Gamma, \\ \dfrac{1}{2}, & \text{if } (x_0, z_0) \in \Gamma, (\Gamma - \text{smooth}), \\ \dfrac{\alpha}{2\pi} & \text{if } (x_0, z_0) \in \Gamma, (\Gamma - \text{non-smooth}), \end{cases} \tag{1.70}$$

where α is the aperture angle. The subsequent section will illustrates the boundary element method (BEM) based numerical solution procedure for the boundary integral equations for the Laplace equation, i.e., for Eqs. (1.68) and (1.69). The numerical implementation of the BEM can be handled using the following steps. There are three popular boundary elements for the discretization of boundary integral in order to solve numerically such as constant element, linear elements, and the quadratic elements. Throughout this thesis, the constant and linear elements are employed for discretization of the boundary integral equations and the same are provided separately in the subsequent sections.

1.6.3 Boundary element method based on constant element approach

The first step in the BEM is the discretization of surface boundary into a finite number of segments (also called the boundary elements). Thus,

$$\Gamma = \bigcup_{i=1}^{N} \Gamma_i, \tag{1.71}$$

The schematic view of single constant element is provided in Fig. 1.13.

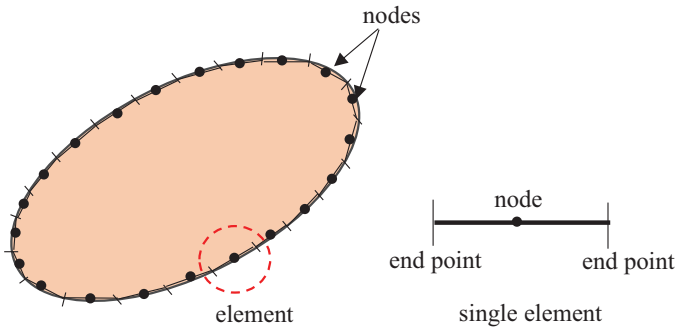

FIGURE 1.13: Discretization of boundary using constant elements.

In constant boundary element method, it is assumed that the values of ϕ and it's normal derivative $\partial\phi/\partial n$ are constants over each elements. Moreover, for constant elements, the boundary is always smooth and the value at the mid point (node) of each boundary element is considered to be the values over the whole boundary element (see Ang [107], Liu [103], Brebbia et al. [104], for more details). As a consequence $c(\tilde{P}) = 1/2$. Under these assumptions, the discretized form of Eq. (1.69) for i^{th} boundary element is written as

$$-\frac{1}{2}\phi_i + \sum_{j=1}^{N}\int_{\Gamma_j}\left(\phi\frac{\partial G}{\partial n}\right)d\Gamma = \sum_{j=1}^{N}\int_{\Gamma_j}\left(G\frac{\partial \phi}{\partial n}\right)d\Gamma. \tag{1.72}$$

Since ϕ and $\partial\phi/\partial n$ are constants over each boundary element, Eq. (1.72) can be re-written as

$$-\frac{1}{2}\phi_i + \sum_{j=1}^{N}\phi_j\left(\int_{\Gamma_j}\frac{\partial G}{\partial n}d\Gamma\right) = \sum_{j=1}^{N}\frac{\partial \phi_j}{\partial n}\int_{\Gamma_j} G d\Gamma. \tag{1.73}$$

The two integrals involving the fundamental solutions termed as influence coefficients and these coefficients are written as

$$H^{ij} = -\frac{1}{2}\delta_{ij} + \int_{\Gamma_j}\frac{\partial G}{\partial n}d\Gamma,\ G^{ij} = \int_{\Gamma_j} G d\Gamma, \tag{1.74}$$

with δ_{ij} being the Kronecker delta which is defined as

$$\delta_{ij} = \begin{cases} 0 & \text{for } i \neq j, \\ 1 & \text{for } i \neq j. \end{cases}$$

Evaluation of integrals associated with the influence coefficients

The line integral present in Eq. (1.74) can be evaluated numerically for $i \neq j$ using the

Gauss–Legendre quadrature formula. Therefore, the influence coefficients can be expressed as

$$G^{ij}(x_0, z_0) \approx h_\gamma \sum_{k=1}^{N_Q} G\left[x(\gamma_k), z(\gamma_k); x_0, z_0\right] w_k, \tag{1.75}$$

$$H^{ij}(x_0, z_0) \approx h_\gamma \left[n_x^i \sum_{k=1}^{N_Q} \frac{\partial G}{\partial x}\left[x(\gamma_k), z(\gamma_k); x_0, z_0\right] w_k + n_z^i \sum_{k=1}^{N_Q} \frac{\partial G}{\partial z}\left[x(\gamma_k), z(\gamma_k); x_0, z_0\right] w_k \right]. \tag{1.76}$$

Here, $h_\gamma = 0.5\sqrt{(x_{i,2} - x_{i,1})^2 + (z_{i,2} - z_{i,1})^2}$ and n_x^i and n_z^i are the $x-$ and $z-$ components of the outward drawn unit normal vector $\vec{n}$. In addition, γ_k $(k = 1, 2, \cdots, N_Q)$ are the zeros of Legendre polynomial $P_n(\gamma)$ of degree N_Q. Moreover, w_k $(k = 1, 2, \cdots, N_Q)$ are termed as the weight functions, and the expression for the same is given as

$$w_k = \frac{2}{(1 - \gamma_k)^2 \left(P_n'(\gamma_k)\right)^2}$$

with $P_n^{'}(\gamma_k)$ being the derivative of $P_n(\gamma_k)$. However, for $i = j$, the integrals becomes improper. Following the analytical procedure as described in Brebbia et al. [104], it can be easily derived that

$$\int_{\Gamma_j} G \, d\Gamma = \frac{l_j}{2\pi}\left[\ln\left(\frac{l_j}{2}\right) - 1\right], \tag{1.77}$$

with l_j being the length of j^{th} boundary element, and

$$\int_{\Gamma_j} \frac{\partial G}{\partial n} \, d\Gamma = 0. \tag{1.78}$$

Using the notations as in Eq. (1.74), Eq. (1.73) is further re-written as

$$\sum_{j=1}^{N} H_{ij}\phi_j = \sum_{j=1}^{N} G_{ij}\frac{\partial \phi_j}{\partial n}. \tag{1.79}$$

In order to generate the number of equations equal to the number of unknowns N, the singular point (x_0, z_0) is moved at every node $i = 1, 2, \cdots, N$. In matrix form, Eq. (1.79) can be written as

$$\begin{bmatrix} H_{11} & H_{12} & H_{13} & \dots & H_{1N} \\ H_{21} & H_{22} & H_{23} & \dots & H_{2N} \\ & \dots\dots\dots\dots & & & \\ H_{N1} & H_{N2} & H_{N3} & \dots & H_{NN} \end{bmatrix} \begin{bmatrix} \phi_1 \\ \phi_2 \\ \vdots \\ \phi_N \end{bmatrix} = \begin{bmatrix} G_{11} & G_{12} & G_{13} & \dots & G_{1N} \\ G_{21} & G_{22} & G_{23} & \dots & G_{2N} \\ \vdots & \vdots & \vdots & \ddots & \vdots \\ G_{N1} & G_{N2} & G_{N3} & \dots & G_{NN} \end{bmatrix} \begin{bmatrix} \frac{\partial \phi_1}{\partial n} \\ \frac{\partial \phi_2}{\partial n} \\ \vdots \\ \frac{\partial \phi_N}{\partial n} \end{bmatrix}. \tag{1.80}$$

The above matrix formulation has some disadvantages as ϕ is described at some boundary elements and it's normal derivatives $\partial\phi/\partial n$ are described at some other boundary elements. In order to solve the linear system of equations, it is required to shuffle the columns of the matrix in an appropriate manner. Once all the unknown quantities are shifted to the left-hand side, one can write the system (1.80) as

$$[A]\{X\} = \{Y\}, \tag{1.81}$$

where X is a matrix of the unknown boundary values consisting of ϕ and $\partial\phi/\partial n$. Now, we can find the unknown values of ϕ and $\partial\phi/\partial n$ on every boundary element using $X = A^{-1}Y$. It is worthy to be noted that, unlike in the case of finite element analysis, the unknowns are the mixture of the velocity potentials and their normal derivatives, rather than just the velocity potentials. This is due to the fact that the BEM is a mixed formulation, and this particular fact is one of the advantage over the finite element analysis (Partridge et al. [108]).

1.6.4 Boundary element method based on linear element approach

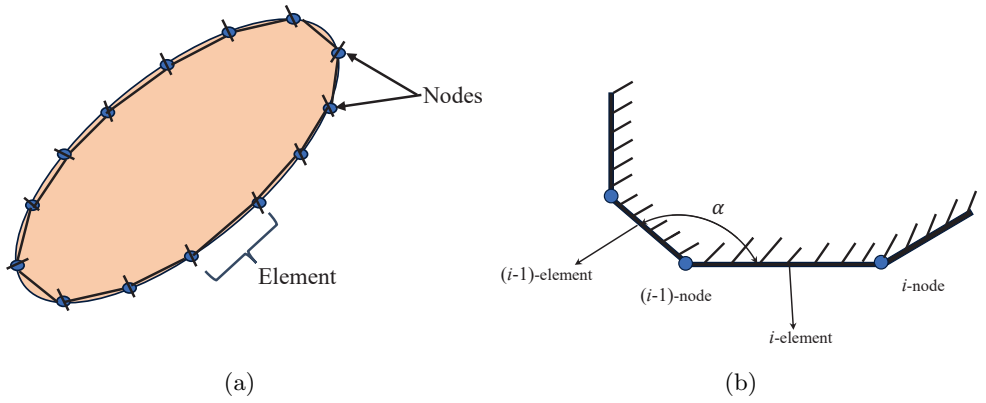

FIGURE 1.14: Discretization of boundary using linear elements.

The constant element approximates the actual geometry with straight lines, whereas the unknown boundary quantity is presumed to be constant on the element, leading to discontinuous distribution on the boundary. To overcome these issues, the linear boundary element method is adopted. These linear elements can properly approximate the boundary geometry by the straight lines as well as unknown boundary quantities by a linear function on each element. Further, for linear elements, the nodes are located at the corners of the polygon (see Fig. 1.14). Consequently, the governing integral equation (1.69) should be used with the replacement of $c(\tilde{P})$ by $c^i(\tilde{P})$. Here, c^i is the angle between the elements $i-1$ and i. Therefore, the governing integral equation can be written as

$$c^i(\tilde{P})\phi\left(x_0, z_0\right) = \int_\Gamma \left(\phi\frac{\partial G}{\partial n} - G\frac{\partial \phi}{\partial n}\right) d\Gamma, \tag{1.82}$$

where $c^i = \alpha/2\pi$ with α is the internal angle of the corner in radians. As a result of discretizing the boundary into N linear elements, Eq. (1.82) is changed as

$$-c^i(\tilde{P})\phi\,(x_0, z_0) + \sum_{j=1}^{N} \int_{\Gamma_j} \left(\phi \frac{\partial G}{\partial n}\right) d\Gamma = \sum_{j=1}^{N} \int_{\Gamma_j} \left(G \frac{\partial \phi}{\partial n}\right) d\Gamma. \tag{1.83}$$

Here, the boundary quantities ϕ and $\partial\phi/\partial n$ are vary linearly over each element Γ_j. Hence, it is not possible to take them out of the integrals. In linear element approach, the value of boundary quantities ϕ and $\partial\phi/\partial n$ at any point on the element can be written in terms of their nodal values and two linear interpolation functions Ξ_1 and Ξ_2 (details are provided in Brebbia and Dominguez [109]) as

$$\phi(\Upsilon) = \Xi_1 \phi^1 + \Xi_2 \phi^2, \tag{1.84}$$

$$\frac{\partial \phi}{\partial n}(\Upsilon) = \Xi_1 \frac{\partial \phi^1}{\partial n} + \Xi_2 \frac{\partial \phi^2}{\partial n}. \tag{1.85}$$

Here, Υ is the dimensionless coordinate varying from -1 to $+1$. Further, the interpolation functions are expressed as

$$\Xi_1 = \frac{1}{2}(1 - \Upsilon), \quad \Xi_2 = \frac{1}{2}(1 + \Upsilon). \tag{1.86}$$

Now, the line integral appearing in the right hand side of Eq. (1.83) can be written as

$$\int_{\Gamma_j} \left(G \frac{\partial \phi}{\partial n}\right) d\Gamma = \hat{g}_1^{ij} \frac{\partial \phi^1}{\partial n} + \hat{g}_2^{ij} \frac{\partial \phi^2}{\partial n}, \tag{1.87}$$

where

$$\hat{g}_1^{ij} = \frac{l_j}{2} \int_{-1}^{1} G \Xi_1(\Upsilon) d\Upsilon, \tag{1.88}$$

and

$$\hat{g}_2^{ij} = \frac{l_j}{2} \int_{-1}^{1} G \Xi_2(\Upsilon) d\Upsilon. \tag{1.89}$$

Here, l_j represents the length of the boundary element Γ_j. In a similar manner, the line intergral appearing on the left hand side of (1.83) can be expressed as

$$\int_{\Gamma_j} \left(\phi \frac{\partial G}{\partial n}\right) d\Gamma = \hat{h}_1^{ij} \phi^1 + \hat{h}_2^{ij} \phi^2, \tag{1.90}$$

where

$$\hat{h}_1^{ij} = \frac{l_j}{2} \int_{-1}^{1} \frac{\partial G}{\partial n} \Xi_1(\Upsilon) d\Upsilon, \tag{1.91}$$

and

$$\hat{h}_2^{ij} = \frac{l_j}{2} \int_{-1}^{1} \frac{\partial G}{\partial n} \Xi_2(\Upsilon) d\Upsilon. \tag{1.92}$$

Now, implementing Eqs. (1.87) and (1.90) into the Eq. (1.83), we get

$$-c^i(\tilde{P})\phi_i\left(x_0,z_0\right)+\sum_{j=1}^{N}\phi_j H^{ij}=\sum_{j=1}^{N}G^{ij}\frac{\partial\phi_j}{\partial n}. \tag{1.93}$$

Here,

$$\begin{aligned} H^{ij} &= -c^i(\tilde{P})\delta_{ij}+\mathcal{H}^{ij}, \quad \mathcal{H}^{ij}=\begin{cases}\hat{h}_1^{i1}+\hat{h}_2^{iN}, & \text{for} \quad j=1,\\ \hat{h}_1^{ij}+\hat{h}_2^{i,j-1}, & \text{for} \quad j=2\cdots N,\end{cases}\\ G^{ij} &= \begin{cases}\hat{g}_1^{i1}+\hat{g}_2^{iN}, & \text{for} \quad j=1,\\ \hat{g}_1^{ij}+\hat{g}_2^{i,j-1}, & \text{for} \quad j=2\cdots N.\end{cases}\end{aligned} \tag{1.94}$$

Here, H^{ij} and G^{ij} are termed as influence coefficients. The line integrals present in Eq. (1.94) can be handled in similar way as provided for constant boundary element approach. The influence coefficients are calculated analytically when the field points match with that of the source points, i.e., $i=j$, whilst the Gauss-Legendre quadrature formula is used when $i\neq j$. Using the point collocation method as stated earlier, a system of linear algebraic equations are obtained which are solved using the Gauss elimination method to obtain the unknown velocity potentials and their normal derivatives over each boundary element.

Chapter 2

Mathematical modeling of oscillating water column wave energy converter devices placed over undulated sea bed

* The work, in this chapter, is covered by the following publication:

1. S. Koley, and K. Trivedi, "Mathematical modeling of oscillating water column wave energy converter devices over the undulated sea bed," *Engineering Analysis with Boundary Elements*, vol. 117 , pp: 26-40, 2020.

2.1 General introduction

In this chapter, the hydrodynamic performance of an OWC (oscillating water column) wave energy converter device placed on an undulated bed. The bed undulation is finitely extended and beyond that, the water bed is uniform in nature. The mathematical problem is studied in the two-dimensional Cartesian coordinate system under the linearized water wave theory. To solve the associated boundary value problem, a coupled eigenfunction expansion - boundary element method is used. The numerical convergence of the coupled eigenfunction expansion - boundary element method is provided. The effects of the width of the OWC device chamber, front wall submergence depth and inclination with the vertical axis, and the bed undulations on the hydrodynamic efficiency of the OWC device is discussed in detail.

2.2 Mathematical formulation

In the present study, the geometric configurations of the OWC device and the coordinate system are provided in Fig. 2.1. The OWC device consists of a rigid and impermeable sloping front wall intersecting the mean free surface $z = 0$ at $x = L - b$. Further, the rear rigid wall of the OWC device is situated at $x = L$ and therefore the chamber width is b along the x-axis. The boundaries of the OWC device are having uniform thickness d. In presence of the OWC device, the total free surface is dived into two parts, namely internal free surface (free surface within the OWC chamber) and external free surface (free surface outside of the OWC chamber). A Wells turbine is placed at the opening mouth of the chamber above the free surface. As waves are coming, the water column within the chamber oscillates (vertical ups and downs motion) and as a result, the trapped air above the internal free surface flows through the turbine to produce electricity. Here, the OWC device is placed over an undulated bottom represented by $z = -h(x)$ with $z = -h_1$ for the region $x < 0$ and $z = -h_2$ at $x = L$. Therefore, the bottom undulation is finitely extended as seen in Fig. 2.1. The immersed boundaries of the front wall of the OWC device are represented by $\Gamma_5 \cup \Gamma_6 \cup \Gamma_7$. The submergence depth of the tip of the front wall is a. Further, the internal and external free surfaces are represented as $\Gamma_4 = \{(x, z) : z = 0; L - b < x < L\}$ and $\Gamma_8 = \{(x, z) : z = 0; 0 < x < L - b - d\}$ respectively. Here, the total water domain is divided into two regions R_1 and R_2 respectively as seen in Fig. 2.1. It is to be noted that the water depth is uniform in the region R_1 whereas the bottom is undulated in nature for region R_2. Further, regions R_1 and R_2 are separated by an auxiliary boundary Γ_1. Since the solution methodology for the present problem is based on coupled eigenfunction expansion - boundary element method, the governing equation and associated boundary conditions are written in a proper manner in the following. For the modeling purpose, the water is assumed to follow the potential flow theory (see Koley and Sahoo [110] for details) and the motion is simple harmonic in time with circular

frequency ω. Therefore, the total velocity potentials $\Phi_j(x,z,t) = \Re\{\phi_j(x,z)e^{-i\omega t}\}$ ($j = 1, 2$ corresponds to regions R_j) exist and satisfies the Laplace equation

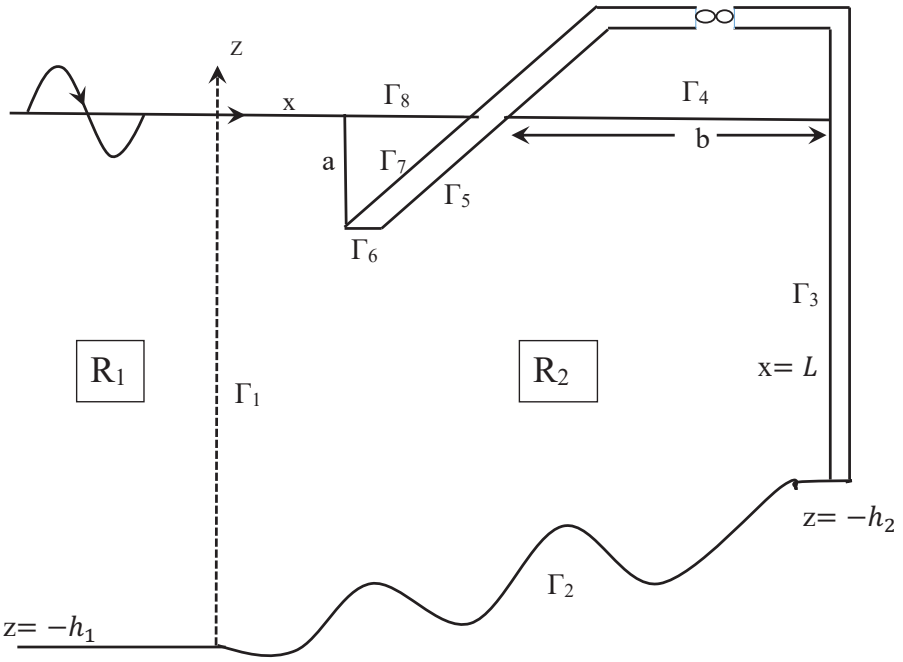

FIGURE 2.1: Vertical cross-section of the OWC device.

$$\nabla^2\phi_j(x,z) = 0, \quad \text{for } j = 1,2, \quad \nabla^2 \equiv \left(\frac{\partial^2}{\partial x^2} + \frac{\partial^2}{\partial z^2}\right) \tag{2.1}$$

The boundary condition at the mean free surface $z = 0$ is given by (see Evans and Porter [5] and Rezanejad et al. [7] for details)

$$\frac{\partial\phi_1}{\partial z} - K\phi_1 = 0, \quad \text{for } x < 0, z = 0, \qquad \frac{\partial\phi_2}{\partial n} - K\phi_2 = \begin{cases} \dfrac{\mathrm{i}\omega p}{\rho g}, & \text{on } \Gamma_4, \\ 0, & \text{on } \Gamma_8 \end{cases} \tag{2.2}$$

where $K = \omega^2/g$, with g being the gravitational acceleration. Here, $\partial/\partial n$ represents the normal derivative. Now, the impervious bottom boundary condition gives

$$\frac{\partial\phi_j}{\partial n} = 0, \quad \text{on } z = -h(x), \tag{2.3}$$

where the bottom profile $h(x)$ is given by

$$h(x) = \begin{cases} h_1, & x < 0 \\ \tilde{h}(x), & 0 < x < L \\ h_2, & x = L \end{cases} \tag{2.4}$$

where $\tilde{h}(x)$ represents the undulated bottom profile and the corresponding bottom boundary is denoted by Γ_2. The boundaries of the OWC device are rigid and impermeable in nature and therefore the rigid wall boundary conditions are given by

$$\frac{\partial \phi_2}{\partial n} = 0, \quad \text{on} \quad \Gamma_3 \cup \Gamma_5 \cup \Gamma_6 \cup \Gamma_7. \tag{2.5}$$

The fluid pressure and normal velocity or mass flux are continuous at Γ_1 and so

$$\phi_1 = \phi_2, \quad \frac{\partial \phi_1}{\partial n} = -\frac{\partial \phi_2}{\partial n}, \quad \text{on} \ \ \Gamma_1 \tag{2.6}$$

Since the velocity potential consists of scattered and radiated velocity potentials and therefore, the total velocity potential can be written as

$$\phi_j = \phi_j^S + \left(\frac{\mathrm{i}\omega p}{\rho g}\right)\phi_j^R, \quad \text{for} \ \ j = 1, 2, \tag{2.7}$$

where ϕ^S and ϕ^R represent the scattered and radiated velocity potential respectively. It is to be noted that in Eq. (2.7), ϕ_j^S represents the scattered velocity potential for region R_j $(j = 1, 2)$. These scattered velocity potentials are the sum of diffracted and incident velocity potentials i.e., $\phi_j^S = \phi_j^D + \phi_j^I$ where ϕ_j^D and ϕ_j^I represent the diffracted and incident velocity components for $j = 1, 2$. Similar decompositions were used by Smith [111] and Evans and Porter [5]. The scattered velocity potential appears because the incoming wave is reflected by the rigid wall boundaries of the OWC device. Further, the radiated velocity potential appears due to the oscillation of the water column in the OWC device wave chamber. Here, $\phi_1^{S,R}$ satisfy the Eqs.(2.1)-(2.3) and (2.6). On the other hand, $\phi_2^{S,R}$ satisfy the Eqs.(2.1)-(2.3) and (2.5)-(2.6). It is to be noted that, in region R_2, Eq. (2.2) is changed into

$$\frac{\partial \phi_2^S}{\partial n} - K\phi_2^S = 0, \quad \text{on} \ \ \Gamma_4 \cup \Gamma_8, \qquad \frac{\partial \phi_2^R}{\partial n} - K\phi_2^R = \begin{cases} 1, & \text{on} \ \ \Gamma_4, \\ 0, & \text{on} \ \ \Gamma_8. \end{cases} \tag{2.8}$$

Further, using Eq. (2.7) into Eq. (2.6), the interface boundary conditions are obtained as

$$\phi_1^{S,R} = \phi_2^{S,R}, \quad \frac{\partial \phi_1^{S,R}}{\partial n} = -\frac{\partial \phi_2^{S,R}}{\partial n}, \quad \text{on} \ \ \Gamma_1 \tag{2.9}$$

Finally, the far-field boundary conditions are given by

$$\begin{cases} \phi_1^S(x, z) = e^{\mathrm{i}k_0 x}\psi_0(k_0, z) + A_0^S e^{-\mathrm{i}k_0 x}\psi_0(k_0, z), & \text{as} \ \ x \to -\infty, \\ \phi_1^R(x, z) = A_0^R e^{-\mathrm{i}k_0 x}\psi_0(k_0, z), & \text{as} \ \ x \to -\infty, \end{cases} \tag{2.10}$$

where A_0^S and A_0^R are the coefficients related to the amplitude of the reflected and radiated waves at $x = -\infty$ respectively. In Eq. (2.10), the expression for vertical eigenfunction $\psi_0(k_0, z)$

is given by $\psi_0(k_0, z) = \dfrac{\cosh k_0(h_1 + z)}{\cosh(k_0 h_1)}$. Here, k_0 is positive real root of the dispersion relation $\omega^2 = gk \tanh(kh_1)$.

2.3 Solution methodology

The BVP (boundary value problem) described in the previous Section is handled for a solution using a coupled eigenfunction expansion and boundary element method. Since the water depth in the region R_1 is uniform and therefore, the eigenfunction expansion method is applicable. In region R_2, the bottom is undulated in nature and so the boundary element method is used to solve the BVP in R_2. Finally, using matching conditions as in Eq. (2.6), an appropriate coupling is done.

2.3.1 Eigenfunction expansion in region R_1

In this Section, eigenfunction expansion and coupling procedure are discussed firstly for radiation problem and a similar approach is adopted for the scattering problem. Using the eigenfunction expansion method, the velocity potential for the radiated potential ϕ_1^R satisfying the boundary conditions as stated earlier is expressed as

$$\phi_1^R(x, z) = \sum_{n=0}^{\infty} A_n^R e^{-\mathrm{i}k_n x} \psi_n(k_n, z), \tag{2.11}$$

where the form of the vertical eigenfunctions $\psi_n(k_n, z)$s for $n = 0, 1, 2, \cdots$ are given by $\psi_n(k_n, z) = \dfrac{\cosh k_n(z + h_1)}{\cosh k_n h_1}$. In Eq. (2.11), $k_n = \mathrm{i}k_n'$'s for $n = 1, 2, \cdots$ are the eigenvalues with k_n' representing the real positive roots of $K = -k \tan kh_1$. Now, the orthogonal properties of the eigenfunctions $\psi_n(k_n, z)$s give

$$\int_{-h_1}^{0} \psi_m(k_m, z)\ \psi_n(k_n, z)\ dz = \mathcal{A}_n \delta_{mn} \tag{2.12}$$

where δ_{mn} is the Kronecker delta function with $\mathcal{A}_n = \dfrac{2k_n h_1 + \sinh(2k_n h_1)}{4k_n \cosh^2(k_n h_1)}$. Using the identity (2.12) in (2.11), the following expression is obtained

$$A_n^R = \frac{1}{\mathcal{A}_n} \int_{-h_1}^{0} \phi_1^R(0, z)\ \psi_n(k_n, z)\ dz. \tag{2.13}$$

Taking the normal derivative of the potential $\phi_1^R(x,z)$ as in Eq. (2.11) and substituting A_n^R from Eq. (2.13), he following relation is derived

$$\left.\frac{\partial \phi_1^R}{\partial n}\right|_{x=0} = \sum_{n=0}^{\infty} \frac{\mathrm{i}k_n}{\mathcal{A}_n}\psi_n\left(k_n,z\right)\int_{-h_1}^{0}\phi_1^R(0,z)\psi_n(k_n,z)\,dz. \tag{2.14}$$

In a similar manner, the eigenfunction expression for the scattered velocity potential ϕ_1^S is given by

$$\phi_1^S(x,z) = e^{\mathrm{i}k_0 x}\psi_0(k_0,z) + \sum_{n=0}^{\infty} A_n^S e^{-\mathrm{i}k_n x}\psi_n(k_n,z), \tag{2.15}$$

where

$$A_n^S = -\delta_{0n} + \frac{1}{\mathcal{A}_n}\int_{-h_1}^{0}\phi_1^S(0,z)\,\psi_n(k_n,z)\,dz \tag{2.16}$$

Taking the normal derivative of the potential $\phi_1^S(x,z)$ as in Eq. (2.15) and substituting A_n^S from Eq. (2.16), the following expression is obtained as

$$\left.\frac{\partial \phi_1^S}{\partial n}\right|_{x=0} = -2\mathrm{i}k_0\psi_0(k_0,z) + \sum_{n=0}^{\infty}\frac{\mathrm{i}k_n}{\mathcal{A}_n}\psi_n\left(k_n,z\right)\int_{-h_1}^{0}\phi_1^S(0,z)\psi_n(k_n,z)\,dz. \tag{2.17}$$

Now, the infinite series present in Eqs. (2.14) and (2.17) are truncated into finite N terms and are used in the boundary element formulation at a later stage.

2.3.2 Boundary element formulation in region R_2

In region R_2, the BVP associated with the radiation potential ϕ_2^R and the scattering potential ϕ_2^S are transformed into Fredholm integral equations and solved numerically using the boundary element method. Firstly, the procedure is discussed for radiation problem and then the same is discussed for the scattering problem. Applying Green's second identity to the velocity potential $\phi_2^R(x,z)$ and the fundamental solution $G(x,z;x_0,z_0)$, the following integral equation is obtained (see Katsikadelis [112] for detailed derivation)

$$\frac{\alpha}{2\pi}\phi_2^R(x_0,z_0) = \int_{\Gamma}\left[\phi_2^R(x,z)\frac{\partial G}{\partial n}(x,z;x_0,z_0) - G(x,z;x_0,z_0)\frac{\partial \phi_2^R}{\partial n}(x,z)\right]d\Gamma(x,z). \tag{2.18}$$

Here (x_0,z_0) and (x,z) are the source and field points respectively. Moreover, $\alpha=\pi$ for smooth boundaries. It is to be noted that in Eq.(2.18), the source point (x_0,z_0) lies on the boundary Γ of the domain. The fundamental solution $G(x,z;x_0,z_0)$ satisfies Eq. (2.1) with the right hand side being replaced by Dirac delta function (Katsikadelis [112]) and takes the form

$$G(x,z;x_0,z_0) = \frac{1}{2\pi}\ln(\tilde{r}), \text{where } \tilde{r} = \sqrt{(x-x_0)^2+(z-z_0)^2}. \tag{2.19}$$

The properties of the aforementioned fundamental solution are provided in Katsikadelis [112] and the details are deferred here. Applying the boundary conditions (2.3), (2.5), (2.6) and (2.8) in Eq. (2.18), the following integral equation is derived

$$-\frac{1}{2}\phi_2^R + \int_{\Gamma_1}\left(\phi_1^R\frac{\partial G}{\partial n} + G\frac{\partial \phi_1^R}{\partial n}\right)d\Gamma + \int_{\Gamma_2\cup\Gamma_3}\phi_2^R\frac{\partial G}{\partial n}d\Gamma + \int_{\Gamma_4}\left(\frac{\partial G}{\partial n} - KG\right)\phi_2^R d\Gamma + \int_{\Gamma_5\cup\Gamma_6\cup\Gamma_7}\frac{\partial G}{\partial n}\phi_2^R d\Gamma + \int_{\Gamma_8}\phi_2^R\left(\frac{\partial G}{\partial n} - KG\right)d\Gamma = \int_{\Gamma_4} G d\Gamma. \quad (2.20)$$

In a similar manner, using the boundary conditions (2.3), (2.5), (2.6) and (2.8), the following integral equation is ontained for scattered potential in region R_2

$$-\frac{1}{2}\phi_2^S + \int_{\Gamma_1}\left(\phi_1^S\frac{\partial G}{\partial n} + G\frac{\partial \phi_1^S}{\partial n}\right)d\Gamma + \int_{\Gamma_2\cup\Gamma_3}\phi_2^S\frac{\partial G}{\partial n}d\Gamma + \int_{\Gamma_4}\left(\frac{\partial G}{\partial n} - KG\right)\phi_2^S d\Gamma + \int_{\Gamma_5\cup\Gamma_6\cup\Gamma_7}\frac{\partial G}{\partial n}\phi_2^S d\Gamma + \int_{\Gamma_8}\phi_2^S\left(\frac{\partial G}{\partial n} - KG\right)d\Gamma = 0. \quad (2.21)$$

Now, Eqs. (2.20) and (2.21) are discretized using the Boundary Element Method to get the system of equations. In this procedure, constant element approach is used (see Katsikadelis [112] for details). In this approach, the entire boundary of the region R_2 is discretized into N constant elements and the values for ϕ_2 and $\partial\phi_2/\partial n$ are assumed to be constants over each element. Further, point collocation method is used to generate a system of equations in which the source point runs over each boundary element. With these assumptions, Eqs. (2.20) and (2.21) can be written in the following discrete form

$$\sum_{j=1}^{N_1}\left(H^{ij}\phi_{1j}^R + G^{ij}\frac{\partial\phi_{1j}^R}{\partial n}\right)\Big|_{\Gamma_1} + \sum_{j=1}^{N_2+N_3}H^{ij}\phi_{2j}^R\big|_{\Gamma_2\cup\Gamma_3} + \sum_{j=1}^{N_4}\left(H^{ij} - KG^{ij}\right)\phi_{2j}^R\big|_{\Gamma_4} + \sum_{j=1}^{N_5+N_6+N_7}H^{ij}\phi_{2j}^R\big|_{\Gamma_5\cup\Gamma_6\cup\Gamma_7} + \sum_{j=1}^{N_8}\left(H^{ij} - KG^{ij}\right)\phi_{2j}^R\big|_{\Gamma_8} = \sum_{j=1}^{N_4}G^{ij}\big|_{\Gamma_4}, \quad (2.22)$$

$$\sum_{j=1}^{N_1}\left(H^{ij}\phi_{1j}^S + G^{ij}\frac{\partial\phi_{1j}^S}{\partial n}\right)\Big|_{\Gamma_1} + \sum_{j=1}^{N_2+N_3}H^{ij}\phi_{2j}^S\big|_{\Gamma_2\cup\Gamma_3} + \sum_{j=1}^{N_4}\left(H^{ij} - KG^{ij}\right)\phi_{2j}^S\big|_{\Gamma_4} + \sum_{j=1}^{N_5+N_6+N_7}H^{ij}\phi_{2j}^S\big|_{\Gamma_5\cup\Gamma_6\cup\Gamma_7} + \sum_{j=1}^{N_8}\left(H^{ij} - KG^{ij}\right)\phi_{2j}^S\big|_{\Gamma_8} = 0, \quad (2.23)$$

where H^{ij} and G^{ij} are defined as

$$H^{ij} = -\frac{1}{2}\delta_{ij} + \int_{\Gamma_j}\frac{\partial G}{\partial n}d\Gamma, \quad G^{ij} = \int_{\Gamma_j} G d\Gamma. \quad (2.24)$$

The values of H^{ij} and G^{ij} are evaluated using Gauss-Legendre quadrature formulae for the case $i \neq j$. For $i = j$ case, $H^{ii} = 0$ and the values of G^{ii} are evaluated analytically. The details

procedure for the same are mentioned in Katsikadelis [112]. Finally, the matrix equations for (2.22) and (2.23) are written as

$$\left([H]\left[\phi_1^R\right]+[G]\left[\frac{\partial\phi_1^R}{\partial n}\right]\right)\Big|_{\Gamma_1}+[H]\left[\phi_2^R\right]\big|_{\Gamma_2\cup\Gamma_3}+\left([H]-K[G]\right)\left[\phi_2^R\right]\big|_{\Gamma_4} + [H]\left[\phi_2^R\right]\big|_{\Gamma_5\cup\Gamma_6\cup\Gamma_7}+\left([H]-K[G]\right)\left[\phi_2^R\right]\big|_{\Gamma_8}=[G]|_{\Gamma_4}\,. \tag{2.25}$$

In a similar manner, the matrix equation for the scattered potential in the region R_2 is obtained as

$$\left([H]\left[\phi_1^S\right]+[G]\left[\frac{\partial\phi_1^S}{\partial n}\right]\right)\Big|_{\Gamma_1}+[H]\left[\phi_2^S\right]\big|_{\Gamma_2\cup\Gamma_3}+\left([H]-K[G]\right)\left[\phi_2^S\right]\big|_{\Gamma_4} + [H]\left[\phi_2^S\right]\big|_{\Gamma_5\cup\Gamma_6\cup\Gamma_7}+\left([H]-K[G]\right)\left[\phi_2^S\right]\big|_{\Gamma_8}=0. \tag{2.26}$$

Now, the aforementioned constant element approach is used in Eqs. (2.14) and (2.17) to get the matrix form of $\partial\phi_1^R/\partial n$ and $\partial\phi_1^S/\partial n$ on the boundary Γ_1. These are used in Eqs. (2.25) and (2.26) and these system of equations are finally solved to get the required unknowns.

It is to be noted that the coupled eigenfunction expansion-boundary element method has the following advantage over the boundary element method. In boundary element method, the auxiliary boundary Γ_1 (see Fig. 2.1) should be placed far-away from the undulated bed regions so that the effect of the local or evanescent wave modes (imaginary roots of the dispersion relation) diminishes on Γ_1 and the far-field boundary condition as in Eq. (2.10) holds on Γ_1. As a result, the computational domain is bigger and the run time increases. On the other hand, in the coupled eigenfunction expansion-boundary element method, the auxiliary boundary Γ_1 is placed at the interface of the undulated and uniform bed regions (see Fig. 2.1). So, the boundary element method is applicable in the undulated bed region R_2 which is comparatively smaller region and the eigenfunction expansion method is applicable in the semi-infinite uniform bed region R_1. Since the eigenfunction expansion method is a semi-analytic method and therefore the run time is very less. In summing up, the run time for the coupled eigenfunction expansion-boundary element method is significantly less than when only the boundary element method is used. Further, the coupled eigenfunction expansion-boundary element method has advantages over the finite element method (FEM). In FEM, the total domain of the physical problem is discretized whereas in the coupled eigenfunction expansion-boundary element method, only the boundaries of the undulated bed region are discretized. So, the run time is significantly less in the coupled eigenfunction expansion-boundary element method compared to the FEM.

2.4 Various quantities associated with OWC devices

In this Section, the expressions for various physical parameters associated with the hydrodynamic performance of the OWC device discussed in Section 2 are derived. The mean energy flux per unit length across a vertical cross-section normal to the incident wave direction is given by (see Dean and Dalrymple [18] for details)

$$P_w = EC_g = \frac{\rho\omega k_0 \mathcal{A}_0}{2}. \tag{2.27}$$

The time harmonic volume flow rate $Q(t) = \Re\{qe^{-\mathrm{i}\omega t}\}$ across the internal free surface Γ_4 is given by (see Evans and Porter [5] and Rezanejad et al. [7] for details)

$$q = \int_{\Gamma_4} \frac{\partial\phi}{\partial z} dx = q^S + \frac{\mathrm{i}\omega p}{\rho g} q^R, \tag{2.28}$$

where q^S and q^R represent the volume flow rate across the internal free surface Γ_4 for the scattering and radiation problems respectively. Now, applying the continuity of flux across the gap Γ_g and the internal free surface Γ_4, the following expressions are derived

$$q^{S,R} = \int_{\Gamma_4} \frac{\partial\phi^{S,R}}{\partial z} dx = \int_{\Gamma_g} \frac{\partial\phi^{S,R}}{\partial x} dz. \tag{2.29}$$

It is to be noted that Γ_g is the vertical auxiliary boundary lies between the tip of the breakwater wall and the bottom. Decomposing the volume flux due to the radiation potential into real and imaginary parts (see Evans and Porter [5] for details) as the following

$$\frac{\mathrm{i}\omega p}{\rho g} q^R = -\left(\tilde{B} - \mathrm{i}\tilde{A}\right) p = -Zp \quad \text{(say)}, \tag{2.30}$$

the expressions obtained for the radiation susceptance parameter $\tilde{A}$ and radiation conductance parameter $\tilde{B}$ respectively as the following

$$\tilde{A} = \frac{\omega}{\rho g}\Re\{q^R\}, \quad \tilde{B} = \frac{\omega}{\rho g}\Im\{q^R\}. \tag{2.31}$$

It is to be noted that the parameter $Z = \left(\tilde{B} - \mathrm{i}\tilde{A}\right)$ is termed as complex radiation admittance. To find explicit expression for the parameter $\tilde{B}$, applying the Green's second identity on ϕ_1^R and its complex conjugate $\overline{\phi}_1^R$ over the domain bounded by $\Gamma = \Gamma_{-\infty} \cup \Gamma_{10} \cup \Gamma_1 \cup \Gamma_9$, the following identity is obtained as

$$\int_{\Gamma} \left(\phi_1^R \frac{\partial \overline{\phi}_1^R}{\partial n} - \overline{\phi}_1^R \frac{\partial \phi_1^R}{\partial n} \right) ds = 0. \tag{2.32}$$

Here $\Gamma_{-\infty}$ is situated at far-field so that the far-field condition Eq. (2.10) is valid over $\Gamma_{-\infty}$. Now, there are no contributions from the boundaries Γ_j for $j = 9, 10$. The contribution from the

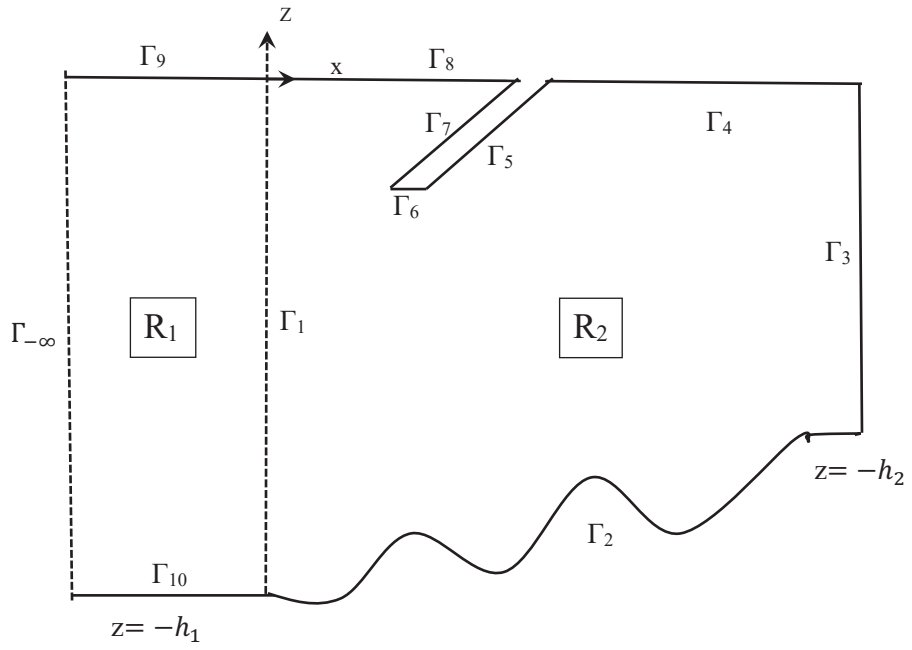

FIGURE 2.2: Contour in region R_j for $j = 1, 2$.

boundary $\Gamma_{-\infty}$ and Γ_1 are the following

$$\Gamma_{-\infty}: \quad -2\mathrm{i}k_0\mathcal{A}_0|A_0^R|^2, \tag{2.33}$$

$$\Gamma_1: \quad \int_{-h_1}^{0}\left(\phi_1^R\frac{\partial\overline{\phi}_1^R}{\partial x}-\overline{\phi}_1^R\frac{\partial\phi_1^R}{\partial x}\right)dz. \tag{2.34}$$

In a similar manner, applying the Green's second identity on ϕ_2^R and its complex conjugate $\overline{\phi}_2^R$ over the domain bounded by $\Gamma = \bigcup_{i=1}^{8}\Gamma_i$, the following expression is derived

$$\int_{\Gamma}\left(\phi_2^R\frac{\partial\overline{\phi}_2^R}{\partial n}-\overline{\phi}_2^R\frac{\partial\phi_2^R}{\partial n}\right)ds = 0. \tag{2.35}$$

There are no contributions from the boundaries Γ_j for $j = 2, 3, 5, 6, 7, 8$. The contribution from the boundaries Γ_1 and Γ_4 are the following

$$\Gamma_1: \quad -\int_{-h_1}^{0}\left(\phi_2^R\frac{\partial\overline{\phi}_2^R}{\partial x}-\overline{\phi}_2^R\frac{\partial\phi_2^R}{\partial x}\right),dz \tag{2.36}$$

$$\Gamma_4: \quad \left(\frac{2\mathrm{i}\rho g}{K\omega}\right)\tilde{B}. \tag{2.37}$$

It is to be noted that to get the expression as in Eq. (2.37), Eqs. (2.8) and (2.31) are used. Summing up Eqs. (2.33), (2.34), (2.36) and (2.37) and using Eq. (2.9), the expression for $\tilde{B}$ is

derived in terms of radiated wave amplitude A_0^R as

$$\tilde{B} = \frac{\omega}{\rho g} k_0 K |A_0^R|^2 \mathcal{A}_0. \tag{2.38}$$

In a similar manner, using Green's identity for scattered potential ϕ^S and radiated potential ϕ^R over the domain bounded by $\Gamma = \bigcup_{i=1}^{8} \Gamma_i$, we get the following

$$q^S = -2\mathrm{i} k_0 K A_0^R \mathcal{A}_0. \tag{2.39}$$

Using Eqs. (2.27), (2.38) and (2.39), the relation between P_w and $\tilde{B}$ is expressed as the following

$$\tilde{B} = \frac{|q^S|^2}{8P_w}. \tag{2.40}$$

Now, the average power absorbed W per unit width of the pressure distribution is given by (see Smith [111] and Evans [23] for details)

$$W = \frac{1}{2} \Re \left\{ \overline{p} q \right\}. \tag{2.41}$$

Using Eqs. (2.28) and (2.30), the above expression is rewritten as

$$W = \frac{1}{2} \Re \left\{ \overline{p} q^S \right\} - \frac{1}{2} |p|^2 \tilde{B}. \tag{2.42}$$

It was shown by Evans [23] that the average power absorbed W attends maximum

$$W_{max} = \frac{1}{8} \frac{|q^S|^2}{\tilde{B}}, \quad \text{for } p = \frac{q^S}{2\tilde{B}}. \tag{2.43}$$

Therefore, the efficiency of power absorption is given by

$$\eta_{max} = \frac{W_{max}}{P_w}. \tag{2.44}$$

It is to be noted that $\eta_{max} = 1/2$ for the case when the pressure distribution is symmetric about the x-axis as pointed by Smith [111]. Now, in practical application, it is not possible always to control the pressure difference across the Wells turbine placed at the top of OWC device. However, it is possible to control the rate of the air flow through the turbine. For simplicity, it is assumed that the volume flux is linearly proportional to the pressure across the turbine and therefore

$$q = \wedge p. \tag{2.45}$$

Here, $\wedge$ is a real positive constant and termed as control parameter. Substituting the relations as in Eqs. (2.30) and (2.45) into Eq. (2.41), the expression for the absorbed power W is written as

$$W = \frac{|q^S|^2}{8\tilde{B}}\left(1 - \frac{|\wedge - \overline{Z}|^2}{|\wedge + \overline{Z}|^2}\right). \tag{2.46}$$

For a given frequency, the absorbed power W takes its optimum value

$$W_{max} = \frac{|q^S|^2}{4}\left\{\frac{1}{\wedge_{opt} + \tilde{B}}\right\}, \quad \text{for } \wedge_{opt} = \sqrt{\tilde{A}^2 + \tilde{B}^2}. \tag{2.47}$$

Using the above expression into Eq. (2.44), the maximum efficiency is expressed as

$$\eta_{max} = \frac{|q^S|^2}{4P_w}\left(\frac{1}{\wedge_{opt} + \tilde{B}}\right). \tag{2.48}$$

Further, using Eq. (2.40), the aforementioned expression for η_{max} can also be written in the following form

$$\eta_{max} = \left(\frac{2\tilde{B}}{\wedge_{opt} + \tilde{B}}\right). \tag{2.49}$$

2.5 Results

In this Section, firstly the numerical convergence of the coupled eigenfunction expansion - boundary element method is provided. For the same, the non-dimensional form of the parameters $\tilde{A}$ and $\tilde{B}$ discussed in the previous Section are written as the following (see Evans and Porter [5]).

$$\mu = \frac{\rho g}{\omega b}\tilde{A}, \qquad \nu = \frac{\rho g}{\omega b}\tilde{B}, \tag{2.50}$$

Using the above expressions, the non-dimensional form of η_{max} can be written as

$$\eta_{max} = \frac{2\nu}{\nu + \sqrt{\nu^2 + \mu^2}} = \frac{2}{1 + \sqrt{1 + \left(\frac{\mu}{\nu}\right)^2}}. \tag{2.51}$$

For the numerical computation, MATLAB software-based programmings are written based on the solution procedure as discussed in Section 3. The values of the wave and OWC device parameters are taken as follows: time period of the incident wave $T = 10$sec, $h_1 = 15m$, $h_2 = h_1/1.5$, angle of inclination of the OWC device front wall with the x-axis $\theta = 45^\circ$, $L/h_1 = 2.0$, $b/h_1 = 1.0$, $a/h_1 = 0.5$, $d/h_1 = 0.1$, $g = 9.81\text{m/s}^2$, $\rho = 1025$ kg/m^3 unless otherwise mentioned. In the present study, two different bottom profiles are considered and the corresponding profiles are given in the following (see Behera et al. [75] and Porter and Porter [113] for details). The formation of sea bed undulation and its application in real ocean engineering problems were discussed in Liu et al. [114].

Type I bed profile:

$$\tilde{h}(x) = h_1 - H\left\{1 - \alpha\left(1 - \frac{x}{L}\right)^2 + (\alpha - 1)\left(1 - \frac{x}{L}\right)\right\}, \tag{2.52}$$

where α is a real constant and $H = h_1 - h_2$. Depending on the nature of α, various shapes of the bottom profiles are obtained. The schematic diagram of the bottom profiles for different values of α is provided in Fig. 2.3.

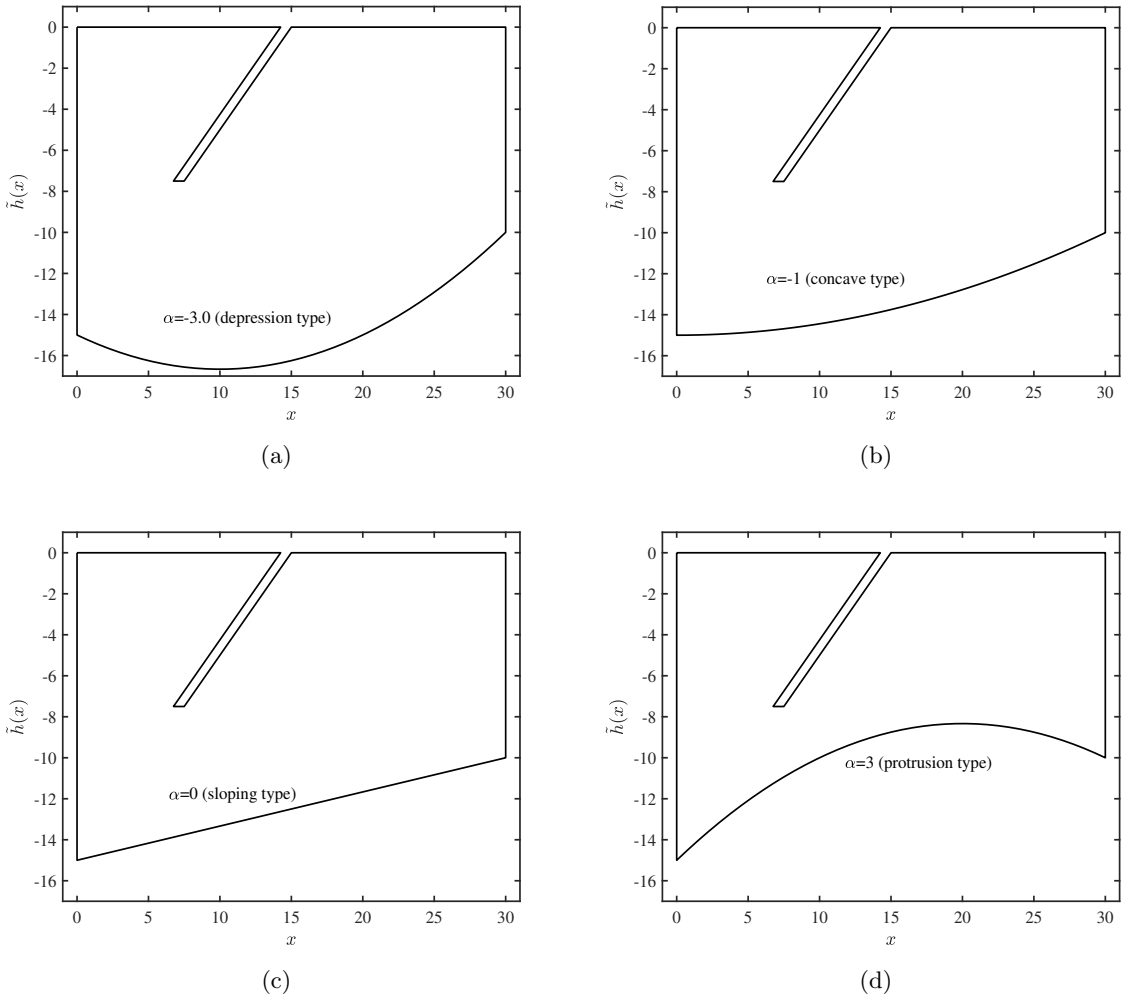

FIGURE 2.3: Computational boundaries of region R_2 for (a) $\alpha = -3.0$, (b) $\alpha = -1.0$, (c) $\alpha = 0$ and (d) $\alpha = 3.0$.

Type II bed profile:

$$\tilde{h}(x) = h_2 + H\left\{1 + 2\left(\frac{x}{L}\right)^3 - 3\left(\frac{x}{L}\right)^2 - \frac{a_1}{H}\sin\left(\frac{2m\pi x}{L}\right)\right\}, \tag{2.53}$$

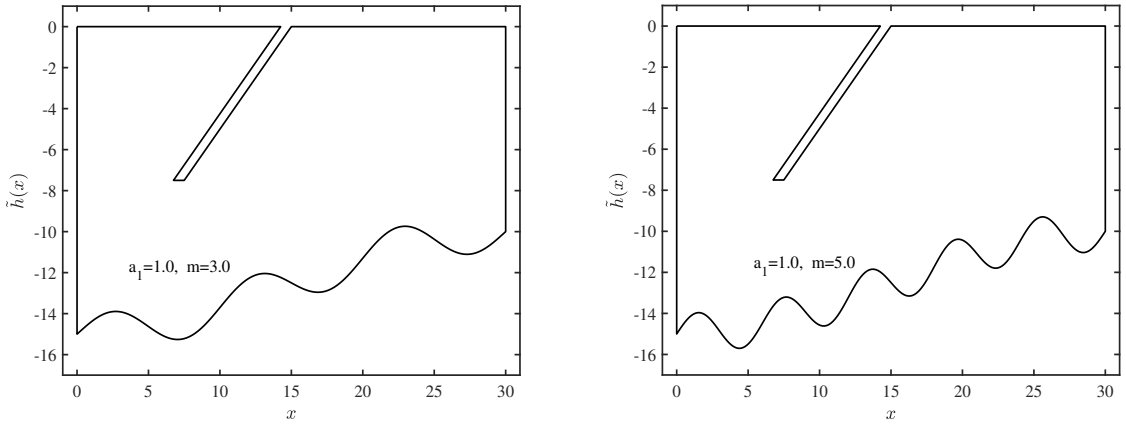

(a) (b)

FIGURE 2.4: Computational boundaries of region R_2 for (a) $a_1 = 1.0$, $m = 3.0$, (b) $a_1 = 1.0$, $m = 5.0$.

where H is defined before, a_1 is the amplitude of the ripples and m is the number of ripples. The schematic diagram of the bottom profiles for different values of m is provided in Fig. 2.4.

2.5.1 Convergence study

κ	b/h_1	Numerical Solution		
		μ	ν	η_{max}
20	1/8	1.34726	0.08144	0.11382
	1/4	1.69632	0.25383	0.25782
	1/2	2.48109	1.30492	0.63527
40	1/8	1.34322	0.08688	0.12126
	1/4	1.67810	0.26732	0.27186
	1/2	2.42419	1.32818	0.64910
60	1/8	1.34447	0.08526	0.11905
	1/4	1.68171	0.26249	0.26722
	1/2	2.44684	1.31392	0.64231
80	1/8	1.34448	0.08525	0.11907
	1/4	1.68131	0.26242	0.26723
	1/2	2.44690	1.31378	0.64235

TABLE 2.1: Comparative study of μ, ν and η_{max} for the OWC device placed on bottom of type II with $a_1 = 0.5$ and $m = 3$. Here $N = 5$ is considered.

The convergence of the numerical computations based on the coupled eigenfunction expansion-boundary element method depends on the panel size used to discretize the boundaries of the domain and the number of evanescent modes N used to truncate the infinite series present in

N	b/h_1	Numerical Solution		
		μ	ν	η_{max}
2	1/8	1.34446	0.08526	0.11905
	1/4	1.68168	0.26248	0.26722
	1/2	2.44672	1.31388	0.64231
5	1/8	1.34447	0.08526	0.11904
	1/4	1.68170	0.26249	0.26722
	1/2	2.44682	1.31392	0.64231
10	1/8	1.34447	0.08526	0.11904
	1/4	1.68171	0.26249	0.26722
	1/2	2.44684	1.31392	0.64231
20	1/8	1.34447	0.08526	0.11904
	1/4	1.68170	0.26249	0.26722
	1/2	2.44684	1.31392	0.64231

TABLE 2.2: Comparative study of μ, ν and η_{max} for the OWC device placed on bottom of type II with $a_1 = 0.5$ and $m = 3$. Here $\kappa = 60$ is considered.

Eqs. (2.11) and (2.15). The panel size p_s can be expressed in the following form (see Wang and Meylan [115] for details)

$$p_s = \frac{1}{\kappa k_0}.$$

Therefore, with an increase in κ, the panel size used in BEM decreases. By varying the values of κ, the panel size for BEM is determined to get numerical convergence. In Tabs. 2.1 and 2.2, the values of the non-dimensional parameters μ, ν and η_{max} are computed for different values of the internal free surface length $b/h_1 = 1/8, 1/4, 1/2$. In Tab. 2.1, κ is varying whilst $N = 5$ is kept fixed. It is seen that the values of μ, ν and η_{max} converge up to three decimal places for $\kappa = 60$. On the other hand, in Tab. 2.2, N is varying whilst $\kappa = 60$ is kept fixed. It is concluded that $N = 5$ and $\kappa = 60$ are sufficient to get convergence up to three decimal places in the numerical results. Therefore, in the subsequent computations, $\kappa = 60$ and $N = 5$ are considered.

2.5.2 Validation

Now, for the sake of validation of the present numerical results, certain results are compared with the results of Evans and Porter [5]. To obtain the OWC device model of Evans and Porter [5], a limiting case of our present OWC model is considered by taking $\theta = 0°$, $d/h_1 = 0.00001$ and the bottom is considered uniform in nature. In Figs. 2.5(a) and 2.5(b), the non-dimensional hydrodynamic efficiency of the power absorption η_{max} are plotted against non-dimensional wave number Kh_1 for different values of (a) b/h_1 and (b) a/h_1. These results are compared with Figures 5 and 9 of Evans and Porter [5]. It is observed that the present numerical results matched well with that of Evans and Porter [5]. Further, in Figs. 2.6, the results obtained by the present method are compared with the results of Ning et al. [6]. It is to be noted that in Fig. 2.6, the

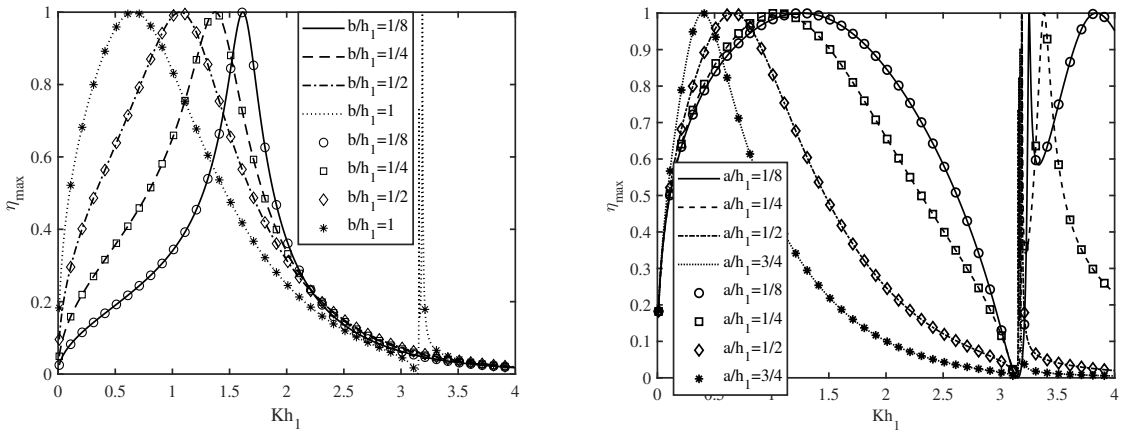

(a) (b)

FIGURE 2.5: Variation of η_{max} vs Kh_1 for different (a) b/h_1 and (b) a/h_1. Lines represent the solutions obtained by the present coupled eigenfunction expansion - boundary element method and symbols represent the solutions provided in Evans and Porter [5].

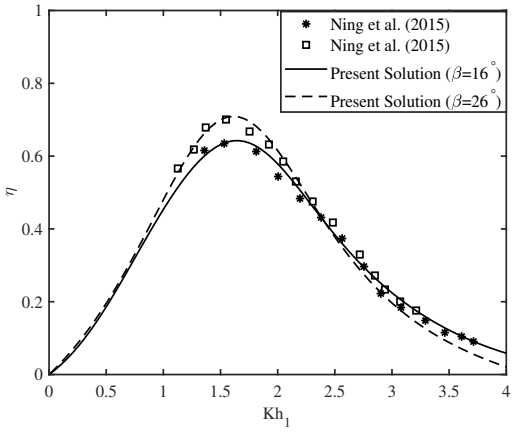

FIGURE 2.6: Variation of η vs Kh_1 for different bottom slopes $\beta = 16°$ and $\beta = 26°$. Lines represent the solutions obtained by the present coupled eigenfunction expansion - boundary element method and symbols represent the solutions provided in Ning et al. [6].

sea bed is sloping in nature with the slope angle β and the $\theta = 0°$. The remaining values of the parameters are the same as provided in Ning et al. [6] in Fig. 14. It is seen that the present numerical results matched well with that of Ning et al. [6]. This shows the accuracy of the present numerical computations.

2.5.3 Resonance mechanism

The most important parameter of designing an OWC device is to increase the hydrodynamic efficiency of the power absorption η_{max}. Now, from Eq. (2.51), it is observed that the value of η_{max} increases with a decrease in μ/ν and the maximum theoretical efficiency is $\eta_{max} = 1$. Now, the radiation susceptance coefficient μ is associated with the wave energy that is not captured

by the OWC device and the radiation conductance coefficient ν is associated with the wave energy that is transformed by the OWC device. So, our aim in the present paper is to obtain an optimized design of the OWC device by increasing the efficiency η_{max} of the OWC device. To achieve the same, the parameter μ/ν should be minimized. Now, to increase the efficiency η_{max}, the resonance mechanism plays an important role. Two different resonance mechanisms can occur in the present problem and the details for the same are given in the following.

- **First resonance mechanism:** Resonance occurs when the water column in the confined region within the OWC device chamber is excited by the incident wave i.e., frequency of the water column motion within the OWC device chamber coincides with the frequency of the incident waves. To achieve the same, the motion of the water column in the OWC device chamber is assumed to be a resonant piston-like motion. The requirement for the same is that b/a should be a small number and the condition is $Ka \approx 1$.
- **Second resonance mechanism:** Resonance can occur when the water in the confined region within the OWC device chamber is excited into an antisymmetric sloshing mode (see Evans and Porter [5] for details). For a closed rectangular tank, the condition for sloshing phenomena is $k_0 b = n\pi$ with n being the sloshing mode number. This resonance mechanism becomes more prominent as the submergence depth of the front wall of the PWC device increases. However, as a consequence, the variation of the air volume in the OWC chamber decreases. This reduces the capture wave power of the devices. A detailed for the same was provided in Ning et al. [116] and Liu et al. [117].

In the following results, the effectiveness of these two resonance mechanisms to increase the hydrodynamic efficiency η_{max} of the OWC device will be analyzed. Firstly, the results will be analyzed for type I bottom profile and thereafter the same will be done for type II bed profile.

2.5.4 Results associated with the type I bed profile:

In Figs. 2.7(a) and 2.7(b), the variation of the non-dimensional radiation susceptance and conductance coefficients μ and ν are plotted respectively for different chamber width b/h_1. It is observed that for smaller values of $b/h_1 = 1/8$, resonance occurs for $Kh_1 \approx 2.26$. This resonance occurs due to the first resonance mechanism as discussed before. Now, the same resonance occurs for smaller wave numbers with an increase in chamber width b/h_1. The reason behind the same is that the water particles have to travel more distance within the wave chamber during a wave period. Further, it is seen that the amplitude of resonance decreases with an increase in b/h_1. This is due to the fact that with an increase in b/h_1, the model of the resonant piston-like motion of the water column within the OWC chamber breaks. Now, the spiky behavior of μ and ν in the neighborhood of $Kh_1 \approx 3.42$ for $b/h_1 = 1.0$ is due to the occurrences of sloshing phenomena

with sloshing mode number $n = 1$. This condition is clearly explained in the second resonance mechanism as discussed before. On the other hand, in Figs. 2.7(c) and 2.7(d), the variation of the non-dimensional volume flux $|\frac{q^S}{q^I}|$ and the hydrodynamic efficiency of power absorption η_{max} are plotted respectively as a function of non-dimensional wave number Kh_1 for different chamber width b/h_1. The overall observations are similar in nature as that of Figs. 2.7(a) and 2.7(b). Further, careful observation reveals that resonance in the efficiency η_{max} occurs for larger values of b/h_1 in the long-wave regime. On the other hand, the resonance in the efficiency η_{max} occurs for smaller values of b/h_1 in the short-wave regime. Therefore, depending on the incident wavelength, the width of the OWC chamber will be determined to get maximum efficiency in wave power absorption. Similar observation were found in Evans and Porter [5] and Rezanejad et al. [7].

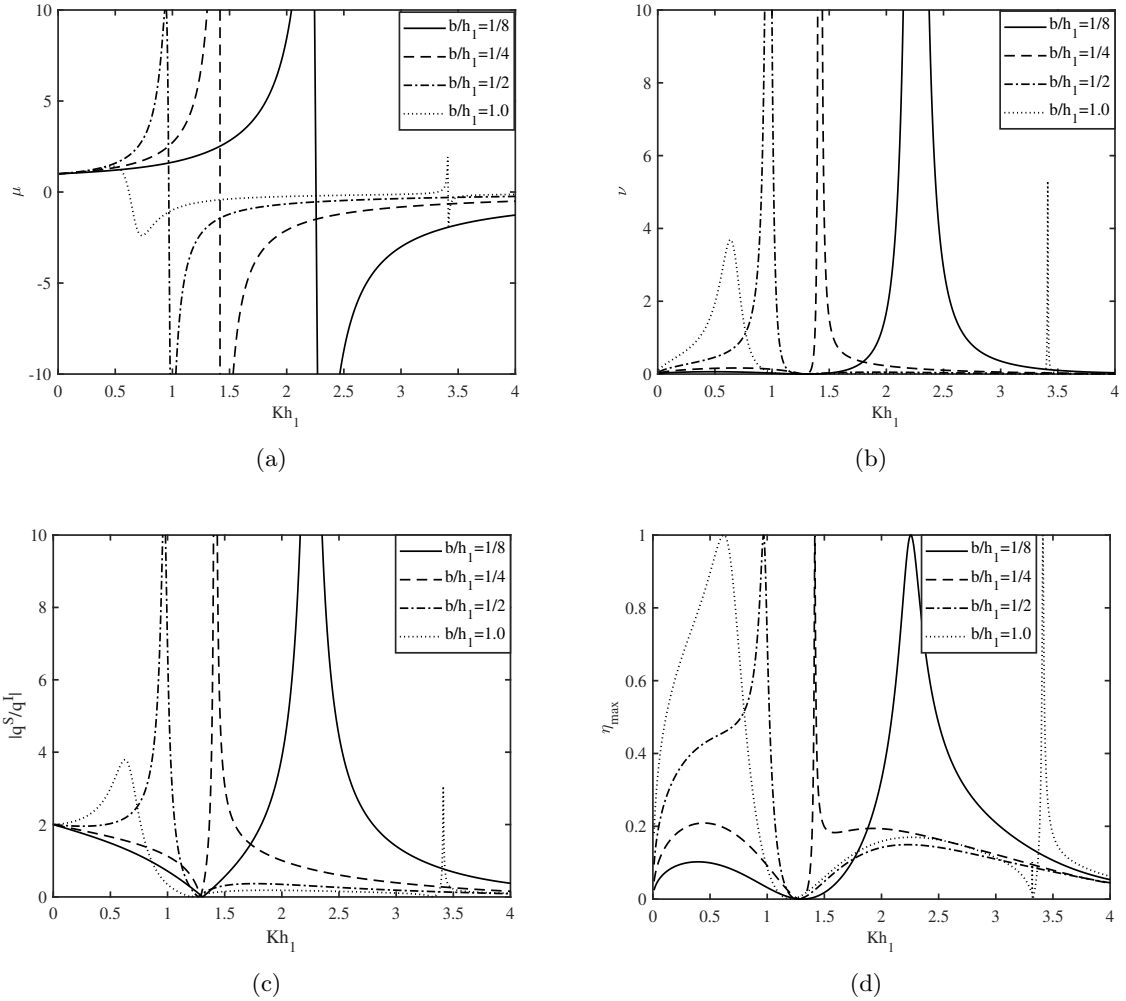

FIGURE 2.7: Variation of (a) μ, (b) ν, (c) $|\frac{q^S}{q^I}|$ and (d) η_{max} vs Kh_1 for different b/h_1 with $\alpha = -3$.

In Figs. 2.8(a) - (d), the variation of the non-dimensional radiation susceptance coefficient μ, radiation conductance coefficient ν, volume flux $|\frac{q^S}{q^I}|$ and the hydrodynamic efficiency of power

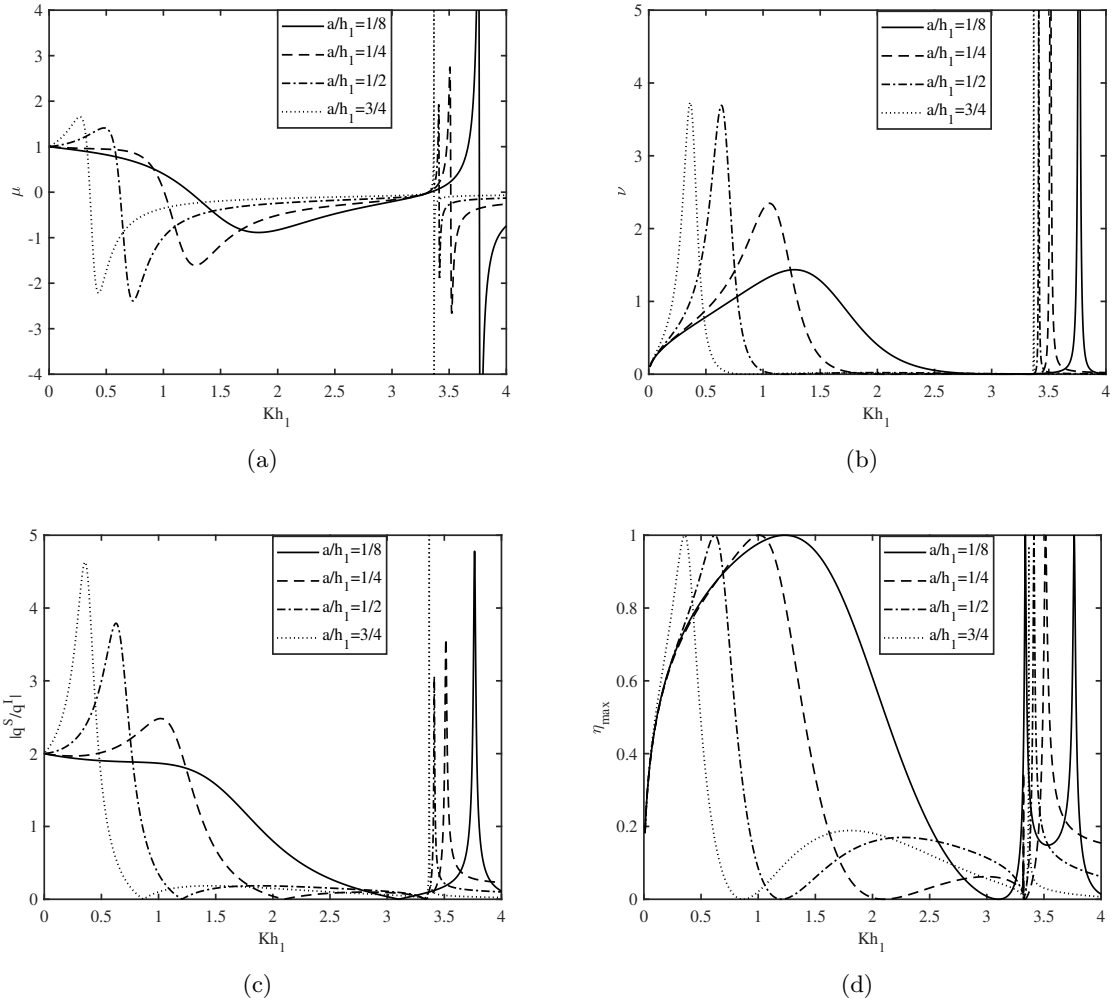

FIGURE 2.8: Variation of (a) μ, (b), ν, (c) $|\frac{q^S}{q^T}|$ and (d) η_{max} vs Kh_1 for different a/h_1 with $\alpha = -3$.

absorption η_{max} are plotted respectively as a function of non-dimensional wave number Kh_1 for different submergence depth of the front wall a/h_1 of the OWC device. In all the figures, the first peak in the curve which occurs for smaller values of Kh_1 is due to the first resonance mechanism as discussed before. Further, it is seen that this resonance occurs for smaller values of Kh_1 with an increase in the submergence depth a/h_1. The second peak which occurs for higher values of Kh_1 is due to the sloshing effects. This particular resonance is more prominent with an increase in front wall submergence depth a/h_1. As the submergence depth a/h_1 increases, the value of the wavenumber for which the second resonance occurs is getting closed to $k_0 b = \pi$. Further, the amplitude of the second resonance is highest for $a/h_1 = 3/4$. A comparison of Fig. 2.8(a) with Fig. 2.8(d) reveals that the efficiency of wave power absorption η_{max} becomes unity whenever the curve of μ crosses the x-axis i.e., becoming zero. This can be clearly explained by Eq. (2.51). Similarly, a comparison of Fig. 2.8(b) with Fig. 2.8(c) shows that the maxima and minima of radiation conductance coefficient ν correspond to the maxima and minima of the

volume flux $|\frac{q^S}{q^I}|$ respectively. The reason is very clear from Eq. (2.40). It is observed from Fig. 2.8(d) that the efficiency of power absorption η_{max} is higher for $a/h_1 = 1/8$ (here $b/h_1 = 1$) for moderate ocean waves having time period between $5 - 15$ seconds. This result indicates that the submergence depth of the front wall of the OWC device plays an important role to increase the hydrodynamic efficiency of the OWC device. It is to be noted that, as $a/h_1 \to 1$, the variation of the air volume in the OWC chamber decreases. This reduces the capture wave power of the device. A detailed for the same was provided in Ning et al. [116] and Liu et al. [117].

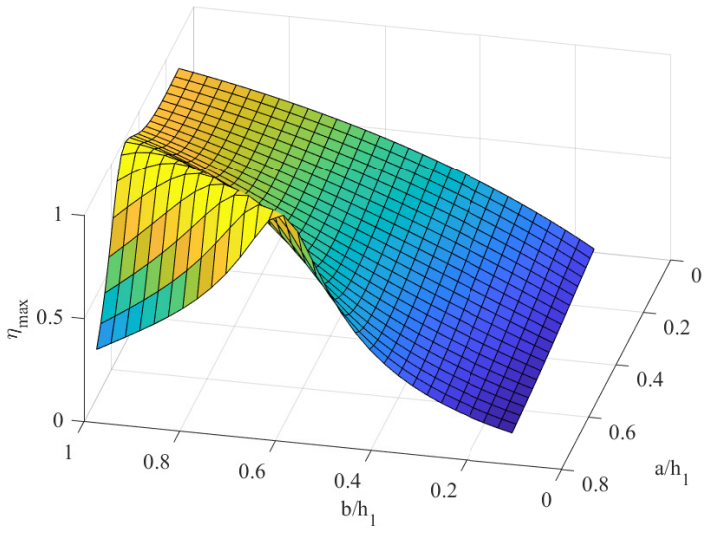

FIGURE 2.9: Surface plot of η_{max} as a function of a/h_1 and (b) b/h_1 with $\alpha = -3$ and $T = 10$sec.

In the discussion of Figs. 2.7 and 2.8, it is observed that the hydrodynamic efficiency of the device η_{max} depends on the chamber width b/h_1 and the submergence depth a/h_1. To get a combined effect of a/h_1 and b/h_1 on the efficiency η_{max}, a surface plot for η_{max} as a function of a/h_1 and b/h_1 is provided in Fig. 2.9. It is observed that a suitable combination of a/h_1 and b/h_1 can provide efficiency η_{max} nearly equal to 1. This combination of a/h_1 and b/h_1 is very important to design an efficient OWC device.

In Figs. 2.10(a) - (c), the variation of the non-dimensional radiation susceptance coefficient μ, radiation conductance coefficient ν, volume flux $|\frac{q^S}{q^I}|$ are plotted respectively as a function of non-dimensional wave number Kh_1 for different angle of inclination θ of the front wall of the OWC device. The general observation of the resonance pattern with the variation in wavenumber Kh_1 remains the same as discussed in Figs. 2.7 and 2.8. In the long-wave regime, the amplitude of the coefficients μ, ν and $|\frac{q^S}{q^I}|$ increases with an increase in the angle of inclination θ of the front wall of the OWC device. Further, in the short-wave regime, the resonance occurs due to the sloshing effects for higher values of wavenumber Kh_1 with an increase in the angle of inclination θ of the front wall of the OWC device. A comparison of Fig. 2.10(b) with Fig. 2.10(c) shows that the pattern of the non-dimensional volume flux $|\frac{q^S}{q^I}|$ are similar in nature to that of non-dimensional radiation conductance coefficient ν. Fig. 2.10(d) shows the variation

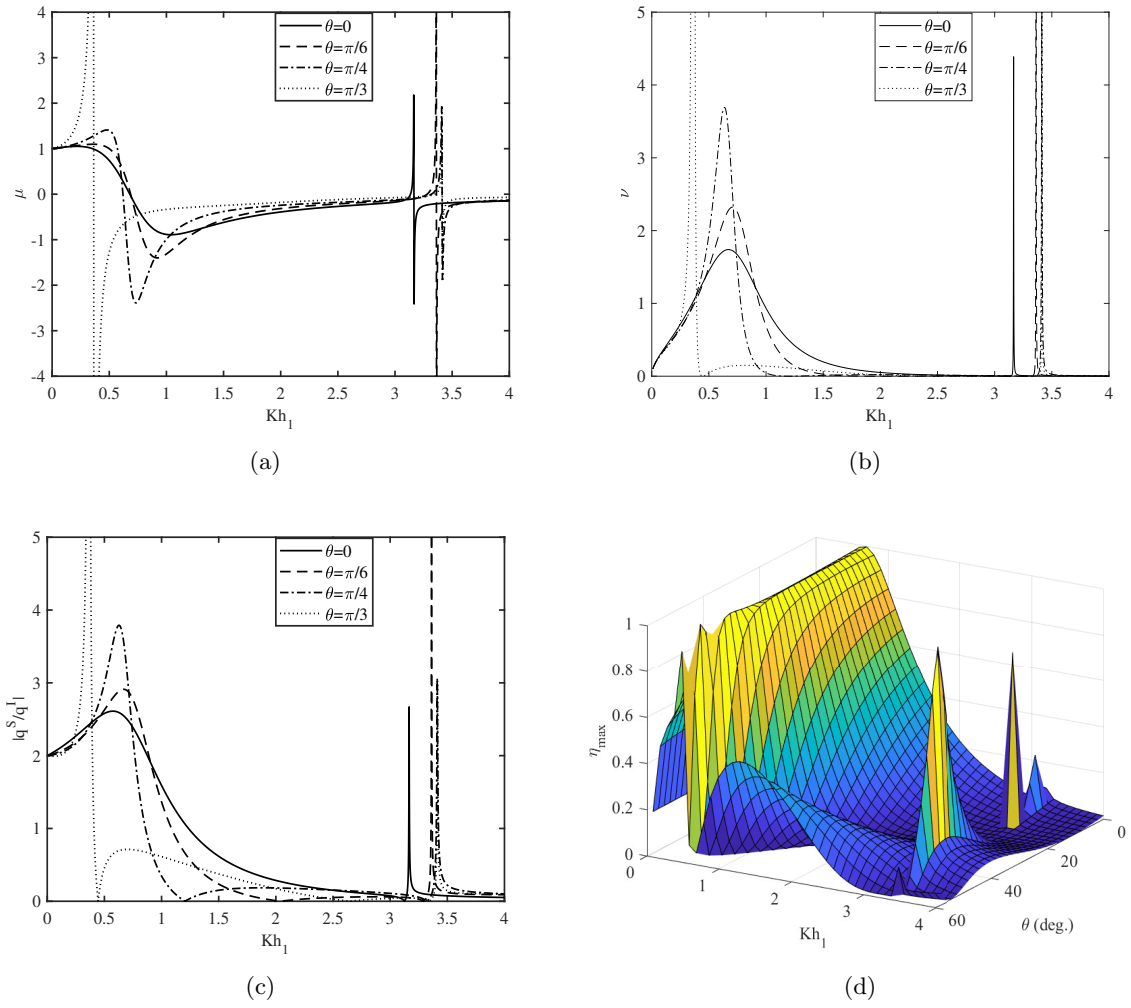

FIGURE 2.10: Variation of (a) μ, (b) ν, (c) $|\frac{q^S}{q^I}|$ vs Kh_1 for different θ, and (d) variation of η_{max} vs Kh_1 and θ with $\alpha = -3$.

of the efficiency of power absorption η_{max} as a function of Kh_1 and θ. This result indicates that depending on the incident wavelength, an optimized design of the OWC device results in maximum efficiency in wave power absorption.

In Figs. 2.11(a) and (b), the variation of the non-dimensional radiation conductance coefficient ν and the hydrodynamic efficiency of power absorption η_{max} are plotted respectively as a function of non-dimensional wave number Kh_1 for different shape parameter α of the bottom profiles. It is to be noted that $\alpha = 3, 0, -1, -3$ represent the bottom profile of protrusion, sloping, concave and depression type respectively. The schematic diagram of the bottom profiles for different values of α is provided in Fig. 2.3. Fig. 2.11(a) reveals that the peak in ν in the long-wave regime increases with a decrease in α. Moreover, with an increase of α, the resonance occurs due to the sloshing effects for smaller values of wavenumber Kh_1. This happens since with a decrease in α, the wave chamber volume increases. The overall geometry of the OWC device (see Fig. 2.3) shows that the relative submergence depth of the front wall of the OWC device is

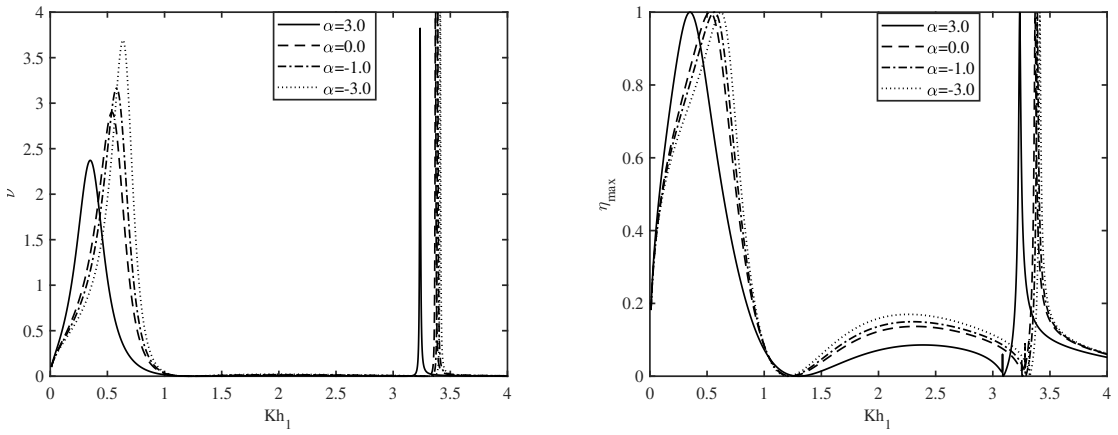

FIGURE 2.11: Variation of (a) ν and (b) η_{max} vs Kh_1 for different α.

less for lower values of α. In this case, the resonance occurs due to the sloshing effects for higher values of Kh_1 (see Evans and Porter [5] for details). On the other hand, Fig. 2.11(b) shows that the resonance pattern of η_{max} is similar in nature as that of ν as a function of Kh_1. Further, it is observed that for the very long-wave regime, the efficiency η_{max} is more for $\alpha = 3.0$ whereas for intermediate values of the wavenumbers Kh_1, the efficiency η_{max} is increasing in nature with a decrease in α. These observations indicate that depending on the incident wave characteristics, suitable bottom profiles can be chosen to get optimum efficiency in wave power absorption.

2.5.5 Results associated with the type II bed profile:

For type II bottom profile, the variation of (a) μ, (b) ν, (c) $|\frac{q^S}{q^I}|$ and η_{max} vs Kh_1 for different values of b/h_1, a/h_1 and θ are similar in nature with that of Figs. 2.7 - 2.10 ((a)-(d)). Due to this reason, the aforementioned figures are not given here for type II bed profiles.

In Figs. 2.12(a) - (d), the variation of the non-dimensional radiation susceptance coefficient μ, radiation conductance coefficient ν, volume flux $|\frac{q^S}{q^I}|$ and the hydrodynamic efficiency of power absorption η_{max} are plotted respectively as a function of non-dimensional wave number Kh_1 for different values of ripple amplitude a_1 of the sinusoidally varying bottom profile. The resonance occurs due to first and second resonance mechanisms which are similar as discussed for type I bed profile. From Figs. 2.12(a) and 2.12(b), it is observed that in the long-wave regime, the peak in the resonance occurs for lower values of wavenumber Kh_1 as the ripple amplitude of bottom a_1 increases. Further, the amplitude of resonance is lower for higher values of ripple amplitude a_1. This happens as the bottom effect on the wave propagation takes place with an increase in the ripple amplitude of the bottom. The same is also seen in Fig. 2.12(c). On the other hand, Fig. 2.12(d) reveals that the efficiency η_{max} alters due to the change in ripple amplitude a_1. In the long-wave regime, the efficiency η_{max} is higher for higher values of a_1 whereas a reverse pattern

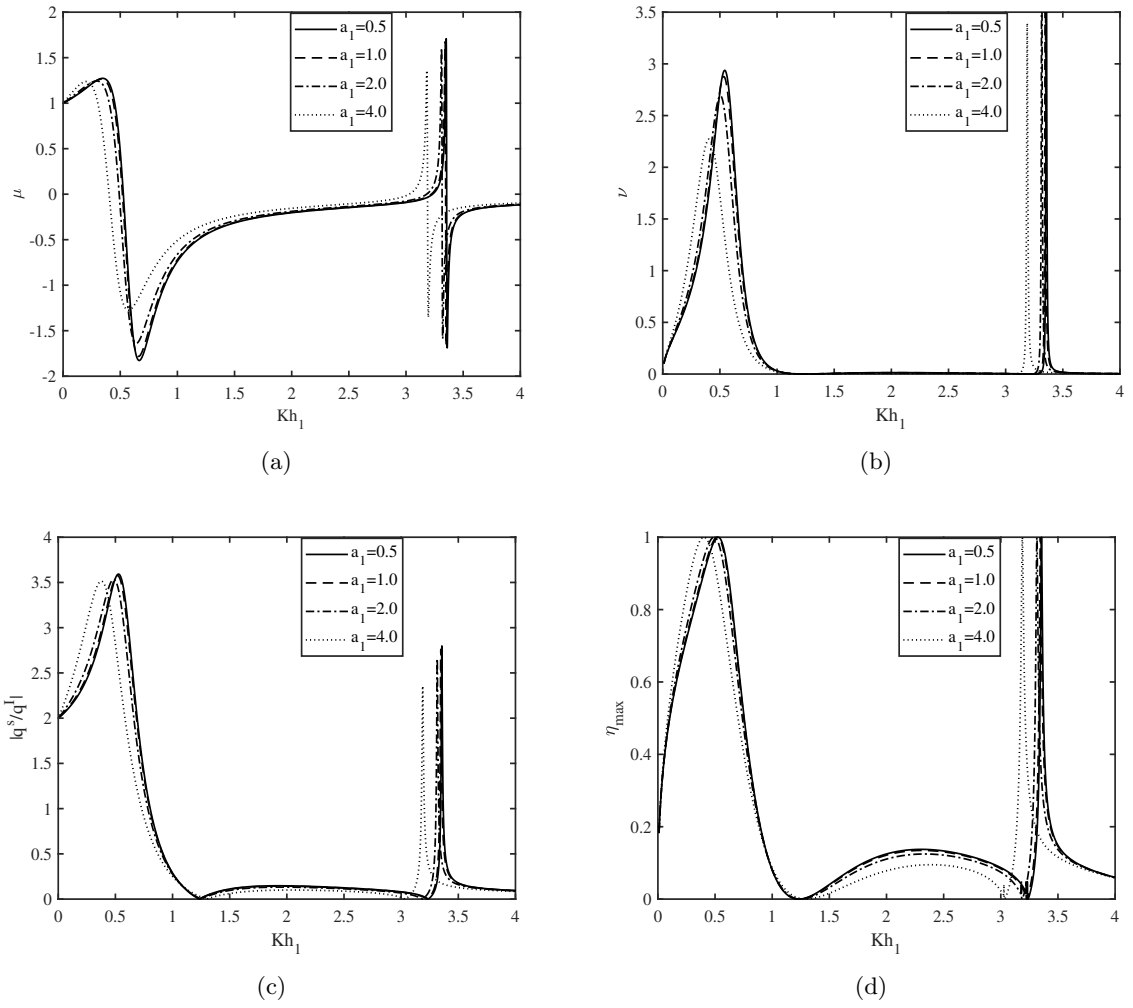

FIGURE 2.12: Variation of (a) μ, (b) ν, (c) $|\frac{q^S}{q^I}|$ and (d) η_{max} vs Kh_1 for different ripple amplitude a_1 with $m = 3.0$.

is observed for intermediate values of the wavenumber. These results indicate that depending on the incident wavelength, bottom profiles can be chosen suitably to increase the efficiency η_{max} of the OWC device.

In Figs. 2.13(a) - (d), the variation of the non-dimensional radiation susceptance coefficient μ, radiation conductance coefficient ν, volume flux $|\frac{q^S}{q^I}|$ and the hydrodynamic efficiency of power absorption η_{max} are plotted respectively as a function of non-dimensional wave number Kh_1 for different number of ripples m of the sinusoidally varying bottom profile. The schematic diagram of the bottom profiles for different values of m is provided in Fig. 2.4. The overall resonance pattern is similar as discussed before. Figs. 2.13(a)-(c) reveals that the amplitude of resonance due to the sloshing effect is higher for sinusoidally varying bottom having fewer ripples. Further, it is seen from Fig. 2.13(d) that the variation in η_{max} is not significant in the long-wave regime due to the variation in the number of ripples m of the bottom. In the short-wave regime, η_{max}

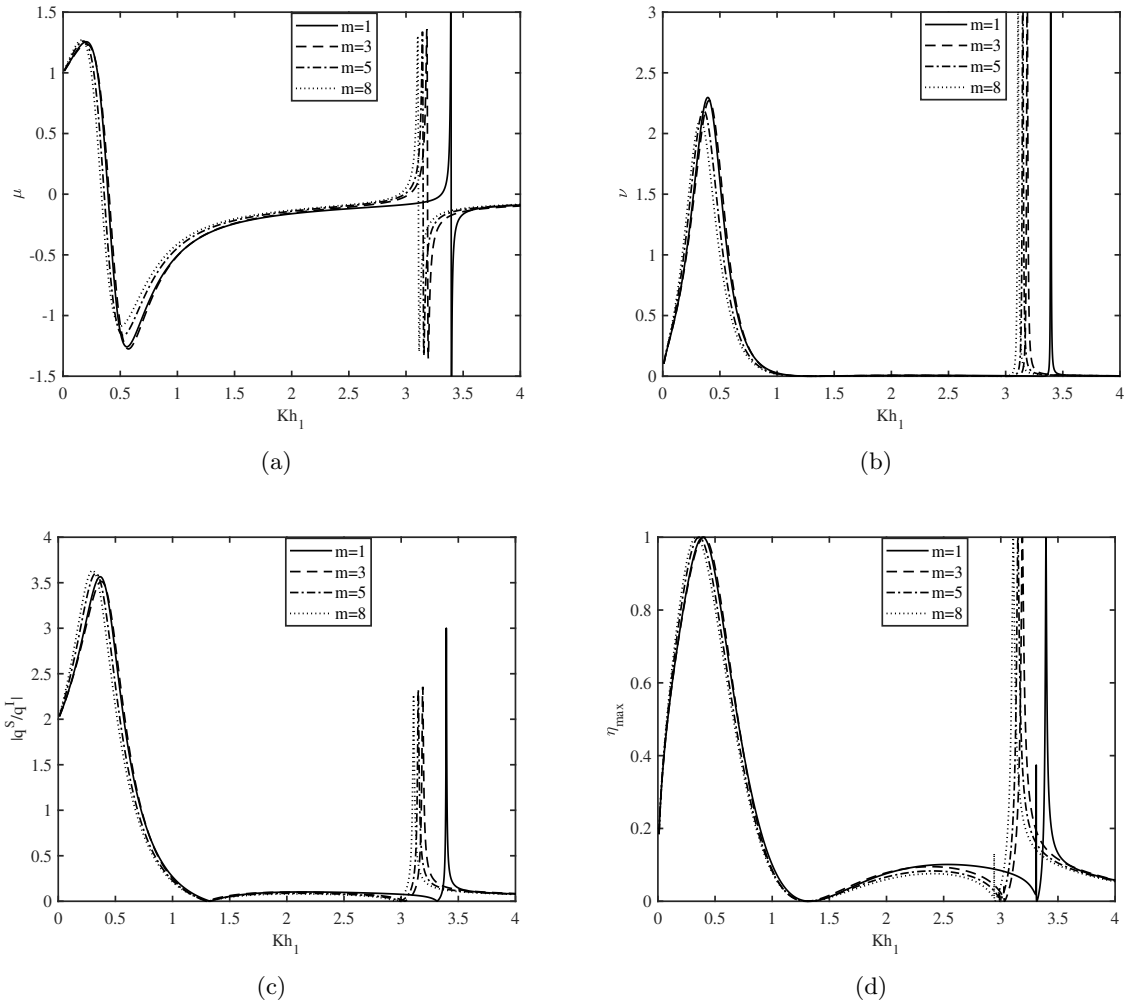

FIGURE 2.13: Variation of (a) μ, (b) ν, (c) $|\frac{q^S}{q^I}|$ and (d) η_{max} vs Kh_1 for different number of ripples m with $a_1 = 4.0$.

becomes unity for lower values of wavenumber Kh_1 with an increase in the number of ripples m of the sinusoidally varying bottom.

2.6 Conclusions

- The hydrodynamic performance and efficiency of an OWC device placed on an undulated seabed in analyzed. The associated boundary value problem is handled for a solution using coupled eigenfunction expansion - boundary element method. The numerical convergence of the solution methodology is analyzed appropriately. Various important physical parameters such as radiation conductance and susceptance coefficients, volume flux and the hydrodynamic efficiency of the OWC device are analyzed for a wide range of wave and structural parameters.

- It is observed that resonance occurs for certain values of wave parameters and the same will increase the hydrodynamic efficiency of the device to unity. Now, this resonance occurs for certain suitable combinations of chamber width and the submergence depth of the front wall of the OWC device. This result concludes that with the proper structural design of the OWC device, 100% efficiency can be obtained.

- The angle of inclination of the front wall of the device has significant effects on the hydrodynamic efficiency in wave power absorption. A moderate angle of inclination $\theta \approx 45^\circ$ of the front wall can significantly increase the efficiency of the device in the short-wave regime whereas in the long-wave regime, angle of inclination $\theta < 15^\circ$ is appropriate.

- The hydrodynamic efficiency of the OWC device significantly depends on the bottom profiles. It is seen that the hydrodynamic efficiency of the OWC device is enhanced for the protrusion type bed profile in the long-wave regime. However, the depression type of bed profile is appropriate for incident waves having a moderate wavelength.

- For the sinusoidally varying bottom topography, it is observed that in the long-wave regime, the hydrodynamic efficiency of the device becomes unity for lower values of the wavenumber as the ripple amplitude of the bottom increases. However, a reverse pattern is observed for intermediate values of the wavenumber. A similar result is observed in the short-wave regime with an increase in the number of ripples of the bottom.

These observations conclude that with the appropriate structural design of the OWC device and suitable bottom profile can significantly increase the hydrodynamic efficiency of the OWC device. The present solution methodology is robust and can easily handle more complex structures.

Chapter 3

Mathematical modeling of breakwater-integrated oscillating water column wave energy converter devices under irregular incident waves

* The work, in this chapter, is covered by the following publications:

1. K. Trivedi, and S. Koley, "Mathematical modeling of breakwater-integrated oscillating water column wave energy converter devices under irregular incident waves," *Renewable Energy*, vol. 178, pp. 403–419, 2021.

2. K. Trivedi, and S. Koley, "Annual mean efficiency of the duct type OWC in regional ocean environments," *Energy Reports*, vol. 8, pp. 346-351, 2022.

3.1 General introduction

This chapter investigates the performance of breakwater-integrated OWC (oscillating water column) wave energy converter devices is analyzed under the action of unidirectional regular and irregular incident waves. Two different types of OWC devices: (i) LIMPET device (sloping-face OWC device) and (ii) quarter-circle-shaped front wall OWC device are considered for the present study. Detailed derivations of the parameters associated with the performance of the OWC devices under the action of irregular waves are provided. To analyze the efficiency of the OWC devices in real sea conditions, the Bretschneider Spectrum is taken as the incident wave spectrum along with nine sea states represent the local wave climate at the OWC plant site Pico, Portugal. The annual-averaged plant efficiencies of the two aforementioned OWC devices are analyzed as a function of chamber length, submergence depth, turbine rotor diameter, and rotational speed of the Wells turbine. It is observed that the annual-averaged plant efficiency can be enhanced significantly with appropriate combinations of chamber length, submergence depth, and turbine characteristics.

3.2 Mathematical Formulation

In this section, the governing equation and boundary conditions for the problem of regular water wave interaction with OWC devices are provided. Two different types of breakwater-integrated OWC devices: (i) LIMPET device (sloping-face OWC device) and (ii) quarter-circle-shaped front wall OWC device are considered. The schematic diagrams for the two types of OWC devices and coordinate systems are given in Fig. 3.1. In the rest of this paper, the LIMPET and quarter-circle-shaped front wall OWC devices are termed as type I and type II OWC devices, respectively. The type I breakwater-integrated OWC device consists of rigid sloping front and rear walls. On the other hand, the type II breakwater-integrated OWC device consists of a quarter circular shape front wall and a sloping rear wall. The front wall of the caisson breakwater intersects the mean free surface $z = 0$ at $x = L$. Further, the front wall of the OWC devices are having uniform thickness d, and the submergence depth of the tip of the front wall is a. The Wells turbine is placed at the rear side of the OWC devices. It is a self-rectifying axial-flow turbine. Some of the major advantages of using the Wells turbine are the following: (i) the Wells turbine has linear pressure drop-flow rate characteristics, which is feasible for producing the electricity from ocean waves (Raghunathan [118]), (ii) high rotational speed can be attained due to low velocity of airflow through the turbine and therefore increases the efficiency of the OWC device, and (iii) cost of construction is relatively cheap compared to other turbines (see Antonio [2] for details). In the presence of the OWC device, the free surface is divided into two parts, namely internal free surface Γ_3 (i.e., free surface within the OWC chamber) and external free surface Γ_5 (i.e., free surface outside of the OWC chamber). The caisson breakwater is placed

on a bottom foundation (see Fig. 3.1) having height b_h. The bottom boundary, the bottom foundation of the breakwater to the sea-side, and the inclined front wall of the breakwater up to the free surface are represented by Γ_2. The immersed boundary of the front wall of the OWC device is represented by Γ_4. To close the domain, an auxiliary boundary Γ_1 is taken at $x = -l$. For the sake of mathematical modeling, the motion of the water is governed by the potential flow theory (see Koley and Sahoo [110] for details). Further, the water motion is assumed to be simple harmonic in time with circular frequency ω. Hence, the total velocity potential is represented as $\Phi(x, z, t) = \Re\{\phi(x, z)e^{-\mathrm{i}\omega t}\}$ and the spatial component of the velocity potential satisfies the Laplace equation

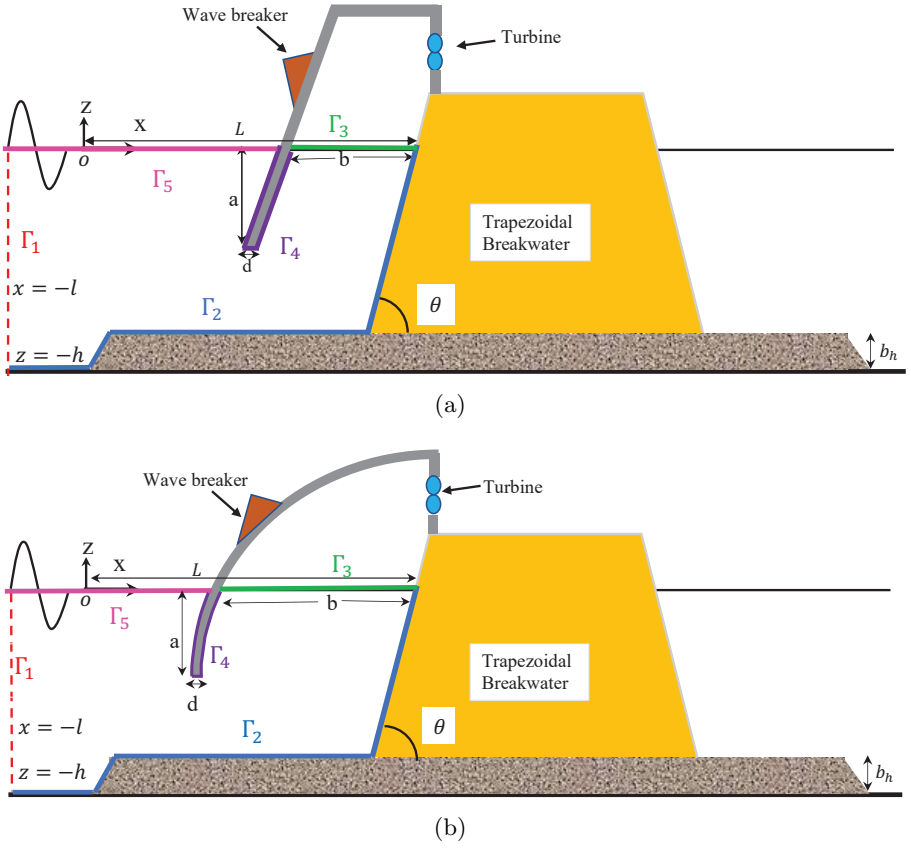

FIGURE 3.1: Vertical cross sections of (a) type *I* OWC device, and (b) type *II* OWC device.

$$\left(\frac{\partial^2}{\partial x^2} + \frac{\partial^2}{\partial z^2}\right)\phi(x, z) = 0. \tag{3.1}$$

The boundary conditions at the mean free surface $\Gamma_3 \cup \Gamma_5$ are given by (see Evans and Porter [5] and Koley and Trivedi [26] for details)

$$\frac{\partial \phi}{\partial n} - K\phi = \begin{cases} \dfrac{\mathrm{i}\omega p}{\rho g}, & \text{on } \Gamma_3, \\ 0, & \text{on } \Gamma_5, \end{cases} \tag{3.2}$$

where $K = \omega^2/g$, with g being the gravitational acceleration. Here, $\partial/\partial n$ represents the normal derivative. Now, the boundary condition on the impervious boundaries $\Gamma_2 \cup \Gamma_4$ is given by

$$\frac{\partial \phi}{\partial n} = 0, \quad \text{on } \Gamma_2 \cup \Gamma_4, \tag{3.3}$$

It is to be noted that the velocity potential consists of scattered and radiated velocity potentials and therefore, the total velocity potential is expressed as

$$\phi = \phi^S + \left(\frac{\mathrm{i}\omega p}{\rho g}\right)\phi^R, \tag{3.4}$$

where ϕ^S and ϕ^R represent the scattered and radiated velocity potential respectively. This scattered velocity potential is the sum of diffracted and incident velocity potentials i.e., $\phi^S = \phi^D + \phi^I$, where ϕ^D and ϕ^I represent the diffracted and incident velocity components (see Smith [111] and Evans and Porter [5] for details). Here, $\phi^{S,R}$ satisfy Eqs. (3.1)-(3.4) with the following changes in Eq. (3.2) as given by

$$\frac{\partial \phi^S}{\partial n} - K\phi^S = 0, \quad \text{on } \Gamma_3 \cup \Gamma_5, \qquad \frac{\partial \phi^R}{\partial n} - K\phi^R = \begin{cases} 1, & \text{on } \Gamma_3, \\ 0, & \text{on } \Gamma_5. \end{cases} \tag{3.5}$$

The far-field boundary conditions are given by

$$\begin{cases} \phi^S(x,z) = e^{\mathrm{i}k_0 x}\psi_0(k_0,z) + A_0^S e^{-\mathrm{i}k_0 x}\psi_0(k_0,z), & \text{as } x \to -\infty, \\ \phi^R(x,z) = A_0^R e^{-\mathrm{i}k_0 x}\psi_0(k_0,z), & \text{as } x \to -\infty, \end{cases} \tag{3.6}$$

where A_0^S and A_0^R are the coefficients related to the amplitude of the reflected and radiated waves at $x = -\infty$ respectively. To solve the aforementioned BVP (boundary value problem), the boundary element method is used in which the Green's function is taken as the free-space Green's function (see Koley [119] for details). In this solution methodology, the domain should be closed and therefore, the auxiliary boundary Γ_1 is considered. This auxiliary boundary Γ_1 is located sufficiently far away from the breakwater-integrated OWC device, and therefore, the far-field boundary conditions (3.6) hold on Γ_1. In the boundary element method, the following modified form of the far-field boundary conditions (3.6) is used

$$\begin{cases} \dfrac{\partial(\phi^S - \phi^{inc})}{\partial n} - \mathrm{i}k_0(\phi^S - \phi^{inc}) = 0, & \text{on } \Gamma_1, \\ \dfrac{\partial \phi^R}{\partial n} - \mathrm{i}k_0\phi^R = 0, & \text{on } \Gamma_1, \end{cases} \tag{3.7}$$

where $\phi^{inc}(x,z) = e^{ik_0 x}\psi_0(k_0,z)$ is the incident velocity potential with the expression of $\psi_0(k_0,z)$ is given by $\psi_0(k_0,z) = \left(\dfrac{-\mathrm{i}gA}{\omega}\right)\dfrac{\cosh k_0(h+z)}{\cosh(k_0 h)}$. Here, k_0 is the real positive root of the dispersion relation $\omega^2 = gk\tanh(kh)$ and A is termed as amplitude of the incident wave.

3.3 Solution methodology based on BEM

In this section, we will discuss the solution procedure of the BVP described in the previous section using the boundary element method. In this methodology, firstly, we convert the BVP corresponding to the radiation potential ϕ^R and the scattered potential ϕ^S into the Fredholm integral equations. Subsequently, these Fredholm integral equations are converted into a system of linear algebraic equations using the boundary element method. Applying Green's second identity on $\phi^{S,R}$ and the free-space Green's function $G(x,z;x_0,z_0)$ over the domain bounded by $\Gamma = \Gamma_1 \cup \Gamma_2 \cup \Gamma_3 \cup \Gamma_4 \cup \Gamma_5$, the following integral equation is obtained (see Katsikadelis [112] for detailed derivation)

$$\frac{\alpha}{2\pi}\phi^{S,R}(x_0,z_0) = \int_\Gamma \left[\phi^{S,R}(x,z)\frac{\partial G}{\partial n}(x,z;x_0,z_0) - G(x,z;x_0,z_0)\frac{\partial \phi^{S,R}}{\partial n}(x,z)\right] d\Gamma(x,z). \tag{3.8}$$

Here, (x,z) and (x_0,z_0) are the field and source points respectively. It is to be noted that $\alpha = \pi$ for smooth boundaries. In Eq. (3.8), the source point (x_0,z_0) lies on the boundary Γ of the domain (Katsikadelis [112]). The free-space Green's function $G(x,z;\tilde{x},\tilde{z})$ satisfies the equation

$$\left(\frac{\partial^2}{\partial x^2} + \frac{\partial^2}{\partial z^2}\right) G(x,z;x_0,z_0) = \delta(x-x_0)\delta(z-z_0), \tag{3.9}$$

and takes the form

$$G(x,z;x_0,z_0) = \frac{1}{2\pi}\ln(\tilde{r}), \quad \text{where } \tilde{r} = \sqrt{(x-x_0)^2 + (z-z_0)^2}. \tag{3.10}$$

The properties of the aforementioned Green's function $G(x,z;x_0,z_0)$ can be found in Katsikadelis [112] and Koley [119]. The details are deferred here. Applying the boundary conditions Eqs. (3.3), (3.5) and (3.7) in Eq. (3.8), the following integral equation for the radiated velocity potential ϕ^R is obtained as

$$\begin{aligned} -\frac{1}{2}\phi^R + \int_{\Gamma_1}\phi^R\left(\frac{\partial G}{\partial n} - \mathrm{i}k_0 G\right)d\Gamma + \int_{\Gamma_2}\phi^R\frac{\partial G}{\partial n}d\Gamma + \int_{\Gamma_3}\phi^R\left(\frac{\partial G}{\partial n} - KG\right)d\Gamma \\ + \int_{\Gamma_4}\phi^R\frac{\partial G}{\partial n}d\Gamma + \int_{\Gamma_5}\phi^R\left(\frac{\partial G}{\partial n} - KG\right)d\Gamma = \int_{\Gamma_3} G d\Gamma. \end{aligned} \tag{3.11}$$

In a similar manner, using the boundary conditions Eqs. (3.3), (3.5) and (3.7) in Eq.(3.8), the following integral equation is obtained for the scattered velocity potential ϕ^S as

$$-\frac{1}{2}\phi^S + \int_{\Gamma_1} \phi^S \left(\frac{\partial G}{\partial n} - \mathrm{i}k_0 G\right) d\Gamma + \int_{\Gamma_2} \phi^S \frac{\partial G}{\partial n} d\Gamma + \int_{\Gamma_3} \phi^S \left(\frac{\partial G}{\partial n} - KG\right) d\Gamma$$
$$+ \int_{\Gamma_4} \phi^S \frac{\partial G}{\partial n} d\Gamma + \int_{\Gamma_5} \phi^S \left(\frac{\partial G}{\partial n} - KG\right) d\Gamma = \int_{\Gamma_1} G \left(\frac{\partial \phi^{inc}}{\partial n} - \mathrm{i}k_0 \phi^{inc}\right) d\Gamma. \tag{3.12}$$

Now, Eqs. (3.11) and (3.12) are transformed into system of equations using the boundary element method. In this solution procedure, constant element approach is used (see Katsikadelis [112] for details). The details are deferred here to avoid mere repetition. It is to be noted that recently, Medina Rodríguez et al. [120] used quadratic boundary element method to convert the Fredholm integral equations into a system of linear algebraic equations. Although the higher order boundary element method can provide better accuracy, but the methodology is much complex as compared to the constant boundary element method. Finally, Eqs. (3.11) and (3.12) can be written in the following discrete form

$$\sum_{j=1}^{N_1} \left(H^{ij} - \mathrm{i}k_0 G^{ij}\right) \phi_j^R\big|_{\Gamma_1} + \sum_{j=1}^{N_2} H^{ij} \phi_j^R\big|_{\Gamma_2} + \sum_{j=1}^{N_3} \left(H^{ij} - KG^{ij}\right) \phi_j^R\big|_{\Gamma_3} + \sum_{j=1}^{N_4} H^{ij} \phi_j^R\big|_{\Gamma_4}$$
$$+ \sum_{j=1}^{N_5} \left(H^{ij} - KG^{ij}\right) \phi_j^R\big|_{\Gamma_5} = \sum_{j=1}^{N_3} G^{ij}\big|_{\Gamma_3}, \tag{3.13}$$

$$\sum_{j=1}^{N_1} \left(H^{ij} - \mathrm{i}k_0 G^{ij}\right) \phi_j^S\big|_{\Gamma_1} + \sum_{j=1}^{N_2} H^{ij} \phi_j^S\big|_{\Gamma_2} + \sum_{j=1}^{N_3} \left(H^{ij} - KG^{ij}\right) \phi_j^S\big|_{\Gamma_3} + \sum_{j=1}^{N_4} H^{ij} \phi_j^S\big|_{\Gamma_4}$$
$$+ \sum_{j=1}^{N_5} \left(H^{ij} - KG^{ij}\right) \phi_j^S\big|_{\Gamma_5} = \sum_{j=1}^{N_1} \left(\frac{\partial \phi_j^{inc}}{\partial n} - \mathrm{i}k_0 \phi_j^{inc}\right) G^{ij}\Big|_{\Gamma_1}, \tag{3.14}$$

where the expressions for H^{ij} and G^{ij} are given by

$$H^{ij} = -\frac{1}{2}\delta_{ij} + \int_{\Gamma_j} \frac{\partial G}{\partial n} d\Gamma, \quad G^{ij} = \int_{\Gamma_j} G d\Gamma. \tag{3.15}$$

For the case $i \neq j$, singularity doesn't occur, and the values of H^{ij} and G^{ij} are calculated using the Gauss-Legendre quadrature formulae. For the case $i = j$, $H^{ii} = 0$ and the values of G^{ii} are evaluated analytically. The details for the same are mentioned in Katsikadelis [112]. Finally, the method of point collocation is used in which the source point (ξ, η) runs over each boundary element. Using this approach, Eqs. (3.13) and (3.14) give the following matrix equations

$$([H] - \mathrm{i}k_0 [G]) \left[\phi^R\right]\big|_{\Gamma_1} + [H] \left[\phi^R\right]\big|_{\Gamma_2} + ([H] - K [G]) \left[\phi^R\right]\big|_{\Gamma_3} + [H] \left[\phi^R\right]\big|_{\Gamma_4} + ([H] - K [G]) \left[\phi^R\right]\big|_{\Gamma_5} = [G]|_{\Gamma_3}, \tag{3.16}$$

$$([H] - \mathrm{i}k_0 [G]) \left[\phi^S\right]\big|_{\Gamma_1} + [H] \left[\phi^S\right]\big|_{\Gamma_2} + ([H] - K [G]) \left[\phi^S\right]\big|_{\Gamma_3} + [H] \left[\phi^S\right]\big|_{\Gamma_4} + ([H] - K [G]) \left[\phi^S\right]\big|_{\Gamma_5} = \left(\frac{\partial \phi_j^{inc}}{\partial n} - \mathrm{i}k_0 \phi_j^{inc}\right) [G]\Big|_{\Gamma_1}. \tag{3.17}$$

These system of equations (3.16) and (3.17) are handled for solution to obtain the values of ϕ and $\partial\phi/\partial n$ at each boundary elements. Various physical quantities of interests can be evaluated using these values of ϕ and $\partial\phi/\partial n$.

3.4 Parameters associated with the performance of OWC devices in regular waves

In this section, the expressions for various physical parameters associated with the performance of the OWC device for the case of regular waves discussed in Section 2 are provided. It is to be noted that the expressions for a number of parameters associated with the performance of the OWC devices under regular incident waves are available in the literature (see Evans and Porter [5] and Medina Rodríguez et al. [120] for detailed derivations). However, for the sake of completeness, the expressions for various parameters are provided in the following in a consolidated manner. The mean energy flow rate per unit length across a vertical cross-section normal to the incident wave direction is given by (see Dean and Dalrymple [18] for details)

$$P_w = EC_g = \frac{\rho L_w g^2 k_0 \mathcal{A}_0 A^2}{2\omega}, \qquad \mathcal{A}_0 = \frac{2k_0h + \sinh(2k_0h)}{4k_0 \cosh^2(k_0h)}. \tag{3.18}$$

Here, L_w is the width of the OWC device chamber taken perpendicular to the incident wave direction. Now, the volume flow rate $Q(t) = \Re\{qe^{-\mathrm{i}\omega t}\}$ through the internal free surface Γ_3 is provided by (see Evans and Porter [5], Rezanejad et al. [66] and Koley and Trivedi [26] for details)

$$q = L_w \int_{\Gamma_3} \frac{\partial \phi}{\partial z} dx = q^S + \frac{\mathrm{i}\omega p}{\rho g} q^R, \tag{3.19}$$

where q^S and q^R are termed as the volume fluxes across Γ_3 correspond to the scattering and radiation problems respectively. Further, the volume flux due to the radiation potential can be

written as the following (see Evans and Porter [5] for details)

$$\frac{\mathrm{i}\omega p}{\rho g} q^R = -\left(\tilde{B} - \mathrm{i}\tilde{A}\right) p, \tag{3.20}$$

where $\tilde{A}$ and $\tilde{B}$ are termed as radiation susceptance and radiation conductance parameters respectively. Now, Eq. (3.20) gives the expressions for $\tilde{A}$ and $\tilde{B}$ as the following

$$\tilde{A} = \frac{\omega}{\rho g} \Re\{q^R\}, \quad \tilde{B} = \frac{\omega}{\rho g} \Im\{q^R\}. \tag{3.21}$$

The relationship between P_w and $\tilde{B}$ is expressed as the following (see Koley and Trivedi [26] for detailed derivations)

$$\tilde{B} = \frac{|q^S|^2}{8P_w}, \qquad \text{where} \quad q^S = 2\mathrm{i}k_0 g A^2 A_0^R \mathcal{A}_0. \tag{3.22}$$

The average power absorbed W per unit width of the pressure distribution is given by (see Smith [111] and Evans [23] for details)

$$W = \frac{1}{2} \Re\left\{\overline{p} q\right\}. \tag{3.23}$$

If air compressibility within the OWC chamber is taken into account and the volume flux is assumed to be linearly proportional to the pressure across the turbine, we get the following relation (see [121] for details)

$$q = \left(\wedge - \frac{\mathrm{i}\omega V_0}{\gamma p_a}\right) p. \tag{3.24}$$

Here, $\wedge$ is a real positive constant termed as control parameter and V_0 is the air volume above the internal free surface Γ_3 (within the OWC chamber). Further, p_a and γ are termed as atmospheric air pressure and specific heat ratio of the air respectively. Using Eqs. (3.19) and (3.20) into Eq. (3.24), the relationship between q^S and p can be expressed as the following

$$p = \left(\wedge + \tilde{B} - \mathrm{i}\left(\tilde{A} + \frac{\omega V_0}{\gamma p_a}\right)\right)^{-1} q^S. \tag{3.25}$$

Now, using the relation as in Eq. (3.24) into Eq. (3.23), the expression for the absorbed power W can be rewritten as

$$W = \frac{1}{2} \wedge |p|^2. \tag{3.26}$$

Further, using the expression of p as in Eq. (3.25) into Eq. (3.26), we get

$$W = \frac{1}{2} \left\{ \frac{\wedge |q^S|^2}{(\wedge + \tilde{B})^2 + \left(\tilde{A} + \frac{\omega V_0}{\gamma p_a}\right)^2} \right\}. \tag{3.27}$$

Therefore, the efficiency of power absorption by the OWC device is given by

$$\eta = \frac{W}{P_w}. \tag{3.28}$$

Substituting the relations as in Eqs. (3.22) and (3.27) into Eq. (3.28), we get

$$\eta = \left\{ \frac{4 \wedge \tilde{B}}{(\wedge + \tilde{B})^2 + \left(\tilde{A} + \dfrac{\omega V_0}{\gamma p_a}\right)^2} \right\}. \tag{3.29}$$

It is to be noted that, the maximum efficiency of the OWC device can be achieved by the optimum value of $\wedge$ (say $\wedge_{opt}$) and the value of $\wedge_{opt}$ is evaluated by taking the first derivative of Eq. (3.29) with respect to $\wedge$ and equating the same to zero. In this approach, the expression for $\wedge_{opt}$ is obtained as

$$\wedge_{opt} = \sqrt{\tilde{B}^2 + \left(\tilde{A} + \frac{\omega V_0}{\gamma p_a}\right)^2}, \tag{3.30}$$

and the expression for η_{max} can be written in the following form

$$\eta_{max} = \left(\frac{2\tilde{B}}{\wedge_{opt} + \tilde{B}} \right). \tag{3.31}$$

3.5 Parameters associated with the performance of OWC devices in irregular waves

In the real sea, the ocean wave environment is random in nature, and the irregular ocean wave is represented by a set of sea states and related wave spectrum (see Goda [62] for details). The local wave climate can be modeled using a stationary ergodic process, and for each sea state, the free surface elevation can be represented by Gaussian random variable (see De O Falcão and Rodrigues [63]). Since the mathematical model is based on the linear water wave theory and the free surface elevation is assumed to be a Gaussian random process, the scattered volume flow rate $Q^S(t) = \Re\{q^S e^{-\mathrm{i}\omega t}\}$ and instantaneous pressure across the turbine $P(t) = \Re\{p e^{-\mathrm{i}\omega t}\}$ are also Gaussian processes. Therefore, the probability density function of instantaneous pressure is given by

$$f(P) = \frac{1}{\sqrt{2\pi}\sigma_P} \exp\left(\frac{-P^2}{2\sigma_P^2}\right), \tag{3.32}$$

where the expression for σ_P is the following

$$\sigma_P^2 = \int_0^\infty S_I(\omega) \left| \frac{p(\omega)}{A_i(\omega)} \right|^2 d\omega, \qquad A_i(\omega) = \sqrt{2 S_I(\omega_i^{av}) \Delta\omega_i}, \tag{3.33}$$

with $S_I(\omega)$ being the incident wave spectrum and A_i represents the incident wave amplitude for each regular wave component (details are available in Goda [62]). Now, the instantaneous power available to the Wells turbine is given by

$$W_a = \frac{\dot{m}P}{\rho_a} = \wedge P^2, \qquad \wedge = \frac{K_a D}{\rho_a N}, \tag{3.34}$$

where ρ_a and $\dot{m}$ are termed as air density and mass flow rate of air across the Wells turbine. Here, N and D represent the rotational speed and turbine rotor diameter of the Wells turbine, respectively, and $K_a = 0.375$. Due to the random nature of ocean waves, the turbine rotational speed varies with the sea states, influencing the pressure drop and flow rate across the turbine. Turbine damping alters the air compressibility and the motion of the entrapped water inside the OWC device chamber. This has a significant impact on the hydrodynamic performance of the OWC device. Here, the classical symmetrical aerofoil sections of the NACA-00 series have been used for the rotor blades of the Wells turbine. Further, the optimal rotational speed and turbine rotor diameter are provided in Table 3.1 (see De O Falcão and Rodrigues [63], and Ezhilsabareesh et al. [122] for details). The average available power to the Wells turbine is expressed as the following

$$\overline{W}_a = E(W_a) = \int_{-\infty}^{\infty} W_a f(P) dP. \tag{3.35}$$

Using the relations Eqs. (3.32) and (3.34) into Eq. (3.35), and using the properties of the Gamma Function, we get the following

$$\overline{W}_a = \wedge \sigma_p^2. \tag{3.36}$$

It is seen from Eq. (3.36) that the averaged power available to the Wells turbine depends on the variance of the air pressure across the turbine and the turbine characteristics. Therefore, $\overline{W}_a$ can be calculated for each incident wave frequencies presents in the incident wave spectrum $S_I(\omega)$. Now, the average incident wave energy flux for the irregular waves is given by

$$\overline{P}_a = L_w \rho g \int_0^{\infty} S_I(\omega) C_g(\omega) d\omega. \tag{3.37}$$

Finally, the average efficiency of an OWC device in irregular sea waves is obtained as

$$\overline{\eta}_a = \frac{\overline{W}_a}{\overline{P}_a} = \frac{\wedge \int_0^{\infty} S_I(\omega) \left| \frac{p(\omega)}{A_i(\omega)} \right|^2 d\omega}{L_w \rho g \int_0^{\infty} S_I(\omega) C_g(\omega) d\omega}. \tag{3.38}$$

To analyze the efficiency of an OWC device under the irregular waves, the Bretschneider Spectrum is taken as the incident wave spectrum (see Goda [62] and De O Falcão and Rodrigues

Sea state	j	1	2	3	4	5	6	7	8	9
	H_s(m)	0.8	1.2	1.6	2.0	2.4	2.9	3.4	4.0	4.5
	T_e(s)	9.0	9.5	10.0	10.5	11.0	11.5	12.0	12.5	13.0
	ψ	0.250	0.200	0.177	0.145	0.100	0.070	0.045	0.007	0.006
	$\overline{P}_a/L_w$	1.3820	3.1836	5.7766	9.1884	13.4404	19.8972	27.6874	38.7427	49.5153
$D = 3.17m$	N_{op}	46.7	60.9	73.0	83.7	93.5	104.7	115.0	119.9	119.9
$D = 2.3m$	N_{op}	75.3	95.4	112.8	128.0	141.8	157.5	165.2	165.2	165.2
Falcao and Rodrigues	$\overline{W}_a$	13.1	31.4	56.9	89.0	127.1	182.8	246.6	330.2	391.4
(2002)	$\overline{W}_a$	14.1	30.2	51.1	76.1	105.0	145.8	190.3	234.4	260.9
Present solutions	$\overline{W}_a$	12.9391	31.1855	56.6408	88.4929	126.9753	181.2574	245.7000	329.8475	392.9847
	$\overline{W}_a$	13.9752	30.3214	51.3608	76.3353	104.6160	144.2920	191.8939	235.9660	259.4187
Type I OWC	$\overline{W}_a$	10.5801	24.6510	43.7016	67.0134	93.9648	132.7287	176.1063	236.7326	292.6758
	$\overline{W}_a$	10.6612	22.6458	37.8707	55.8133	76.0305	104.3282	138.3630	189.2579	236.5322
Type II OWC	$\overline{W}_a$	11.0165	29.1566	56.6374	92.9584	137.2598	202.1161	276.6568	379.9635	477.5240
	$\overline{W}_a$	13.5684	32.0682	57.4679	88.6610	124.5706	175.0496	234.3387	320.7807	400.9967

TABLE 3.1: Set of nine sea states represent the local wave climate at the OWC plant site Pico, Azores, Portugal. Here, the units of $\overline{P}_a/L_w$, N_{op} and $\overline{W}_a$ are kW/m, rad/sec and kW respectively. Further, $V_0 = 1050m^3$, $\gamma = 1.4$, $\rho_a = 1.25kg/m^3$, $p_a = 1.013 \times 10^5 Pa$.

[63] for details). The formula for the same is given by the following

$$S_I(\omega) = 131.5 H_s^2 T_e^{-4} \omega^{-5} \exp(-1054 T_e^{-4} \omega^{-4}), \tag{3.39}$$

where H_s and T_e represent the significant wave height and energy period related to various sea states. It is to be noted that the energy period T_e is related to the significant wave period $T_{1/3}$ by the formula $T_e = 0.8997 T_{1/3}$. Table 3.1 represents the set of nine sea states characterizing the local wave climate at OWC plant site Pico, Portugal. Each sea states can be distinguished by their significant wave height, energy periods, and its frequency of occurrence. Now, the annual spectral density is calculated using the following formula

$$S_{I,ann} = \sum_{j=1}^{9} S_{I,j}\ \psi_j. \tag{3.40}$$

The annual-averaged incident wave energy flux can be obtained from Eq. (3.37) by replacing $S_I(\omega)$ with $S_{I,ann}$ as the following

$$\overline{P}_{a,ann} = L_w \rho g \int_0^\infty S_{I,ann}(\omega) C_g(\omega) d\omega = \sum_{j=1}^{9} \overline{P}_{a,j}\ \psi_j. \tag{3.41}$$

Finally, the annual-averaged plant efficiency of an OWC device is given by

$$\overline{\eta}_{a,ann} = \frac{\wedge \int_0^\infty S_{I,ann}(\omega) \left| \dfrac{p(\omega)}{A_i(\omega)} \right|^2 d\omega}{L_w \rho g \displaystyle\int_0^\infty S_{I,ann}(\omega) C_g(\omega) d\omega} = \frac{\displaystyle\sum_{j=1}^{9} \overline{W}_{a,j}\ \psi_j}{\displaystyle\sum_{j=1}^{9} \overline{P}_{a,j}\ \psi_j}. \tag{3.42}$$

It is to be noted that the overall concept to model the hydrodynamics of OWC devices along with few parameters associated with the performance of the OWC devices under irregular incident waves were provided in De O Falcão and Rodrigues [63] in a scattered manner. The detailed

expressions for all the parameters are provided in the present section in a consolidated manner, along with the expression for the annual-averaged plant efficiency of the OWC device in the local wave climate.

3.6 Results and Discussions

In this section, various results associated with the performances and efficiencies of the type I and type II OWC devices are plotted and discussed in detailed manner. Firstly, the results associated with the regular incident waves are discussed and subsequently, the results associated with the irregular incident waves are discussed. The parameters associated with the incident waves and OWC devices are taken as follows: $h = 8$m, $L_w = 12$m, $\rho = 1025$ kg/m^3, $g = 9.81$m/s^2, $L/h = 2.0$, $l/h = 3.0$ (auxilliary boundary Γ_1 is located at $x = -l$), $b/h = 1.0$ (type I OWC device), $a/h = 0.5$ (type I OWC device), $d/h = 0.05$, $b_h/h = 0.1$, $\theta = 45^\circ$, $V_0 = 1050$ m^3, $\gamma = 1.4$, $\rho_a = 1.25$ kg/m^3 and $p_a = 1.013 \times 10^5$Pa unless otherwise mentioned. It is to be noted that for type II OWC device, the center of the quarter circle lies within the breakwater. The radius of the circle is taken as $r/h = 2.5$ and the y-coordiate of the center of the circle is taken as $y_0/h = -0.72$ unless otherwise stated. The non-dimensional horizontal and vertical wave forces F_h and F_v acting on the sea-side surface of Γ_4 are calculated using the following formulae

$$F_h = \Re\left\{\frac{\mathrm{i}\omega}{gh^2}\int_{\Gamma_4}\phi n_x d\Gamma\right\}, \quad F_v = \Re\left\{\frac{\mathrm{i}\omega}{gh^2}\int_{\Gamma_4}\phi n_z d\Gamma\right\}, \tag{3.43}$$

where n_x and n_z are the x and z-components of the outward drawn unit normal $\vec{n}$. Now, the resonance mechanism plays an important role in achieving maximum efficiency η_{max}. The following two resonance mechanisms are applicable to the present problem.

- **Resonance mechanism I:** For smaller values of b/a, resonance occurs at $Ka \approx 1$ due to the resonant piston-like motion of the water column.
- **Resonance mechanism II:** For higher values of a/h, resonance occurs due to the antisymmetric sloshing mode (see Evans and Porter [5] for details). The condition for sloshing phenomena is $k_0 b = n\pi$ with n represents the sloshing mode number.

3.6.1 Numerical convergence of the BEM based solution

The convergence of the numerical computations based on the boundary element method (as discussed in Section 3) depends on the length of the boundary element used to discretize the boundaries of the domain. The panel size p_s is given by (see Wang and Meylan [115])

$$p_s = \frac{1}{\kappa k_0}. \tag{3.44}$$

κ	b/h	Type I OWC device η_{max}	r/h	Type II OWC device η_{max}
20	0.5	0.74853	1.0	0.78133
	1.0	0.99339	1.5	0.79915
	1.5	0.83979	2.0	0.73039
	2.0	0.70388	2.5	0.68133
40	0.5	0.74036	1.0	0.77810
	1.0	0.99588	1.5	0.79300
	1.5	0.84796	2.0	0.73574
	2.0	0.71112	2.5	0.68631
60	0.5	0.73830	1.0	0.77384
	1.0	0.99588	1.5	0.79270
	1.5	0.84653	2.0	0.73565
	2.0	0.70888	2.5	0.68736
80	0.5	0.73861	1.0	0.77355
	1.0	0.99590	1.5	0.79263
	1.5	0.84698	2.0	0.73560
	2.0	0.70836	2.5	0.68736

TABLE 3.2: Comparative study of η_{max} for type I and type II OWC devices with $a/h = 0.5$, $y_0/h = -0.72$ and $Kh = 0.5$.

κ	a/h	Type I OWC device η_{max}	y_0/h	Type II OWC device η_{max}
20	1/8	0.90900	−0.36	0.99380
	1/4	0.92354	−0.45	0.97415
	1/2	0.99339	−0.60	0.86714
	3/4	0.35735	−0.72	0.68133
40	1/8	0.90443	−0.36	0.99480
	1/4	0.92127	−0.45	0.97524
	1/2	0.99488	−0.60	0.86240
	3/4	0.37070	−0.72	0.68631
60	1/8	0.90852	−0.36	0.99879
	1/4	0.92007	−0.45	0.97921
	1/2	0.99588	−0.60	0.86528
	3/4	0.36146	−0.72	0.68736
80	1/8	0.90849	−0.36	0.99878
	1/4	0.92033	−0.45	0.97921
	1/2	0.99590	−0.60	0.86530
	3/4	0.36153	−0.72	0.68736

TABLE 3.3: Comparative study of η_{max} for type I and type II OWC devices with $b/h = 1.0$, $r/h = 2.5$ and $Kh = 0.5$.

By varying the values of κ, we can determine the length of the boundary elements using Eq. (3.44) to get numerical convergence. It is seen from Eq. (3.44) that the panel size p_s decreases as the value of κ increases. Therefore, to determine the panel size p_s to get numerical convergence in the computational results, the values of κ should be taken in increasing order. In Tabs. 3.2 and 3.3, the values of κ are taken $20, 40, 60$ and 80 and for each κ value, the efficiency η_{max} is computed for certain values of wave and structural parameters. It is to be noted that increasing κ gives lower panel size p_s, but the computational time will increase significantly. So, our aim is to balance between the computational time and the accuracy of the numerical results. In Tab. 3.2, the non-dimensional efficiency η_{max} is computed for type I and type II OWC devices for different values of the chamber length $b/h = 0.5, 1.0, 1.5, 2.0$ and radius of the quarter circle $r/h = 1.0, 1.5, 2.0, 2.5$ respectively. It is observed that the values of η_{max} converge up to three decimal places for $\kappa = 60$. On the other hand, in Tab. 3.3, the non-dimensional efficiency η_{max} is computed for type I and type II OWC devices for different values of submergence depth $a/h = 1/8, 1/4, 1/2, 3/4$ and $y_0/h = -0.36, -0.45, -0.60, -0.72$ respectively. It is concluded from Tab. 3.3 that the panel size p_s in the boundary element method corresponds to $\kappa = 60$ is sufficient to get numerical convergence up to three decimal places in the computational results. Therefore, in the subsequent computations, the panel size p_s corresponds to $\kappa = 60$ is considered. In the following sections, results for regular and irregular incident waves are discussed separately.

3.6.2 Comparison with existing results

Now, for the sake of validation of the present numerical results, certain results are compared with the results of Evans and Porter [5] for the case of regular incident waves. To obtain the OWC device model of Evans and Porter [5], we have considered a limiting case of our present type I OWC device model placed over the uniform bottom with $\theta = 90°$. In Fig. 3.2, the efficiency η_{max} of the OWC device are plotted against the non-dimensional wave number Kh for different values of submergence depth a/h. These results are compared with Fig. 9 of Evans and Porter [5]. It is observed that the present numerical results matched well with that of Evans and Porter [5]. This shows the accuracy of the present numerical computations for regular incident waves. On the other hand, to validate the results for irregular incident waves, certain results are reproduced for the rectangular OWC device (limiting case of the present type I OWC device) and presented in Tab. 3.1 (5^{th} row in Tab. 3.1). It is observed from Tab. 3.1 that the present numerical results matched well with that of De O Falcão and Rodrigues [63]. This demonstrates the accuracy of the present numerical computations for irregular incident waves.

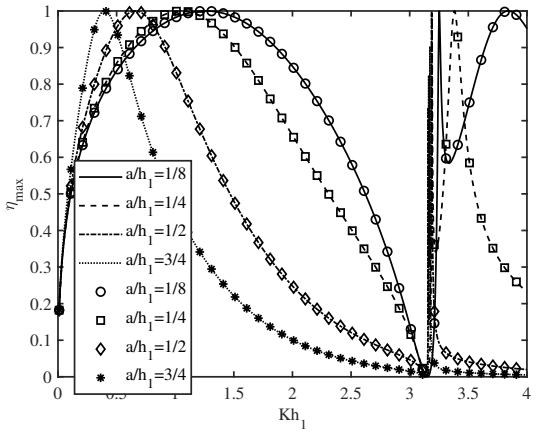

(a)

FIGURE 3.2: Variation of η_{max} vs Kh for different a/h for type I OWC device placed over uniform bottom with $\theta = 90°$. Lines represent the solutions obtained by the present boundary element method and symbols represent the solutions provided in Evans and Porter [5].

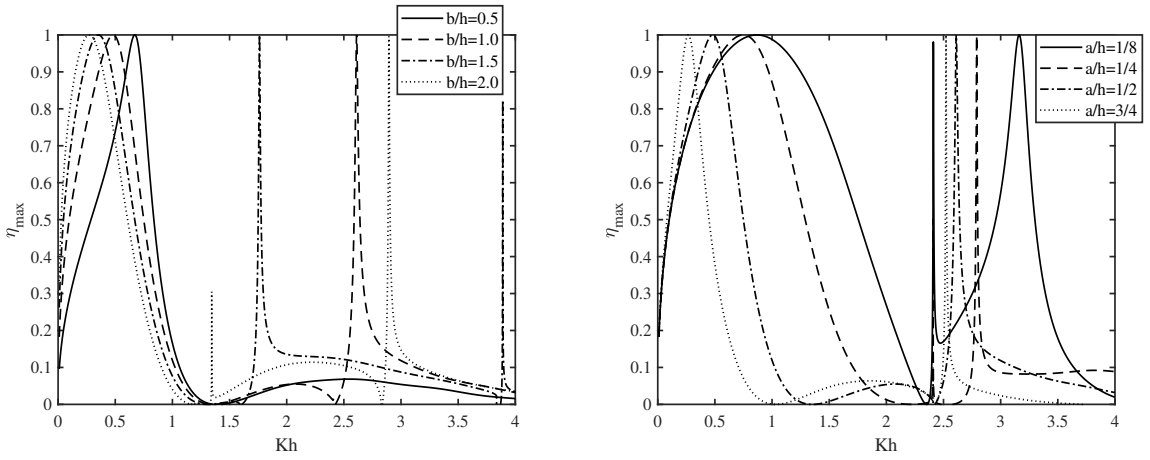

(a) (b)

FIGURE 3.3: Variation of η_{max} vs Kh for different (a) b/h and (b) a/h for type I OWC device.

3.6.3 Results for regular incident waves

In Figs. 3.3(a) and 3.3(b), the variation of η_{max} versus the non-dimensional wave number Kh are plotted for different values of b/h and a/h respectively. In Fig. 3.3(a), it is observed that the resonance occurs at $Kh \approx 0.677$ for smaller values of chamber length $b/h = 0.5$. This resonance phenomenon occurs due to the resonance mechanism I. Further, the same resonance pattern in η_{max} occurs for smaller values of Kh with an increase in the chamber length b/h. The reason behind this phenomenon is that in the case of the larger value of chamber length b/h, water particles have to travel more distance inside the chamber during one oscillation period. Further, sharp peak in the efficiency η_{max} occurs at $Kh \approx 1.344$ for larger values of $b/h = 2.0$. Moreover, it is observed that the third peak (resonance) in the efficiency η_{max} occurs at $Kh \approx 2.894$ for

$b/h = 2.0$. These resonances occur due to the resonance mechanism II with sloshing mode number $n = 1, 2$ (see Evans and Porter [5] for details). Similar resonances occur for higher values of Kh with a decrease in chamber length b/h. On the other hand, Fig. 3.3(b) shows the effect of different submergence depth of the front wall a/h on the efficiency η_{max} of type I OWC device. It is seen that the first peak in the efficiency curve occurs for smaller values of Kh with an increase in a/h. This resonance occurs due to the resonance mechanism I. Further, it is observed that the second peak in the efficiency curve η_{max} arises in the intermediate and short wave regime due to the resonance mechanism II. Careful observation reveals that for $a/h = 1/8$, the area under the efficiency curve is more, and this area decreases with an increase in a/h. In summary, it can be concluded that the efficiency η_{max} of the type I OWC device strongly depends on the chamber length b/h and the submergence depth a/h.

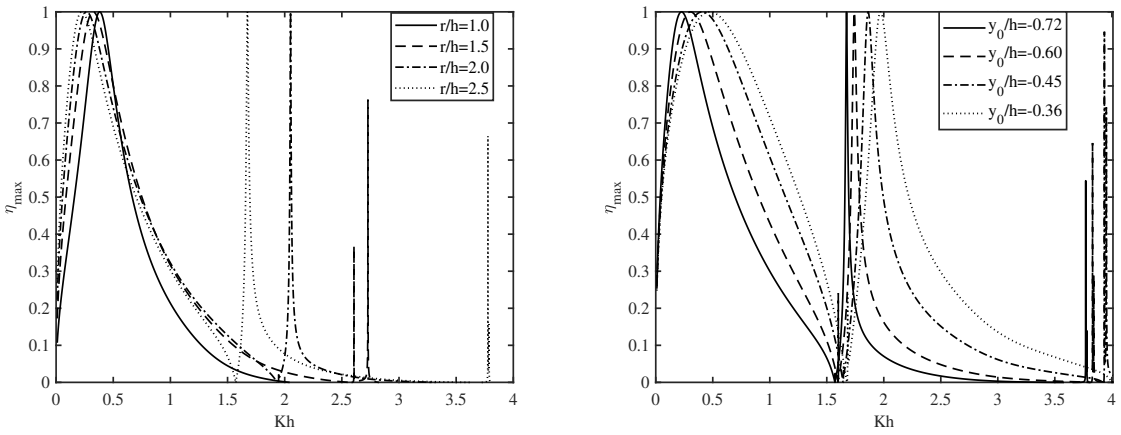

FIGURE 3.4: Variation of η_{max} vs Kh for different (a) r/h and (b) y_0/h for type II OWC device.

In Fig. 3.4(a), the variation of the efficiency η_{max} as a function of non-dimensional wave number Kh are plotted for different values of the radius of the quarter circle r/h. It is noticed that the first peak in the efficiency curve appears for a smaller value of Kh with an increase in the radius of quarter circle r/h. This resonance occurs due to the resonance mechanism I. These observations are similar in nature, as seen in Fig. 3.3(a). The reason behind this phenomenon is that when r/h increases, the chamber length of the OWC device increases, and as a result, water particles have to travel more distance inside the chamber during one oscillation period. Further, sharp peak in the efficiency η_{max} occurs at $Kh \approx 1.673$ for $r/h = 2.5$. Moreover, it is observed that the third peak (resonance) in the efficiency η_{max} occurs at $Kh \approx 3.778$ for $r/h = 2.5$. These resonances occur due to the sloshing phenomena with sloshing mode number $n = 1, 2$ respectively. Similar resonances occur for higher values of Kh with a decrease in the radius of quarter circle r/h. On the other hand, Fig. 3.4(b) shows the variation of η_{max} with respect to the non-dimensional wave number Kh for various values of y_0/h. It is seen that the first peak in the efficiency curve occurs for smaller values of Kh with an increase in $|y_0/h|$. This

resonance occurs due to the resonance mechanism I. Further, it is observed that the second peak in the efficiency curve η_{max} arises for $1.6 < Kh < 2.0$, and the third peak arises in the short wave regime due to the resonance mechanism II. Careful observation reveals that for $y_0/h = -0.36$, the area under the efficiency curve η_{max} is more, and this area decreases with an increase in $|y_0/h|$. These observations are similar in nature to that of Fig. 3.3(b). In summary, it can be concluded that the efficiency η_{max} of the type II OWC device strongly depends on the radius of the quarter circle r/h and the submergence depth y_0/h.

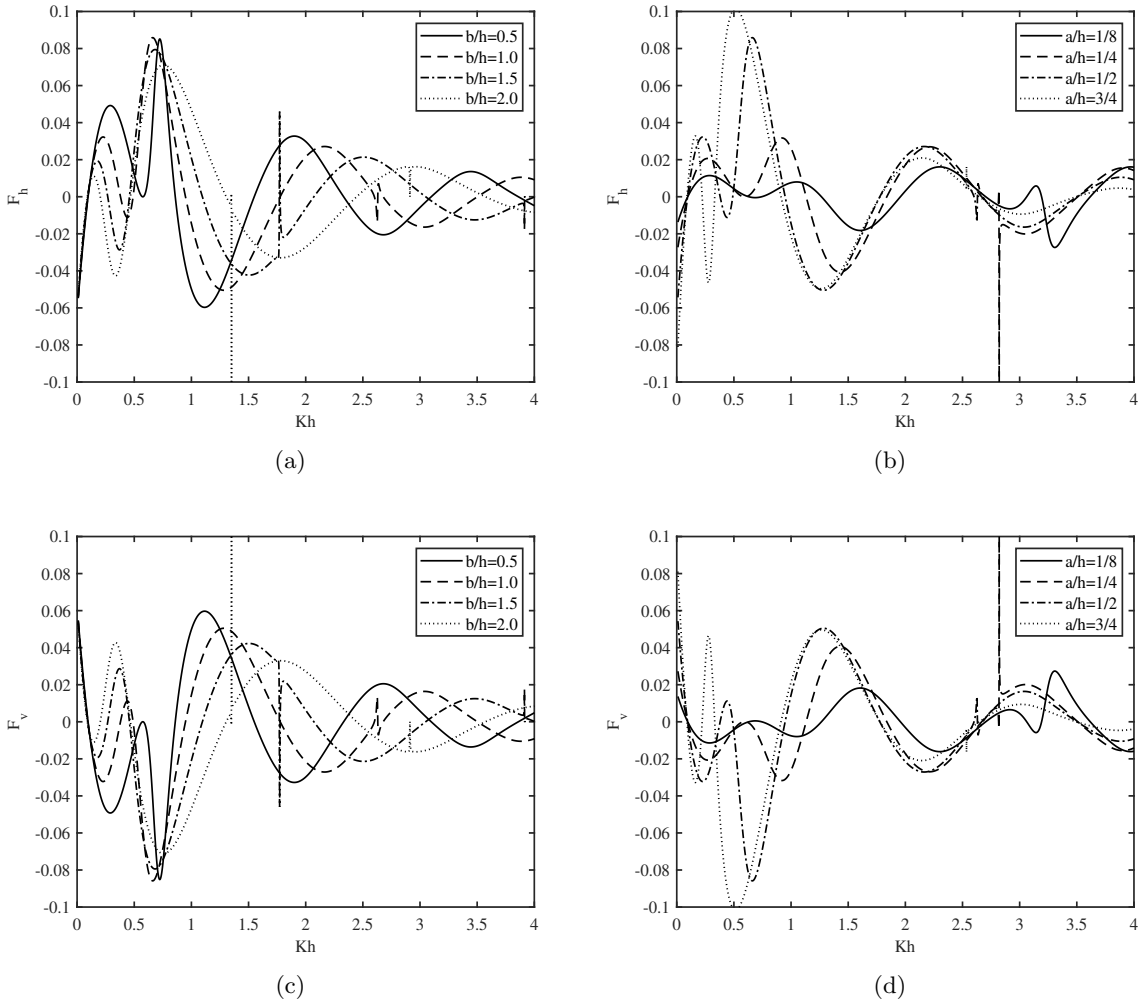

FIGURE 3.5: Variation of (a) F_h for different b/h, (b) F_h for different a/h, (c) F_v for different b/h and (d) F_v for different a/h as a function of Kh for type I OWC device.

In Figs. 3.5(a) and 3.5(b), the variation of the horizontal wave force F_h are plotted against the non-dimensional wave number Kh for various values of chamber length b/h and submergence depth a/h respectively. A comparison of Figs. 3.5(a) and 3.5(b) with Figs. 3.3(a) and 3.3(b) reveals that the resonances occur in the horizontal wave force F_h and the efficiency η_{max} at the same values of wavenumber Kh. Further, it is seen that the variation of the horizontal wave force F_h is oscillatory in nature with the variation in wavenumber Kh. Moreover, the amplitude

of oscillation in F_h decreases with an increase in Kh. Careful observation reveals that the change in phase in the horizontal wave force F_h occurs with the change in b/h and a/h. On the other hand, Figs. 3.5(c) and 3.5(d) show the variation of the vertical wave force F_v as a function of non-dimensional wave number Kh for various values of b/h and a/h respectively. A comparison of Figs. 3.5(c) and 3.5(d) with Figs. 3.5(a) and 3.5(b) reveals that the overall resonance pattern in the horizontal wave force F_h and the vertical wave force F_v are the same with the variation in Kh. However, the local and global maxima in the horizontal wave force correspond to the local and global minima in the vertical wave force and vice versa.

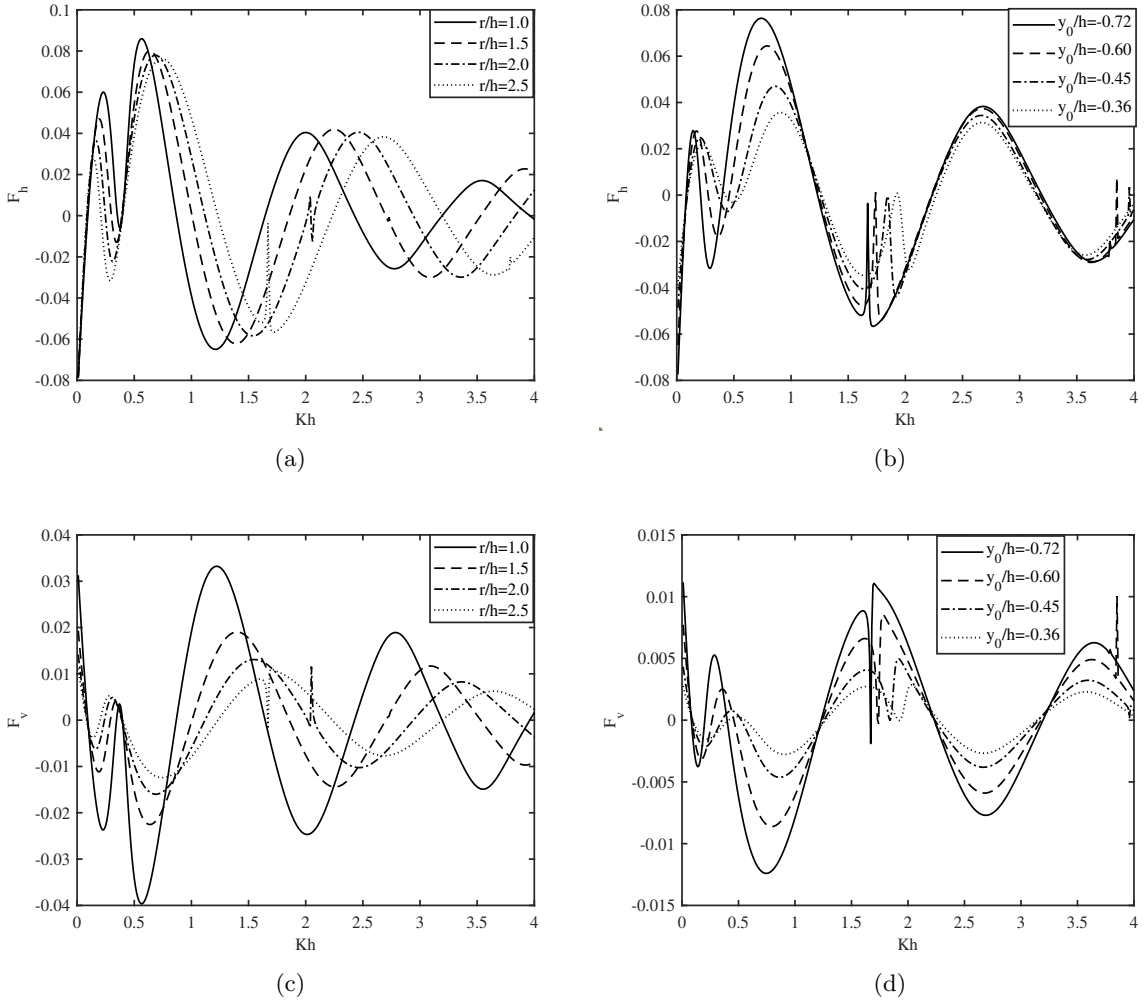

FIGURE 3.6: Variation of (a) F_h for different r/h, (b) F_h for different y_0/h, (c) F_v for different r/h and (d) F_v for different y_0/h as a function of Kh for type II OWC device.

In Figs. 3.6(a) and 3.6(b), the variation of the horizontal wave force F_h are plotted against the non-dimensional wave number Kh for different values of r/h and y_0/h respectively. It is observed that the pattern of the horizontal wave force F_h is oscillatory in nature with the variation in the non-dimensional wave number Kh. Moreover, the amplitude of oscillation decreases for higher values of wavenumber Kh. Further, certain phase change in the horizontal wave force

F_h occurs with the variation in r/h and y_0/h. A comparison of Figs. 3.6(a) and 3.6(b) with Figs. 3.5(a) and 3.5(b) reveals that except for resonances, the overall pattern of the horizontal wave force F_h are similar in nature for type I and type II OWC devices. A further comparison with Fig. 3.4 reveals that the resonance in the efficiency η_{max} and horizontal wave force F_h occurs at the same values of the wavenumber Kh due to sloshing phenomena. On the other hand, in Figs. 3.6(c) and 3.6(d), the variation of the vertical wave force F_v are plotted against the non-dimensional wave number Kh for different values of r/h and y_0/h respectively. It is observed that the resonances occur in the vertical wave force F_v and efficiency η_{max} at the same values of Kh. A comparison with Figs. 3.5(c) and 3.5(d) shows that the overall pattern of the vertical wave force F_v as a function of wavenumber Kh are similar in nature for type I and type II OWC devices except for the resonances. A further comparison of Figs. 3.6(c) and 3.6(d) with Figs. 3.6(a) and 3.6(b) reveals that the local and global maxima in the horizontal wave force F_h correspond to the local and global minima in the vertical wave force F_v and vice versa.

3.6.4 Results for irregular incident waves

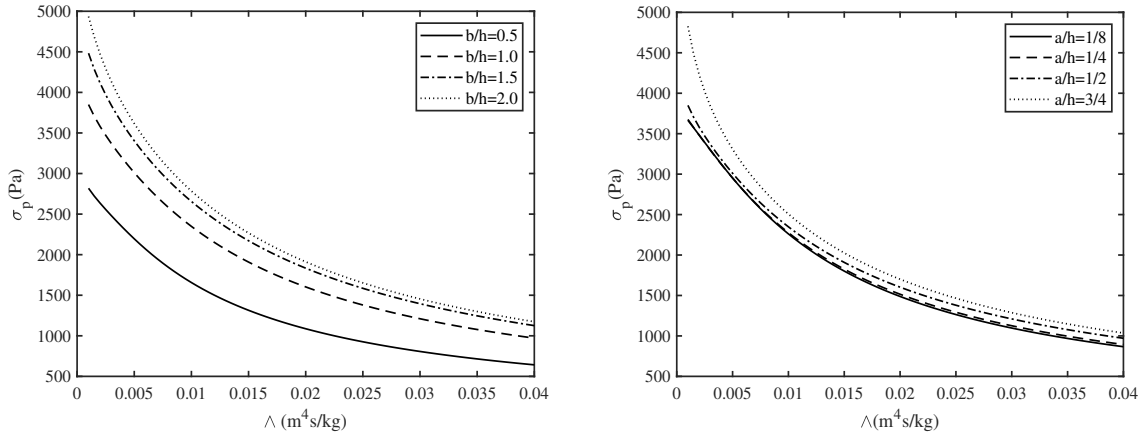

FIGURE 3.7: Variation of σ_p vs $\wedge$ for different (a) b/h and (b) a/h for the annual wave spectral density $S_{I,ann}$ and for type I OWC device.

Figs. 3.7(a) and 3.7(b) show the variation of chamber pressure standard deviation σ_p as a function of turbine damping coefficient $\wedge$ for different values of chamber length b/h and submergence depth a/h respectively for type I OWC device. It is to be noted that to calculate σ_p from Eq. (3.33), the annual wave spectral density $S_{I,ann}$ is used. It is observed that the chamber pressure standard deviation σ_p decreases with an increase in the turbine damping coefficient $\wedge$. Further, the chamber pressure standard deviation σ_p increases with an increase in the chamber length b/h. This happens as more amount of water mass entered the OWC device chamber as the chamber length increases. Higher values of σ_p will increase the efficiency of the OWC device as the average power absorbed from the irregular waves $\overline{W}_a$ directly proportional to σ_p (see Eq.

(3.36)). On the other hand, Fig. 3.7(b) shows that the chamber pressure standard deviation σ_p slightly increases with an increase in submergence depth a/h of the front wall of the OWC device. For $a/h = 3/4$, the pressure fluctuation inside the OWC device chamber becomes higher due to the occurrences of sloshing phenomena as described in the resonance mechanism II. As a consequence, the chamber pressure standard deviation σ_p increases.

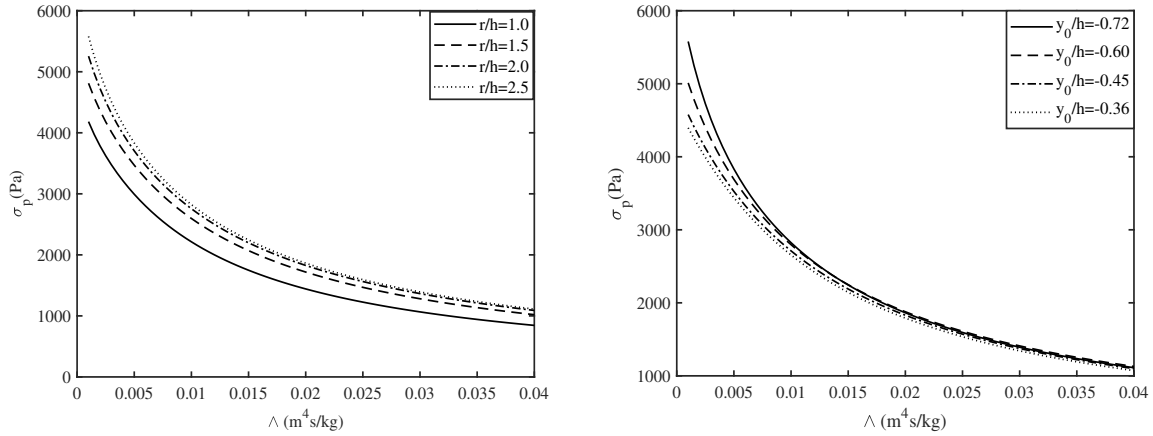

FIGURE 3.8: Variation of σ_p vs $\wedge$ for different (a) r/h and (b) y_0/h for the annual wave spectral density $S_{I,ann}$ and for type II OWC device.

Figs. 3.8(a) and 3.8(b) show the variation of chamber pressure standard deviation σ_p as a function of turbine damping coefficient $\wedge$ for different values of radius of the quarter circle r/h and submergence depth y_0/h respectively for type II OWC device. A comparison with Figs. 3.7(a) and 3.7(b) reveals that the overall pattern of the chamber pressure standard deviation σ_p as a function of turbine damping coefficient $\wedge$ is similar in nature for type I and type II OWC devices. Fig. 3.8(a) depicts that the chamber pressure standard deviation σ_p increases with an increase in r/h. On the other hand, Fig. 3.8(b) shows that for smaller values of turbine damping coefficient $\wedge$, the chamber pressure standard deviation σ_p increases with an increase in the submergence depth $|y_0/h|$ of the front wall of the OWC device. However, for higher values of $\wedge$, there are no significant variations in σ_p are observed due to the variation in y_0/h. For $y_0/h = -0.72$, the pressure fluctuation inside the OWC device chamber becomes higher due to the occurrences of sloshing phenomena as mentioned in the discussion of Fig. 3.7(b). It is to be noted that higher values of σ_p will increase the average power absorbed from the irregular waves $\overline{W}_a$ as $\overline{W}_a$ is directly proportional to σ_p (see Eq. (3.36)).

Figs. 3.9(a) and 3.9(b) show the variation of annual-averaged plant efficiency $\overline{\eta}_{a,ann}$ versus turbine damping coefficient $\wedge$ for different values of chamber length b/h and submergence depth a/h respectively for type I OWC device. Figs. 3.9(a) and 3.9(b) depict that the annual-averaged plant efficiency $\overline{\eta}_{a,ann}$ initially increases with an increase in the turbine damping coefficient $\wedge$ and attains maximum for intermediate values of $\wedge$. Hereafter, the annual-averaged plant efficiency

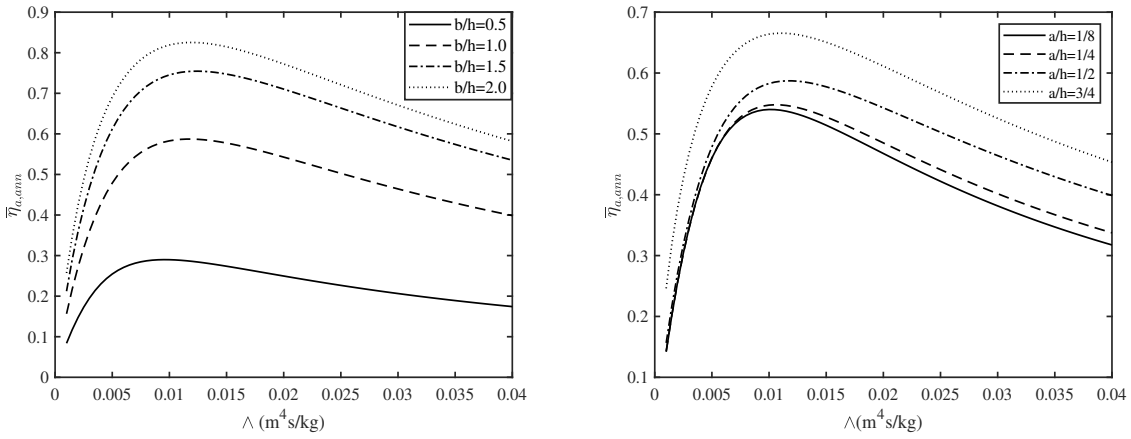

(a) (b)

FIGURE 3.9: Variation of $\overline{\eta}_{a,ann}$ vs $\wedge$ for different (a) b/h and (b) a/h for type I OWC device.

$\overline{\eta}_{a,ann}$ decreases for further increase in the turbine damping coefficient $\wedge$. The reason behind the same is that the average power absorbed from the irregular waves $\overline{W}_a$ is proportional to $\wedge$ and σ_p (see Eq. (3.36)), however, σ_p decreases with an increase in $\wedge$ as seen in Fig. 3.7(a) and 3.7(b). Further, Fig. 3.9(a) shows that the annual-averaged plant efficiency $\overline{\eta}_{a,ann}$ increases with an increase in the chamber length b/h of the OWC device. This happens as the chamber pressure standard deviation σ_p increases with an increase in chamber length b/h (see Figs. 3.7(a)). On the other hand, Fig. 3.9(b) shows that the annual-averaged plant efficiency $\overline{\eta}_{a,ann}$ increases with an increase in the submergence depth a/h. This happens as the chamber pressure standard deviation σ_p increases with an increase in submergence depth a/h (see Figs. 3.7(b)).

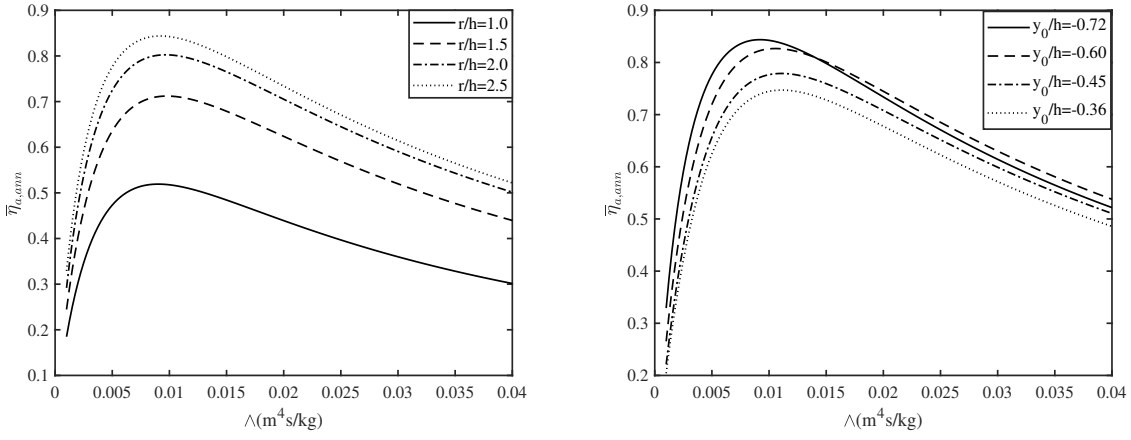

(a) (b)

FIGURE 3.10: Variation of $\overline{\eta}_{a,ann}$ vs $\wedge$ for different (a) r/h and (b) y_0/h for type II OWC device.

Figs. 3.10(a) and 3.10(b) show the variation of annual-averaged plant efficiency $\overline{\eta}_{a,ann}$ versus

turbine damping coefficient $\wedge$ for different values of radius of the quarter circle r/h and submergence depth y_0/h respectively for type II OWC device. A comparison of Figs. 3.10(a) and 3.10(b) with Figs. 3.9(a) and 3.9(b) reveals that the overall pattern of the annual-averaged plant efficiency $\overline{\eta}_{a,ann}$ as a function of $\wedge$ is similar in nature for type I and type II OWC devices. Moreover, Fig. 3.10(a) shows that the annual-averaged plant efficiency $\overline{\eta}_{a,ann}$ increases with an increase in r/h. This can be explained from the observation of Fig. 3.8(a) in which the chamber pressure standard deviation σ_p increases with an increase in r/h. On the other hand, Fig. 3.10(b) shows that the annual-averaged plant efficiency $\overline{\eta}_{a,ann}$ increases with an increase in the submergence depth $|y_0/h|$ of the front wall of the OWC device except for higher values of $\wedge$. The reason behind the same is clearly explained in Fig. 3.8(b).

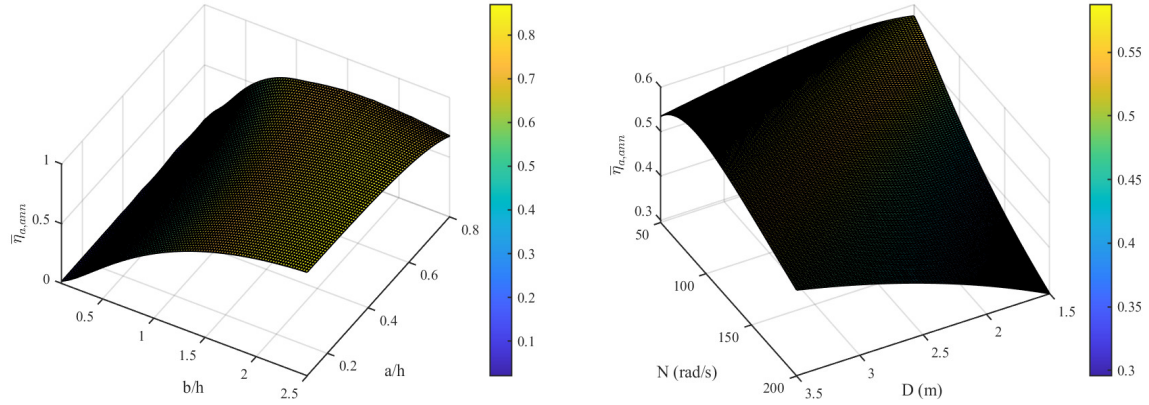

(a) (b)

FIGURE 3.11: Surface plot of $\overline{\eta}_{a,ann}$ as a function of (a) a/h and b/h with $\wedge = 0.01$ and (b) N and D with $K_a = 0.375$.

In the discussion of Figs. 3.9(a) and 3.9(b), we have observed that the annual-averaged plant efficiency $\overline{\eta}_{a,ann}$ strongly depend on the chamber length b/h, the submergence depth a/h and the turbine damping coefficient $\wedge$ for type I OWC device. To get a combined effects of a/h and b/h on the annual-averaged plant efficiency $\overline{\eta}_{a,ann}$, a surface plot for $\overline{\eta}_{a,ann}$ as a function of a/h and b/h is provided in Fig. 3.11(a). It is observed that for fixed values of a/h, efficiency $\overline{\eta}_{a,ann}$ increases with an increase in b/h. However, the change is negligible for higher values of b/h. Further, for fixed smaller values of b/h, the efficiency $\overline{\eta}_{a,ann}$ increases with an increase in a/h. However, for higher values of b/h, the efficiency $\overline{\eta}_{a,ann}$ decreases with a variation in a/h in the range $0.6 < a/h < 0.8$. These observations suggest that the annual-averaged plant efficiency $\overline{\eta}_{a,ann}$ becomes higher for type I OWC device with $0.3 < a/h < 0.6$ and $1.5 < b/h < 2.5$. This combination of chamber length b/h and submergence depth a/h is very important to design an efficient type I OWC device. On the other hand, to check the combined effects of turbine rotor diameter D and rotational speed N on the annual-averaged plant efficiency $\overline{\eta}_{a,ann}$, a surface plot of $\overline{\eta}_{a,ann}$ as a function of N and D is provided in Fig. 3.11(b). It is to be noted that the turbine damping coefficient $\wedge$ is a function of N and D (see Eq. (3.34)). Fig. 3.11(b) shows

that for smaller values of rotor diameter D, the efficiency $\overline{\eta}_{a,ann}$ decreases with an increase in rotational speed N. However, for higher values of the rotor diameter D, the efficiency $\overline{\eta}_{a,ann}$ initially increases with an increase in rotational speed N and attains maximum. Hereafter, the efficiency $\overline{\eta}_{a,ann}$ decreases for further increase in the rotational speed N. In a similar manner, for lower rotational speed N of the turbine, the efficiency $\overline{\eta}_{a,ann}$ decreases with an increase in the rotor diameter D, whereas, for higher values of N, efficiency $\overline{\eta}_{a,ann}$ increases with an increase in the rotor diameter D. Similar observations were reported in De O Falcão and Rodrigues [63]. These observations suggest that suitable combination of turbine rotor diameter D and rotational speed N can enhance the annual-averaged plant efficiency $\overline{\eta}_{a,ann}$ of the type I OWC device.

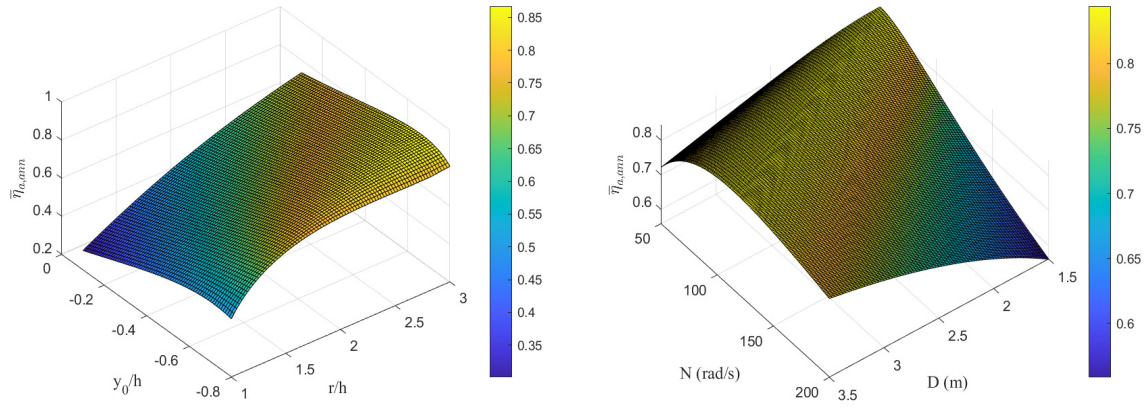

(a) (b)

FIGURE 3.12: Surface plot of $\overline{\eta}_{a,ann}$ as a function of (a) r/h and y_0/h with $\wedge = 0.01$ and (b) N and D with $K_a = 0.375$.

In the discussion of Figs. 3.10(a) and 3.10(b), we have observed that the annual-averaged plant efficiency $\overline{\eta}_{a,ann}$ strongly depend on the radius of the quarter circle r/h, submergence depth y_0/h and the turbine damping coefficient $\wedge$ for type II OWC device. To get a combined effects of r/h and y_0/h on the annual-averaged plant efficiency $\overline{\eta}_{a,ann}$, a surface plot for $\overline{\eta}_{a,ann}$ as a function of r/h and y_0/h is provided in Fig. 3.12(a). It is observed that for fixed values of y_0/h, the annual-averaged plant efficiency $\overline{\eta}_{a,ann}$ increases with an increase in r/h. However, the change is negligible for higher values of r/h. Further, for fixed values of r/h, the efficiency $\overline{\eta}_{a,ann}$ increases with an increase in $|y_0/h|$ except for very higher values of $|y_0/h|$. The reason behind the same is that for very higher values of submergence depth $|y_0/h|$, less amount of water can enter into the OWC device chamber. In summary, it can be concluded that the maximum efficiency $\overline{\eta}_{a,ann}$ is acheived for type II OWC device with $2.5 < r/h < 3.0$ and $-0.7 < y_0/h < -0.5$. On the other hand, to analyze the combined effects of turbine rotor diameter D and rotational speed N on the annual-averaged plant efficiency $\overline{\eta}_{a,ann}$, a surface plot of $\overline{\eta}_{a,ann}$ as a function of N and D is provided in Fig. 3.12(b). It is observed that for lower values of rotational speed N, the annual-averaged plant efficiency $\overline{\eta}_{a,ann}$ decreases as the rotor diameter D increases. However, for higher values of rotational speed N, the annual-averaged plant efficiency $\overline{\eta}_{a,ann}$ increases

as the rotor diameter D increases. In a similar manner, for lower values of D, efficiency $\overline{\eta}_{a,ann}$ decreases with an increase in N. Further, for higher values of D, the efficiency $\overline{\eta}_{a,ann}$ initially increases with an increase in N and attains maximum. Hereafter, the efficiency $\overline{\eta}_{a,ann}$ decreases for further increase in N. Similar observations were found in De O Falcão and Rodrigues [63] and also seen for type I OWC device. These results suggest that suitable combination of turbine rotor diameter D and rotational speed N can enhance the annual-averaged plant efficiency $\overline{\eta}_{a,ann}$ of the type II OWC device.

It is to be noted that for the set of nine sea states represent the local wave climate at the OWC plant site Pico, Portugal (see Tab. 3.1), the annual-averaged plant efficiency for type I OWC device with the rotor diameters $D = 3.17$m and $D = 2.3$m are 0.5816 and 0.4846 respectively. On the other hand, the annual-averaged plant efficiency for type II OWC device with the rotor diameters $D = 3.17$m and $D = 2.3$m are 0.8234 and 0.7685 respectively.

3.7 Conclusions

In the present study, the performance of two different breakwater-integrated OWC wave energy converter devices: (i) LIMPET device and (ii) quarter-circle-shaped front wall OWC device is analyzed under the action of unidirectional regular and irregular incident waves. Detailed derivations of the physical parameters associated with the efficiencies of the two types of OWC devices are provided.

- For type I OWC device, resonance occurs in the efficiency curve for smaller values of the incident wavenumber with an increase in chamber length and submergence depth. A similar resonance pattern is observed for the type II OWC device with an increase in the radius of the quarter circle and submergence depth of the front wall.
- The resonances in the horizontal and vertical wave forces acting on the front wall of the OWC devices occur for the same values of the wavenumber. However, the curves of horizontal and vertical wave forces as a function of wavenumber are out-of-phase.
- The horizontal and vertical wave forces are oscillatory in nature, and the amplitude of oscillation decreases in the short wave regime.
- For irregular incident waves (spectral density is taken as annual wave spectral density at the OWC plant site Pico, Portugal), the chamber pressure standard deviation decreases with an increase in the turbine damping coefficient. Moreover, the chamber pressure standard deviation increases with an increase in the chamber length and draft of the front wall of the type I OWC device. Similar results are observed for type II OWC device with an increase in radius and draft of the front wall.

- The annual-averaged plant efficiency increases with an increase in chamber length and submergence depth of type I OWC device except for significantly higher values of the shape parameters.

- For type I OWC device, the annual-averaged plant efficiency becomes higher for $0.3 < a/h < 0.6$ and $1.5 < b/h < 2.5$. Similarly, for type II OWC device, the maximum efficiency is achieved for $2.5 < r/h < 3.0$ and $-0.7 < y_0/h < -0.5$.

- For smaller values of rotor diameter, the annual-averaged plant efficiency decreases with an increase in the rotational speed of the Wells turbine. However, for higher values of the rotor diameter, the efficiency initially increases with an increase in rotational speed and attains a maximum. Hereafter, the efficiency decreases for further increase in the rotational speed of the turbine. In a similar manner, for the lower rotational speed of the turbine, the efficiency decreases with an increase in the rotor diameter, whilst, for higher values of the rotational speed of the turbine, the efficiency increases with an increase in the rotor diameter.

These observations conclude that maximum efficiency can be achieved with appropriate combinations of the turbine rotor diameter and rotational speed. The present solution methodology is robust and can be applied easily to study the OWC devices having arbitrary shapes and complex structural configurations. The present study is based on linear wave-structure interaction theory. The same can be extended to study the effect of non-linearities present in waves and structures in the near future.

Chapter 4

Performance of a hybrid wave energy converter device consisting of a piezoelectric plate and oscillating water column device placed over an undulated seabed

* The work, in this chapter, is covered by the following publication:

K. Trivedi, and S. Koley, "Performance of a hybrid wave energy converter device consisting of a piezoelectric plate and oscillating water column device placed over an undulated seabed," *Applied Energy*, vol. 333, 120627, 2023.

4.1 General introduction

This chapter investigates the hydrodynamic performance of a hybrid wave energy converter device consisting of a piezoelectric plate and the oscillating water column wave energy converter device placed over an undulated seabed. Primary emphasis is given to analyze the power extraction of the hybrid wave energy converter device, piezoelectric plate, and the OWC devices for various values of incident wave parameters and shape parameters associated with the hybrid wave energy converter device and undulated seabed. Moreover, the time-domain analysis is carried out by considering the Bretschneider spectrum as the incident wave spectrum for irregular incident waves. A multi-parameter optimization based on the Taguchi method is provided. The study reveals that the power extraction by the hybrid wave energy converter device consisting of a piezoelectric plate and the oscillating water column device is significantly higher than the power extraction by the standalone piezoelectric plate and the OWC device for a wider range of frequencies. Further, the present study shows that the power extraction by the hybrid wave energy converter device is higher when the piezoelectric plate is placed in the close proximity of the OWC device. Moreover, the time-domain simulation reveals that the piezoelectric plate is able to capture the incident wave energy for a longer period of time in real sea conditions.

4.2 Mathematical formulation

In the present section, the mathematical modeling of a hybrid wave energy converter device consisting of a piezoelectric plate and oscillating water column device is provided under the assumption of linear water wave theory. The geometric configurations of the hybrid wave energy converter device are provided in Fig. 4.1. The Cartesian coordinate system is considered with the vertical cross-section of the OWC device lying in the XZ-plane. The wave energy converter device is placed over an undulated seabed $z = -h(x)$. The undulated seabed is finitely extended as shown in Fig. 4.1. In addition, the thin piezoelectric plate of length l_1 is submerged at $z = -d_1$. Further, the submergence depth and thickness of the front wall of the OWC device are d_2 and d, respectively. Moreover, the chamber width of the OWC device is b, and the rear wall of the OWC device is positioned at $x = L$. Due to the presence of the OWC device and the piezoelectric plate, the total free surface is divided into four parts: (i) internal free surface $\Gamma_4 = \{(x, z) : z = 0; L - b < x < L\}$, (ii) open free surfaces $\Gamma_8 = \{(x, z) : z = 0; c + l_1 < x < L - b - d\}$ and $\Gamma_{13} = \{(x, z) : z = 0; -l < x < c\}$, and (iii) free surface in the plate region $\Gamma_{12} = \{(x, z) : z = 0; c < x < c + l_1\}$. Further, the seabed is rigid and impermeable in nature. Moreover, the immersed boundaries of the front wall of the OWC device are represented by $\Gamma_5 \cup \Gamma_6 \cup \Gamma_7$. In the presence of floating piezoelectric plate and OWC device, the fluid domain is divided into two regions R_j $(j = 1, 2)$ where $R_1 = \{-l < x < L, -h(x) < z < 0\}$ except the region above the plate, and $R_2 = \{c < x < c + l_1, -d_1 < z < 0\}$. To solve the above

boundary value problem, the boundary element method is used. To close the computational domain R_1, an auxiliary boundary Γ_1 is placed at $x = -l$. Further, to close the computational domain R_2, two auxiliary boundaries Γ_{11} and Γ_9 are placed at $x = c$ and $x = c + l_1$, respectively. For the modeling purpose, the water is assumed to follow the potential flow theory (see Babarit [123] for detailed assumptions), and the motion is simple harmonic in time with the angular frequency ω. Therefore, the total velocity potentials $\Phi_j(x, z, t) = \Re\{\phi_j(x, z)e^{-i\omega t}\}$ exist and satisfy the Laplace equation

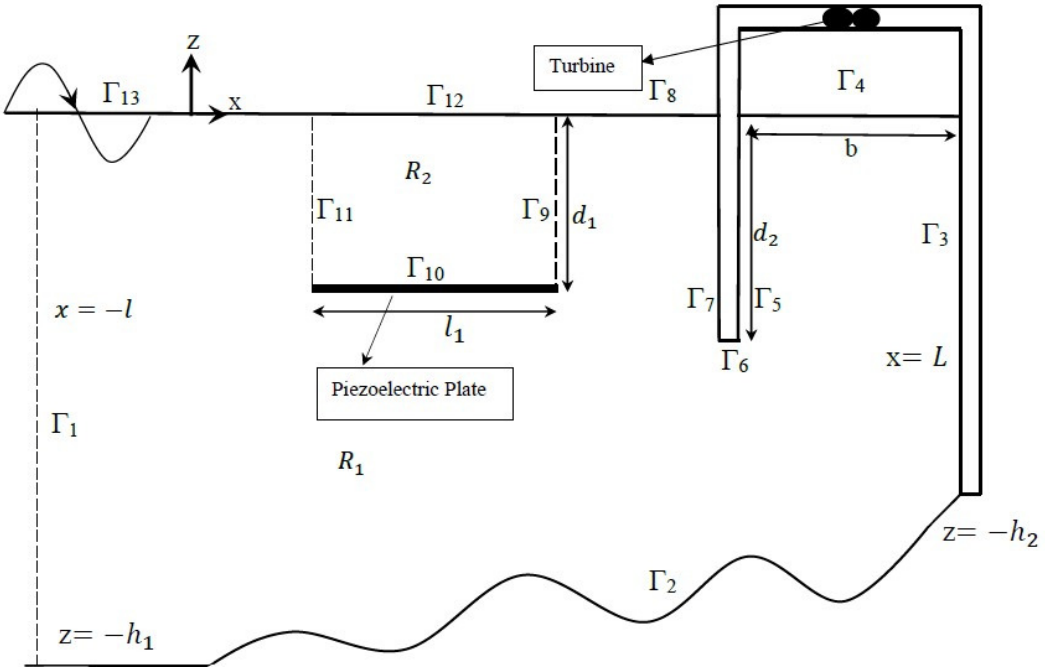

FIGURE 4.1: Vertical cross section of wave energy converter device.

$$\nabla^2\phi_j(x, z) = 0, \quad \text{for } j = 1, 2, \quad \nabla^2 \equiv \left(\frac{\partial^2}{\partial x^2} + \frac{\partial^2}{\partial z^2}\right). \tag{4.1}$$

The boundary condition at the mean free surface $z = 0$ is given by (see Evans and Porter [5], Koley and Trivedi [26] for details)

$$\begin{cases} \dfrac{\partial\phi_1}{\partial n} - K\phi_1 = \begin{cases} \dfrac{\mathrm{i}\omega p}{\rho g}, & \text{on } \Gamma_4, \\ 0, & \text{on } \Gamma_8 \cup \Gamma_{13}, \end{cases} \\ \dfrac{\partial\phi_2}{\partial n} - K\phi_2 = 0, \quad \text{on } \Gamma_{12} \end{cases} \tag{4.2}$$

where $K = \omega^2/g$, with g being the gravitational acceleration. Here, $\partial/\partial n$ represents the derivative in the normal direction. Now, the boundary condition on the impentrable bottom Γ_2 is given by

$$\frac{\partial\phi_1}{\partial n} = 0, \quad \text{on } z = -h(x), \tag{4.3}$$

where $h(x)$ represents the bottom profile

$$h(x) = \begin{cases} h_1, & x < 0, \\ \tilde{h}(x), & 0 < x < L, \\ h_2, & x = L. \end{cases} \tag{4.4}$$

Here, $\tilde{h}(x)$ yields the undulated bottom profile. Further, the no flow condition on the rear side wall and the submerged boundaries of the front wall of the OWC device is given by

$$\frac{\partial \phi_1}{\partial n} = 0, \quad \text{on} \quad \Gamma_3 \cup \Gamma_5 \cup \Gamma_6 \cup \Gamma_7. \tag{4.5}$$

The continuity of pressure and normal velocities along the two auxiliary boundaries Γ_{11} and Γ_9 placed at $x = c$ and $x = c + l_1$, respectively are given by

$$\phi_1 = \phi_2, \quad \text{and} \quad \frac{\partial \phi_1}{\partial n} = -\frac{\partial \phi_2}{\partial n} \quad \text{on} \ \ \Gamma_9 \cup \Gamma_{11}. \tag{4.6}$$

It is assumed that the motion of the piezoelectric plate is uniform in the longitudinal direction. The displacement of the piezoelectric plate can be written in the form $\tilde{\zeta}(x,t) = \Re\{\zeta(x)e^{-i\omega t}\}$ with $\zeta(x)$ being the complex deflection amplitude. Now, the dynamic boundary condition on the piezoelectric plate Γ_{10} is given by

$$g\chi\left(1 + \frac{\beta^2\xi\omega}{\mathrm{i} + \xi\omega}\right)\frac{\partial^4 \zeta}{\partial x^4} - \omega^2\gamma\zeta = \mathrm{i}\omega\left(\phi_1 - \phi_2\right), \quad \text{on} \quad z = -d_1, \quad x \in [c, c + l_1], \tag{4.7}$$

where the expressions for χ, β, ξ, and γ are given as (Renzi [4], Zheng et al. [71])

$$\chi = \frac{B'}{\rho g}, \ \beta = \frac{\theta'}{\sqrt{B'C'}}, \ \xi = \frac{C'}{G'}, \ \gamma = \frac{I_b}{\rho}, \tag{4.8}$$

with B', θ', C', and G' being termed as flexural rigidity of the bimorph, piezoelectric coupling factor, electric surface capacitance, and surface conductance, respectively. Further, I_b represents the surface density of the bimorph. Now, the linearized kinematic boundary condition on the plate Γ_{10} is given by

$$\frac{\partial \phi_1}{\partial n} = -\frac{\partial \phi_2}{\partial n} = -\mathrm{i}\omega\zeta, \quad \text{on} \quad z = -d_1, c < x < c + l_1. \tag{4.9}$$

Further, it is assumed that the plate has fixed edges and therefore, vanishing of plate displacement and the slope of the displacement near both the edges of the plate yield

$$\zeta = 0, \ \ \frac{\partial \zeta}{\partial n} = 0, \ \ \text{at} \ \ x = c, c + l_1, \ \ z = -d_1. \tag{4.10}$$

Similarly, when the plate edges are free, the edge conditions are given by

$$\frac{\partial^2\zeta}{\partial n^2}=0,\quad \frac{\partial^3\zeta}{\partial n^3}=0,\quad \text{at}\ \ x=c,c+l_1,\quad z=-d_1. \tag{4.11}$$

Now, the total velocity potential ϕ_j $(j=1,2)$ and the plate deflection ζ consist of the scattered and the radiated velocity potentials, respectively. Therefore, the total velocity potential and the plate deflection can be expressed as (see Evans and Porter [5]).

$$\phi_j=\phi_j^S+\left(\frac{\mathrm{i}\omega p}{\rho g}\right)\phi_j^R,\quad (j=1,2),\qquad \zeta=\zeta^S+\left(\frac{\mathrm{i}\omega p}{\rho g}\right)\zeta^R. \tag{4.12}$$

Here, ϕ_j^S and ϕ_j^R are termed as the scattered and radiated velocity potentials, respectively for regions R_j $(j=1,2)$. Moreover, the scattered velocity potential can be separated into the diffracted potential ϕ_j^D and the incident potential ϕ^I for $j=1,2$ (see Evans and Porter [5], Koley and Trivedi [26] for details). Further, ζ^S and ζ^R are termed as the plate deflection associated with the scattered and radiated waves, respectively. Now, $\phi_1^{S,R}$ satisfies the Eqs. (4.1)-(4.9), and $\phi_2^{S,R}$ satisfies Eqs. (4.1)-(4.2), (4.6)-(4.9). On the other hand, $\zeta^{S,R}$ satisfies the Eqs. (4.7)-(4.11). It is to be mentioned that in region R_1 and R_2, all the boundary conditions remain same as mentioned above except Eq. (4.2) in region R_1. Here, Eq. (4.2) is rewritten as

$$\frac{\partial\phi_1^S}{\partial n}-K\phi_1^S=0,\quad \text{on}\ \ \Gamma_4\cup\Gamma_8\cup\Gamma_{13},\qquad \frac{\partial\phi_1^R}{\partial n}-K\phi_1^R=\begin{cases}1, & \text{on}\ \ \Gamma_4,\\ 0, & \text{on}\ \ \Gamma_8\cup\Gamma_{13}.\end{cases} \tag{4.13}$$

Finally, the far-field boundary conditions on Γ_1 are given as

$$\begin{cases}\dfrac{\partial(\phi_1^S-\phi^I)}{\partial n}-ik_0(\phi_1^S-\phi^I)=0, & \text{on}\quad \Gamma_1,\\ \dfrac{\partial\phi_1^R}{\partial n}-ik_0\phi_1^R=0, & \text{on}\quad \Gamma_1.\end{cases} \tag{4.14}$$

Here, ϕ^I is the incident wave potential of the form $\phi^I=e^{\mathrm{i}k_0x}\psi_0(k_0,z)$ with $\psi_0(k_0,z)=\left(\dfrac{-\mathrm{i}gA}{\omega}\right)\dfrac{\cosh k_0(z+h_1)}{\cosh(k_0h_1)}$. It is to be noted that k_0 is the positive real root of the dispersion relation $\omega^2=gk_0\tanh(k_0h_1)$.

4.3 Solution methodology based on BEM

The present section yields the detailed formulation of integral equations and the associated numerical solution technique.

4.3.1 Formulation of the integral equations

Applying Green's second identity to the scattered and radiated velocity potentials $\phi_j^{S,R}(x,z)$ $(j=1,2)$, and the free space Green's function $G(P;Q)$ over the domain Ω bounded by Γ (see Katsikadelis [112] for detailed derivation), we get

$$\epsilon(Q)\phi_j^{S,R}(Q)=\int_\Gamma\left[\phi_j^{S,R}(P)\frac{\partial G}{\partial n}(P;Q)-G(P;Q)\frac{\partial\phi_j^{S,R}}{\partial n}(P)\right]d\Gamma(P),\quad \text{for } j=1,2, \tag{4.15}$$

where the free term coefficient is given as

$$\epsilon(Q)=\begin{cases}1, & P\in\Omega,\\ \frac{1}{2}, & P\in\Gamma,\\ 0, & P\notin\Omega\cup\Gamma.\end{cases} \tag{4.16}$$

Here, $P=(x,z)$ and $Q=(x_0,z_0)$ are the field and source points, respectively. It is to be noted that the free space Green's function $G(P,Q)$ satisfies the governing equation (see Katsikadelis [112], Behera et al. [75] for details)

$$\left(\frac{\partial^2}{\partial x^2}+\frac{\partial^2}{\partial z^2}\right)G(P,Q)=\delta(x-x_0)\delta(z-z_0), \tag{4.17}$$

and takes the form

$$G(P,Q)=\frac{1}{2\pi}\ln(\tilde{r}),\text{where }\ \tilde{r}=\sqrt{(x-x_0)^2+(z-z_0)^2}. \tag{4.18}$$

Now, implementing the boundary conditions (4.3), (4.5), (4.6), (4.9), (4.13)-(4.14) into Eq. (4.15), the following integral equation is derived for the scattered potential ϕ_1^S in region R_1 as

$$\begin{aligned}
&-\frac{1}{2}\phi_1^S+\int_{\Gamma_1}\left(\frac{\partial G}{\partial n}-\mathrm{i}k_0G\right)\phi_1^S d\Gamma+\int_{\Gamma_2}\frac{\partial G}{\partial n}\phi_1^S d\Gamma+\int_{\Gamma_3}\frac{\partial G}{\partial n}\phi_1^S d\Gamma\\
&+\int_{\Gamma_4}\left(\frac{\partial G}{\partial n}-KG\right)\phi_1^S d\Gamma+\int_{\Gamma_5\cup\Gamma_6\cup\Gamma_7}\frac{\partial G}{\partial n}\phi_1^S d\Gamma+\int_{\Gamma_8}\left(\frac{\partial G}{\partial n}-KG\right)\phi_1^S d\Gamma\\
&+\int_{\Gamma_9}\left(\phi_1^S\frac{\partial G}{\partial n}-G\frac{\partial\phi_1^S}{\partial n}\right)d\Gamma+\int_{\Gamma_{10}}\phi_1^S\frac{\partial G}{\partial n}d\Gamma+\mathrm{i}\omega\int_{\Gamma_{10}}G\zeta^S d\Gamma+\int_{\Gamma_{11}}\left(\phi_1^S\frac{\partial G}{\partial n}-G\frac{\partial\phi_1^S}{\partial n}\right)d\Gamma\\
&+\int_{\Gamma_{13}}\left(\frac{\partial G}{\partial n}-KG\right)\phi_1^S d\Gamma=\int_{\Gamma_1}\left(\frac{\partial\phi^I}{\partial n}-\mathrm{i}k_0\phi^I\right)Gd\Gamma.
\end{aligned} \tag{4.19}$$

Similarly, applying the boundary conditions (4.2), (4.6), and (4.9) into Eq. (4.15), the integral equation associated with the scattered velocity potential ϕ_2^S in region R_2 is given as

$$-\frac{1}{2}\phi_2^S + \int_{\Gamma_{11}} \left(\phi_1^S \frac{\partial G}{\partial n} + G\frac{\partial \phi_1^S}{\partial n}\right) d\Gamma + \int_{\Gamma_{10}} \phi_2^S \frac{\partial G}{\partial n} d\Gamma - \mathrm{i}\omega \int_{\Gamma_{10}} G\zeta^S d\Gamma + \int_{\Gamma_9} \left(\phi_1^S \frac{\partial G}{\partial n} + G\frac{\partial \phi_1^S}{\partial n}\right) d\Gamma + \int_{\Gamma_{12}} \left(\frac{\partial G}{\partial n} - KG\right) \phi_2^S d\Gamma = 0. \tag{4.20}$$

In a similar manner, using the boundary conditions (4.3), (4.5), (4.6), (4.9), (4.13)-(4.14) into Eq. (4.15), the following integral equation is derived for the radiated velocity potential ϕ_1^R in R_1 as

$$\begin{aligned}
&-\frac{1}{2}\phi_1^R + \int_{\Gamma_1} \left(\frac{\partial G}{\partial n} - \mathrm{i}k_0 G\right) \phi_1^R d\Gamma + \int_{\Gamma_2} \frac{\partial G}{\partial n}\phi_1^R d\Gamma + \int_{\Gamma_3} \frac{\partial G}{\partial n}\phi_1^R d\Gamma \\
&+ \int_{\Gamma_4} \left(\frac{\partial G}{\partial n} - KG\right) \phi_1^R d\Gamma + \int_{\Gamma_5 \cup \Gamma_6 \cup \Gamma_7} \frac{\partial G}{\partial n}\phi_1^R d\Gamma + \int_{\Gamma_8} \left(\frac{\partial G}{\partial n} - KG\right) \phi_1^R d\Gamma \\
&+ \int_{\Gamma_9} \left(\phi_1^R \frac{\partial G}{\partial n} - G\frac{\partial \phi_1^R}{\partial n}\right) d\Gamma + \int_{\Gamma_{10}} \phi_1^R \frac{\partial G}{\partial n} d\Gamma + \mathrm{i}\omega \int_{\Gamma_{10}} G\zeta^R d\Gamma \\
&+ \int_{\Gamma_{11}} \left(\phi_1^R \frac{\partial G}{\partial n} - G\frac{\partial \phi_1^R}{\partial n}\right) d\Gamma + \int_{\Gamma_{13}} \left(\frac{\partial G}{\partial n} - KG\right) \phi_1^R d\Gamma = \int_{\Gamma_4} G d\Gamma.
\end{aligned} \tag{4.21}$$

On the other hand, using the boundary conditions (4.2), (4.6), and (4.9) into Eq. (4.15), the integral equation for the radiated velocity potential ϕ_2^R in R_2 is obtained as

$$-\frac{1}{2}\phi_2^R + \int_{\Gamma_{11}} \left(\phi_1^R \frac{\partial G}{\partial n} + G\frac{\partial \phi_1^R}{\partial n}\right) d\Gamma + \int_{\Gamma_{10}} \phi_2^R \frac{\partial G}{\partial n} d\Gamma - \mathrm{i}\omega \int_{\Gamma_{10}} G\zeta^R d\Gamma + \int_{\Gamma_9} \left(\phi_1^R \frac{\partial G}{\partial n} + G\frac{\partial \phi_1^R}{\partial n}\right) d\Gamma + \int_{\Gamma_{12}} \left(\frac{\partial G}{\partial n} - KG\right) \phi_2^R d\Gamma = 0. \tag{4.22}$$

Now, Eqs. (4.19)-(4.22) are solved numerically using the BEM-based solution approach. For the execution of BEM, the boundaries of each region R_j for $j = 1, 2$ are discretized into a finite number of straight-line segments referred to as boundary elements in a counter-clockwise sense. The values of $\phi_j^{S,R}$ and their normal derivatives $\partial\phi_j^{S,R}/\partial n$ are assumed to be constants over each element and equal to the value at the mid-element node (see Katsikadelis [112]). With these

assumptions, the discretized form of the system of integral Eqs. (4.19)-(4.22) can be written as

$$\sum_{j=1}^{N_1}\left(H^{ij}-\mathrm{i}k_0G^{ij}\right)\phi_{1j}^{S}\big|_{\Gamma_1}+\sum_{j=1}^{N_2}H^{ij}\phi_{1j}^{S}\big|_{\Gamma_2}+\sum_{j=1}^{N_3}H^{ij}\phi_{1j}^{S}\big|_{\Gamma_3}+\sum_{j=1}^{N_4}\left(H^{ij}-KG^{ij}\right)\phi_{1j}^{S}\big|_{\Gamma_4}$$
$$+\sum_{j=1}^{N_5+N_6+N_7}H^{ij}\phi_{1j}^{S}\big|_{\Gamma_5\cup\Gamma_6\cup\Gamma_7}+\sum_{j=1}^{N_8}\left(H^{ij}-KG^{ij}\right)\phi_{1j}^{S}\big|_{\Gamma_8}+\sum_{j=1}^{N_9}\left(\phi_{1j}^{S}H^{ij}-G^{ij}\frac{\partial\phi_{1j}^{S}}{\partial n}\right)\Bigg|_{\Gamma_9}$$
$$+\sum_{j=1}^{N_{10}}\phi_{1j}^{S}H^{ij}\big|_{\Gamma_{10}}+\mathrm{i}\omega\sum_{j=1}^{N_{10}}G^{ij}\zeta_j^{S}\big|_{\Gamma_{10}}+\sum_{j=1}^{N_{11}}\left(\phi_{1j}^{S}H^{ij}-G^{ij}\frac{\partial\phi_{1j}^{S}}{\partial n}\right)\Bigg|_{\Gamma_{11}}+$$
$$\sum_{j=1}^{N_{13}}\left(H^{ij}-KG^{ij}\right)\phi_{1j}^{S}\big|_{\Gamma_{13}}=\sum_{j=1}^{N_1}\left(\frac{\partial\phi_j^{I}}{\partial n}-\mathrm{i}k_0\phi_j^{I}\right)G^{ij}\Bigg|_{\Gamma_1},\tag{4.23}$$

$$\sum_{j=1}^{N_{11}}\left(H^{ij}\phi_{1j}^{S}+G^{ij}\frac{\partial\phi_{1j}^{S}}{\partial n}\right)\Bigg|_{\Gamma_{11}}+\sum_{j=1}^{N_{10}}\phi_{2j}^{S}H^{ij}\big|_{\Gamma_{10}}-\mathrm{i}\omega\sum_{j=1}^{N_{10}}G^{ij}\zeta_j^{S}\big|_{\Gamma_{10}}$$
$$+\sum_{j=1}^{N_9}\left(H^{ij}\phi_{1j}^{S}+G^{ij}\frac{\partial\phi_{1j}^{S}}{\partial n}\right)\Bigg|_{\Gamma_9}+\sum_{j=1}^{N_{12}}\left(H^{ij}-KG^{ij}\right)\phi_{2j}^{S}\big|_{\Gamma_{12}}=0,\tag{4.24}$$

$$\sum_{j=1}^{N_1}\left(H^{ij}-\mathrm{i}k_0G^{ij}\right)\phi_{1j}^{R}\big|_{\Gamma_1}+\sum_{j=1}^{N_2}H^{ij}\phi_{1j}^{R}\big|_{\Gamma_2}+\sum_{j=1}^{N_3}H^{ij}\phi_{1j}^{R}\big|_{\Gamma_3}+\sum_{j=1}^{N_4}\left(H^{ij}-KG^{ij}\right)\phi_{1j}^{R}\big|_{\Gamma_4}$$
$$+\sum_{j=1}^{N_5+N_6+N_7}H^{ij}\phi_{1j}^{R}\big|_{\Gamma_5\cup\Gamma_6\cup\Gamma_7}+\sum_{j=1}^{N_8}\left(H^{ij}-KG^{ij}\right)\phi_{1j}^{R}\big|_{\Gamma_8}+\sum_{j=1}^{N_9}\left(\phi_{1j}^{R}H^{ij}-G^{ij}\frac{\partial\phi_{1j}^{R}}{\partial n}\right)\Bigg|_{\Gamma_9}$$
$$+\sum_{j=1}^{N_{10}}\phi_{1j}^{R}H^{ij}\big|_{\Gamma_{10}}+\mathrm{i}\omega\sum_{j=1}^{N_{10}}G^{ij}\zeta_j^{R}\big|_{\Gamma_{10}}+\sum_{j=1}^{N_{11}}\left(\phi_{1j}^{R}H^{ij}-G^{ij}\frac{\partial\phi_{1j}^{R}}{\partial n}\right)\Bigg|_{\Gamma_{11}}$$
$$+\sum_{j=1}^{N_{13}}\left(H^{ij}-KG^{ij}\right)\phi_{1j}^{R}\big|_{\Gamma_{13}}=\sum_{j=1}^{N_4}G^{ij}\big|_{\Gamma_4},\tag{4.25}$$

$$\sum_{j=1}^{N_{11}}\left(H^{ij}\phi_{1j}^{R}+G^{ij}\frac{\partial\phi_{1j}^{R}}{\partial n}\right)\Bigg|_{\Gamma_{11}}+\sum_{j=1}^{N_{10}}\phi_{2j}^{R}H^{ij}\big|_{\Gamma_{10}}-\mathrm{i}\omega\sum_{j=1}^{N_{10}}G^{ij}\zeta_j^{R}\big|_{\Gamma_{10}}$$
$$+\sum_{j=1}^{N_9}\left(H^{ij}\phi_{1j}^{R}+G^{ij}\frac{\partial\phi_{1j}^{R}}{\partial n}\right)\Bigg|_{\Gamma_9}+\sum_{j=1}^{N_{12}}\left(H^{ij}-KG^{ij}\right)\phi_{2j}^{R}\big|_{\Gamma_{12}}=0,\tag{4.26}$$

where

$$H^{ij}=-\frac{1}{2}\delta_{ij}+\int_{\Gamma_j}\frac{\partial G}{\partial n}d\Gamma,\quad G^{ij}=\int_{\Gamma_j}Gd\Gamma,\tag{4.27}$$

are termed as the influence coefficients. For $i=j$, i.e., when the source point $Q(\tilde{x},\tilde{z})$ and the field point $P(x,z)$ lies on the same boundary element, the influence coefficients H^{ij} and G^{ij} are

evaluated analytically. On the other hand, for $i \neq j$, i.e., when the source point $Q(\varsigma, \eta)$ and the field point $P(x, z)$ lies on different boundary element, the Gauss quadrature formulae is adopted to evaluate the influence coefficient H^{ij} and G^{ij} (see Katsikadelis [112] for details). Further, the point collocation method is employed to generate a number of equations equal to the number of unknowns. At this point, it is worthy of being mentioned that Eqs. (4.23)-(4.26) contain the unknown plate deflection $\zeta_j^{S,R}$. To overcome this problem, the plate dynamic boundary condition (4.7) is discretized using central difference formulae as given below

$$\left(\frac{\zeta_{j+2}^{S,R} - 4\zeta_{j+1}^{S,R} + 6\zeta_j^{S,R} - 4\zeta_{j-1}^{S,R} + \zeta_{j-2}^{S,R}}{\Delta_j^4}\right) + A\zeta_j^{S,R} = B\left(\phi_{1j}^{S,R} - \phi_{2j}^{S,R}\right). \tag{4.28}$$

Here, $A = \dfrac{-\omega^2\gamma}{g\chi\left(1 + \frac{\beta^2\xi\omega}{\mathrm{i}+\xi\omega}\right)}$, and $B = \dfrac{\mathrm{i}\omega}{g\chi\left(1 + \frac{\beta^2\xi\omega}{\mathrm{i}+\xi\omega}\right)}$. In a similar manner, the edge conditions of the plate as mentioned in Eqs. (4.10) and (4.11) can be written as

$$\zeta_j^{S,R} = 0, \quad \zeta_{j-1}^{S,R} = \zeta_{j+1}^{S,R}, \tag{4.29}$$

and

$$\zeta_{j+1}^{S,R} - 2\zeta_j^{S,R} + \zeta_{j-1}^{S,R} = 0, \quad \zeta_{j+2}^{S,R} - 2\zeta_{j+1}^{S,R} + 2\zeta_{j-1}^{S,R} - \zeta_{j-2}^{S,R} = 0. \tag{4.30}$$

Now, Eqs. (4.24)-(4.27), and (4.29)- (4.30) are solved together to get the unknown velocity potentials, their normal derivatives and plate deflections over each boundary element (see Koley [124] for details).

4.4 Parameters associated with the hybrid wave energy converter device

4.4.1 Wave power extraction by the OWC device

The average power absorbed P_{OWC} per unit width of the pressure distribution is given by

$$P_{OWC} = \frac{1}{2}\Re\{\overline{p}q\}. \tag{4.31}$$

Here, q and p are termed as the volume flux and pressure across the turbine, respectively. It is to be noted that the volume flux is assumed to be linearly proportional to the pressure across the turbine and therefore, we get the following relation

$$q = \wedge p, \tag{4.32}$$

where $\wedge$ is a control parameter. Finally, the expression for the average power absorbed P_{OWC} per unit width of the pressure distribution is given as

$$P_{OWC} = \frac{1}{2}\frac{\wedge |q^S|^2}{\left(\wedge + \tilde{B}\right)^2 + \tilde{A}^2}. \tag{4.33}$$

Here, q^S is termed as the volume flux associated with the scattered potential. Further, $\tilde{A}$ and $\tilde{B}$ are termed as the radiation susceptance and radiation conductance parameters, respectively. The detailed derivations are available in Koley and Trivedi [26], Trivedi and Koley [125], and the same are deferred here.

4.4.2 Wave power extraction by the piezoelectric plate

Wave power extracted by the piezoelectric plate can be evaluated as (see Zheng et al. [71] for details)

$$P_{plate} = \frac{\omega^2 \rho g}{2}\frac{\beta^2 \chi \xi}{1+\omega^2\xi^2}\int_c^{c+l_1}\left|\frac{\partial^2 \zeta}{\partial x^2}\right|^2 dx. \tag{4.34}$$

Further, the total plate deflection ζ consists of the scattered and radiated plate deflections. Now, applying (4.12) into (4.34), we get

$$P_{plate} = \frac{\omega^2 \rho g}{2}\frac{\beta^2 \chi \xi}{1+\omega^2\xi^2}\int_c^{c+l_1}\left|\frac{\partial^2}{\partial x^2}\left(\zeta^S + \left(\frac{\mathrm{i}\omega p}{\rho g}\right)\zeta^R\right)\right|^2 dx, \tag{4.35}$$

where $\dfrac{\partial^2 \zeta^S}{\partial x^2}$ and $\dfrac{\partial^2 \zeta^R}{\partial x^2}$ are evaluated employing central difference formulae.

4.4.3 Wave power extracted by the wave energy converter device consists of piezoelectric plate and OWC device

The total wave power extracted P_{Total} by the present wave energy converter device is the sum of power extracted by the OWC device P_{OWC} and the power extracted by the piezoelectric plate P_{plate}, and therefore, P_{Total} is calculated as

$$P_{Total} = P_{OWC} + P_{plate}. \tag{4.36}$$

4.5 Results

In the present study, to analyze the effect of various structural and seabed parameters on the hydrodynamic performance of the wave energy converter device consists of piezoelectric

plate and OWC device, the structural and seabed parameters are considered as: $h_1 = 10$m, $h_2/h_1 = 0.75$, $l_1/h_1 = 3.0$, $l/h_1 = 3.0$, $b/h_1 = 2.0$, $d_1/h_1 = 0.3$, $d_2/h_1 = 0.3$, $d/h_1 = 0.1$, $c/h_1 = 1.0$, $gp/h_1 = 0.5$ and $L = c + l_1 + gp + d + b$ unless otherwise mentioned. Further, the parameters associated with the waves are taken as follows: $g = 9.81$ kg/m^3, and $\rho = 1025$ kg/m^3, $A/h_1 = 0.1$. In the present analysis, the sinusoidally varying bottom profile is considered, and the corresponding profile is given in the following (see Koley and Trivedi [26],Koley [124] for details). The shape function for the bottom profile as in Eq. ((4.4)) is given as

$$\tilde{h}(x) = h_2 + h\left\{1 + 2\left(\frac{x}{L}\right)^3 - 3\left(\frac{x}{L}\right)^2 - \frac{a_1}{h}\sin\left(\frac{2m\pi x}{L}\right)\right\}, \tag{4.37}$$

where $h = h_1 - h_2$, a_1 is the amplitude of the ripples and m is the number of ripples. The bottom profile parameters are considered as $a_1/h_1 = 0.1$, and $m = 5.0$ unless otherwise mentioned. It is to be noted that the panel size in the BEM is judiciously taken by performing numerical convergence of the results obtained using BEM. The detailed procedure is available in Koley and Trivedi [26], Trivedi and Koley [125], and the same is deferred here.

4.5.1 Validation

Since there are no analytical and numerical results available in the literature for the present configuration of the wave energy converter device, the results associated with the performance of the OWC and piezoelectric plate are obtained independently as limiting cases of the present configuration, and the same are compared with the standard results available in the literature.

For this purpose, the present BEM-based numerical results of the piezoelectric plate are compared with the analytical solutions of Buriani and Renzi [126]. Further, to replicate the piezoelectric plate model of Buriani and Renzi [126], a limiting case of the present configuration is considered by choosing $b/h_1 \to 0.001$, $d_2/h_1 \to 0.001$ and bottom is considered as uniform in nature. In Fig. 4.2(a), the power extraction P_{plate} by the piezoelectric plate is plotted as a function of time period T of the incident waves. The results are compared with Fig. 4 of Buriani and Renzi [126]. Fig. 4.2(a) reveals that the present numerical results matched well with that of Buriani and Renzi [126].

Further, Fig. 4.2(b) demonstrates the comparison of the present BEM-based numerical results of the OWC device with the numerical solutions of Ning et al. [6]. In Fig. 4.2(b), the efficiency of the OWC device η is plotted as a function of the incident wavenumber Kh_1 for the case when the OWC device is placed over the sloping seabed with slopping angle $\beta = 16°$. To obtain the OWC device model of Ning et al. [6] (see Fig. 14 of Ning et al. [6]), a limiting case of the present model is considered by taking $l_1/h_2 \to 0.001$, and $d_1/h_2 \to 1.5$. Moreover, the remaining values of the device parameters are the same as provided in Ning et al. [6]. It is seen that the present BEM-based solution provides higher values of efficiency as compared to the results of Ning et al.

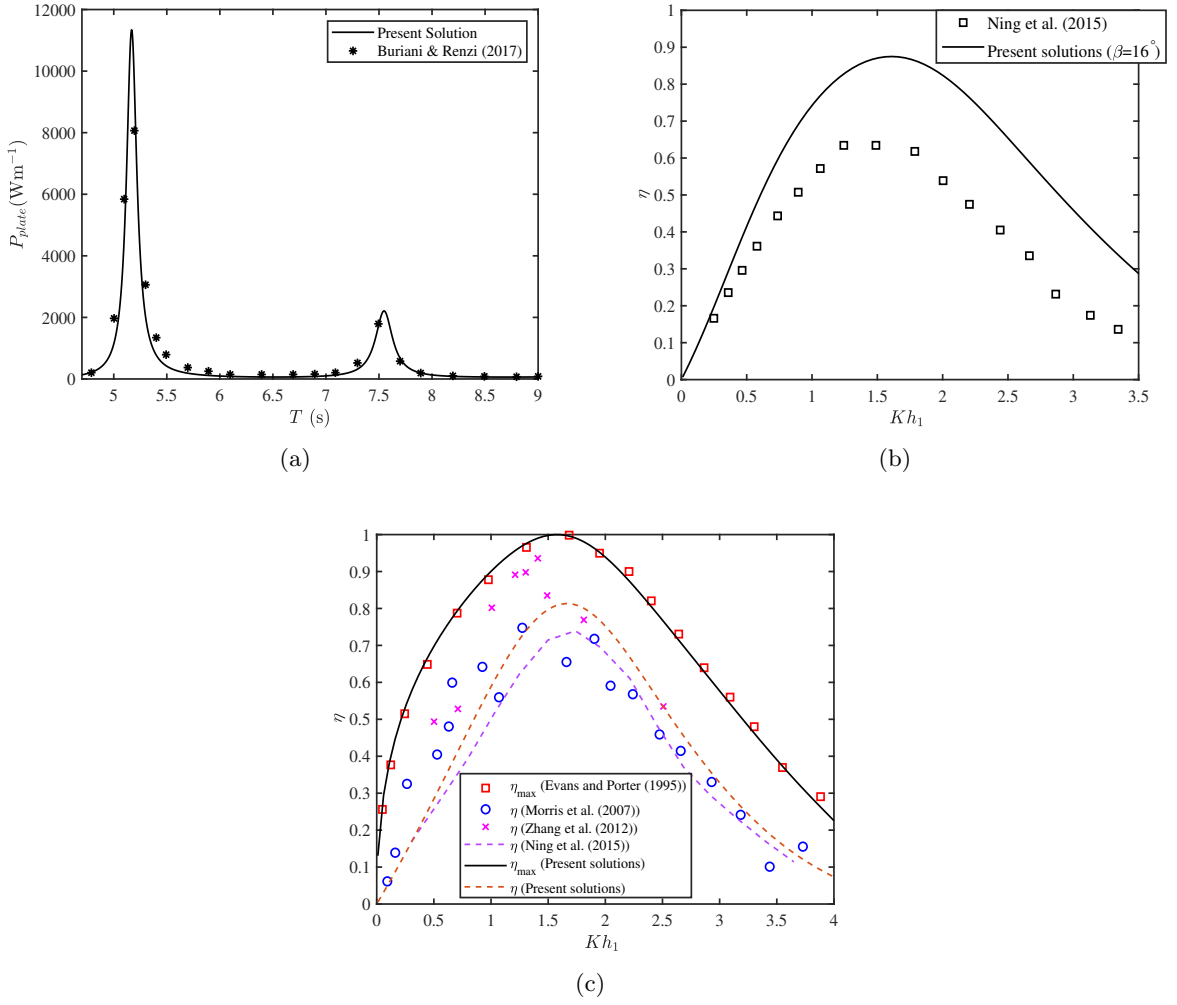

FIGURE 4.2: Variation of (a) power extraction P_{plate} by the piezoelectric plate as a function of incident wave period T, (b) η as a function wavenumber Kh_1 for sloping seabed with sloping angle $\beta = 16°$, and (c) η as function of Kh_1 in the presence of uniform seabed.

[6]. This happens as the present linear theory-based model doesn't take into account the effects of wave non-linearity and viscous dissipation. However, the resonant frequencies predicted by the present method and the nonlinear model of Ning et al. [6] agree well.

Fig. 4.2(c) provides the comparison between the linear analytical solutions Evans and Porter [5], experimental data Morris-Thomas et al. [127], numerical results based on the two-phase flow model Zhang et al. [128], higher-order boundary element method Ning et al. [6], and the present BEM-based numerical results. Here, the efficiency of the OWC device is plotted when placed over the uniform seabed. The values of shape and wave parameters associated with the OWC device are the same as given in Ning et al. [6]. In Fig. 4.2(c), it is seen that the maximum hydrodynamic efficiency of the OWC device using the present BEM method matches well with the results of Evans and Porter [5]. Moreover, it is seen that the present BEM-based hydrodynamic efficiency of the OWC device is higher as compared to the numerical results of

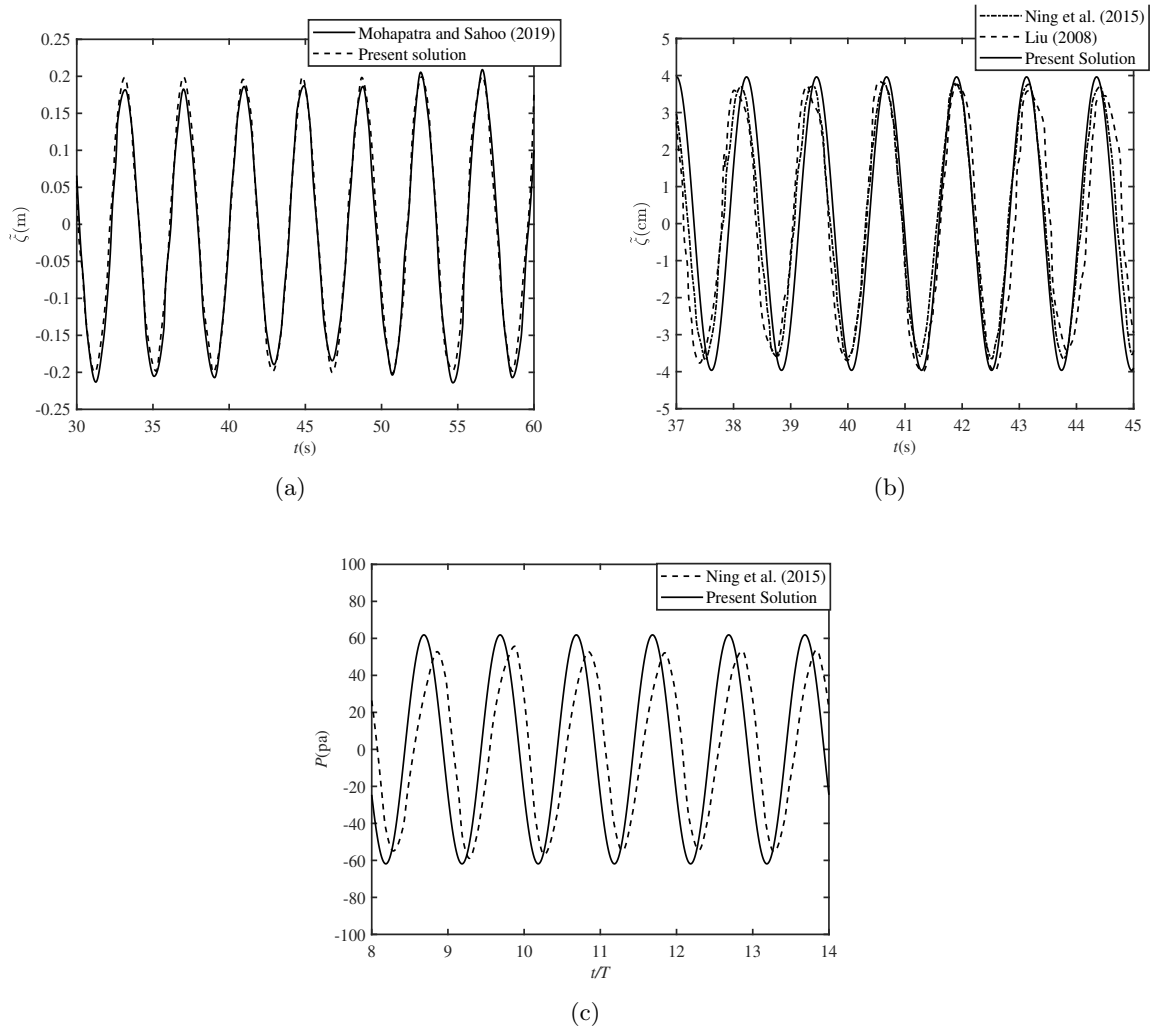

FIGURE 4.3: Time series of (a) free surface elevation outside the chamber, (b) free surface elevation at the chamber center, and (c) air pressure inside the OWC device chamber.

Ning et al. [6] due to the absence of wave non-linearity and viscous dissipation. However, the resonant frequencies predicted by the analytical method, HOBEM numerical method, and the proposed numerical model agree well. Furthermore, the general shapes of the hydrodynamic efficiency curves agree satisfactorily. In addition, the present results agree well with the results of Morris-Thomas et al. [127], and Zhang et al. [128]. In Figs. 4.3(a) and (b), the comparison between the present numerical results and the results of Mohapatra and Sahoo [129], Ning et al. [6] and Liu [130] are provided for specific cases. Further, the parameters associated with the OWC device chamber and seabed configurations are the same as mentioned in Mohapatra and Sahoo [129], Ning et al. [6] and Liu [130]. It is observed that the free surface elevations outside and inside the OWC device chamber obtained by the present method follow a similar pattern and show a good agreement with the results provided in Mohapatra and Sahoo [129], Ning et al. [6] and Liu [130]. The discrepancies are due to the comparison of present linear model-based results with that of the results obtained using nonlinear models (Mohapatra and Sahoo [129],

Ning et al. [6]), and experimental results (Liu [130]). Further, Fig. 4.3 (c) demonstrates the comparison between the air pressure inside the OWC device chamber obtained using the present model with that of HOBEM based model Ning et al. [6] for $Kh_1 = 2.93$, and the results show good agreement.

4.5.2 Results associated with the hydrodynamic performance of the standalone OWC device

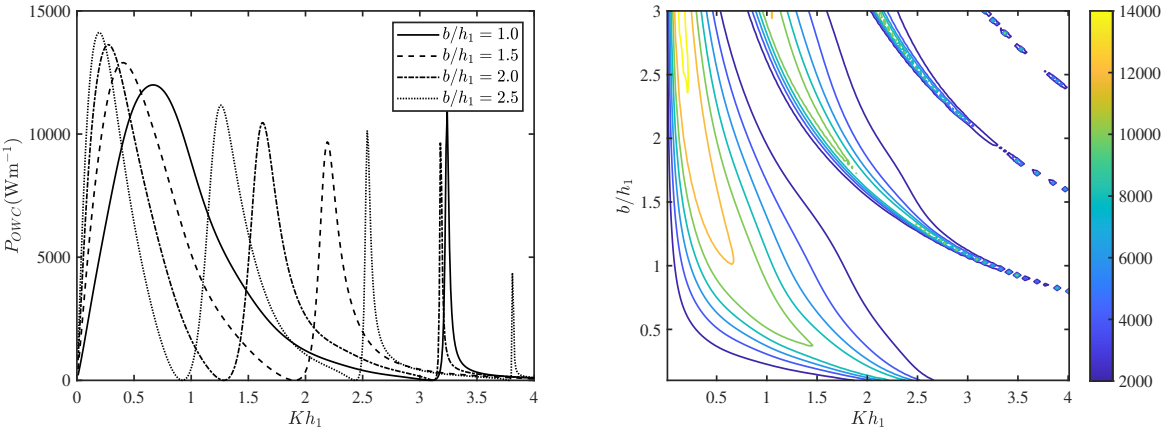

(a) (b)

FIGURE 4.4: (a) variation of P_{OWC} vs Kh_1 for various b/h_1, and (b) contour plot of P_{OWC} as a function of Kh_1 and b/h_1.

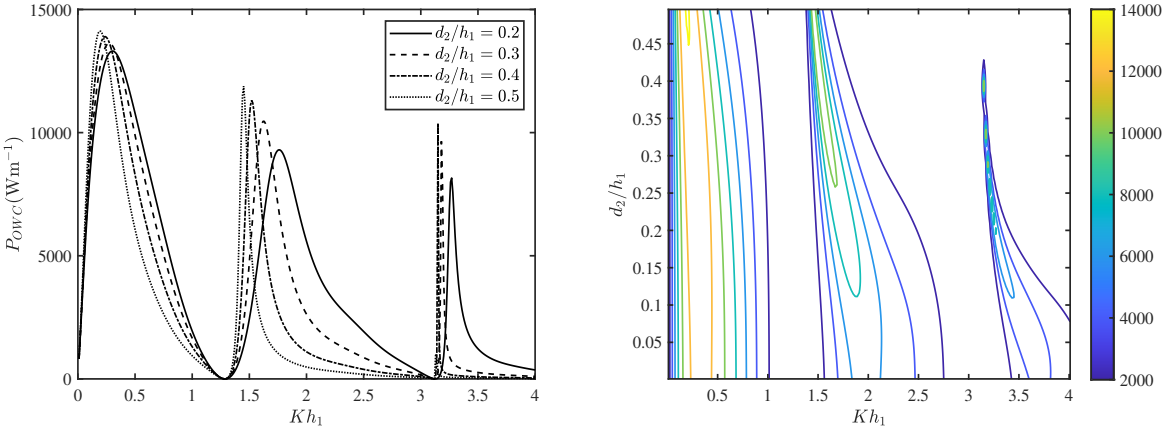

(a) (b)

FIGURE 4.5: (a) variation of P_{OWC} vs Kh_1 for various d_2/h_1, and (b) contour plot of P_{OWC} as a function of Kh_1 and d_2/h_1.

In Fig. 4.4(a), the variation of the power extraction P_{OWC} by the OWC device as a function of non-dimensional wavenumber Kh_1 is plotted for various chamber width b/h_1 of the OWC device. It is seen that the resonances in the power extraction P_{OWC} by the OWC device occur

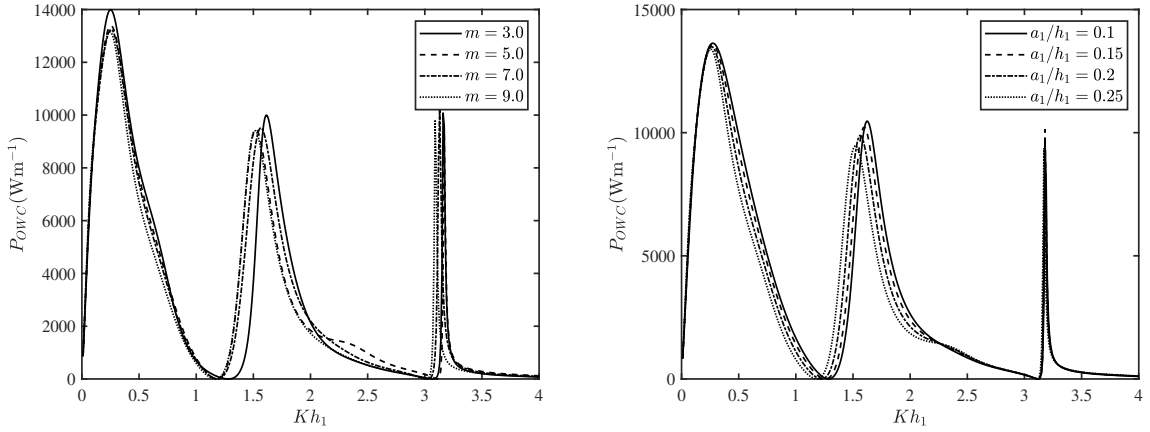

FIGURE 4.6: Variation of P_{OWC} vs Kh_1 for various (a) m, and (b) a_1/h_1.

for larger values of chamber width b/h_1 in the long-wave regime. Further, the same resonance occurs for smaller values of chamber width b/h_1 with an increase in wavenumber Kh_1. The reason behind this phenomenon is that as the chamber width increases, the wave particles have to travel more distance during one oscillation. Consequently, the resonant-piston-like motion inside the OWC device chamber is collapsed. A similar pattern can be accomplished by increasing the submergence depth d_2/h_1 of the front wall of the OWC device, which forces the water particles to travel a greater distance during a period of motion and thus directly impacts the resonance frequency of the first mechanism (Evans and Porter [5], Koley and Trivedi [26]). Similar observations were reported in Evans and Porter [5], Rezanejad et al. [7]. On the other hand, the amplitude of resonances is higher in the long-wave regime, whereas the amplitude of resonances decreases in the moderate and short-wave regimes. Moreover, these resonances arise due to the first and second resonance mechanisms, respectively (see Koley and Trivedi [26] for details about the first and second resonance mechanisms). To demonstrate the effect of the incident wavenumber Kh_1 and the chamber width b/h_1 of the OWC device on the power extraction P_{OWC}, a contour plot of P_{OWC} as a function of Kh_1 and b/h_1 is given in Fig. 4.4(b). It is seen that the power extraction P_{OWC} by the OWC device is higher for the moderate and higher values of the chamber width in the long wave regime.

Fig. 4.5(a) demonstrates the variation of the power extraction P_{OWC} by the OWC device as a function of non-dimensional wavenumber Kh_1 for different submergence depth d_2/h_1 of the front wall of the OWC device. It is seen that the resonance occurs in the P_{OWC} curve for smaller values of incident wavenumber Kh_1 with an increase in submergence depth d_2/h_1 of the front wall of the device. These resonances occur in the long-wave regime due to the first resonance mechanism (see Evans and Porter [5], Koley and Trivedi [26] for details about the first resonance mechanism). Further, the second and subsequent peaks in the power extraction P_{OWC} by the OWC device arise in the intermediate and short wave regime due to the second

resonance mechanism (see Trivedi and Koley [125] for details). Moreover, it is observed that in the long and intermediate wave regimes, the amplitudes of resonances are higher for higher values of the submergence depth d_2/h_1 of the front wall of the device. In addition, it is seen that the area under the power extraction P_{OWC} curve is more for $d_2/h_1 = 0.2$. To analyze the effect of the submergence depth d_2/h_1 of the front wall of the device and incident wavenumber Kh_1 on the power extraction P_{OWC} by the OWC device, a contour plot of P_{OWC} as a function of Kh_1 and d_2/h_1 is provided in Fig. 4.5(b). It is seen that the resonances arise in the power extraction P_{OWC} for smaller incident wavenumber with an increase in submergence depth of the front wall of the OWC device.

Figs. 4.6(a) and (b) depict the change in power extraction P_{OWC} by the OWC device vs incident wavenumber Kh_1 for different number of ripples m and ripple amplitude a_1/h_1 associated with the sinusoidally varying bottom profile, respectively. In Fig. 4.6(a), it is seen that the resonating peaks in the power extraction curve take higher values for $m = 3$. On the other hand, Fig. 4.6(b) illustrates that significant variation in the power extraction P_{OWC} curve occurs due to the variation in the ripple amplitude a_1/h_1 of the seabed profile. Further, a closer look on Fig. 4.6(b) demonstrates that the amplitudes of the primary and secondary resonating peaks in the power extraction P_{OWC} curve are higher for smaller values of the ripple amplitude a_1/h_1 of the seabed. The reason behind the same is that as the ripple amplitude a_1/h_1 of the seabed profile increases, the distance between the free surface and undulated seabed decreases, which significantly influences the power extraction P_{OWC} by the OWC device. A similar observation was reported in Koley and Trivedi [26].

4.5.3 Results associated with the hydrodynamic performance of the standalone piezoelectric plate having fixed edges

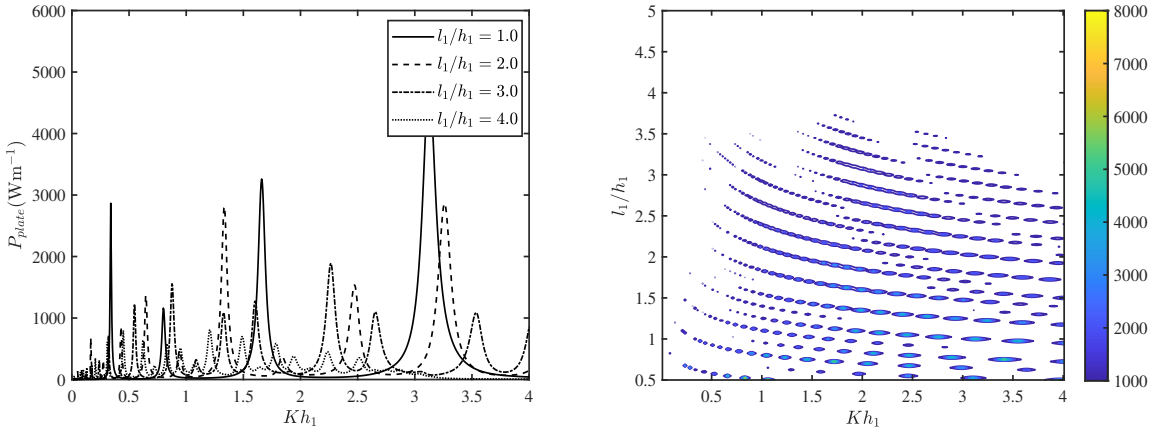

(a) (b)

FIGURE 4.7: Variation of (a) P_{plate} vs Kh_1 for various l_1/h_1, and (b) contour plot of P_{plate} as a function of Kh_1 and l_1/h_1.

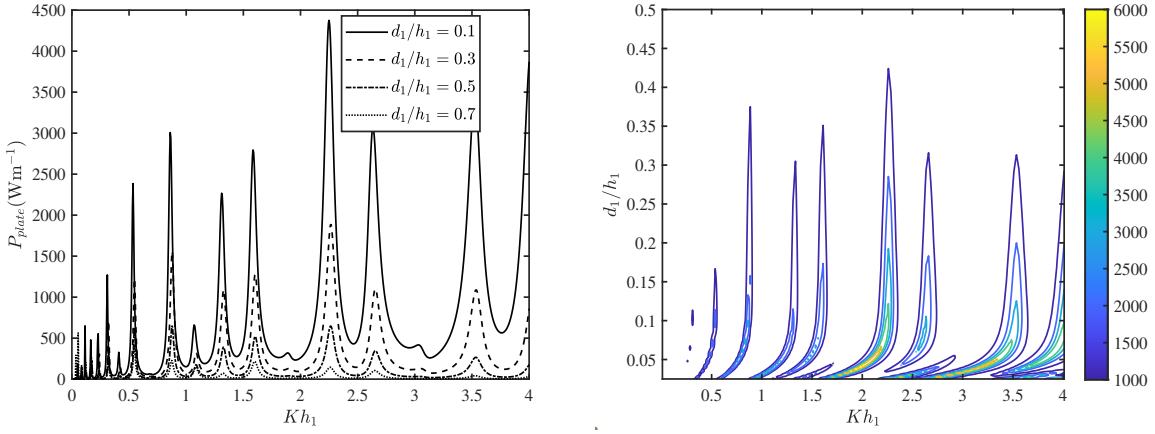

(a) (b)

FIGURE 4.8: (a) variation of P_{plate} vs Kh_1 for various d_1/h_1, and (b) contour plot of P_{plate} as a function of Kh_1 and d_1/h_1.

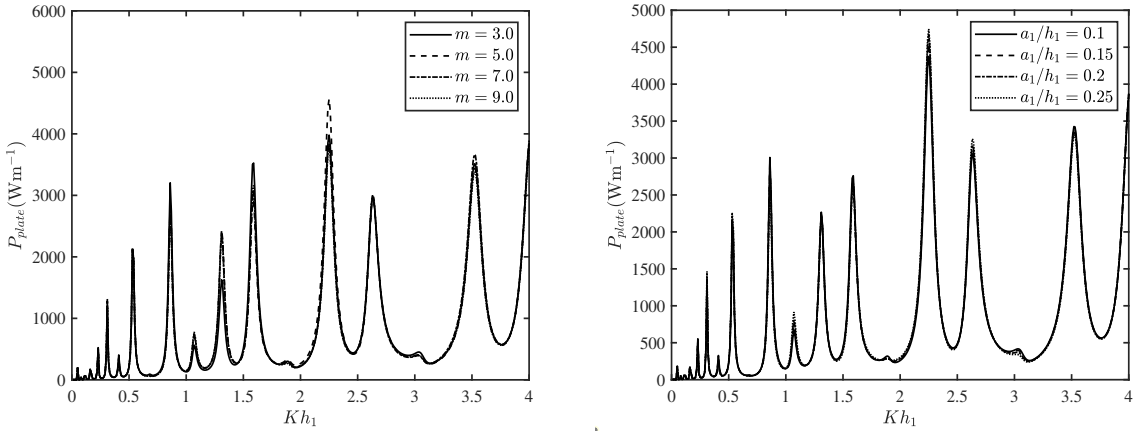

(a) (b)

FIGURE 4.9: Variation of P_{plate} vs Kh_1 for various (a) m, and (b) a_1/h_1.

In Figs. 4.7(a), the variation of the power extraction P_{plate} by the piezoelectric plate vs the non-dimensional wave number Kh_1 is plotted for various plate length l_1/h_1 of the piezoelectric plate. It is demonstrated that the number of peaks corresponding to the resonances of the power extraction P_{plate} curve increases with an increase in the plate length l_1/h_1 of the piezoelectric plate, whereas the amplitude of resonating peaks decreases with an increase in plate length l_1/h_1. The primary resonating peak in the P_{plate} curve occurs due to the fact that as the length of the piezoelectric plate increases, the frequencies associated with the natural vibration of the plate decrease, and consequently, there is a possibility that the natural frequency of the piezoelectric plate and the frequency of the hydroelastic wave is getting matched. Moreover, it is noticed that the amplitude of the resonance is higher for $l_1/h_1 = 1.0$ in the neighborhood of $2.5 < Kh_1 < 3.5$. To demonstrate the effect of the plate length l_1/h_1 and incident wavenumber Kh_1 on the power extraction P_{plate} by the piezoelectric plate, a contour plot of the power extraction P_{plate} by the

plate as a function of plate length l_1/h_1 and wavenumber Kh_1 is provided in Fig. 4.7(b). It is seen that the power extraction P_{plate} by the piezoelectric plate is higher for the plate length having the range $0.5 \leq l_1/h_1 < 1.8$ in moderate and short wave regimes.

Fig. 4.8(a) illustrates the variation of the power extraction P_{plate} by the piezoelectric plate vs the non-dimensional wave number Kh_1 for various submergence depth d_1/h_1 of the piezoelectric plate. The amplitude of the resonances in the P_{plate} curve increases with a decrease in submergence depth d_1/h_1 of the piezoelectric plate. The reason behind this phenomenon is that for smaller values of d_1/h_1, the distance between the free surface and the piezoelectric plate decreases, and consequently, the interaction of the dense wave energy near the free surface with the piezoelectric plate increases. As a result, a higher amount of wave power is extracted by the piezoelectric plate. Moreover, it is also reported that the resonances in the P_{plate} curve occur around the same values of incident wavenumber irrespective of the variations in the submergence depth d_1/h_1 of the piezoelectric plate. To demonstrate the effect of the incident wavenumber Kh_1 and the submergence depth d_1/h_1 of the piezoelectric plate on the power extraction P_{plate}, a contour plot of P_{plate} as a function of Kh_1 and d_1/h_1 is provided in Fig. 4.8(b). It is found that the resonances in the power extraction P_{plate} by the piezoelectric plate occur for intermediate and higher values of wavenumber Kh_1 when the piezoelectric plate is placed near to the mean free surface $z = 0$.

In Figs. 4.9(a) and (b), the variation of the power extraction P_{plate} by the piezoelectric plate is plotted as a function of wavenumber Kh_1 for the various number of ripples m, and the ripple amplitude a_1/h_1 of the sinusoidally varying bed profile, respectively. In both the figures, it is observed that the resonances in the power extraction P_{plate} curve occur for the same wavenumber Kh_1 irrespective of the variation in the number of ripples m and the ripple amplitude a_1/h_1. This happens due to the fact that the natural frequency of the piezoelectric plate does not alter with the variations in the parameters associated with the seabed profiles. Further, it is noticed that the height of the resonating peaks in the power extraction P_{plate} increases as the number of ripples m decreases. In Fig. 4.9(b), it is seen that the amplitude of the resonances in the power extraction P_{plate} increases with an increase in ripple amplitude a_1/h_1 within a certain range of incident wavenumbers Kh_1. This phenomenon happens as the ripple amplitude a_1/h_1 of the undulated seabed increases, and the distance between the submerged piezoelectric plate and undulated seabed decreases. As a result, undulated seabed significantly influences the power extraction P_{plate} by the piezoelectric plate.

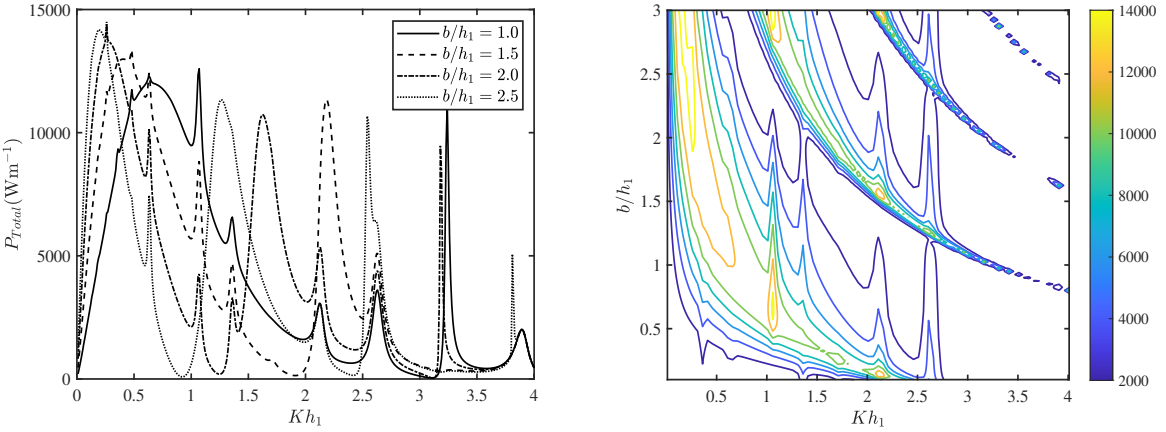

(a) (b)

FIGURE 4.10: (a) variation of P_{Total} vs Kh_1 for various b/h_1, and (b) contour plot of P_{Total} as a function of Kh_1 and b/h_1.

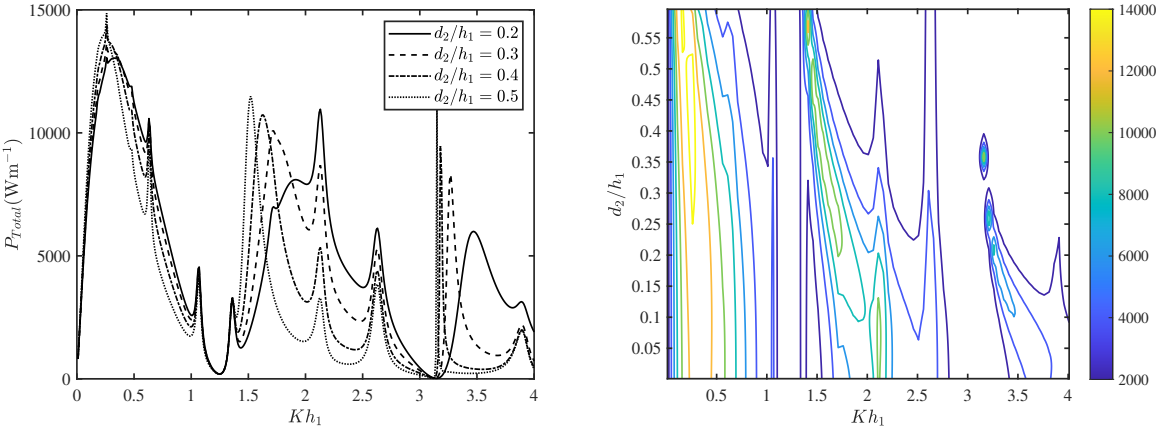

(a) (b)

FIGURE 4.11: (a) variation of P_{Total} vs Kh_1 for various d_2/h_1, and (b) contour plot of P_{Total} as a function of Kh_1 and d_2/h_1.

4.5.4 Results associated with the hydrodynamic performance of hybrid wave energy converter device consists of piezoelectric plate (fixed edges) and OWC device

Fig. 4.10(a) illustrates the effect of various chamber width b/h_1 on the power extraction P_{Total} by the hybrid wave energy converter device consisting of a piezoelectric plate and the OWC device. The overall pattern of the power extraction P_{Total} curve, as shown in Fig. 4.10(a) is similar to the observation as seen in Fig. 4.4(a). A comparison between Figs. 4.10(a) and 4.4(a) reveal that the power extraction P_{Total} by the hybrid wave energy converter device is more as compared to the power extraction P_{OWC} by the OWC device. The reason for the same is that some parts of the wave energy are absorbed by the piezoelectric plate in addition to the OWC

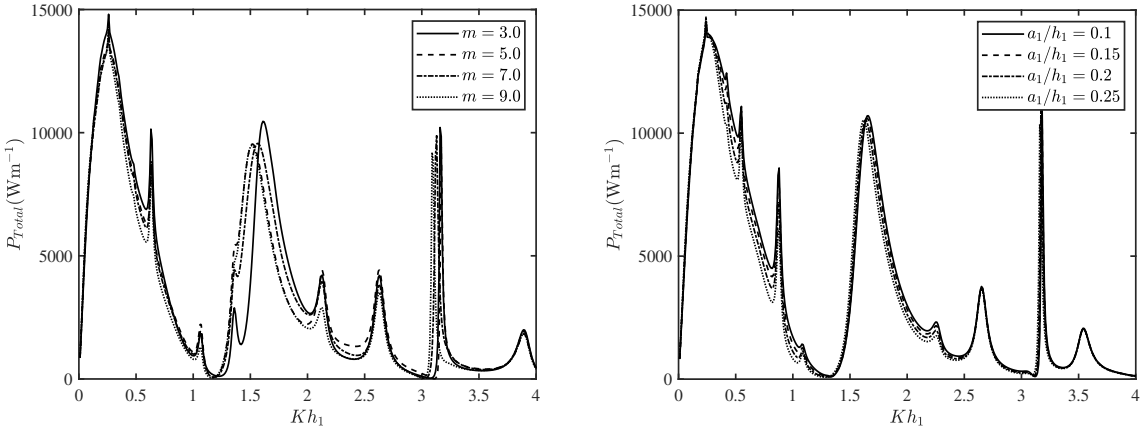

FIGURE 4.12: Variation of P_{Total} vs Kh_1 for various (a) m, and (b) a_1/h_1.

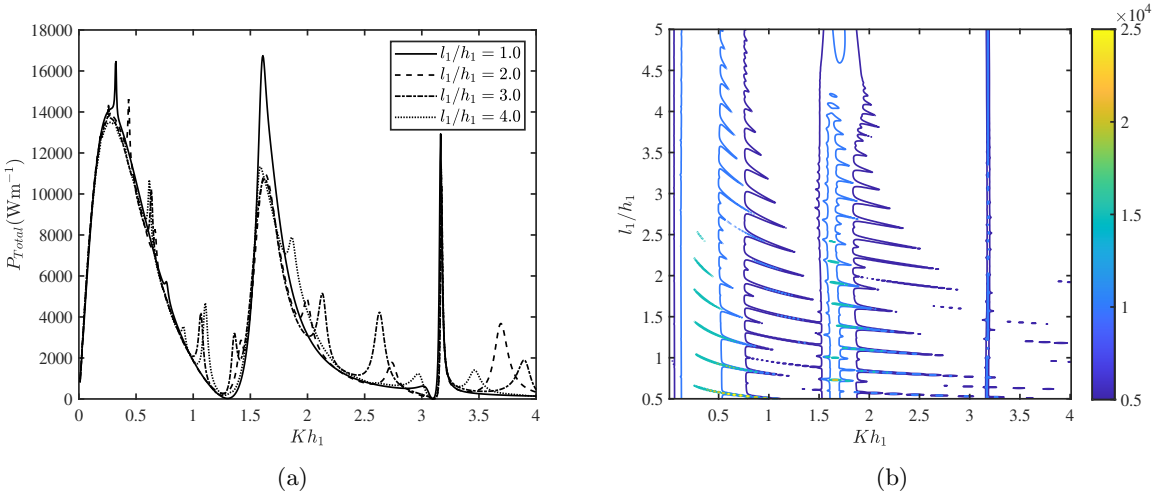

FIGURE 4.13: (a) variation of P_{Total} vs Kh_1 for various l_1/h_1, and (b) contour plot of P_{Total} as a function of Kh_1 and l_1/h_1.

device. As a result, the power extraction P_{Total} by the hybrid wave energy converter device is higher than the solely placed OWC device. To analyze the effect of the wavenumber Kh_1 and the chamber width b/h_1 of the OWC device on the power extraction P_{Total}, a contour plot of P_{Total} as a function of Kh_1 and b/h_1 is provided in Fig. 4.10(b). It is found that the power extraction P_{Total} by the hybrid wave energy converter device is higher for moderate and larger values of the chamber width b/h_1 in the long wave and intermediate wave regimes. A comparison of Fig. 4.10(b) with Figs. 4.4(b) and 4.7(b) reveal that the power extraction P_{Total} by the hybrid wave energy converter device is higher for a wider range of incident wave number Kh_1 as compared to the cases of solely present OWC device and piezoelectric plate. This happens due to the occurrences of multiple resonances in the P_{Total} curve when both the OWC device and piezoelectric plate are present. This particular result clearly demonstrates the effectiveness of the hybrid wave energy converter device over the standalone OWC and piezoelectric plate.

Figs. 4.11(a) and (b) depict the effect of the submergence depth d_2/h_1 of the front wall of the OWC device on the power extraction P_{Total} by the hybrid wave energy converter device consisting of a piezoelectric plate and the OWC device. The overall resonating pattern of the power extraction P_{Total} by the hybrid wave energy converter device due to the variation in wavenumber Kh_1 as shown in Fig. 4.11(a) is similar in nature to that of Fig. 4.5(a). Further, careful observation reveals that the number of resonating peaks in the power extraction P_{Total} curve is more as compared to the power extraction P_{OWC} in Fig. 4.5(a). The reason for the same is that multiple resonances occur in the power extraction P_{Total} due to the combined effect of the OWC device and the piezoelectric plate. A comparison between Figs. 4.11(a) and 4.5(a) reveals that the power extraction P_{Total} by the hybrid wave energy converter device is more as compared to the power extraction P_{OWC} by the standalone OWC device. The reason for the same is already provided in the discussion of Fig. 4.10(a). In Fig. 4.11(b), the contour plot of the power extraction P_{Total} by the hybrid wave energy converter device is plotted as functions of the incident wavenumber Kh_1 and submergence depth d_2/h_1 of the front wall of the OWC device. It is clearly seen that the hybrid wave energy converter device generates a higher amount of wave power P_{Total} for a wider range of frequencies Kh_1 and submergence depth d_2/h_1 as compared to the cases of standalone OWC device and piezoelectric plate.

The effect of the sinusoidally varying bottom undulation on the power extraction P_{Total} by the hybrid wave energy converter device is demonstrated in Figs. 4.12(a) and 4.12(b). Fig. 4.12(a) depicts that the power extraction P_{Total} by the hybrid wave energy converter device varies significantly due to the variation in the number of ripples m of the seabed. In addition, the resonating peak amplitude in the P_{Total} curve is higher for the number of ripples $m = 3$. On the other hand, in Fig. 4.12(b), it is noticed that the ripple amplitude a_1/h_1 of the undulated seabed significantly influences the power extraction P_{Total} by the hybrid wave energy converter device in the long wave regime. The reason for the same is provided in the discussion of Fig. 4.6(b).

In Fig. 4.13(a), the variation of the power extraction P_{Total} by the hybrid wave energy converter device consisting of a piezoelectric plate and the OWC device is plotted as a function of incident wavenumber Kh_1 for various values of plate length l_1/h_1 of the piezoelectric plate. It is to be noted that the overall resonating pattern of Fig. 4.13(a) is similar to that of Fig. 4.10(a). Further, it is found that the number of resonating peaks in the power extraction P_{Total} increases, and the amplitude of the resonating peaks reduces gradually as the plate length l_1/h_1 of the piezoelectric plate increases. A similar observation was found in Fig. 4.7(a). The reason for this phenomenon is already mentioned in the discussion of Fig. 4.7(a). A comparison between Figs. 4.13(a) and 4.7(a) reveal that the power extraction P_{Total} by the hybrid wave energy converter device is significantly higher as compared to the power extraction P_{plate} by the piezoelectric plate. The reason behind this phenomenon is that a major part of the incident wave energy that the piezoelectric plate is not able to capture can be captured by the OWC device. As a result, the hybrid wave energy converter device extracts more power as compared to the standalone

piezoelectric plate. To demonstrate the effect of the wavenumber Kh_1 and the plate length l_1/h_1 of the piezoelectric plate on the power extraction P_{Total} by the hybrid wave energy converter device, a contour plot of P_{Total} as functions of Kh_1 and l_1/h_1 is provided in Fig. 4.13(b). A comparison between Figs. 4.13(b), and 4.7(b) depicts that the power extraction P_{Total} by the hybrid wave energy converter device having small plate length l_1/h_1 is more for smaller and moderate wavenumber Kh_1.

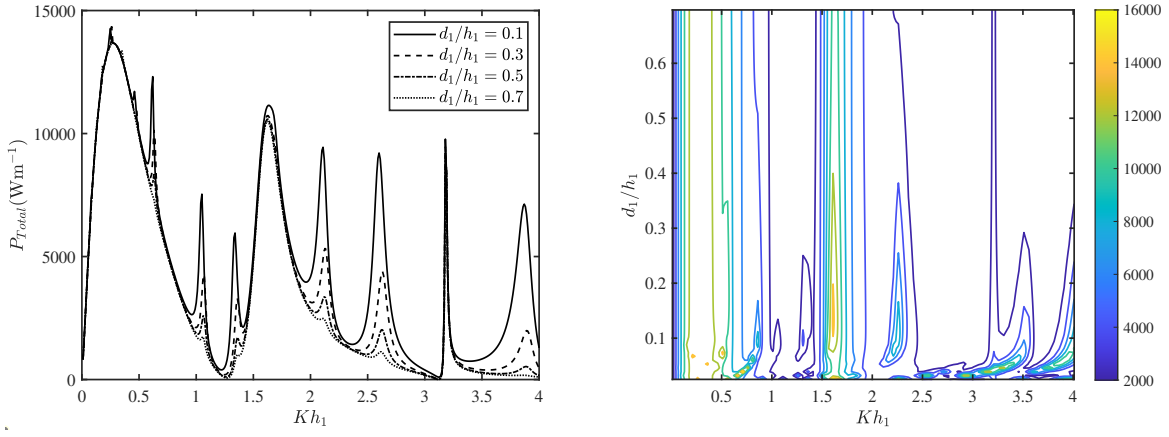

FIGURE 4.14: (a) variation of P_{Total} vs Kh_1 for various d_1/h_1, and (b) contour plot of P_{Total} as a function of Kh_1 and d_1/h_1.

Fig. 4.14(a) illustrates the variation of the power extraction by the hybrid wave energy converter device P_{Total} as a function of incident wavenumber Kh_1 for various values of submergence depth d_1/h_1 of the piezoelectric plate. The overall pattern of the power extraction curve P_{Total} as seen in Fig. 4.14(a) is similar in nature to that of Fig. 4.11(a). Further, it is seen that the amplitude of the resonance in the power extraction P_{Total} by the hybrid wave energy converter device is higher when the piezoelectric plate is situated near the free surface $z = 0$. The reason for the same is already provided in the discussion of Fig. 4.8(a). A comparison between Figs. 4.14(a) and 4.8(a) reveal that the power extraction P_{Total} by the hybrid wave energy converter device is significantly higher as compared to the power extraction P_{plate} by the standalone piezoelectric plate. The reason for the same is already provided in the discussion of Fig. 4.13(a). In Fig. 4.14(b), the contour plot of the power extraction P_{Total} by the hybrid wave energy converter device is plotted as functions of the incident wavenumber Kh_1 and submergence depth d_1/h_1 of the piezoelectric plate. It is seen that the hybrid wave energy converter device extracts a higher amount of wave power P_{Total} for long and intermediate wave regimes when the submergence depth d_1/h_1 is smaller as compared to the cases of the isolated OWC devices and piezoelectric plates.

In Fig. 4.15(a), the variation of the power extraction P_{Total} by the hybrid wave energy converter is plotted as a function of wavenumber Kh_1 for various gap length between the piezoelectric

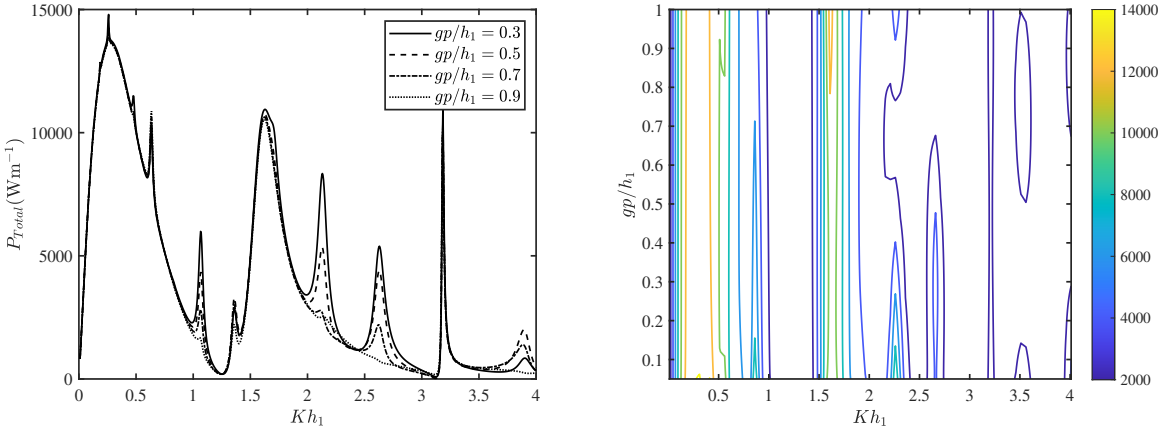

FIGURE 4.15: (a) variation of P_{Total} vs Kh_1 for various gp/h_1, and (b) contour plot of P_{Total} as a function of Kh_1 and gp/h_1.

plate and the OWC device gp/h_1. The overall pattern of the power extraction P_{Total} curve as shown in Fig. 4.15(a) is similar to the observation as seen in Fig. 4.14(a). It is demonstrated that the resonances in the power extraction P_{Total} curve occur for the same wavenumber Kh_1 irrespective of the variation in the gap length between the piezoelectric plate and the OWC device. This happens due to the fact that the natural frequency of the piezoelectric plate does not alter with the variations in the gap length between the piezoelectric plate and the OWC device. Further, it is observed that the amplitude of the resonating peaks is higher for smaller values of gp/h_1. The reason for the same is that as the gap length gp/h_1 between the piezoelectric plate and the OWC device increases, the higher amount of incident wave energy is absorbed by the piezoelectric plate, and a tranquility zone will be created in between the piezoelectric plate and the OWC device. As a result, the amplitude of the power extraction P_{Total} curve decreases with an increase in gap length gp/h_1. To illustrate the effect of the wavenumber Kh_1 and the gap length gp/h_1 on the power extraction P_{Total} by the hybrid wave energy converter device, a contour plot of P_{Total} as functions of Kh_1 and gp/h_1 is provided in Fig. 4.15(b). It is noticed that the power extraction P_{Total} by the hybrid wave energy converter device is higher in the long wave and intermediate wave regimes irrespective of the variation in gap length gp/h_1.

4.5.5 Results associated with the hydrodynamic performance of the piezoelectric plate having seaside free edge and shore side fixed edge

In Fig. 4.16(a), the variation of the power extraction P_{plate} by the piezoelectric plate vs the non-dimensional wave number Kh_1 is plotted for various plate length l_1/h_1 of the piezoelectric plate. The associated surface plot is provided in Fig. 4.16(b). The overall pattern of the P_{plate} curve in Fig. 4.16 is the same as in Fig. 4.7. A comparison between Figs. 4.16 and 4.7 reveal

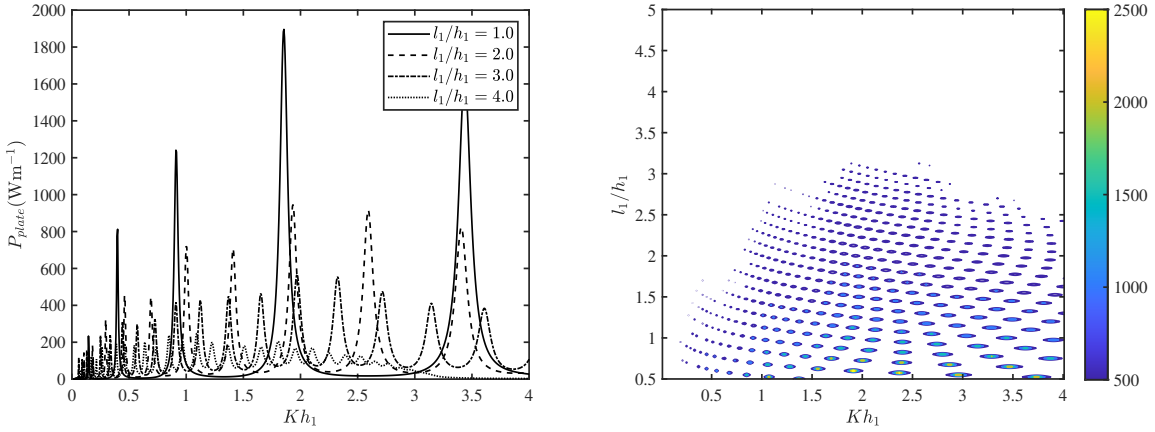

(a) (b)

FIGURE 4.16: (a) variation of P_{plate} vs Kh_1 for various l_1/h_1, and (b) contour plot of P_{plate} as a function of Kh_1 and l_1/h_1.

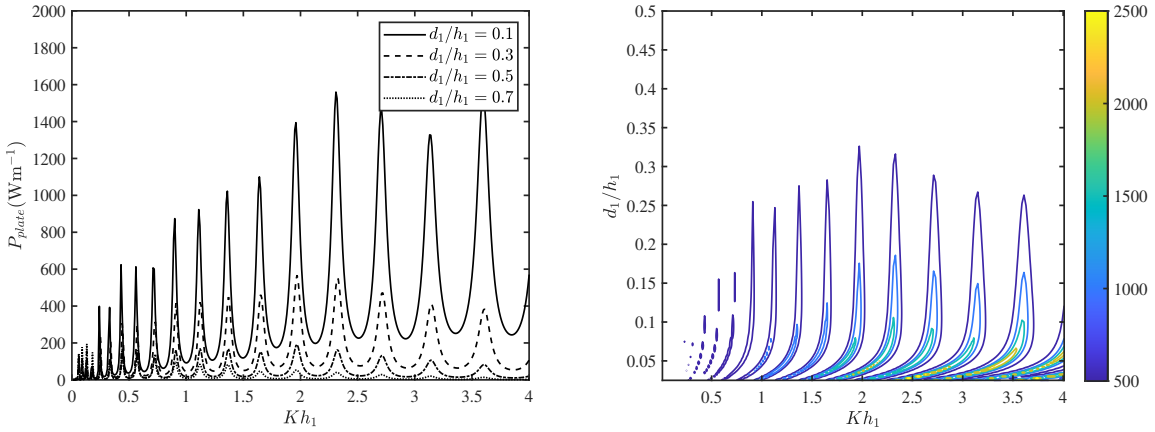

(a) (b)

FIGURE 4.17: (a) variation of P_{plate} vs Kh_1 for various d_1/h_1, and (b) contour plot of P_{plate} as a function of Kh_1 and d_1/h_1.

that the number of resonating peaks is higher when the front edge of the piezoelectric plate is free. This is due to the reason that the more the plate edges are constrained, the stiffness of the plate increases. Consequently, the resonance occurs at larger wave frequencies. Similar results were reported in Zheng et al. [71]. On the other hand, the amplitudes of the resonating peaks P_{plate} are higher for a piezoelectric plate having a fixed seaside edge as compared to a free seaside edge.

Fig. 4.17(a) demonstrates the variation of the power extraction P_{plate} by the piezoelectric plate vs the non-dimensional wave number Kh_1 for various submergence depth d_1/h_1 of the piezoelectric plate. The associated surface plot is provided in Fig. 4.17(b). The overall pattern of Fig. 4.17 is similar to that of Fig. 4.8. A comparison between Figs. 4.17 and 4.8 reveals that the number of

resonating peaks is higher when the front edge of the piezoelectric plate is free. Whereas the amplitude of the resonating peaks P_{plate} is higher for a piezoelectric plate having a fixed seaside edge as compared to a free seaside edge. A similar observation was reported in Vipin and Koley [72].

The variation of the power extraction P_{plate} as a function of wavenumber Kh_1 for various ripples number m and ripple amplitude a_1/h_1 is similar in nature to that of Fig. 4.9 and therefore, the same are deferred here.

4.5.6 Results associated with the hydrodynamic performance of hybrid wave energy converter device consists of piezoelectric plate (fixed edge near to the OWC device and seaside free edge) and OWC device

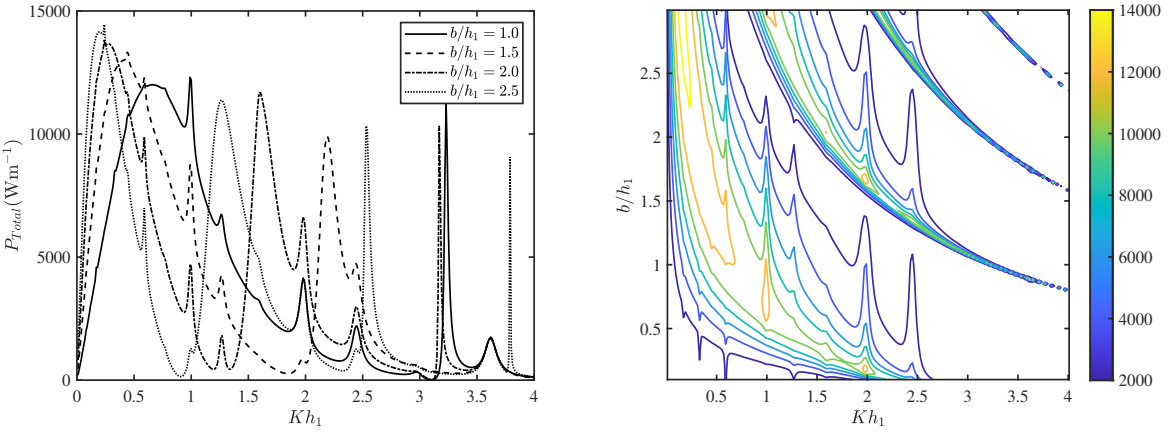

FIGURE 4.18: (a) variation of P_{Total} vs Kh_1 for various b/h_1, and (b) contour plot of P_{Total} as a function of Kh_1 and b/h_1.

Fig. 4.18(a) illustrates the effect of various chamber widths b/h_1 on the power extraction P_{Total} by the hybrid wave energy converter device consisting of a piezoelectric plate and the OWC device. The surface plot of P_{Total} as functions of b/h_1 and Kh_1 is provided in Fig. 4.18(b). The overall pattern of the power extraction P_{Total} curve as shown in Fig. 4.18 is similar to the observation as seen in Fig. 4.10. A comparison between Figs. 4.18(a) and 4.10(a) reveals that for a wider range of wave frequencies, the power extraction P_{Total} by the hybrid wave energy converter device is more when the seaside edge of the piezoelectric plate is fixed as compared to the case when the seaside edge of the piezoelectric plate is free. Similar observations are seen when Fig. 4.19 is compared with Fig. 4.11.

In Fig. 4.20(a), the variation of the power extraction P_{Total} by the hybrid wave energy converter device is plotted as a function of incident wavenumber Kh_1 for various values of plate length l_1/h_1 of the piezoelectric plate. The associated surface plot is provided in Fig. 4.20(b). It is

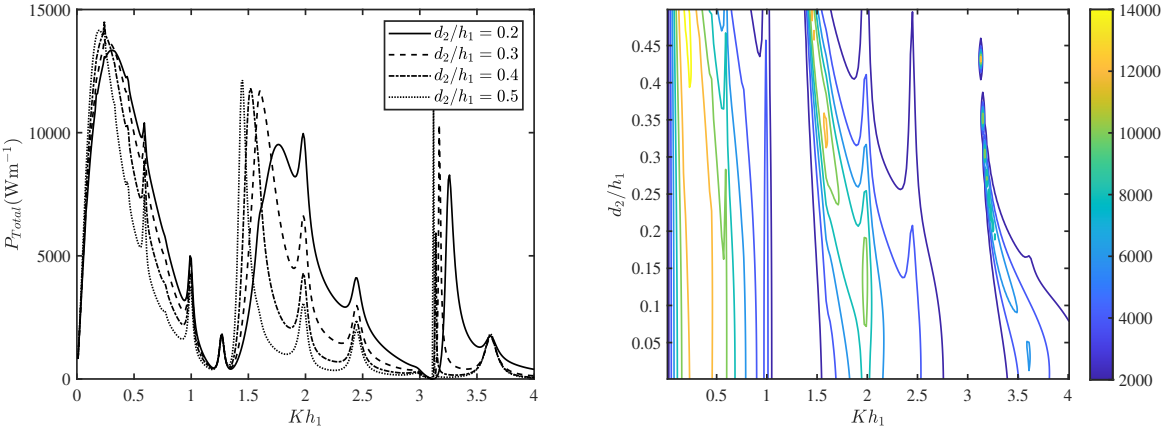

FIGURE 4.19: (a) variation of P_{Total} vs Kh_1 for various d_2/h_1, and (b) contour plot of P_{Total} as a function of Kh_1 and d_2/h_1.

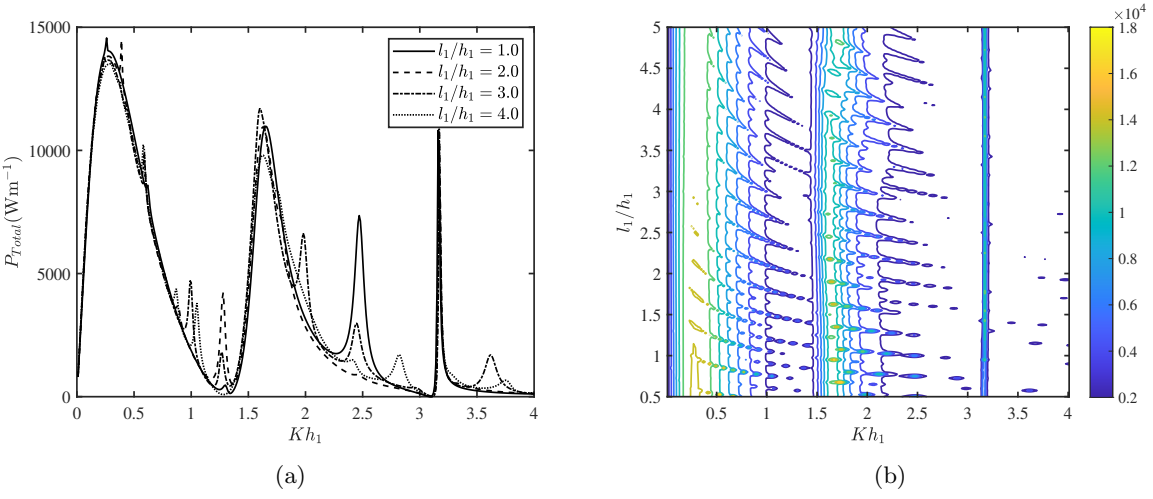

FIGURE 4.20: (a) variation of P_{Total} vs Kh_1 for various (a) l_1/h_1, and (b) contour plot of P_{Total} as a function of Kh_1 and l_1/h_1.

to be noted that the overall resonating pattern of Fig. 4.20 is similar to that of Fig. 4.13. A comparison between Figs. 4.20 and 4.13 show that the power extraction P_{Total} by the hybrid wave energy converter device having fixed edges of the piezoelectric plate is significantly higher as compared to the power extraction P_{Total} by the hybrid wave energy converter device when the front edge of the piezoelectric plate is free.

In Figs. 4.21(a) and (b), the line and surface plots of the power extraction P_{Total} for various wavenumber Kh_1 and plate submergence depth d_1/h_1 are provided. The overall pattern of Fig. 4.21 is similar to that of Fig. 4.14 except the fact that the power extraction P_{Total} by the hybrid wave energy converter device having fixed edges of the piezoelectric plate is higher as compared to the power extraction P_{Total} by the hybrid wave energy converter device when the front edge

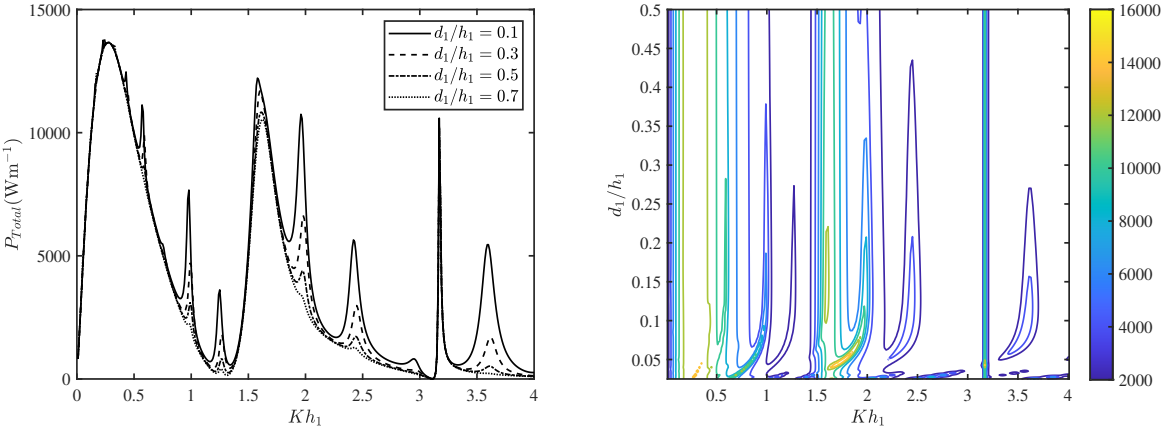

(a) (b)

FIGURE 4.21: (a) variation of P_{Total} vs Kh_1 for various (a) d_1/h_1, and (b) contour plot of P_{Total} as a function of Kh_1 and l_1/h_1.

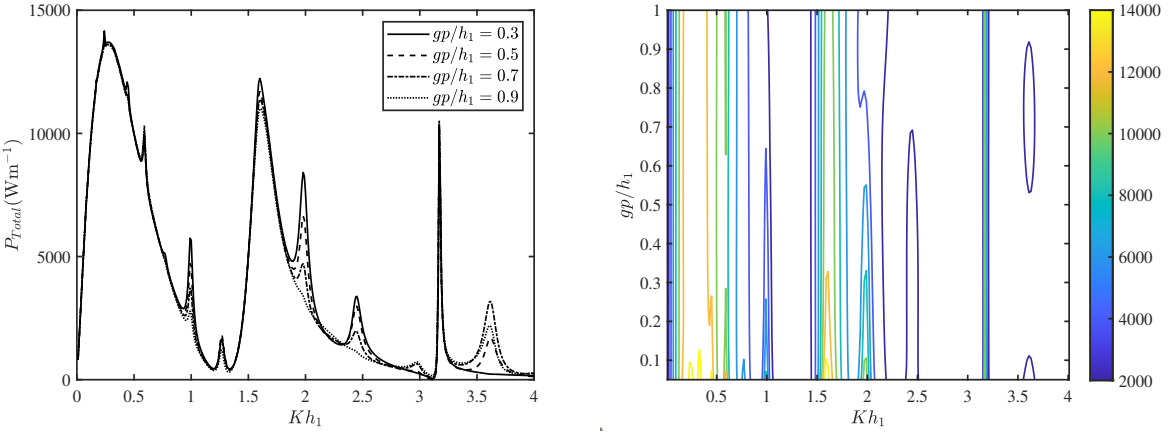

(a) (b)

FIGURE 4.22: (a) variation of P_{Total} vs Kh_1 for various (a) gp/h_1, and (b) contour plot of P_{Total} as a function of Kh_1 and gp/h_1.

of the piezoelectric plate is free. A similar observation is reported while comparing Figs. 4.22 with 4.15.

4.5.7 Summary comparison among standalone OWC, piezoelectric plate and the hybrid device

In the present section, a summary comparison of the power extraction by the standalone OWC, piezoelectric plate, and the hybrid device is provided. All the aforementioned figures show that the power extraction P_{Total} by the hybrid device is higher than the power extraction by the standalone OWC device P_{OWC} and the standalone piezoelectric plate P_{plate}. A closer looks reveal that the P_{Total} is significantly higher than P_{plate} throughout the entire range of wave

numbers. In addition, the maximum P_{Total} value is slightly higher than the maximum P_{OWC} value. However, the number of resonating peaks in the P_{Total} curve is considerably higher than the number of resonating peaks in the P_{OWC} curve. This demonstrates that the present hybrid wave energy converter device can extract a significantly higher amount of wave power P_{Total} for a wider range of incident wave frequencies as compared to the standalone OWC device. The higher number of resonating peaks in the P_{plate} curve results in a higher number of peaks in the P_{Total} curve. In summary, the OWC device enhances the maximum power extraction, and the presence of a piezoelectric plate results in a higher number of resonating peaks in the P_{Total} curve. Therefore, the main advantage of using a hybrid wave energy converter device over a standalone OWC device and the piezoelectric plate is that the proposed hybrid device can generate maximum power for a wider range of incident wave frequencies and therefore is suitable for locations having broadband incident wave spectrum.

4.6 Time-dependent simulations

For time-dependent simulations, the method proposed in Perez and Blanke [131] is used. For the present problem, the Bretschneider Spectrum is considered as the incident wave spectrum (see Lewandowski [132] for details). This spectrum is represented as the following

$$S_{inc}(\omega) = 0.3125 \frac{\omega_m^4}{\omega^5} H_{1/3}^2 \exp\left(-1.25\left(\frac{\omega_m}{\omega}\right)^4\right), \tag{4.38}$$

where $H_{1/3}$ and ω_m represent the significant wave height and modal frequency, respectively, which depend on the sea states. The reason to choose the Bretschneider spectrum is that this spectrum is the most widely used spectrum in the marine environment and is often used to represent the wave climate in the nearshore regions (Lewandowski [132]). For the present time-dependent simulations, sea state 3 is considered for which $\omega_m = 0.837$ (most probable) and $H_{1/3} = 0.875$m (Koley [133]). Firstly, the frequency range associated with the incident wave spectrum is partitioned into N subintervals, and the average frequencies ω_n within each subinterval are calculated. For each wave component ω_n, the incident wave amplitude is determined using the following formula

$$A_n = \sqrt{2\ S_{inc}\left(\omega_n\right)\ \Delta\omega_n}, \tag{4.39}$$

where $\Delta\omega_n$ is the bandwidth of each aforementioned subintervals. The detailed procedure is provided in Koley [133], and the same is deferred here. Now, the free surface elevation and the plate deflection are represented as the following (Perez and Blanke [131])

$$\tilde{\zeta}(x,t) = \sum_{n=1}^{N} \Re\left\{\zeta_n\left(x,\omega_n\right) e^{-\mathrm{i}(\omega_n t+\theta_n)}\right\}, \tag{4.40}$$

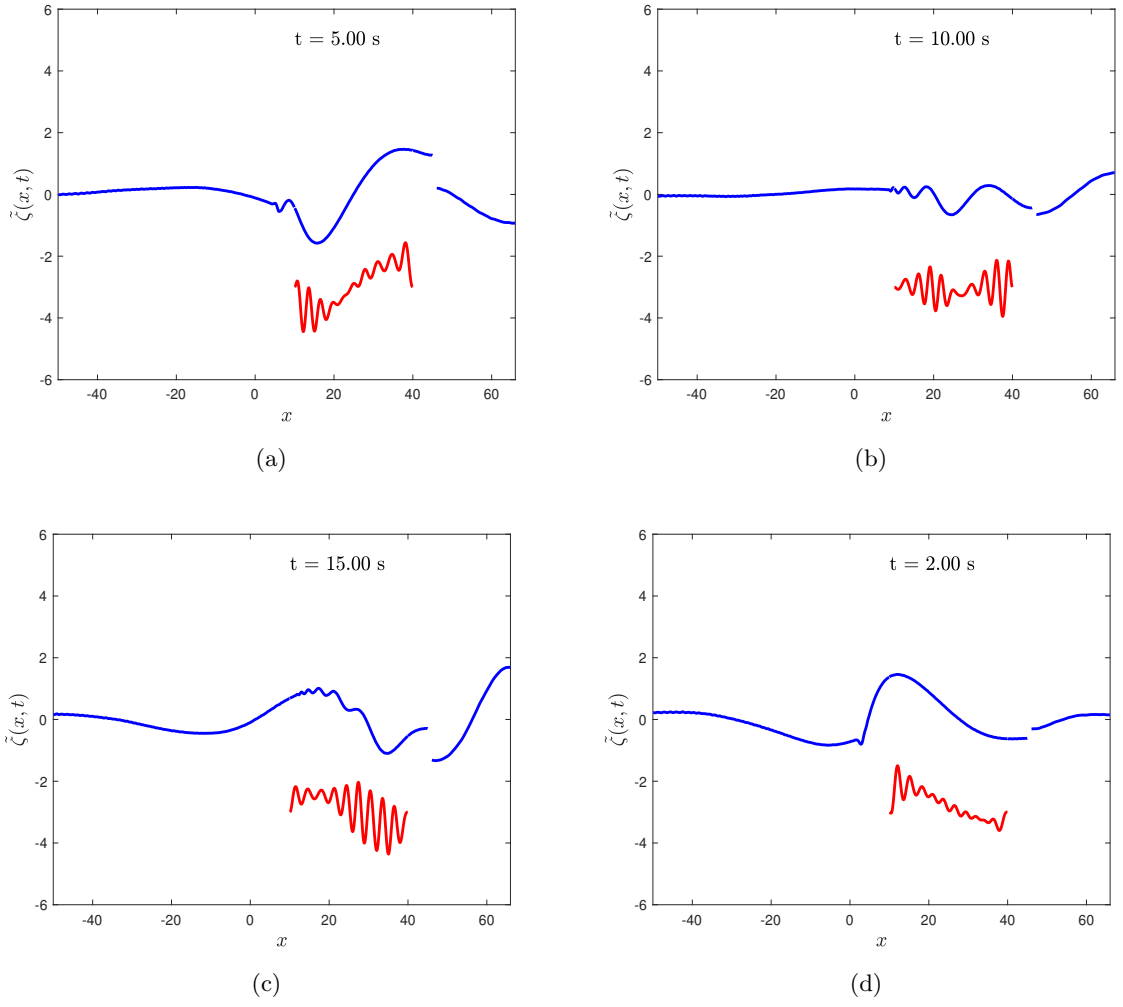

FIGURE 4.23: Variation of the free surface displacement $\tilde{\zeta}(x,t)$ (blue lines) and plate displacement $\tilde{\zeta}(x,t)$ (red lines) versus x at various time t (a) $t = 2$ s, (b) $t = 5$ s, (c) $t = 10$ s, and (d) $t = 15$ s . Here the phase angle is taken zero. The evolution is also shown as an animation in the Multimedia file (Fig_15.mp4). Multimedia view: `https://github.com/santanukoley/Movie-Files.git`

where the phase θ_n is chosen to be a random variable having uniform distribution on the interval $[-\pi\ \pi]$. To generate the time domain simulation as given in Eq. (4.40), $\zeta_n\,(x, \omega_n)$ is calculated using the procedure as mentioned in Sections 4.2-4.3 for each incident wave component $(A_n,\ \omega_n)$.

Figs. 4.23 and 4.24 show the time-dependent motion of the free surface displacement $\tilde{\zeta}(x,t)$ (blue lines) and piezoelectric plate displacement $\tilde{\zeta}(x,t)$ (red lines) at various instant of time. The associated movie files are provided in `https://github.com/santanukoley/Movie-Files.git`. It is to be noted that in Fig. 4.23, the phase angle is considered as $\theta_n = 0^\circ$ and in Fig. 4.24, the phase angle is varied according to the formulae provided in Eq. (4.40). The figures demonstrate that the short-crested oscillations occur in the plate due to the presence of short-crested and weakly damped progressive waves as reported by Renzi [4], Zheng et al. [71]. The effect of reflected waves by the OWC device and the plate is also clearly visible in Figs. 4.23 (c)-(d). Further, due to phase angle, the incident wave amplitude diminishes significantly, and the same

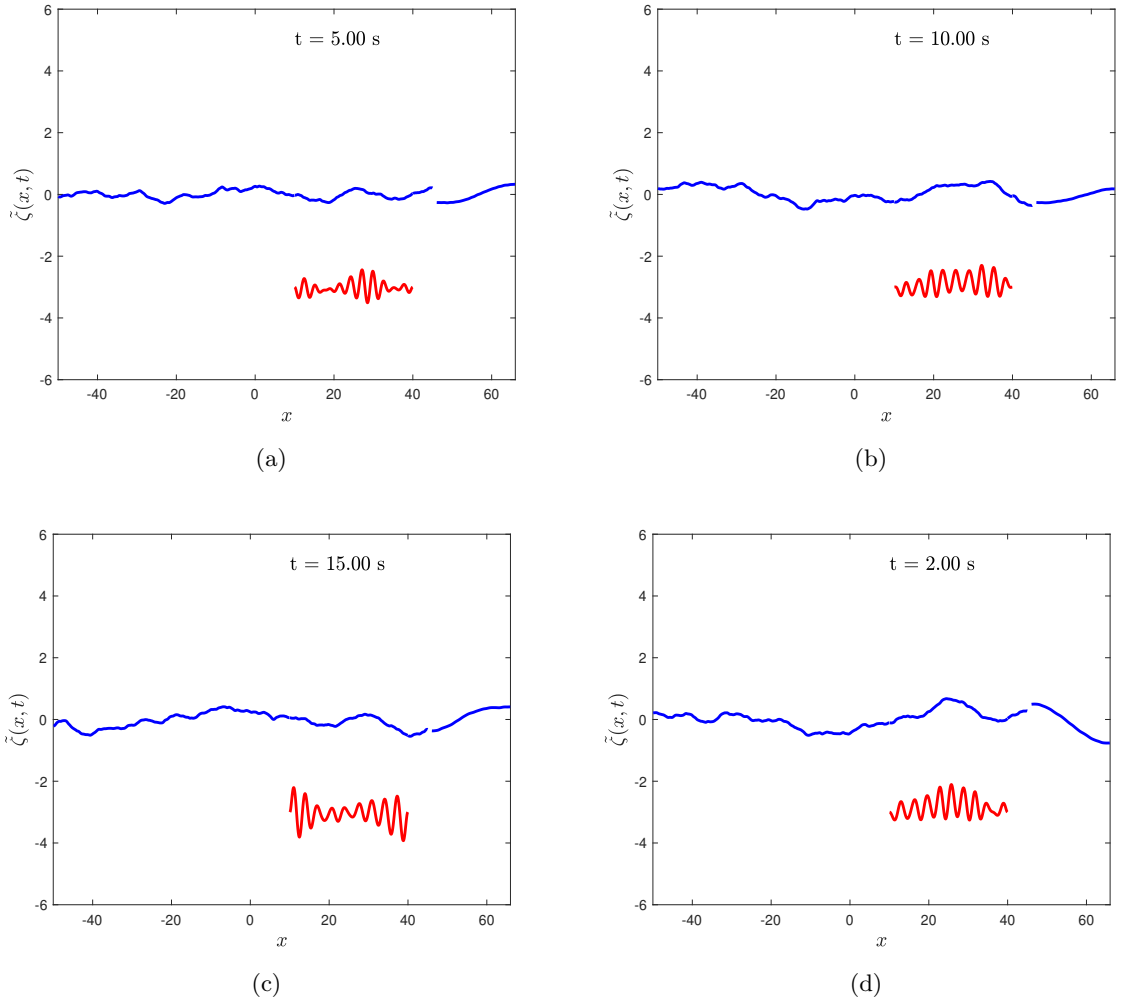

FIGURE 4.24: Variation of the free surface displacement $\tilde{\zeta}(x,t)$ (blue lines) and plate displacement $\tilde{\zeta}(x,t)$ (red lines) versus x at various time t (a) $t = 2$ s, (b) $t = 5$ s, (c) $t = 10$ s, and (d) $t = 15$ s . Here the phase angle is varied according to Eq. (4.40). The evolution is also shown as an animation in the Multimedia file (Fig_16.mp4). Multimedia view: `https://github.com/santanukoley/Movie-Files.git`

is observed in Fig. 4.24. In addition, it is seen that the piezoelectric plate is able to capture the incident wave energy for a very long period of time. These particular phenomena are also visible in Figs. 4.25(a) and (b).

In Figs. 4.26(a)-(d), the instantaneous power extraction P_{Total} by the hybrid wave energy converter device is provided for various values of chamber width b/h_1. It is seen that the higher resonating peaks in the instantaneous power extraction P_{Total} occur nearly at the same time, irrespective of variations in chamber width b/h_1.

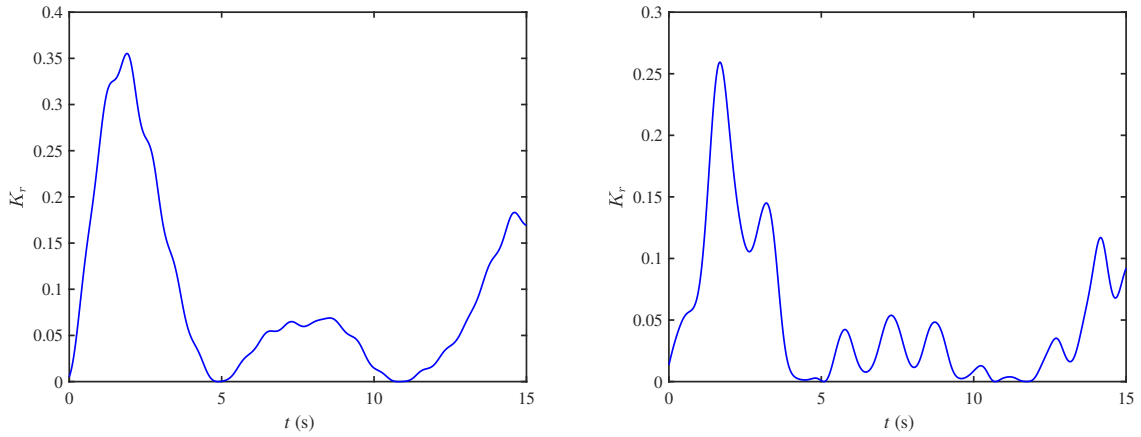

FIGURE 4.25: Variation of the instantaneous reflection coefficient K_r for the case when (a) phase angle is taken zero, and (b) phase angle is varied according to Eq. (4.40).

4.7 Optimization of various parameters associated with the hybrid wave energy converter device and seabed

		Level 1 (min)	Level 2 (max)
Parameter 1	OWC chamber width (b/h_1)	1.0	2.5
Parameter 2	OWC front wall draft (d_2/h_1)	0.2	0.5
Parameter 3	Plate length (l_1/h_1)	1.0	4.0
Parameter 4	Plate draft (d_1/h_1)	0.1	0.5
Parameter 5	Gap length (gp/h_1)	0.1	1.0
Parameter 6	Ripples number (m)	3.0	9.0
Parameter 7	Ripple amplitude (a_1/h_1)	0.1	0.25

TABLE 4.1: Taguchi method parameters.

System	Parameter 1 b/h_1	Parameter 2 d_2/h_1	Parameter 3 l_1/h_1	Parameter 4 d_1/h_1	Parameter 5 gp/h_1	Parameter 6 m	Parameter 7 a_1/h_1
1	1.0	0.2	1.0	0.1	0.1	3.0	0.1
2	1.0	0.2	1.0	0.5	1.0	9.0	0.25
3	1.0	0.5	4.0	0.1	0.1	9.0	0.25
4	1.0	0.5	4.0	0.5	1.0	3.0	0.1
5	2.5	0.2	4.0	0.1	1.0	3.0	0.25
6	2.5	0.2	4.0	0.5	0.1	9.0	0.1
7	2.5	0.5	1.0	0.1	1.0	9.0	0.1
8	2.5	0.5	1.0	0.5	0.1	3.0	0.25

TABLE 4.2: Taguchi method L8 matrix.

The present section provides the detailed optimization procedure to analyze the effect of shape parameters associated with the piezoelectric plate and OWC device, and seabed parameters on the power extraction P_{Total} by the hybrid wave energy converter device, resonance frequency, and bandwidth. In the present section, the Taguchi method is employed to optimize seven parameters: OWC chamber width, OWC front wall draft, piezoelectric plate length and draft, gap length between the OWC device and the piezoelectric plate, ripples number and ripple amplitude of the sinusoidally varying seabed to get maximum power, resonating frequency in the

System	Max Power (kW/m)	Resonance frequency (rad/s)	Half power bandwidth (rad/s)	Modified bandwidth (rad/s)
1	15.613	1.2425	0.4095	0.9368
2	8.576	0.7925	0.6560	0.6560
3	10.149	0.5465	0.2490	0.3573
4	9.852	0.6695	0.3675	0.3975
5	10.173	0.6155	0.4035	0.4915
6	10.323	0.5015	0.4055	0.4855
7	15.252	0.5495	0.1545	0.3445
8	17.135	0.5615	0.0365	0.1760

TABLE 4.3: Output performance attributes of the 8 systems.

close proximity of $\omega_m = 0.837$ and maximum bandwidth. It is to be noted that the incident wave spectrum and associated parameters are taken the same as Eq. (4.38). Our aim is to get the appropriate combination of parameters that yields the maximum power at operating frequency in the close proximity of $\omega_m = 0.837$ and with an acceptable bandwidth.

Tab. 4.1 presents the different parameters studied by the Taguchi method. The minimum and maximum values of each parameter are provided in Levels 1 and 2, respectively. These minimum and maximum values are in line with the values provided in Section 4.5. Tab. 4.2 provides the Taguchi method L8 matrix in which the columns represent every parameter and value associated with their levels. Further, every row of this L8 matrix combines different parameters and the values associated with their levels which represent a standalone system. Therefore, every row provides the values of the device and seabed parameters. The detailed procedure is provided in Al Shami et al. [93], Bao et al. [94]. Here, the simulations are carried out for these eight different systems by considering the incident wave spectrum 4.38. In all the simulations, the incident wave frequency range is considered as $0.5 \leq \omega \leq 2.0$, which covers more than 90% area under the spectrum 4.38 about the most probable frequency $\omega_m = 0.837$. From the aforementioned carried simulations, Tab. 4.3 is constructed, which provides maximum power, resonance frequency, and bandwidth associated with each of the eight systems. The bandwidth (fourth column of Tab. 4.3) is calculated from the frequency range where the generated power P_{Total} is more than 50% of the maximum power. This bandwidth is also termed as half power bandwidth in the literature (see Al Shami et al. [93] for details). It is seen from Tab. 4.3 that Systems 1, 7, and 8 produce the highest maximum power. However, the resonating frequency is quite far from the most probable incident wave frequency $\omega_m = 0.837$. In addition, the bandwidth for system 1 is quite larger than the bandwidth of systems 7 and 8. On the other hand, system 2 is having resonating frequency 0.7925, which lies in the close proximity of $\omega_m = 0.837$ and also has larger bandwidth. However, the maximum power is the lowest among all the eight systems. Therefore, we need to further investigate Systems 1, 2, 7, and 8 to get an optimized system. In this regard, the modified bandwidth is calculated from the frequency range where the generated power P_{Total} is more than 50% of the maximum power associated with system 2. The modified bandwidth is

presented in the fifth column of Tab. 4.3, which shows that system 1 bandwidth is the maximum among all the eight systems. To get a comparison about the resonance frequency and bandwidth, the power extraction P_{Total} is depicted in Fig. 4.27 as a function of incident wave frequency ω for systems 1, 2, 7, and 8. It is clearly seen in Fig. 4.27 that the power extraction P_{Total} and bandwidth associated with system 1 are higher as compared to other systems around the most probable frequency $\omega_m = 0.837$. This concludes that system 1 is best suited at the locations where the incident wave frequency follows 4.38 as this particular system extracts the highest power P_{Total} around the most probable incident wave frequency $\omega_m = 0.837$ and has the largest bandwidth around $\omega_m = 0.837$.

4.8 Shortcomings of the present study

The present study is based on linear water wave theory. In reality, the water flow around the device may not be irrotational. The free surface elevations inside and outside of the device are nonlinear in nature. Further, the turbulence and vortex shedding around the device will certainly affect the performance of the hybrid device. Due to these aforementioned effects, the present linear wave-structure interaction theory overestimates the power extraction by the hybrid device (see Ning et al. [6], Ning et al. [134], Ning et al. [116]). However, the present results can be used to design various parameters of the hybrid wave energy converter device at the initial stages and also can be used to compare with CFD-based results for validation purposes.

4.9 Conclusions

The present study investigates the hydrodynamic performance of a hybrid wave energy converter device consisting of a piezoelectric plate and the oscillating water column device in the frequency domain as well as in the time-domain. A detailed comparison of the power extraction by the present hybrid wave energy converter device with that of the standalone piezoelectric plate and OWC device is studied. Further, a detailed optimization procedure based on the Taguchi method is provided to analyze the effect of shape parameters associated with the piezoelectric plate and the OWC device and seabed parameters on the power extraction by the hybrid wave energy converter device, resonance frequency, and bandwidth. The present study leads to the following conclusions:

- The power extraction by the hybrid wave energy converter device consisting of a piezoelectric plate and OWC device is considerably higher than the power extraction by the

standalone piezoelectric plate and OWC device for a wider range of incident wave frequencies. Consequently, the present hybrid device is suitable in locations having broadband incident wave spectrum.

- Due to the occurrences of multiple resonances, the power extraction by the present hybrid wave energy converter device is higher for moderate and larger values of the chamber width in the long and intermediate wave regimes.
- Irrespective of the front wall draft, the power extraction by the present hybrid device is higher in the long-wave regime. In contrast, the power extraction decreases with an increase in the front wall draft as the incident wavelength becomes shorter. Similar observations are reported for the standalone OWC devices.
- The power extraction by the present hybrid wave energy converter device is higher for smaller plate lengths and smaller submergence depths of the piezoelectric plate. Similar observations are reported in the power extraction by the standalone piezoelectric plate.
- The ripple amplitude and the number of ripples of the sinusoidally varying seabed significantly influence the power extraction by the hybrid wave energy converter. Similar results are also reported for the standalone OWC devices and piezoelectric plates.
- The power extraction by the hybrid wave energy converter device becomes higher when the piezoelectric plate is placed in the closed proximity of the OWC device.
- The amplitudes of the resonating peaks are higher for a piezoelectric plate having fixed edges, and the number of resonating peaks is more when the seaside edge of the piezoelectric plate is free.
- The piezoelectric plate is able to capture the incident wave energy for an extended period of time.
- Based on the Taguchi method, System 1 is best suited at the locations where the incident wave frequency follows the Bretschneider spectrum in terms of extracting the highest power around the most probable incident wave frequency $\omega_m = 0.837$ and associated largest bandwidth.

In summary, it is concluded that the hydrodynamic performance of the present hybrid wave energy converter device can be enhanced significantly with the appropriate combinations of shape parameters associated with the OWC device, piezoelectric plate, and undulated seabed.

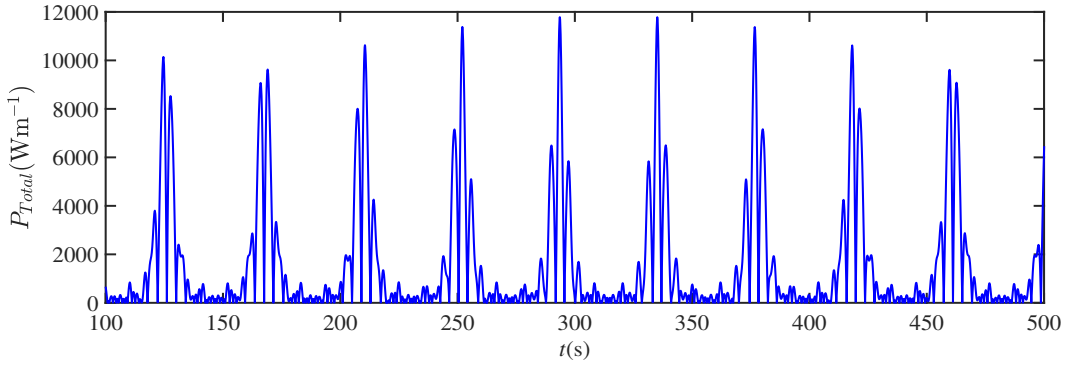

(a)

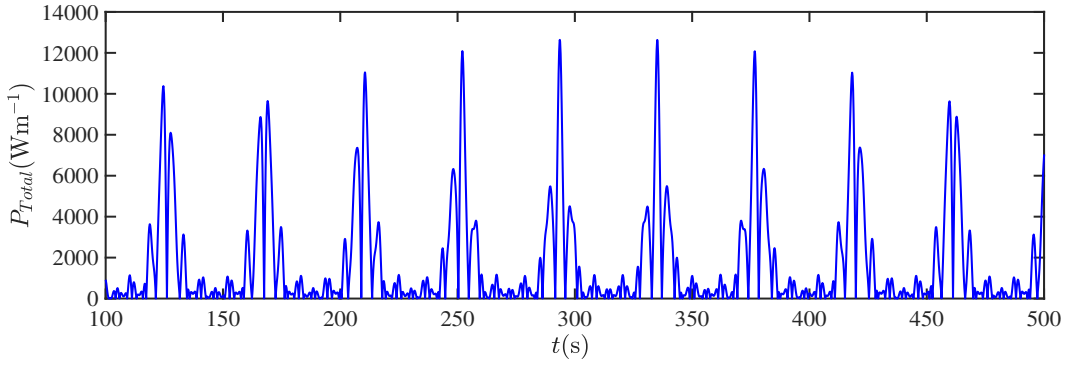

(b)

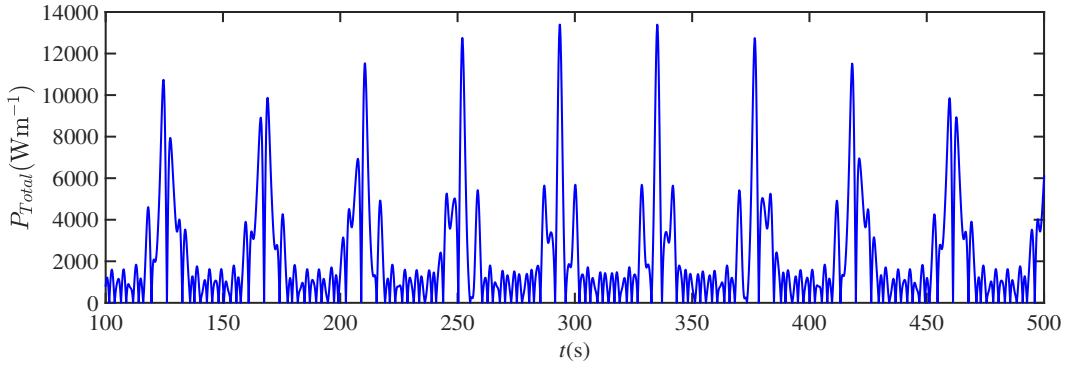

(c)

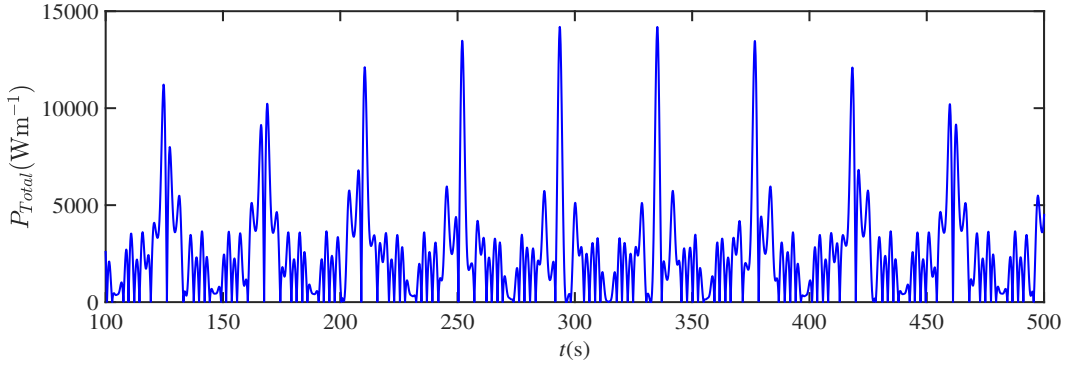

(d)

FIGURE 4.26: Variation of the instantaneous power extraction P_{Total} for (a) $b/h_1 = 1.0$, (b) $b/h_1 = 1.5$, (c) $b/h_1 = 2.0$, and (d) $b/h_1 = 2.5$.

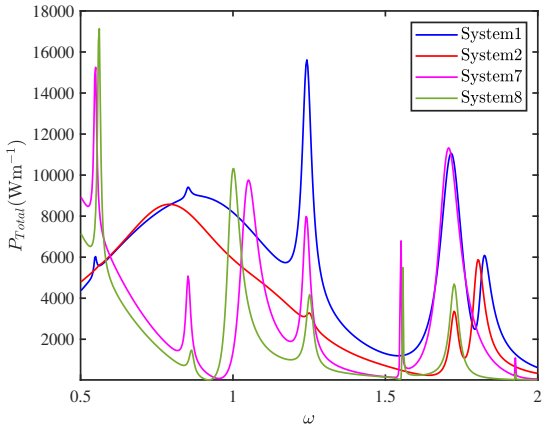

FIGURE 4.27: Optimized systems' power extraction P_{Total} vs frequency ω based on Eq. (4.38).

Chapter 5

Mathematical modeling of oscillating water column wave energy converter devices placed over an undulated seabed in a two-layer fluid system

* The work, in this chapter, is covered by the following publications:

1. K. Trivedi, and S. Koley, "Hydrodynamics of an U-shaped OWC device in a two-layer fluid system," *Energy Reports*, vol. 8, pp. 106-111, 2022.

2. K. Trivedi, and S. Koley, "Mathematical modeling of oscillating water column wave energy converter devices placed over an undulated seabed in a two-layer fluid system," *Renewable Energy*, vol. 216, pp. 119092, 2023.

5.1 General introduction

The present study investigates the hydrodynamic performance of the two types of oscillating water column wave energy converter devices, namely (i) INP (interface non-piercing) OWC device and (ii) IP (interface piercing) OWC device placed over an undulated seabed in a two-layer fluid system. The boundary element method is used to handle the associated boundary value problems. Major emphasis is given to analyze the efficiency of the OWC devices for various values of incident wave parameters and shape parameters associated with the OWC devices and undulated seabed. Further, the time-domain analysis is provided in which the free surface and interface elevations are demonstrated for different instants of time. It is observed that the efficiency of both the OWC devices associated with the internal wave mode is highly oscillatory and periodic in nature. Further, the resonating pattern in the efficiency curve occurs due to the exchange of wave energy between the surface and internal waves and also due to the multiple resonances and near-resonance interactions of waves with the bottom ripples. Moreover, the results show that the incoming wave energy associated with the internal wave mode is distributed to cover a broadband spectrum, and consequently, the multiple resonances occur in the efficiency curve. In addition, air compressibility significantly influences the hydrodynamic efficiency of the OWC devices.

5.2 Mathematical Formulation

In this section, the mathematical formulation, i.e., the governing equations and associated boundary conditions for the problem of water wave interaction with the interface non-piercing (INP) OWC device, are provided. The geometric configurations of the INP OWC device are provided in Fig. 5.1. The Cartesian coordinate system is considered with the vertical cross-section of the OWC device lying in the XZ-plane. Here, the problem is studied in a two-layer fluid domain with a mean free surface at $z = 0$ and interface at $z = -h$. The upper layer fluid domain having fluid density ρ_1 occupies the region $-\infty < x < L, -h < z < 0$, whereas the lower layer fluid domain having fluid density ρ_2 ($\rho_1 < \rho_2$) occupies the region $-\infty < x < L, -H(x) < z < -h$. In the case of the INP OWC device, the front wall doesn't intersect the interface boundary $-\infty < x < L, z = -h$. The draft and thickness of the front wall of the OWC device are a and d, respectively. Further, the chamber width of the OWC device is b, and the rear wall of the device is situated at $x = L$. The OWC device is placed over an undulated sea bed $z = -H(x)$. The undulated seabed is finitely extended as shown in Fig. 5.1. In addition, a Wells turbine is positioned at the top of the OWC device chamber, which converts the ocean energy into electricity (see Trivedi and Koley [125]). Due to the presence of OWC device, the total free surface is divided into two regions: (i) internal free surface Γ_4 and (ii) external free surface Γ_8 occupy the regions $\Gamma_4 = \{(x, z) : z = 0; L - b < x < L\}$, and $\Gamma_8 = \{(x, z) : z = 0; -\infty < x < L - b - d\}$

respectively. Further, the seabed is rigid and impenetrable in nature. Moreover, the immersed boundaries of the front wall of the OWC device are represented by $\Gamma_5 \cup \Gamma_6 \cup \Gamma_7$. Here, the total fluid domain is divided into two regions R_1 (upper layer fluid) and R_2 (lower layer fluid) respectively. Further, regions R_1 and R_2 are separated by an interface boundary Γ_9. For the modeling purpose, the water is assumed to follow the potential flow theory (see Babarit [123] for detailed assumptions), and the motion is simple harmonic in time with angular frequency σ. Therefore, the total velocity potentials $\Phi_j(x,z,t) = \Re\{\phi_j(x,z)e^{-\mathrm{i}\omega t}\}$ exist and satisfy the Laplace equation

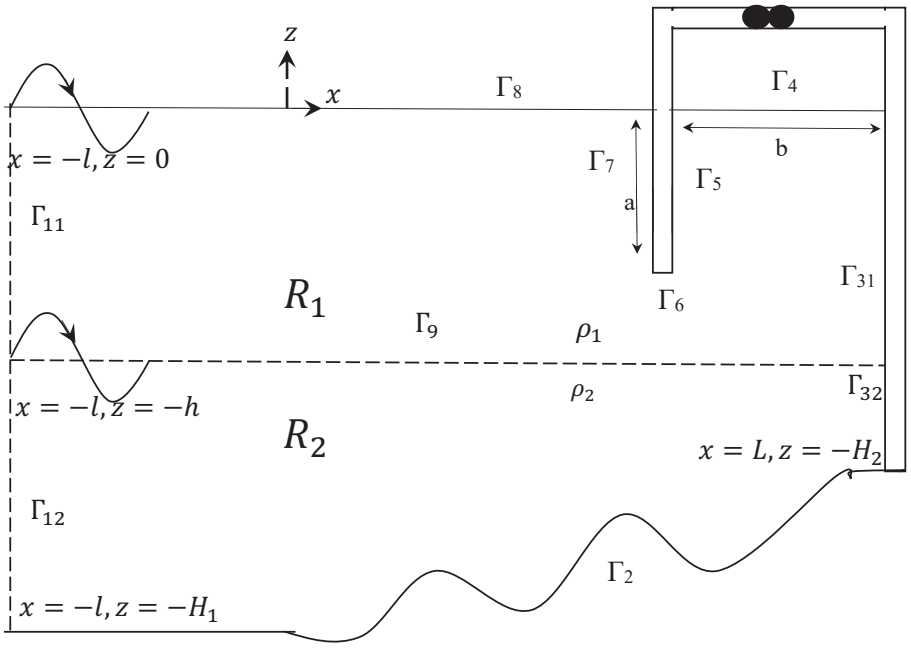

FIGURE 5.1: Vertical cross section of the INP OWC device.

$$\nabla^2\phi_j(x,z) = 0, \quad \text{for } j = 1,2, \quad \nabla^2 \equiv \left(\frac{\partial^2}{\partial x^2} + \frac{\partial^2}{\partial z^2}\right). \tag{5.1}$$

The boundary condition at the mean free surface $z = 0$ is given by (see Evans and Porter [5] and Koley and Trivedi [26] for details)

$$\frac{\partial\phi_1}{\partial n} - K\phi_1 = \begin{cases} \dfrac{\mathrm{i}\omega p}{\rho_1 g}, & \text{on } \Gamma_4, \\ 0, & \text{on } \Gamma_8, \end{cases} \tag{5.2}$$

where $K = \omega^2/g$, with g being the gravitational acceleration. Here, $\partial/\partial n$ represents the derivative in the normal direction. Now, the boundary condition on the impentrable bottom Γ_2 is given by

$$\frac{\partial\phi_2}{\partial n} = 0, \quad \text{on } z = -H(x), \tag{5.3}$$

where $H(x)$ represents the bottom profile

$$H(x) = \begin{cases} H_1, & x < 0, \\ \tilde{H}(x), & 0 < x < L, \\ H_2, & x = L. \end{cases} \tag{5.4}$$

Here, $\tilde{H}(x)$ yields the undulated bottom profile. Further, the no flow condition on the rear side wall of the OWC and the submerged boundaries of the front wall of the OWC device is given by

$$\begin{cases} \dfrac{\partial \phi_1}{\partial n} = 0, & \text{on} \quad \Gamma_{31} \cup \Gamma_5 \cup \Gamma_6 \cup \Gamma_7, \\ \dfrac{\partial \phi_2}{\partial n} = 0, & \text{on} \quad \Gamma_{32}. \end{cases} \tag{5.5}$$

The linearized boundary conditions at the mean interface boundary $z = -h$ are given by

$$\begin{cases} \dfrac{\partial \phi_1}{\partial n}\Big|_{z=-h_+} = -\dfrac{\partial \phi_2}{\partial n}\Big|_{z=-h_-}, & \text{on} \quad \Gamma_9, \\ s\left(\dfrac{\partial \phi_1}{\partial n} - K\phi_1\right)\Big|_{z=-h_+} = -\left(\dfrac{\partial \phi_2}{\partial n} + K\phi_2\right)\Big|_{z=-h_-}, & \text{on} \quad \Gamma_9, \end{cases} \tag{5.6}$$

where $s = \rho_1/\rho_2$. Now, the total velocity potential ϕ_j $(j = 1, 2)$ is splitted into two parts as mentioned in Evans and Porter [5], and the same is given by

$$\phi_j = \phi_j^S + \left(\frac{\mathrm{i}\sigma p}{\rho_1 g}\right)\phi_j^R, \quad \text{for} \quad j = 1, 2. \tag{5.7}$$

Here, ϕ_j^S and ϕ_j^R are termed as the scattered and radiated velocity potentials respectively for regions R_j $(j = 1, 2)$. Moreover, the scattered velocity potential can be separated into the diffracted potential ψ_j^D and incident potential ψ_j^I for $j = 1, 2$ (see Koley and Trivedi [26] and Evans and Porter [5] for details). Now, $\psi_1^{S,R}$ satisfies the Eqs. (5.1), (5.2), (5.5), and (5.6). On the other hand, $\phi_2^{S,R}$ satisfies the Eqs. (5.1), (5.3)-(5.6) with the following changes in Eq. (5.2) and (5.6) as given by

$$\frac{\partial \phi_1^S}{\partial n} - K\phi_1^S = 0, \quad \text{on} \quad \Gamma_4 \cup \Gamma_8, \qquad \frac{\partial \phi_1^R}{\partial n} - K\phi_1^R = \begin{cases} 1, & \text{on} \quad \Gamma_4, \\ 0, & \text{on} \quad \Gamma_8, \end{cases} \tag{5.8}$$

$$s\left(\frac{\partial \phi_1^{S,R}}{\partial n} - K\phi_1^{S,R}\right)\Big|_{z=-h_+} = -\left(\frac{\partial \phi_2^{S,R}}{\partial n} + K\phi_2^{S,R}\right)\Big|_{z=-h_-}, \quad \text{on} \quad \Gamma_9. \tag{5.9}$$

When the incident wave contains the wave number k_I, the far-field boundary conditions are given by (Panda and Martha [85])

$$\begin{cases} \phi_j^S(x,z) = e^{\mathrm{i}k_I x}\psi_I(k_I,z) + A_{I,I}^S e^{-\mathrm{i}k_I x}\psi_I(k_I,z) + A_{II,I}^S e^{-\mathrm{i}k_{II} x}\psi_{II}(k_{II},z), \quad \text{as } x \to -\infty, \\ \phi_j^R(x,z) = A_{I,I}^R e^{-\mathrm{i}k_I x}\psi_I(k_I,z) + A_{II,I}^R e^{-\mathrm{i}k_{II} x}\psi_{II}(k_{II},z), \quad \text{as } x \to -\infty, \end{cases} \tag{5.10}$$

where $j = 1, 2$ correspond to the regions R_1 and R_2 respectively. Further, $A_{I,I}^{S,R}$ and $A_{II,I}^{S,R}$ are the coefficients related to the amplitudes of the reflected and radiated waves for the wave modes k_I and k_{II} respectively due to the incident wave mode k_I. On the other hand, when the incident wave contains the wave number k_{II}, the far-field boundary conditions are given by

$$\begin{cases} \phi_j^S(x,z) = e^{\mathrm{i}k_{II} x}\psi_{II}(k_{II},z) + A_{I,II}^S e^{-\mathrm{i}k_I x}\psi_I(k_I,z) + A_{II,II}^S e^{-\mathrm{i}k_{II} x}\psi_{II}(k_{II},z), \quad \text{as } x \to -\infty, \\ \phi_j^R(x,z) = A_{I,II}^R e^{-\mathrm{i}k_I x}\psi_I(k_I,z) + A_{II,II}^R e^{-\mathrm{i}k_{II} x}\psi_{II}(k_{II},z), \quad \text{as } x \to -\infty. \end{cases} \tag{5.11}$$

Here, $A_{I,II}^{S,R}$ and $A_{II,II}^{S,R}$ are the coefficients associated with the amplitudes of the reflected and radiated waves for the wave modes k_I and k_{II} respectively due to the incident wave mode k_{II}. In Eqs. (5.10) and (5.11), the expressions for the vertical eigenfunctions $\psi_n(k_n, z)$ for $n = I, II$ are given by

$$\psi_n(k_n,z) = \begin{cases} \dfrac{N_n^{-1}\sinh k_n(H_1-h)\{k_n\cosh k_n z + K\sinh k_n z\}}{K\cosh k_n h - k_n \sinh k_n h}, & \text{for} \quad -h < z < 0, \\ N_n^{-1}\cosh k_n(z+H_1), & \text{for} \quad -H_1 < z < -h. \end{cases} \tag{5.12}$$

Here, k_n satisfies the dispersion relation

$$\mathcal{G}(k) \equiv (1-s)k^2 + K^2\{s + \coth k(H_1-h)\coth kh\} - kK\{\coth kh + \coth k(H_1-h)\} = 0. \tag{5.13}$$

It is to be noted that the dispersion relation in Eq. (5.13) have two positive real roots $k_n = k_I, k_{II}$ $(0 < k_I < k_{II})$, and infinite number of imaginary roots of the form $\mathrm{i}p_n$ for $n \geq 1$. For each K and s, these two positive real roots $k_n = k_I, k_{II}$ give rise to two different propagating wave modes. These two wavenumbers present on both the free surface and the interface. The smaller wavenumber k_I is referred to as the surface-wave mode and the larger wavenumber k_{II} is referred to as the internal-wave mode. For $\rho_1 \to \rho_2$, i.e., for $s \to 1$ and $h \to H_1$ simultaneously, the dispersion relation Eq. (5.13) reduces to the usual dispersion relation for a single-layer fluid case. The vertical eigenfunctions $\psi_n(k_n, z)$ for $n = I, II$ in Eq. (5.12) are orthonormal with respect to the inner product

$$\langle \psi_n, \psi_m \rangle = \int_{-H_1}^{-h} \psi_n(z)\psi_m(z)dz + s\int_{-h}^{0} \psi_n(z)\psi_m(z)dz = \delta_{nm}, \tag{5.14}$$

where δ_{nm} is the Kronecker delta function, and the expression for N_n is given by

$$\begin{aligned} N_n^2 &= \frac{s\sinh^2 k_n(H_1-h)}{4k_n\left(K\cosh k_nh - k_n\sinh k_nh\right)^2} \\ &\quad \left\{K^2\left(\sinh 2k_nh - 2k_nh\right) + k_n^2\left(2k_nh + \sinh 2k_nh\right) - 2Kk_n\left(\cosh 2k_nh - 1\right)\right\} \\ &\quad + \frac{\left\{2(H_1-h)k_n + \sinh 2k_n(H_1-h)\right\}}{4k_n}. \end{aligned} \tag{5.15}$$

5.3 Solution methodology based on BEM

In the present section, the boundary element-based solution technique is used to solve the BVP (boundary value problem) described in Section 5.2. In this solution procedure, firstly, we convert the BVP associated with the scattered velocity potential ϕ_j^S and radiated velocity potential ϕ_j^R into the Fredholm integral equations. Further, the boundary element method is used to convert these Fredholm integral equations into a system of linear algebraic equations. Initially, we will discuss the method of solution for the scattering problem ϕ_j^S in both the regions R_1 and R_2, and subsequently, the same is discussed for the radiation problem ϕ_j^R for $j = 1, 2$.

Now, applying Green's second identity to the velocity potential $\phi_j^{S,R}(x,z)$ $(j=1,2)$ and the free space Green's function $G(x,z;x_0,z_0)$, the following integral equation is obtained (see Katsikadelis [112] for detailed derivation)

$$\frac{\alpha}{2\pi}\phi_j^{S,R}(x_0,z_0) = \int_\Gamma \left[\phi_j^{S,R}(x,z)\frac{\partial G}{\partial n}(x,z;x_0,z_0) - G(x,z;x_0,z_0)\frac{\partial \phi_j^{S,R}}{\partial n}(x,z)\right] d\Gamma(x,z). \tag{5.16}$$

Here, (x_0,z_0) and (x,z) are the source and field points respectively. It is to be noted that the fundamental solution $G(x,z;x_0,z_0)$ as in Eq. (5.16) satisfies the governing equation (see Katsikadelis [112] and Behera et al. [75] for details)

$$\left(\frac{\partial^2}{\partial x^2} + \frac{\partial^2}{\partial z^2}\right) G(x,z;x_0,z_0) = \delta(x-x_0)\delta(z-z_0), \tag{5.17}$$

and takes the form

$$G(x,z;x_0,z_0) = \frac{1}{2\pi}\ln(\tilde{r}), \text{where } \tilde{r} = \sqrt{(x-x_0)^2 + (z-z_0)^2}. \tag{5.18}$$

Now, applying the boundary conditions (5.5), (5.6), and (5.8)-(5.10) into Eq. (5.16), the following integral equation is derived for the scattered potential ϕ_1^S in region R_1 as

$$-\frac{1}{2}\phi_1^S + \int_{\Gamma_{11}} \left(\frac{\partial G}{\partial n} - \mathrm{i}k_I G\right) \phi_1^S d\Gamma + \int_{\Gamma_9} \left(\frac{\partial \phi_1^S}{\partial n}\left[\left(\frac{1-s}{sK}\right)\frac{\partial G}{\partial n} - G\right] + \frac{1}{s}\phi_2^S \frac{\partial G}{\partial n}\right) d\Gamma$$
$$+ \int_{\Gamma_{31}} \frac{\partial G}{\partial n}\phi_1^S d\Gamma + \int_{\Gamma_4} \left(\frac{\partial G}{\partial n} - KG\right) \phi_1^S d\Gamma + \int_{\Gamma_5 \cup \Gamma_6 \cup \Gamma_7} \frac{\partial G}{\partial n}\phi_1^S d\Gamma$$
$$+ \int_{\Gamma_8} \left(\frac{\partial G}{\partial n} - KG\right) \phi_1^S d\Gamma = \int_{\Gamma_{11}} \left(\frac{\partial \phi_1^I}{\partial n} - \mathrm{i}k_I \phi_1^I\right) G d\Gamma. \tag{5.19}$$

Here, $\phi^I(x,z) = e^{\mathrm{i}k_I x}\psi_I(k_I, z)$ represents the velocity potential corresponds to the incident waves containing the wavenumber k_I. Similarly, using the boundary conditions (5.3)-(5.6), (5.9), and (5.10) into Eq. (5.16), we get

$$-\frac{1}{2}\phi_2^S + \int_{\Gamma_{12}} \left(\frac{\partial G}{\partial n} - \mathrm{i}k_I G\right) \phi_2^S d\Gamma + \int_{\Gamma_2 \cup \Gamma_{32}} \frac{\partial G}{\partial n}\phi_2^S d\Gamma + \int_{\Gamma_9} \left(\phi_2^S \frac{\partial G}{\partial n} + G\frac{\partial \phi_1^S}{\partial n}\right) d\Gamma$$
$$= \int_{\Gamma_{12}} \left(\frac{\partial \phi_2^I}{\partial n} - \mathrm{i}k_I \phi_2^I\right) G d\Gamma. \tag{5.20}$$

In a similar manner, using the boundary conditions (5.5), (5.6), and (5.8)-(5.10) into Eq. (5.16), the following integral equation is obtained for radiated potential ϕ_1^R in region R_1 as

$$-\frac{1}{2}\phi_1^R + \int_{\Gamma_{11}} \left(\frac{\partial G}{\partial n} - \mathrm{i}k_I G\right) \phi_1^R d\Gamma + \int_{\Gamma_9} \left(\frac{\partial \phi_1^R}{\partial n}\left[\left(\frac{1-s}{sK}\right)\frac{\partial G}{\partial n} - G\right] + \frac{1}{s}\phi_2^R \frac{\partial G}{\partial n}\right) d\Gamma$$
$$+ \int_{\Gamma_{31}} \frac{\partial G}{\partial n}\phi_1^R d\Gamma + \int_{\Gamma_4} \left(\frac{\partial G}{\partial n} - KG\right) \phi_1^R d\Gamma + \int_{\Gamma_5 \cup \Gamma_6 \cup \Gamma_7} \frac{\partial G}{\partial n}\phi_1^R d\Gamma$$
$$+ \int_{\Gamma_8} \left(\frac{\partial G}{\partial n} - KG\right) \phi_1^R d\Gamma = \int_{\Gamma_4} G d\Gamma. \tag{5.21}$$

Likewise, applying the boundary conditions (5.3)-(5.6), (5.9) and (5.10) into Eq. (5.16), the following intergral equation is obtained for the radiated potential ϕ_2^R in region R_2 as

$$-\frac{1}{2}\phi_2^R + \int_{\Gamma_{12}} \left(\frac{\partial G}{\partial n} - \mathrm{i}k_I G\right) \phi_2^R d\Gamma + \int_{\Gamma_2 \cup \Gamma_{32}} \frac{\partial G}{\partial n}\phi_2^R d\Gamma + \int_{\Gamma_9} \left(\phi_2^R \frac{\partial G}{\partial n} + G\frac{\partial \phi_1^R}{\partial n}\right) d\Gamma = 0. \tag{5.22}$$

In a similar manner, using the boundary conditions (5.3)-(5.11) into Eq. (5.16), we can get the Fredholm integral equations for the velocity potentials $\phi_j^{S,R}$ associated with the incident waves containing the wavenumber k_{II}. Now, Eqs. (5.19)-(5.22) are converted into a system of equations using the boundary element method (see Katsikadelis [112] for details). In this approach, the boundaries of each region R_j for $j = 1, 2$ are discretized into a large number of line segments and the values for $\phi_j^{S,R}$ and their normal derivatives $\partial\phi_j^{S,R}/\partial n$ are linearly varying over each segment. With these assumptions, the discretized form of the integral Eqs. (5.19)-(5.22)

are given by

$$\sum_{j=1}^{N_{11}} \left(H^{ij} - \mathrm{i}k_I G^{ij}\right) \phi_{1j}^S\big|_{\Gamma_{11}} + \sum_{j=1}^{N_9} \left(\frac{1}{s} H^{ij} \phi_{2j}^S + \left[\left(\frac{1-s}{sK} \right) H^{ij} - G^{ij} \right] \frac{\partial \phi_{1j}^S}{\partial n} \right)\Bigg|_{\Gamma_9}$$
$$+ \sum_{j=1}^{N_{31}} H^{ij} \phi_{1j}^S\big|_{\Gamma_{31}} + \sum_{j=1}^{N_4} \left(H^{ij} - KG^{ij}\right) \phi_{1j}^S\big|_{\Gamma_4} + \sum_{j=1}^{N_5+N_6+N_7} H^{ij} \phi_{1j}^S\big|_{\Gamma_5 \cup \Gamma_6 \cup \Gamma_7}$$
$$+ \sum_{j=1}^{N_8} \left(H^{ij} - KG^{ij}\right) \phi_{1j}^S\big|_{\Gamma_8} = \sum_{j=1}^{N_{11}} \left(\frac{\partial \phi_1^I}{\partial n} - \mathrm{i}k_I \phi_1^I \right) G^{ij}\Big|_{\Gamma_{11}}, \tag{5.23}$$

$$\sum_{j=1}^{N_{12}} \left(H^{ij} - \mathrm{i}k_I G^{ij}\right) \phi_{2j}^S\big|_{\Gamma_{12}} + \sum_{j=1}^{N_2+N_{32}} H^{ij} \phi_{2j}^S\big|_{\Gamma_2 \cup \Gamma_{32}} + \sum_{j=1}^{N_9} \left(H^{ij} \phi_{2j}^S + G^{ij} \frac{\partial \phi_{1j}^S}{\partial n} \right)\Bigg|_{\Gamma_9}$$
$$= \sum_{j=1}^{N_{12}} \left(\frac{\partial \phi_2^I}{\partial n} - \mathrm{i}k_I \phi_2^I \right) G^{ij}\Big|_{\Gamma_{12}}, \tag{5.24}$$

$$\sum_{j=1}^{N_{11}} \left(H^{ij} - \mathrm{i}k_I G^{ij}\right) \phi_{1j}^R\big|_{\Gamma_{11}} + \sum_{j=1}^{N_9} \left(\frac{1}{s} H^{ij} \phi_{2j}^R + \left[\left(\frac{1-s}{sK} \right) H^{ij} - G^{ij} \right] \frac{\partial \phi_{1j}^R}{\partial n} \right)\Bigg|_{\Gamma_9}$$
$$+ \sum_{j=1}^{N_{31}} H^{ij} \phi_{1j}^R\big|_{\Gamma_{31}} + \sum_{j=1}^{N_4} \left(H^{ij} - KG^{ij}\right) \phi_{1j}^R\big|_{\Gamma_4}$$
$$+ \sum_{j=1}^{N_5+N_6+N_7} H^{ij} \phi_{1j}^R\big|_{\Gamma_5 \cup \Gamma_6 \cup \Gamma_7} + \sum_{j=1}^{N_8} \left(H^{ij} - KG^{ij}\right) \phi_{1j}^R\big|_{\Gamma_8} = \sum_{j=1}^{N_4} G^{ij}\big|_{\Gamma_4}, \tag{5.25}$$

$$\sum_{j=1}^{N_{12}} \left(H^{ij} - \mathrm{i}k_I G^{ij}\right) \phi_{2j}^R\big|_{\Gamma_{12}} + \sum_{j=1}^{N_2+N_{32}} H^{ij} \phi_{2j}^R\big|_{\Gamma_2 \cup \Gamma_{32}} + \sum_{j=1}^{N_9} \left(H^{ij} \phi_{2j}^R + G^{ij} \frac{\partial \phi_{1j}^R}{\partial n} \right)\Bigg|_{\Gamma_9} = 0, \tag{5.26}$$

where

$$\begin{aligned} H^{ij} &= -\frac{1}{2}\delta_{ij} + \mathcal{H}^{ij}, \quad \mathcal{H}^{ij} = \begin{cases} \hat{h}_1^{i1} + \hat{h}_2^{iN}, & \text{for} \quad j = 1, \\ \hat{h}_1^{ij} + \hat{h}_2^{i,j-1}, & \text{for} \quad j = 2 \cdots N, \end{cases} \\ G^{ij} &= \begin{cases} \hat{g}_1^{i1} + \hat{g}_2^{iN}, & \text{for} \quad j = 1, \\ \hat{g}_1^{ij} + \hat{g}_2^{i,j-1}, & \text{for} \quad j = 2 \cdots N, \end{cases} \end{aligned} \tag{5.27}$$

are termed as influence coefficients, and the expressions for $\hat{h}_m^{ij}$ and $\hat{g}_m^{ij}$ $(m = 1, 2)$ as in Eq. (5.27) are evaluated using the following formulae

$$\hat{h}_1^{ij} = \frac{l_j}{4} \int_{-1}^{1} \frac{\partial G}{\partial n} \left(x(\xi), z(\xi); x_i, z_i\right) (1 - \Upsilon)\, d\xi, \tag{5.28}$$

$$\hat{h}_2^{ij} = \frac{l_j}{4} \int_{-1}^{1} \frac{\partial G}{\partial n} \left(x(\xi), z(\xi); x_i, y_i\right) (1 + \Upsilon)\, d\xi, \tag{5.29}$$

$$\hat{g}_1^{ij} = \frac{l_j}{4} \int_{-1}^{1} G\left(x(\xi), z(\xi); x_i, z_i\right) (1 - \Upsilon)\, d\xi, \tag{5.30}$$

$$\hat{g}_2^{ij} = \frac{l_j}{4} \int_{-1}^{1} G\left(x(\xi), z(\xi); x_i, z_i\right) (1 + \Upsilon)\, d\xi. \tag{5.31}$$

Here, l_j is the length of the boundary element Γ_j. The influence coefficients as in Eqs. (5.28)-(5.31) are estimated analytically for $i = j$, i.e., when the source and field points lie on the same boundary element. However, for $i \neq j$, the values of H^{ij} and G^{ij} are calculated using Gauss quadrature formula (see Katsikadelis [112] for details). Further, the point collocation method is adopted in which the source point $(\tilde{x}, \tilde{z})$ runs over the midpoints of each boundary element. This yields a system of linear algebraic equations and is solved using the Gauss elimination method to obtain the unknown velocity potentials and their normal derivatives over each boundary element (see Kar et al. [135] for details).

5.4 Mathematical formulation and solution methodology for interface piercing (IP) OWC device

In this section, the mathematical formulation and solution methodology for the scattering and radiation of water waves by the interface piercing OWC device are provided. The fluid domain is divided into the three computational domains, namely regions R_1, R_2 and R_3 as seen in Fig. 5.2. Here, R_1 and R_3 correspond to the upper layer fluid domain outside and within the OWC device, respectively. Further, the lower layer fluid domain in represented by R_2. In the present interface piercing case, the governing equation and boundary conditions remain same as the interface non-piercing cases provided in Section 5.2 except the interface boundary conditions. Due to the presence of interface piercing front wall, the total interface is divided into two boundaries: (i) external interface boundary $\Gamma_{91} = \{(x, z) : z = -h, -l < x < L - b - d\}$, and (ii) internal interface boundary $\Gamma_{92} = \{(x, z) : z = -h, L - b < x < L\}$. The linearized boundary conditions

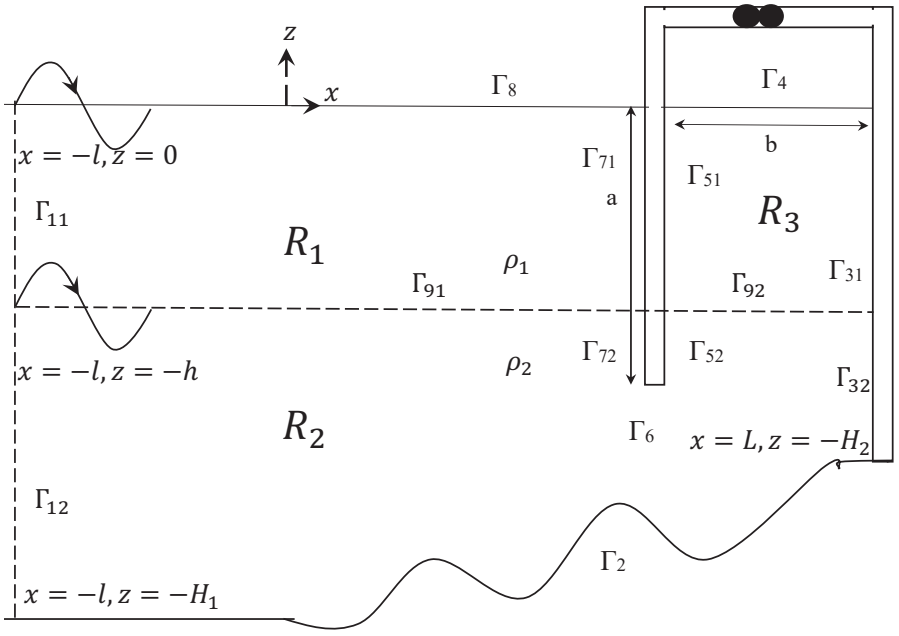

FIGURE 5.2: Vertical cross-section of the IP OWC device.

(5.6) at the mean interface boundary $z = -h$ are rewritten as

$$\begin{cases} \left.\dfrac{\partial \phi_1}{\partial n}\right|_{z=-h_+} = -\left.\dfrac{\partial \phi_2}{\partial n}\right|_{z=-h_-}, & \text{on } \Gamma_{91}, \\ s\left(\dfrac{\partial \phi_1}{\partial n} - K\phi_1\right)\Big|_{z=-h_+} = -\left(\dfrac{\partial \phi_2}{\partial n} + K\phi_2\right)\Big|_{z=-h_-}, & \text{on } \Gamma_{91}, \end{cases} \tag{5.32}$$

$$\begin{cases} \left.\dfrac{\partial \phi_3}{\partial n}\right|_{z=-h_+} = -\left.\dfrac{\partial \phi_2}{\partial n}\right|_{z=-h_-}, & \text{on } \Gamma_{92}, \\ s\left(\dfrac{\partial \phi_3}{\partial n} - K\phi_3\right)\Big|_{z=-h_+} = -\left(\dfrac{\partial \phi_2}{\partial n} + K\phi_2\right)\Big|_{z=-h_-}, & \text{on } \Gamma_{92}. \end{cases} \tag{5.33}$$

Now, the boundary conditions on the submerged boundaries of the front wall of the OWC device are given by

$$\begin{cases} \dfrac{\partial \phi_1}{\partial n} = 0, & \text{on } \Gamma_{71}, \\ \dfrac{\partial \phi_2}{\partial n} = 0, & \text{on } \Gamma_{52} \cup \Gamma_6 \cup \Gamma_{72}, \\ \dfrac{\partial \phi_3}{\partial n} = 0, & \text{on } \Gamma_{51}. \end{cases} \tag{5.34}$$

Now, proceeding in the same way as done before in Section 3, the Fredholm integral equations for the velocity potentials $\phi_j^{S,R}, (j = 1, 2, 3)$ associated with the incident waves containing the

wavenumber k_I in regions $R_j \quad (j = 1, 2, 3)$ are given by

$$-\frac{1}{2}\phi_1^S + \int_{\Gamma_{11}} \left(\frac{\partial G}{\partial n} - \mathrm{i}k_I G\right) \phi_1^S d\Gamma + \int_{\Gamma_{91}} \left(\frac{\partial \phi_1^S}{\partial n} \left[\left(\frac{1-s}{sK}\right) \frac{\partial G}{\partial n} - G\right] + \frac{1}{s}\phi_2^S \frac{\partial G}{\partial n}\right) d\Gamma$$
$$+ \int_{\Gamma_{71}} \frac{\partial G}{\partial n}\phi_1^S d\Gamma + \int_{\Gamma_8} \left(\frac{\partial G}{\partial n} - KG\right) \phi_1^S d\Gamma = \int_{\Gamma_{11}} \left(\frac{\partial \phi_1^I}{\partial n} - \mathrm{i}k_I \phi_1^I\right) G d\Gamma. \tag{5.35}$$

$$-\frac{1}{2}\phi_2^S + \int_{\Gamma_{12}} \left(\frac{\partial G}{\partial n} - \mathrm{i}k_I G\right) \phi_2^S d\Gamma + \int_{\Gamma_2 \cup \Gamma_{32}} \frac{\partial G}{\partial n}\phi_2^S d\Gamma + \int_{\Gamma_{92}} \left(\phi_2^S \frac{\partial G}{\partial n} + G\frac{\partial \phi_3^S}{\partial n}\right) d\Gamma$$
$$+ \int_{\Gamma_{52}} \frac{\partial G}{\partial n}\phi_2^S d\Gamma + \int_{\Gamma_6 \cup \Gamma_{72}} \frac{\partial G}{\partial n}\phi_2^S d\Gamma + \int_{\Gamma_{91}} \left(\phi_2^S \frac{\partial G}{\partial n} + G\frac{\partial \phi_1^S}{\partial n}\right) d\Gamma$$
$$= \int_{\Gamma_{12}} \left(\frac{\partial \phi_2^I}{\partial n} - \mathrm{i}k_I \phi_2^I\right) G d\Gamma. \tag{5.36}$$

$$-\frac{1}{2}\phi_3^S + \int_{\Gamma_{51}} \frac{\partial G}{\partial n}\phi_3^S d\Gamma + \int_{\Gamma_{92}} \left(\frac{\partial \phi_3^S}{\partial n} \left[\left(\frac{1-s}{sK}\right) \frac{\partial G}{\partial n} - G\right] + \frac{1}{s}\psi_2^S \frac{\partial G}{\partial n}\right) d\Gamma + \int_{\Gamma_{31}} \frac{\partial G}{\partial n}\phi_3^S d\Gamma$$
$$+ \int_{\Gamma_4} \left(\frac{\partial G}{\partial n} - KG\right) \phi_3^S d\Gamma = 0. \tag{5.37}$$

$$-\frac{1}{2}\phi_1^R + \int_{\Gamma_{11}} \left(\frac{\partial G}{\partial n} - \mathrm{i}k_I G\right) \phi_1^R d\Gamma + \int_{\Gamma_{91}} \left(\frac{\partial \phi_1^R}{\partial n} \left[\left(\frac{1-s}{sK}\right) \frac{\partial G}{\partial n} - G\right] + \frac{1}{s}\phi_2^R \frac{\partial G}{\partial n}\right) d\Gamma$$
$$+ \int_{\Gamma_{71}} \frac{\partial G}{\partial n}\phi_1^R d\Gamma + \int_{\Gamma_8} \left(\frac{\partial G}{\partial n} - KG\right) \phi_1^R d\Gamma = 0. \tag{5.38}$$

$$-\frac{1}{2}\phi_2^R + \int_{\Gamma_{12}} \left(\frac{\partial G}{\partial n} - \mathrm{i}k_I G\right) \phi_2^R d\Gamma + \int_{\Gamma_2 \cup \Gamma_{32}} \frac{\partial G}{\partial n}\phi_2^R d\Gamma + \int_{\Gamma_{92}} \left(\phi_2^R \frac{\partial G}{\partial n} + G\frac{\partial \phi_3^R}{\partial n}\right) d\Gamma$$
$$+ \int_{\Gamma_{52}} \frac{\partial G}{\partial n}\phi_2^R d\Gamma + \int_{\Gamma_6 \cup \Gamma_{72}} \frac{\partial G}{\partial n}\phi_2^R d\Gamma + \int_{\Gamma_{91}} \left(\phi_2^R \frac{\partial G}{\partial n} + G\frac{\partial \phi_1^R}{\partial n}\right) d\Gamma = 0. \tag{5.39}$$

$$-\frac{1}{2}\phi_3^R + \int_{\Gamma_{51}} \frac{\partial G}{\partial n}\phi_3^R d\Gamma + \int_{\Gamma_{92}} \left(\frac{\partial \phi_3^R}{\partial n} \left[\left(\frac{1-s}{sK}\right) \frac{\partial G}{\partial n} - G\right] + \frac{1}{s}\phi_2^R \frac{\partial G}{\partial n}\right) d\Gamma + \int_{\Gamma_{31}} \frac{\partial G}{\partial n}\phi_3^R d\Gamma$$
$$+ \int_{\Gamma_4} \left(\frac{\partial G}{\partial n} - KG\right) \phi_3^R d\Gamma = \int_{\Gamma_4} G d\Gamma. \tag{5.40}$$

5.5 Various parameters associated with the hydrodynamic performance of the OWC device

Firstly, the expressions for various parameters associated with the performance and efficiency of the interface non-piercing OWC device discussed in Section 5.3 are provided. The average

energy flux per unit length across a vertical cross-section is given by (see Koley and Trivedi [26] for details)

$$P_{w,j} = E_j C_{g,j}, \quad \text{for} \quad j = I, II. \tag{5.41}$$

Here, $P_{w,j}$ and $C_{g,j}$ for $j = I, II$ are termed as the average energy fluxes and group velocities correspond to the incident wave numbers k_I and k_{II} respectively. Now, the volume flow rate q_j for $j = I, II$ across the internal free surface Γ_4 can be expressed as

$$q_j = q_j^S + \frac{\mathrm{i}\omega p}{\rho_1 g} q_j^R, \quad \text{for} \quad j = I, II, \tag{5.42}$$

with q_j^S and q_j^R being the volume flow rate across the internal free surface Γ_4 associated with the scattering and radiation problems respectively. Now, the volume flux q_j^R due to the radiation potential can be decomposed into real and imaginary parts (see Evans and Porter [5] for details) as the following

$$\frac{\mathrm{i}\omega p}{\rho_1 g} q_j^R = \left(\mathrm{i}\tilde{A}_j - \tilde{B}_j\right) p, \quad \text{for} \quad j = I, II, \tag{5.43}$$

where $\tilde{A}_j$ and $\tilde{B}_j$ are termed as the radiation susceptance and radiation conductance parameters associated with the wavenumbers k_I and k_{II} respectively. Now, Eq. (5.43) gives the expressions for $\tilde{A}_j$ and $\tilde{B}_j$ as the following

$$\tilde{A}_j = \frac{\omega p}{\rho_1 g} \Re\left\{q_j^R\right\}, \qquad \tilde{B}_j = \frac{\omega p}{\rho_1 g} \Im\left\{q_j^R\right\}, \quad \text{for} \quad j = I, II. \tag{5.44}$$

To obtain an explicit expression for the radiation conductance parameter $\tilde{B}_j$ correspond to the incident wave modes k_I and k_{II}, Green's second identity is applied on ϕ_j^R and its complex conjugate $\overline{\phi}_j^R$ over the domain bounded by Γ_{Rj} for $j = 1, 2$ as follows

$$\int_{\Gamma_{Rj}} \left(\phi_j^R \frac{\partial \overline{\phi}_j^R}{\partial n} - \overline{\phi}_j^R \frac{\partial \phi_j^R}{\partial n}\right) = 0, \quad \text{for} \quad j = 1, 2. \tag{5.45}$$

Here, Γ_{R1} represents the total boundary of the closed domain R_1 and is written as $\Gamma_{R1} = \Gamma_{11} \cup \Gamma_9 \cup \Gamma_{31} \cup \Gamma_4 \cup \Gamma_5 \cup \Gamma_6 \cup \Gamma_7 \cup \Gamma_8$. Further, the boundary Γ_{R2} composed of $\Gamma_{R2} = \Gamma_{12} \cup \Gamma_2 \cup \Gamma_{32} \cup \Gamma_9$. Here, there will be no contributions from the boundaries Γ_{31}, Γ_5, Γ_6, Γ_7, and Γ_8. Now, summing up all the contributions from the boundaries Γ_{11}, Γ_9 and Γ_4, we get

$$\begin{aligned}
&\int_{\Gamma_9} \left(\phi_1^R \frac{\partial \overline{\phi}_1^R}{\partial n} - \overline{\phi}_1^R \frac{\partial \phi_1^R}{\partial n}\right) d\Gamma - 2\mathrm{i}k_I |A_{I,I}^R|^2 \int_{-h}^{0} \psi_I^2(k_I, z)\, dz - 2\mathrm{i}k_{II} |A_{II,I}^R|^2 \int_{-h}^{0} \psi_{II}^2(k_{II}, z)\, dz \\
&+ \frac{2\mathrm{i}\tilde{B}\rho_1 g}{\omega K} - \mathrm{i}k_I \left[\overline{A}_{I,I}^R A_{II,I}^R e^{i(k_I - k_{II})x} + \overline{A}_{II,I}^R A_{I,I}^R e^{i(k_{II} - k_I)x}\right] \int_{-h}^{0} \psi_I(k_I, z)\, \psi_{II}(k_{II}, z)\, dz \\
&- \mathrm{i}k_{II} \left[\overline{A}_{II,I}^R A_{I,I}^R e^{i(k_{II} - k_I)x} + \overline{A}_{I,I}^R A_{II,I}^R e^{i(k_I - k_{II})x}\right] \int_{-h}^{0} \psi_I(k_I, z)\, \psi_{II}(k_{II}, z)\, dz = 0.
\end{aligned} \tag{5.46}$$

Similarly, in region R_2, there are no contributions from the boundaries Γ_2 and Γ_{32}. The contributions from the boundaries Γ_{12} and Γ_9 are the following

$$\int_{\Gamma_9}\left(\phi_2^R\frac{\partial\overline{\phi}_2^R}{\partial n}-\overline{\phi}_2^R\frac{\partial\phi_2^R}{\partial n}\right)d\Gamma-2\mathrm{i}k_I|A_{I,I}^R|^2\int_{-H_1}^{-h}\psi_I^2\left(k_I,z\right)dz-2\mathrm{i}k_{II}|A_{II,I}^R|^2\int_{-H_1}^{-h}\psi_{II}^2\left(k_{II},z\right)dz$$
$$-\mathrm{i}k_I\left[\overline{A}_{I,I}^RA_{II,I}^Re^{i(k_I-k_{II})x}+\overline{A}_{II,I}^RA_{I,I}^Re^{i(k_{II}-k_I)x}\right]\int_{-H_1}^{-h}\psi_I\left(k_I,z\right)\psi_{II}\left(k_{II},z\right)dz$$
$$-\mathrm{i}k_{II}\left[\overline{A}_{II,I}^RA_{I,I}^Re^{i(k_{II}-k_I)x}+\overline{A}_{I,I}^RA_{II,I}^Re^{i(k_I-k_{II})x}\right]\int_{-H_1}^{-h}\psi_I\left(k_I,z\right)\psi_{II}\left(k_{II},z\right)dz=0. \tag{5.47}$$

Now, multiplying (5.46) by s and added to (5.47), and using the interface boundary condition as in Eq. (5.9) along with the inner product as in Eq. (5.14), the following expression is derived

$$\tilde{B}_I=\left(\frac{\sigma K}{s\rho_1 g}\right)\left[k_I|A_{I,I}^R|^2+k_{II}|A_{II,I}^R|^2\right]. \tag{5.48}$$

Similarly, when the incident wave contains the wave number k_{II}, the expression for $\tilde{B}_{II}$ is obtained as

$$\tilde{B}_{II}=\left(\frac{\sigma K}{s\rho_1 g}\right)\left[k_I|A_{I,II}^R|^2+k_{II}|A_{II,II}^R|^2\right]. \tag{5.49}$$

Now, to get the explicit expressions for the volume fluxes associated with the scattered potentials q_j^S correspond to the incident wave modes k_I and k_{II}, Green's second identity is employed on ψ_1^R and ψ_1^S over the domain bounded by Γ_{R1} as mentioned in (5.46). There will be no contributions from the boundaries Γ_{31}, Γ_5, Γ_6, Γ_7, and Γ_8. Now, summing up all the contributions from the boundaries Γ_{11},Γ_9 and Γ_4, we get

$$\int_{\Gamma_9}\left(\phi_1^R\frac{\partial\overline{\phi}_1^R}{\partial n}-\overline{\phi}_1^R\frac{\partial\phi_1^R}{\partial n}\right)d\Gamma-\frac{sq^S}{K}$$
$$-2\mathrm{i}k_IA_{I,I}^R\int_{-h}^{0}\psi_I^2\left(k_I,z\right)dz-\mathrm{i}\left(k_I+k_{II}\right)A_{II,I}^Re^{i(k_I-k_{II})x}\int_{-h}^{0}\psi_I\left(k_I,z\right)\psi_{II}\left(k_{II},z\right)dz$$
$$-\mathrm{i}\left(k_I-k_{II}\right)A_{I,I}^RA_{II,I}^Se^{-i(k_I+k_{II})x}\int_{-h}^{0}\psi_I\left(k_I,z\right)\psi_{II}\left(k_{II},z\right)dz$$
$$-\mathrm{i}\left(k_{II}-k_I\right)A_{II,I}^RA_{I,I}^Se^{-i(k_I+k_{II})x}\int_{-h}^{0}\psi_I\left(k_I,z\right)\psi_{II}\left(k_{II},z\right)dz=0. \tag{5.50}$$

Similarly, in region R_2, there are no contributions from the boundaries Γ_2 and Γ_{32}. The contributions from the boundaries Γ_{12} and Γ_9 are the following

$$\begin{aligned}
&\int_{\Gamma_9}\left(\phi_2^R\frac{\partial\overline{\phi}_2^R}{\partial n}-\overline{\phi}_2^R\frac{\partial\phi_2^R}{\partial n}\right)d\Gamma\\
&-2\mathrm{i}k_IA_{I,I}^R\int_{-H_1}^{-h}\psi_I^2\left(k_I,z\right)dz-\mathrm{i}\left(k_I+k_{II}\right)A_{II,I}^Re^{i(k_I-k_{II})x}\int_{-H_1}^{-h}\psi_I\left(k_I,z\right)\psi_{II}\left(k_{II},z\right)dz\\
&-\mathrm{i}\left(k_I-k_{II}\right)A_{I,I}^RA_{II,I}^Se^{-i(k_I+k_{II})x}\int_{-H_1}^{-h}\psi_I\left(k_I,z\right)\psi_{II}\left(k_{II},z\right)dz\\
&-\mathrm{i}\left(k_{II}-k_I\right)A_{II,I}^RA_{I,I}^Se^{-i(k_I+k_{II})x}\int_{-H_1}^{-h}\psi_I\left(k_I,z\right)\psi_{II}\left(k_{II},z\right)dz=0.
\end{aligned}\tag{5.51}$$

Now, multiplying (5.50) by s and added to (5.51), and using the interface boundary condition as in Eq. (5.9) along with the inner product as in Eq. (5.14), the following expression for the scattered volume flux q_I^S associated with the incident wave mode k_I is derived as

$$q_I^S=-\frac{K}{s}2\mathrm{i}k_IA_{I,I}^R.\tag{5.52}$$

Similarly, in the presence of incident wave mode k_{II}, the expression for the scattered volume flux q_{II}^S can be written as

$$q_{II}^S=-\frac{K}{s}2\mathrm{i}k_{II}A_{II,II}^R.\tag{5.53}$$

The average power absorbed W_j for $j=I,II$ per unit width of the pressure distribution is given by (see Koley and Trivedi [26] for details)

$$W_j=\frac{1}{2}\Re\left\{\overline{p}q_j\right\},\quad\text{for}\quad j=I,II.\tag{5.54}$$

It is considered that the volume flux q_j is linearly proportional to the pressure across the turbine p. Therefore, we get

$$q_j=\wedge p,\tag{5.55}$$

where $\wedge$ is a real control parameter that depends on the turbine characteristics (details are provided in Sarmento et al. [136], Falcão and Justino [137]). Substituting (5.55) into (5.54), and using the relations (5.43) and (5.44), we get

$$W_j=\frac{1}{2}\frac{\wedge|q_j^S|^2}{\left(\wedge+\tilde{B}_j\right)^2+\tilde{A}_j{}^2},\quad\text{for}\quad j=I,II.\tag{5.56}$$

The maximum efficiencies $\eta_{max,j}$ for $j=I,II$ associated with the incident wave modes k_I and k_{II} are expressed as (see Koley and Trivedi [26] for detailed derivations)

$$\eta_{max,j}=\left(\frac{2\tilde{B}_j}{\wedge_{opt}+\tilde{B}_j}\right),\quad\wedge_{opt}=\sqrt{\tilde{A}_j{}^2+\tilde{B}_j{}^2},\quad\text{for}\quad j=I,II.\tag{5.57}$$

Now, the dimensionless form of the parameters $\tilde{A}_j$ and $\tilde{B}_j$ are written as (see Evans and Porter [5])

$$\mu_j = \frac{\rho g}{\omega b}\tilde{A}_j, \qquad \nu_j = \frac{\rho g}{\omega b}\tilde{B}_j, \quad \text{for} \quad j = I, II. \tag{5.58}$$

Using (5.58) into (5.57), we get the dimensionless form of $\eta_{max,j}$ for $j = I, II$ as

$$\eta_{max,j} = \frac{2\nu_j}{\nu_j + \sqrt{\nu_j^2 + \mu_j^2}} = \frac{2}{1 + \sqrt{1 + \left(\frac{\mu_j}{\nu_j}\right)^2}}, \quad \text{for} \quad j = I, II. \tag{5.59}$$

In a similar manner, we can obtain the explicit expressions for the various parameters associated with the hydrodynamic performance of the surface piercing OWC device. Further, the expressions for the radiation conductance coefficients $\tilde{B}_j, j = I, II$, volume flux associated with the scattered potentials $q_j^S, j = I, II$, and maximum efficiency of the OWC device $\eta_{max,j}, j = I, II$ are the same as derived for the interface non-piercing (INP) device, and the details are deferred here to avoid the mere repetitions.

5.6 Results and discussions

The present section provides various results associated with the performances and efficiencies of the INP and IP OWC devices in a detailed manner. In the present analysis, the hydrodynamic performance and efficiency of the OWC devices are investigated in intermediate water depth. Form intermediate water depth results, the results associated with long and short water waves are obtained for smaller and higher values of KH_1, respectively. The wave frequency and wavenumber are associated with the water depth in which it propagates by the dispersion relation. Further, the water depth significantly influences the celerity, and group velocity which affects power extraction and efficiency of the device (see Noble et al. [138] for details). Furthermore, to scaled up the results from model to prototype, the water depth should be scaled properly as associated discrepancies will result into errors in various wave parameters. In view of these reasons, the water depth H_1 is considered to dimensionalize the other parameters associated with the structural configuration of the OWC devices and sinusiodally varying seabed. The parameters associated with the incident waves and OWC devices are taken as follows: $H_1 = 10$m, $H_2/H_1 = 0.75$, $h/H_1 = 0.5$, $L/H_1 = 5.0$, $l/H_1 = 3.0$, $b/H_1 = 2.0$, $s = 0.85$, $d/H_1 = 0.1$ and $g = 9.81$ m/s^2. Further, for INP devices, the draft of the front wall is considered as $a/H_1 = 0.3$. On the other hand, for IP OWC devices, the draft of the front wall is taken as $a/H_1 = 0.65$. Further, the parameters associated with the air compressibility are taken as follows: air volume of the air chamber in the undisturbed state $V_0 = 2400$m^3, specific heat ratio $\gamma = 1.4$ and atmospheric air pressure $P_a = 1.013 \times 10^5$Pa, unless otherwise mentioned. In the following discussions, the wavenumbers k_I and k_{II} refer to the surface wave mode (SM) and internal wave mode (IM), respectively. In the present study, the sinusoidally varying bottom profile is taken,

and the corresponding profile is given in the following (see Koley and Trivedi [26] and Porter and Porter [113] for details). The shape function for the bottom profile as in Eq. (5.4) is given as

$$\tilde{H}(x) = H_2 + H\left\{1 + 2\left(\frac{x}{L}\right)^3 - 3\left(\frac{x}{L}\right)^2 - \frac{a_1}{H}\sin\left(\frac{2m\pi x}{L}\right)\right\}, \tag{5.60}$$

where $H = H_1 - H_2$, a_1 is the amplitude of the ripples and m is the number of ripples. For INP OWC device, the bottom profile parameters are taken as $a_1/H_1 = 0.1$, and $m = 3.0$. Further, for IP OWC device, the bottom profile parameters are considered as $a_1/H_1 = 0.025$, and $m = 3.0$.

5.6.1 Numerical convergence

The convergence of the numerical solutions based on the boundary element method depends on the panel size used to discretize the boundaries of the domain. The panel size p_s is given by (see Wang and Meylan [115])

$$p_s = \frac{1}{\kappa k_j}, \quad j = I, II.$$

Here, κ is proportionality constant. To achieve numerical convergence, we can vary the values of κ to determine the length of the boundary elements. In Tables 5.1 and 5.2, the convergence of the numerical computations based on boundary element method is illustrated for INP and IP OWC devices for different values of the chamber length $b/H_1 = 1.0, 1.5, 2.0$ corresponding to the wavenumbers k_I and k_{II} respectively. It is noticed that for $\kappa \geq 60$, the values of $\eta_{max,I}$ converge up to three decimal places for INP and IP OWC devices. Similarly, for $\kappa \geq 15$, the values of $\eta_{max,II}$ converge up to three decimal places for INP and IP OWC devices. Therefore, it is concluded that for the computational purpose, the panel size p_s is chosen suitably with $\kappa = 60$ for $\eta_{max,I}$ and $\kappa = 15$ for $\eta_{max,II}$.

5.6.2 Comparison with existing results

In the present section, a comparison between the present numerical results and the results of Evans and Porter [5] and Rezanejad et al. [7] are provided for specific cases. In Fig. 5.3(a), to achieve the OWC device model of Evans and Porter [5], a limiting case of the present model is considered by taking $m \to 0$, $a_1/H_1 \to 0$, and $H_2/H_1 \to 1$. Fig. 5.3(a) illustrates the variation of the efficiency η_{max} as a function of non-dimensional wavenumber KH_1 for various values of chamber length b/H_1 of the OWC device. In Fig. 5.3(b), to achieve the OWC device model of Rezanejad et al. [7], the limiting case of the present model is considered by $m \to 0$, and $a_1/H_1 \to 0$. Fig. 5.3(b) depicts the efficiency η_{max} as a function of non-dimensional wavenumber KH_1 for various values of step length H_2/H_1 of the bottom. Both the figures show that the results obtained using the present BEM method match well with the results of Evans and Porter [5] and Rezanejad et al. [7]. These comparisons validate the present numerical solution

κ	b/H_1	$\eta_{max,I}$	
		INP OWC device	IP OWC device
20	1.0	0.97050	0.69712
	1.5	0.83351	0.58993
	2.0	0.56544	0.44133
40	1.0	0.97175	0.67447
	1.5	0.85347	0.58473
	2.0	0.54442	0.44497
60	1.0	0.97294	0.67218
	1.5	0.86130	0.58162
	2.0	0.54627	0.44251
80	1.0	0.97291	0.67225
	1.5	0.86145	0.58124
	2.0	0.54635	0.44227

TABLE 5.1: Comparative study of $\eta_{max,I}$ for INP and IP OWC devices.

κ	b/H_1	$\eta_{max,II}$	
		INP OWC device	IP OWC device
5	1.0	0.72452	0.68680
	1.5	0.87692	0.99250
	2.0	0.34408	0.30322
10	1.0	0.72940	0.66451
	1.5	0.87620	0.99239
	2.0	0.34517	0.29766
15	1.0	0.72939	0.65934
	1.5	0.87598	0.99253
	2.0	0.34541	0.29720
20	1.0	0.72935	0.65951
	1.5	0.87591	0.99213
	2.0	0.34539	0.29721

TABLE 5.2: Comparative study of $\eta_{max,II}$ for INP and IP OWC devices.

methodology. In the following sections, various physical quantities of interests associated with the performance of INP and IP OWC devices are discussed separately.

5.6.3 Results associated with INP OWC device

In the present section, the results and discussions associated with the INP OWC device are provided. In the following results, variations in $\eta_{max,II}$ are provided for two different values of the parameters in each figure due to the highly oscillatory pattern of $\eta_{max,II}$.

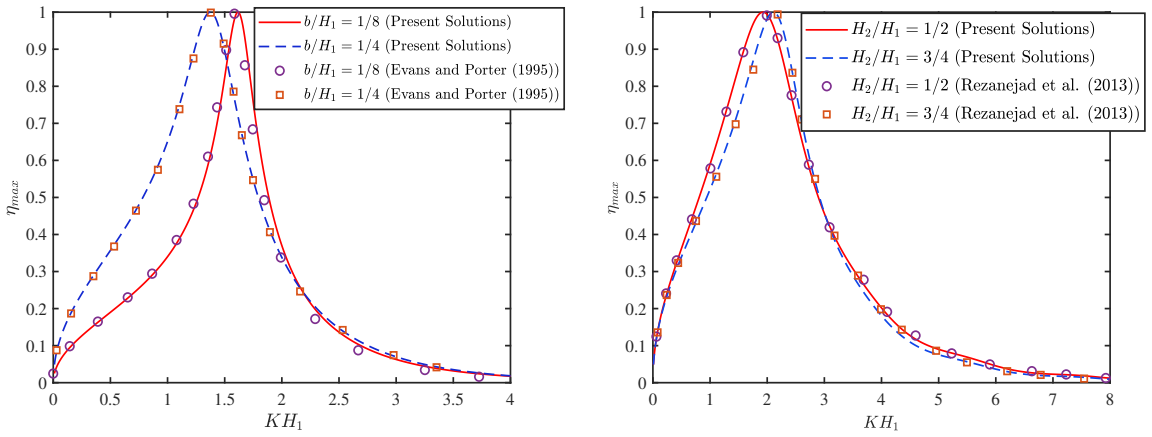

(a) (b)

FIGURE 5.3: Comparison of present numerical results with the results of (a) Evans and Porter [5] for η_{max} vs KH_1 for different b/H_1, and (b) Rezanejad et al. [7] for η_{max} vs KH_1 for different H_2/H_1 with $s = 1$.

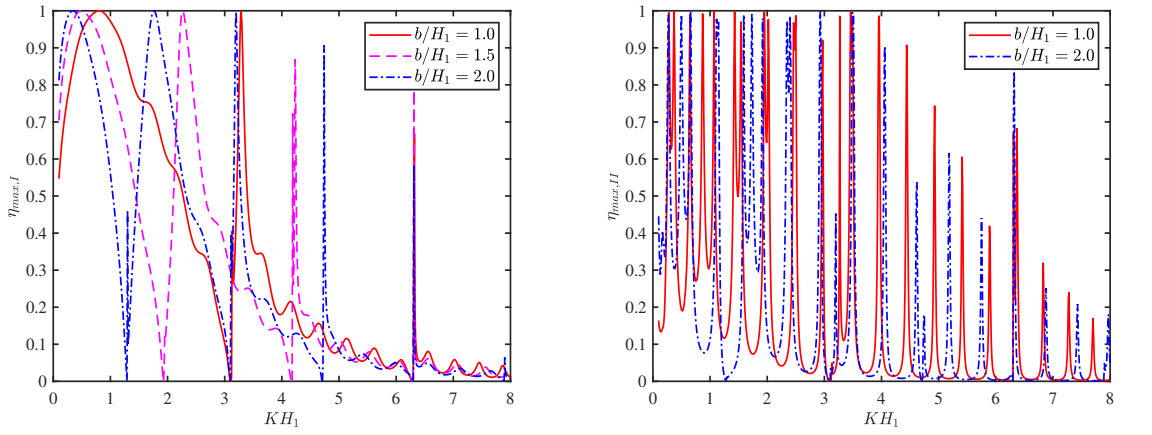

(a) (b)

FIGURE 5.4: Variation of (a) $\eta_{max,I}$, and (b) $\eta_{max,II}$ vs KH_1 for different chamber length b/H_1.

Figs. 5.4(a) and (b) illustrate the variation of the efficiency $\eta_{max,j}$ for $j = I, II$ vs wavenumber KH_1 in the surface mode (SM) and internal mode (IM) respectively for various chamber width b/H_1. The overall pattern of the efficiency curve $\eta_{max,I}$ as shown in Fig. 5.4(a) is similar in nature to that of the efficiency curve for the case of single-layer fluid (see Fig. 5 of Evans and Porter [5] and Fig. 7 of Koley and Trivedi [26]). It is seen that resonance in the efficiency $\eta_{max,I}$ occurs for smaller wavenumbers $KH_1 < 1.0$ due to the first resonance mechanism as discussed in Koley and Trivedi [26]. It is to be noted that in this resonance mechanism, the frequency of the heave motion of the water column inside the chamber coincides with the incident wave frequency. Further, multiple resonances in the efficiency $\eta_{max,I}$ curve occurs for higher wavenumbers $KH_1 > 1.0$. This happens due to the second resonance mechanism as mentioned in Koley and Trivedi [26] and Evans and Porter [5]. It is to be noted that in this resonance

mechanism, the water column inside the chamber is excited into an antisymmetric sloshing mode. For the sloshing phenomena, the condition is $k_I b = n\pi, \quad n = 1, 2, 3, \cdots$ with n being the sloshing mode number (Evans and Porter [5]). For clarity, Tab. 5.3 provides the values of KH_1 and associated $k_I b/\pi$ for $b/H_1 = 1.0, 1.5, 2.0$. It is seen that for resonances, the values of $k_I b/\pi$ are around $n = 1, 2, 3, \cdots$. Obviously, slight differences are there in some cases as the aforementioned criteria for sloshing phenomena is valid for a closed rectangular tank. However, in the present case, the front wall is not submerged up to the seabed.

TABLE 5.3: Resonating frequencies in $\eta_{max,I}$ curve for INP OWC device (corresponding to Fig. 5.4(a)).

$b/H_1 = 1.0$	$KH_1 = 3.29$	$k_I b/\pi = 1.0501$
	$KH_1 = 6.32$	$k_I b/\pi = 2.0117$
$b/H_1 = 1.5$	$KH_1 = 2.26$	$k_I b/\pi = 1.1009$
	$KH_1 = 4.23$	$k_I b/\pi = 2.0205$
	$KH_1 = 6.31$	$k_I b/\pi = 3.0128$
$b/H_1 = 2.0$	$KH_1 = 1.75$	$k_I b/\pi = 1.1720$
	$KH_1 = 3.20$	$k_I b/\pi = 2.0439$
	$KH_1 = 4.74$	$k_I b/\pi = 3.0180$
	$KH_1 = 6.31$	$k_I b/\pi = 4.0171$
	$KH_1 = 7.90$	$k_I b/\pi = 5.0293$

On the other hand, Fig. 5.4(b) depicts that the efficiency $\eta_{max,II}$ varies in a highly oscillatory manner with the variation in wavenumber KH_1. This highly oscillatory pattern diminishes for higher values of KH_1 for smaller values of b/H_1. This chaotic pattern occurs due to the following reasons: (i) exchange of energy between the surface and internal waves as mentioned in Alam et al. [83], and (ii) resonating interaction between the internal waves with the rippled bottom. In this regard, it is worthy of being mentioned that initially, the wave energy is confined within two incident-free waves and subsequently distributed to cover a broadband spectrum due to the multiple resonances and near-resonance interactions of waves with the bottom ripples and also due to the interactions of waves generated by propagating wave modes and local wave modes (see Alam et al. [83] for details).

In Figs. 5.5(a) and (b), the variation of the efficiency $\eta_{max,j}$ for $j = I, II$ are plotted as a function of the wavenumber KH_1 in SM and IM respectively for various submergence depth of the front wall a/H_1 of the device. Fig. 5.5(a) demonstrates that the first peak in the efficiency curve $\eta_{max,I}$ occurs for smaller values of KH_1 as a result of the first resonance mechanism as mentioned in Koley and Trivedi [26]. Further, peaks in the efficiency curve arise for higher values of KH_1 due to the sloshing effect as discussed in Koley and Trivedi [26]. Moreover, it is to be noted that the area under the efficiency curve is more as the draft of the front wall of the OWC device takes lower values. The reason for this is that as the immersion depth of the lip wall decreases, more amount of wave energy can enter into the device chamber. In Fig. 5.5(b), it is noticed that the variation in the efficiency $\eta_{max,II}$ is highly oscillatory in nature

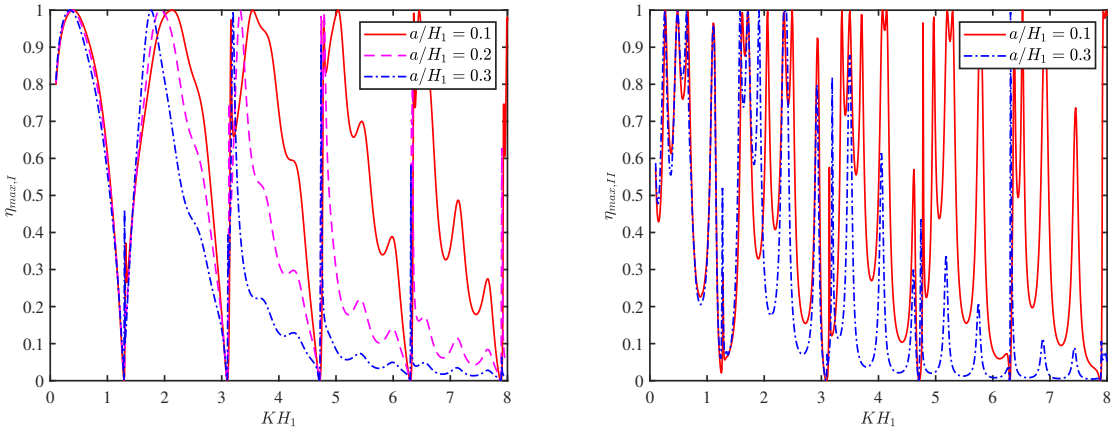

FIGURE 5.5: Variation of (a) $\eta_{max,I}$, and (b) $\eta_{max,II}$ vs KH_1 for different submergence depth a/H_1.

with the variation in incident wavenumber KH_1. Moreover, the amplitude of the peak is higher for smaller values of front wall's draft a/H_1 in the short wave regime. This highly oscillatory pattern in the efficiency curve $\eta_{max,II}$ occurs due to the distribution of incoming wave energy associated with the incident wavenumber k_{II} to cover a broadband spectrum. Further, the resonant motion due to the interaction between the waves reflected by the bottom and OWC device also contributes to the aforementioned chaotic pattern in the efficiency curve.

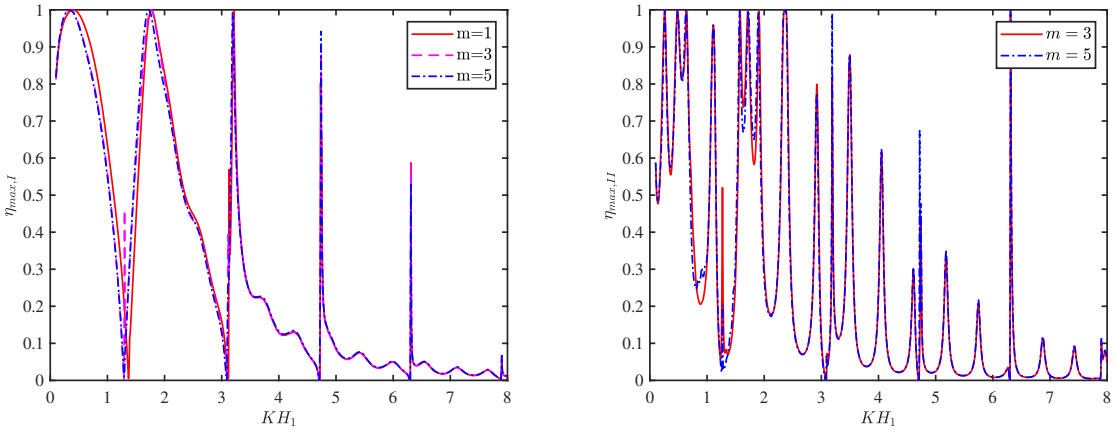

FIGURE 5.6: Variation of (a) $\eta_{max,I}$, and (b) $\eta_{max,II}$ vs KH_1 for various ripples m.

Figs. 5.6(a) and (b) show the variation of the efficiency $\eta_{max,j}$ for $j = I, II$ vs wavenumber KH_1 in the SM and IM respectively for different number of ripples m of the bottom profile. The overall resonating pattern of the efficiency $\eta_{max,I}$ due to the variation in wavenumber KH_1 as shown in Fig. 5.6(a) is similar in nature as that of Fig. 5.5(a). Further, it is noticed that for smaller values of KH_1, significant variation in the efficiency $\eta_{max,I}$ is observed due to the change

in the number of bottom ripples. However, no significant variation in the efficiency $\eta_{max,I}$ curve is observed for higher values of KH_1. The reason behind this phenomenon is that when the ratio of the water depth and wavelength of the incident wave is greater than 1/2, the incident wave does not interact with the seabed. As a consequence, the effect of bottom undulation on the waves scattering and radiation diminishes in the short wave regime. ([18]). The overall pattern of Fig 5.6 (b) is similar to the pattern as observed in Fig. 5.4(b). Further, it is reported that the amplitude of the resonance is higher for the bottom bed having more number of ripples. In addition, no significant variation is observed for moderate and higher values of KH_1 due to the variation in the number of ripples of the bottom profile. The reason for the same is provided in the discussion of Fig. 5.6(a).

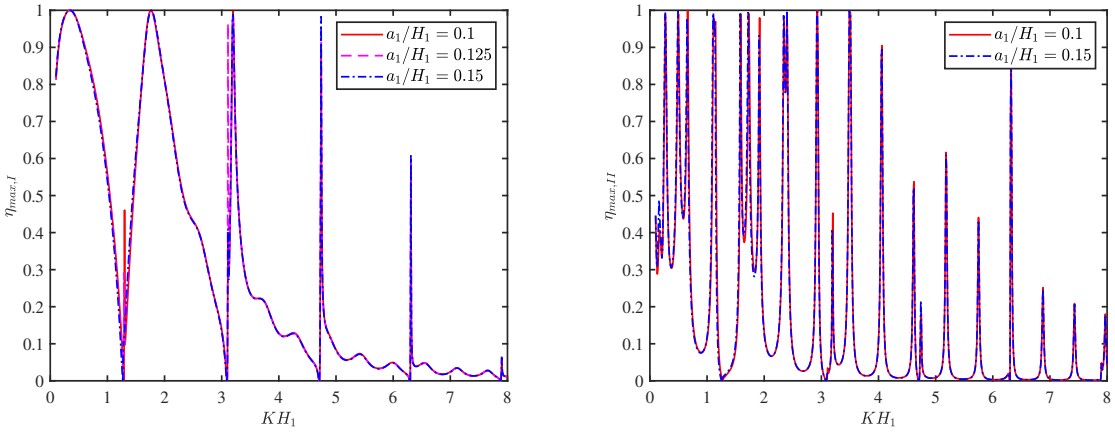

(a) (b)

FIGURE 5.7: Variation of (a) $\eta_{max,I}$, and (b) $\eta_{max,II}$ vs KH_1 for various ripple amplitude a_1

Figs. 5.7(a) and (b) show the variation of the efficiency $\eta_{max,j}$ for $j = I, II$ vs wavenumber KH_1 in the SM and IM respectively for different values of ripple amplitude a_1/H_1 of the bottom profile. In Fig. 5.7(a), the overall resonance pattern in the efficiency curve $\eta_{max,I}$ is similar as shown in Fig. 5.6(a). Further, it is observed that the amplitude of resonance is higher for higher values of ripple amplitude a_1/H_1 for certain values of incident wave frequencies. The overall pattern of the efficiency curve $\eta_{max,II}$ as shown in Fig 5.7(b) is similar to the observations as seen in Fig. 5.4(b). In addition, in the long and intermediate wave regimes, the amplitude of the peaks is slightly higher for the higher values of the ripple amplitude a_1/H_1. The reason behind this phenomenon is that for the higher values of a_1/H_1, the distance between the interface and undulated seabed decreases, which significantly enhances the effect of the undulated seabed on the wave propagation associated with the internal as well as surface wave mode. A similar observation was found in Medina-Rodríguez and Silva [87].

In Figs. 5.8(a) and (b), the variation of the efficiency $\eta_{max,j}$ for $j = I, II$ vs incident wavenumber KH_1 are plotted in the SM and IM respectively for different values of density ratio s. The overall pattern of Fig. 5.8(a) is similar to Fig. 5.5(a). Further, there is a negligible variation

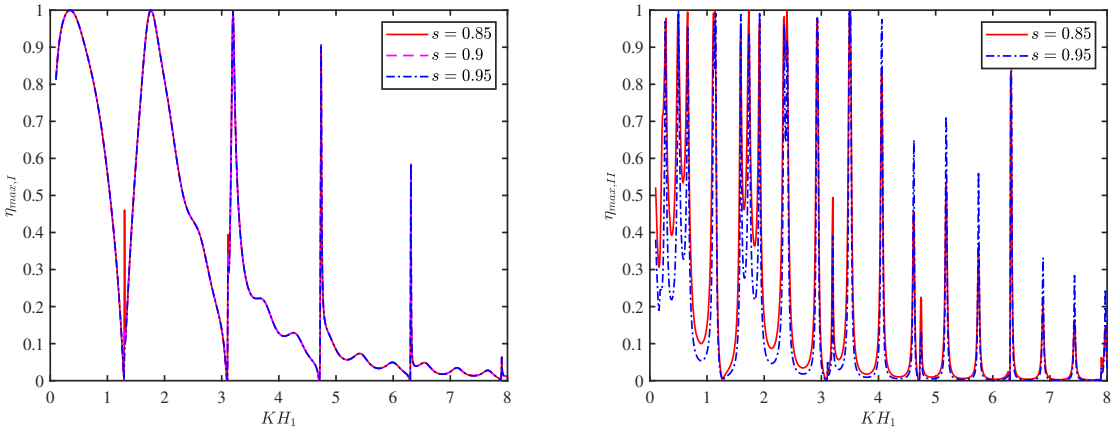

(a) (b)

FIGURE 5.8: Variation of (a) $\eta_{max,I}$, and (b) $\eta_{max,II}$ vs KH_1 for various density ratio s.

observed in the efficiency curve $\eta_{max,I}$ due to variation in density ratios s. Similar observations were reported in Behera et al. [75]. On the other hand, in Fig. 5.8(b), significant variations in the efficiency curve $\eta_{max,II}$ are observed due to the variation in density ratio s for smaller and moderate values of wave number KH_1. Further, it is found that the amplitude of the oscillations in the efficiency curve $\eta_{max,II}$ is higher for the higher values of density ratio s.

5.6.4 Results associated with the IP OWC device

In the present section, the results and discussions associated with the IP OWC device are provided.

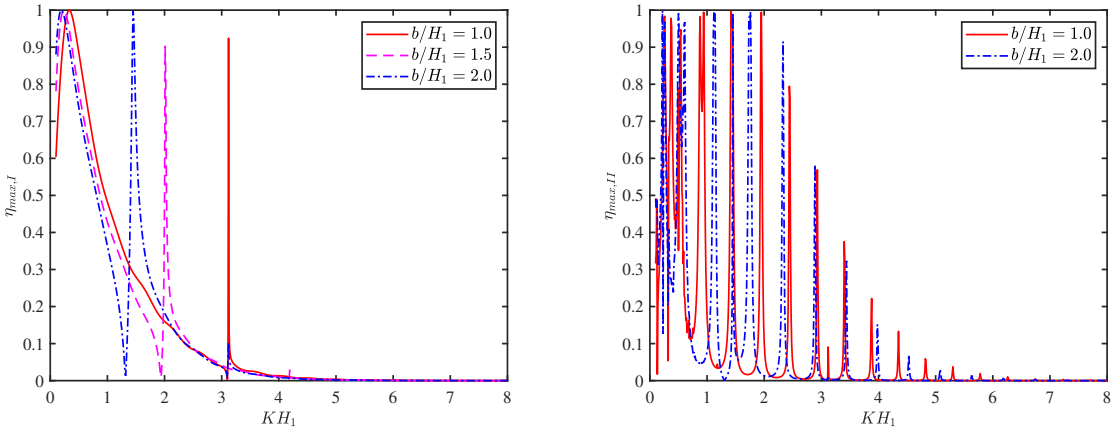

(a) (b)

FIGURE 5.9: Variation of (a) $\eta_{max,I}$, and (b) $\eta_{max,II}$ vs KH_1 for different chamber length b/H_1.

Figs. 5.9(a) and (b) depict the variation of the efficiency $\eta_{max,j}$ for $j = I, II$ versus incident wavenumber KH_1 in the surface mode (SM) and internal mode (IM) respectively for different

chamber lengths b/H_1. In Fig. 5.9(a), it is seen that the efficiency $\eta_{max,I}$ varies in a highly oscillatory manner with the variation in the wavenumber KH_1 smaller and moderate values of wave number KH_1. Further, this oscillatory pattern diminishes for higher values of KH_1. Moreover, it is found that the resonance occurs in the efficiency $\eta_{max,I}$ within $KH_1 < 1.0$ due to the first resonance mechanism (see Koley and Trivedi [26]). In addition, the resonance occurs in the efficiency $\eta_{max,I}$ in wave regime $KH_1 > 1.0$ as a result of the sloshing effect. In Fig. 5.9(b), it is noticed that the efficiency $\eta_{max,II}$ follows a highly oscillatory pattern with the variation in wavenumber KH_1 for smaller and moderate values of wavenumber KH_1, whereas this oscillatory pattern diminishes for higher values of wavenumber KH_1. The reason behind the same is already provided in the discussion of Fig. 5.4(b). A comparison of Fig. 5.9 with Fig. 5.4 reveals that the variation in the efficiency $\eta_{max,j}$ for $j = I, II$ is more in wave regime having smaller KH_1 for INP OWC device as compared to IP OWC device. However, the oscillatory pattern in the efficiency curve $\eta_{max,I}$ is more prominent in the wave regime having higher KH_1 for IP OWC devices.

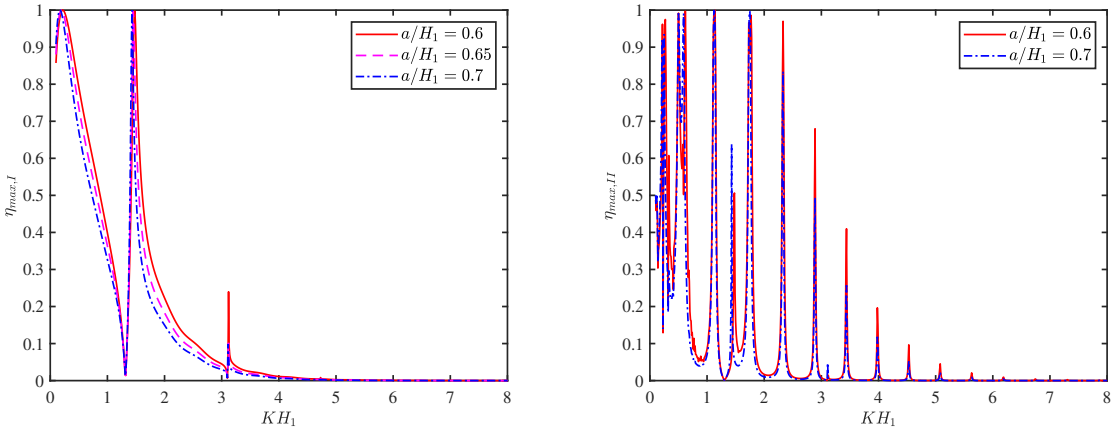

(a) (b)

FIGURE 5.10: Variation of (a) $\eta_{max,I}$, and (b) $\eta_{max,II}$ vs KH_1 for different chamber length a/H_1.

In Figs. 5.10(a) and (b), the variation of the efficiency $\eta_{max,j}$ for $j = I, II$ are plotted as a function of the incident wavenumber KH_1 in the SM and IM wave modes, respectively, for different submergence depth of the front wall a/H_1 of the device. In Fig. 5.10(a), it is observed that for smaller wavenumber (i.e., $KH_1 < 1.0$), the amplitude of the resonance in the efficiency curve $\eta_{max,I}$ increases with a decrease in the submergence depth a/H_1. Moreover, for moderate values of KH_1, the amplitude of the resonance is higher for the smaller values of a/H_1. This happens due to the fact that as the incident waves become shorter, the waves can't easily enter into the device chamber, having a higher draft of the front wall. The details about the resonating wave frequencies are provided in the discussions of Fig. 5.4(a). A careful observation reveals that for $a/H_1 = 0.6$, the area under the efficiency curve is more. This result indicates that the smaller

submergence depth of the front wall of the OWC device plays an important role to increase the hydrodynamic efficiency $\eta_{max,I}$ of the OWC device. On the other hand, as $a/H_1 \to 0.7$, the variation of the air volume in the OWC chamber decreases. This reduces the capture wave power of the OWC device. Similar observations found in Ning et al. [116]. Further, the overall oscillatory pattern of the efficiency curve $\eta_{max,II}$ as seen in Fig. 5.10(b) is similar in nature to that of Fig. 5.9(b). A comparison between Fig. 5.5(b) and 5.10(b) shows that the variation in the efficiency $\eta_{max,II}$ for INP OWC device and IP OWC device follow the oscillatory pattern in the wave regimes associated with smaller and moderate wavenumbers. Further, this oscillatory pattern diminishes for higher wavenumbers KH_1 for the IP OWC device.

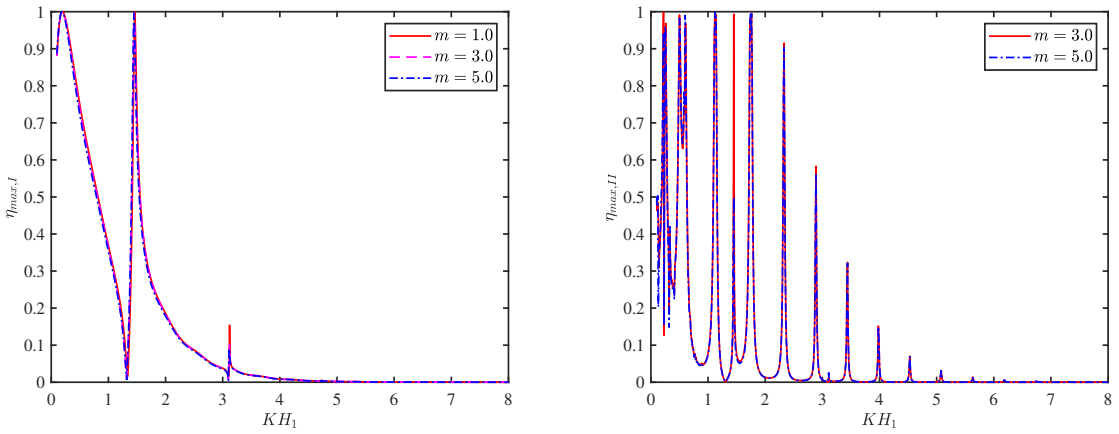

FIGURE 5.11: Variation of (a) $\eta_{max,I}$, and (b) $\eta_{max,II}$ vs KH_1 for various number of ripples m.

Figs. 5.11(a) and (b) demonstrate the variation of the efficiency $\eta_{max,j}$ for $j = I, II$ versus wavenumber KH_1 in the SM and IM respectively for different number of ripples m of the sinusoidally varying bottom profile. In Fig. 5.11(a), it is found that the variation in the efficiency curve is higher for the sinusoidally varying bottom having higher ripples for smaller KH_1. Further, it is noticed that no significant variation is observed in the efficiency curve $\eta_{max,I}$ with the change in ripples number m for higher values of KH_1. The overall pattern of the efficiency curve $\eta_{max,II}$ as shown in Fig. 5.11(b) is similar in nature as that of Fig. 5.10(b).

In Figs. 5.12(a) and (b), the variation of the efficiency $\eta_{max,j}$ for $j = I, II$ versus incident wavenumber KH_1 in the SM and IM are plotted respectively for different values of ripple amplitude a_1/H_1 of the sinusoidally varying bottom profile. Fig. 5.12(a) demonstrates that for smaller wavenumbers KH_1, the variation in the efficiency curve $\eta_{max,I}$ is higher for higher values of ripple amplitude a_1/H_1 of the sinusoidally varying bottom profile. The reason for the same is that for higher values of a_1/H_1, the distance between the interface $z = -h$ and seabed decreases, and consequently, the effect of the seabed on the wave propagation increases due to the transfer of energy from internal mode to surface mode and vice versa. A comparison between Figs. 5.12(a) and (b) shows that for smaller values of wavenumber KH_1, the effect of the seabed

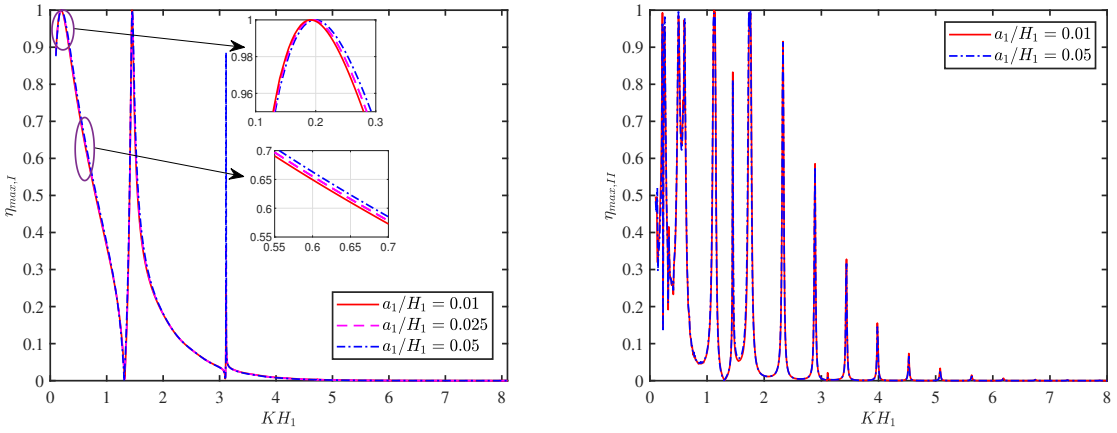

(a) (b)

FIGURE 5.12: Variation of (a) $\eta_{max,I}$, and (b) $\eta_{max,II}$ vs KH_1 for various ripple amplitudes a_1/H_1.

on the efficiency $\eta_{max,II}$ is more as compared to the effect of the bottom on the efficiency $\eta_{max,I}$. A comparison of Fig. 5.12 with Fig. 5.7 illustrates that for smaller and moderate values of wavenumber KH_1, the overall pattern of the efficiency curve $\eta_{max,j}$ for $j = I, II$ is similar in nature for INP OWC device and IP OWC device. On the other hand, for IP OWC device, there is no significant variation observed in the efficiency $\eta_{max,j}$ for $j = I, II$ in the wave regime corresponds to smaller wavenumbers KH_1.

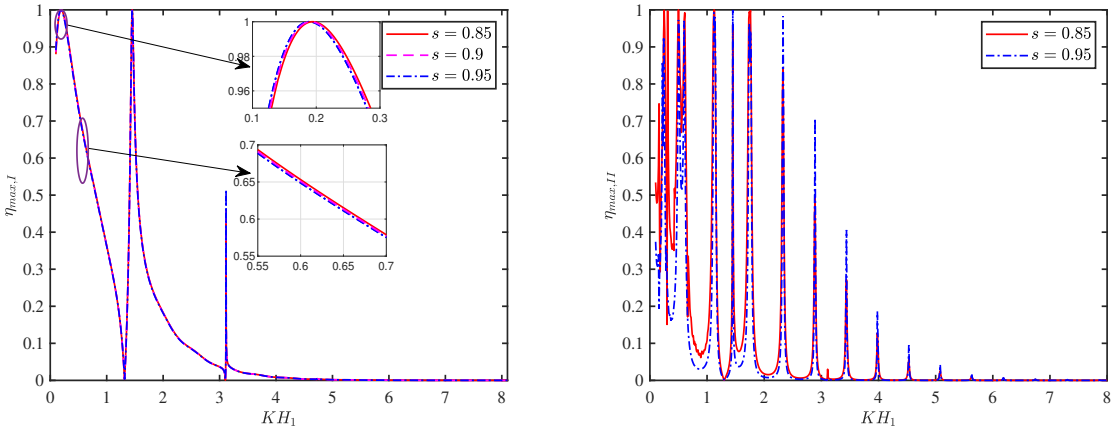

(a) (b)

FIGURE 5.13: Variation of (a) $\eta_{max,I}$, and (b) $\eta_{max,II}$ vs KH_1 for various density s.

In Figs. 5.13(a) and (b), the variation of the efficiency $\eta_{max,j}$ for $j = I, II$ vs wavenumber KH_1 in the SM and IM are plotted respectively for different values of density ratio s. The overall pattern of Fig. 5.13 is similar to the Fig. 5.12. Further, it is observed that the variation in the efficiency curve decreases with an increase in density ratio s. This happens as the values of

surface and internal mode becomes close to each other as the density ratio s increases. Similar observation was found in Medina-Rodríguez and Silva [87].

5.7 Time-dependent simulations

In this section, the numerical simulation of the time-dependent free surface elevation $\zeta_c(x,t)$ is provided. Here, the Fast Fourier transform is used to analyze the free surface elevation $\zeta_c(x,t)$. In general, high frequencies of the incident waves are used for the Fast Fourier Transform (FFT). Further, the free surface elevation $\zeta_c(x,t)$ is calculated using the following Fourier integral (see Kar et al. [139])

$$\zeta_c(x,t) = \Re\left\{\int_{-\infty}^{\infty} \tilde{f}(\sigma)\zeta(x,\sigma)e^{-\mathrm{i}\sigma t}d\sigma\right\}. \tag{5.61}$$

Here, $\tilde{f}(\sigma)$ is the Fourier transform of the incoming wave pulse, and $\zeta(x,\sigma)$ is the free surface displacement of the internal and external free surfaces. In addition, $\zeta(x,\sigma)$ is frequency-dependent. It is to be noted that the incoming wave pulse is considered as a Gaussian wave packet with an appropriate spreading function and central frequency. Here, the form of Gaussian wave packet is given by (see Mohanty and Sidharth [140])

$$\tilde{f}(\sigma) = \sqrt{\frac{\tilde{r}}{\pi}}e^{-\tilde{r}\,(\sigma-\sigma_c)^2}. \tag{5.62}$$

Here, $\tilde{r}$, and σ_c are termed as spreading function and central frequency of the incoming wave pulse respectively.

Figs. 5.14, 5.15, 5.16, and 5.17 depict the change in free surface elevation and interface elevation $\zeta_c(x,t)$ as a function of x and for different time instant t corresponding to the incident wavenumber k_I and k_{II}, respectively in presence of INP OWC device. All figures demonstrate the combination of scattered and radiated waves in the internal and external free surfaces. In Figs. 5.14 and 5.15, the blue line corresponds to the external free surface elevation, and the red line corresponds to the internal free surface elevation. Further, in Figs. 5.16 and 5.17, the blue line corresponds to the interface elevation. All the figures show the non-periodic pattern in the free surface and interface elevations which occurs due to the mutual interaction between the scattered and radiated waves. Moreover, the figures illustrate that the OWC device can capture and retain wave energy for extended periods of time. A comparison between Figs. 5.14 and 5.16 reveal that the amplitude of free surface elevation is higher than the interface elevation when the incident wave contains the wavenumber k_I. On the other hand, a comparison between Figs. 5.15 and 5.17 reveal that the amplitude of free surface elevation is lower than the interface elevation when the incident wave contains the wavenumber k_{II}. Similar observations were reported in Koo [74]. Moreover, in all the figures, certain peaks in the free surface and interface elevations are observed. This happens due to the occurrences of resonance, as shown in Figs. 5.4-5.13. It is

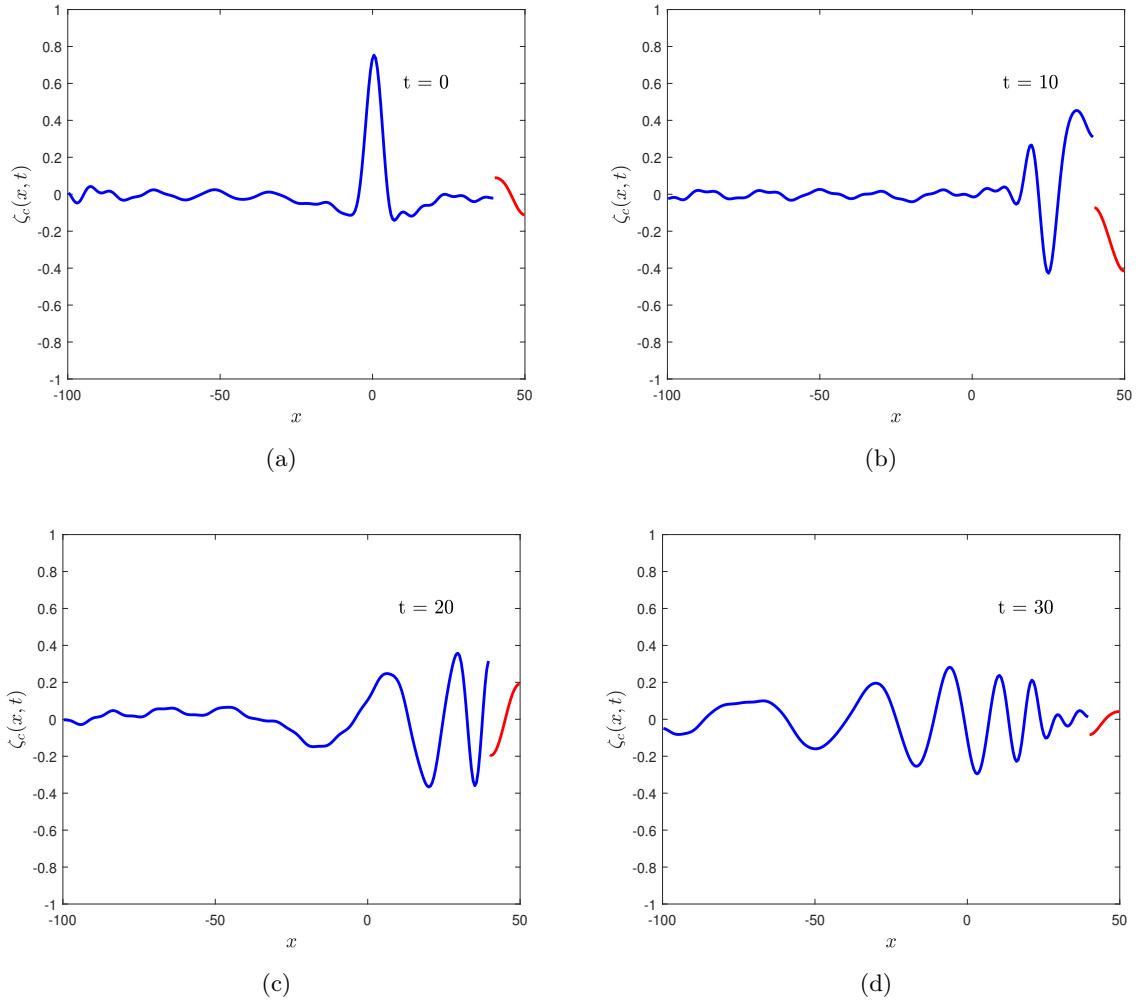

FIGURE 5.14: Variation of free surface elevation $\zeta_c(x,t)$ vs x associated with the wavenumber k_I in presence of INP device for different time (a) $t = 0$, (b) $t = 10$, (c) $t = 20$, and (d) $t = 30$.

to be noted that, the liquid level inside the chamber is not horizontal as all the possible wave frequencies are considered for time-domain simulations. So, the time domain simulation figures represent the free surface elevations associated with irregular incident waves. Further, the free surface elevations plotted in the present manuscript are combination of scattered and radiated waves. Due to these reasons, the free surface elevation inside the chamber is not horizontal.

Figs. 5.18, 5.19, 5.20, and 5.21 illustrate the variation in free surface elevation and interface elevation $\zeta_c(x,t)$ as a function of x and for different time instant t associated with the incident wavenumber k_I and k_{II} respectively in the presence of IP OWC device. All figures demonstrate the combination of scattered and radiated waves in the internal and external free surfaces. In Figs. 5.18 and 5.19, the blue and red lines show the external and internal free surface elevations, respectively. Moreover, in Figs. 5.20 and 5.21, the blue and red lines are associated with the external and internal interface elevations, respectively. A comparison between Fig. 5.18 with Fig. 5.20 depicts that in the presence of incident wave mode k_I, the free surface elevation is

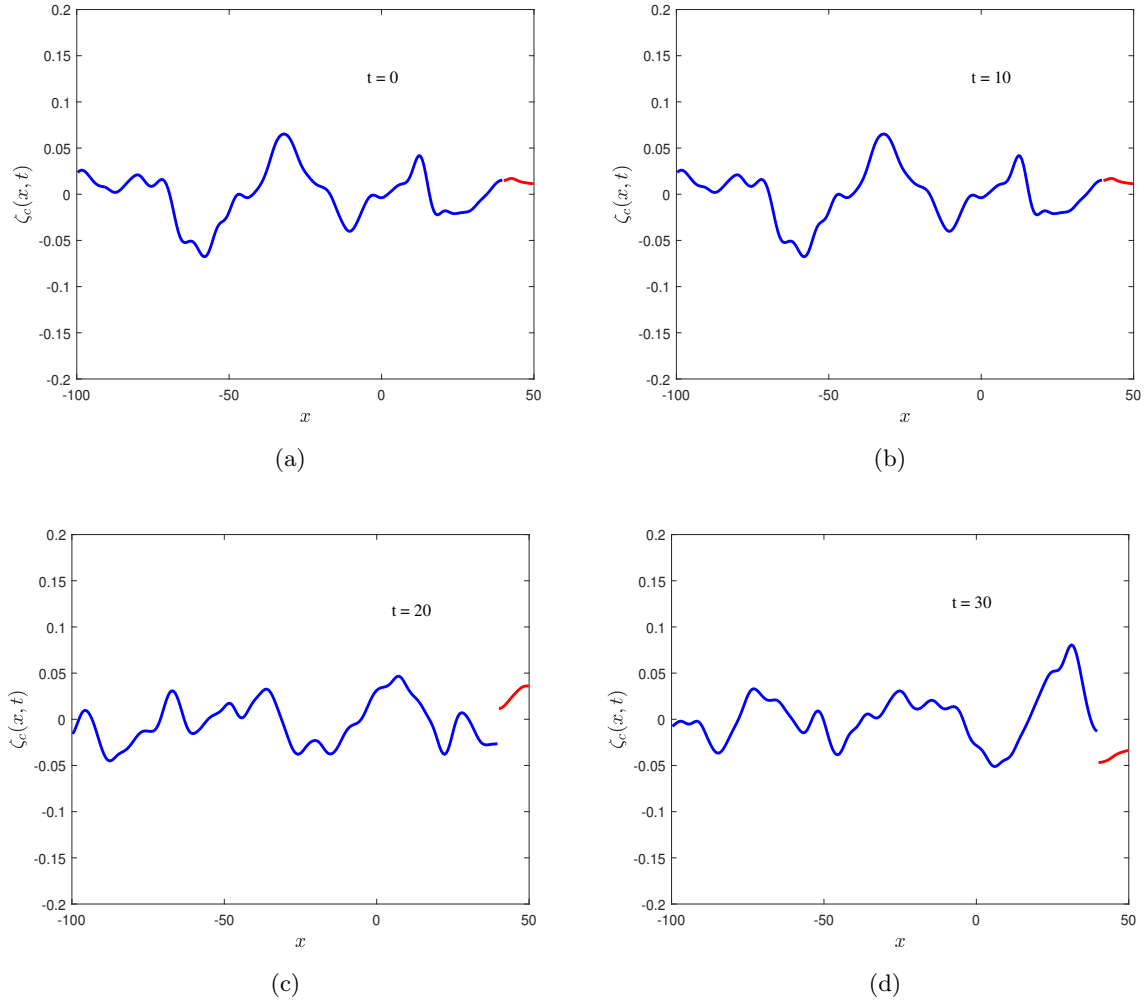

FIGURE 5.15: Variation of free surface elevation $\zeta_c(x,t)$ vs x associated with the wavenumber k_{II} in presence of INP device for different time (a) $t = 0$, (b) $t = 10$, (c) $t = 20$, and (d) $t = 30$.

higher than the interface elevation. Moreover, Figs. 5.19 and 5.21 show that when the incident wave contains the wave mode k_{II}, the variation in the interface elevation is highly oscillatory in nature as compared to the free surface elevation. This phenomenon occurs due to the sloshing effect as discussed in Fig. 5.9. Moreover, this sloshing effect is more prominent for IP OWC devices as IP OWC device behaves like a closed rectangular tank. The figures also depict the resonance behavior of the waves, which occurs due to the mutual interaction of scattered and radiated waves.

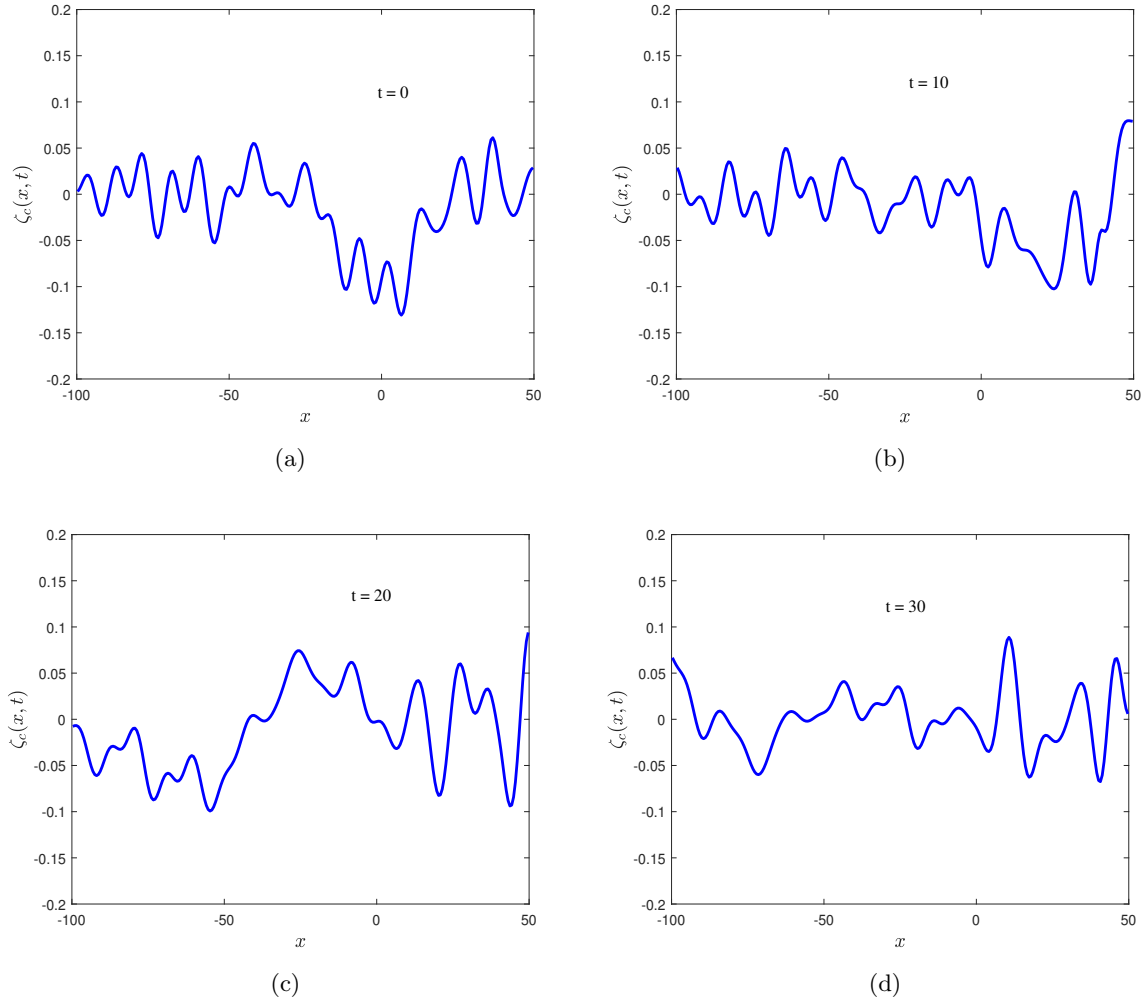

FIGURE 5.16: Variation of interface elevation $\zeta_c(x,t)$ vs x associated with the wavenumber k_I in presence of INP device for different time (a) $t = 0$, (b) $t = 10$, (c) $t = 20$, and (d) $t = 30$.

5.8 Effect of air compressibility on the hydrodynamic performance of the OWC devices

In the present section, the effect of air compressibility on the hydrodynamic performance and efficiency of the (i) INP OWC device and (ii) IP OWC device are provided. The addition of an imaginary term to the turbine proportionality constant is similar to the springlike effect of air compressibility (see Sarmento and Falcão [141], Falcão et al. [142] for details). Due to the presence of air compressibility, Eq. (5.55) is rewritten as

$$q_j = \left(\wedge - \frac{\mathrm{i}\omega V_0}{\gamma p_a} \right) p. \tag{5.63}$$

Here, $\wedge$ is a real positive constant termed as control parameter and $V_0 = 2400\mathrm{m}^3$ is the air volume above the internal free surface Γ_4 (within the device chamber) in the undisturbed state.

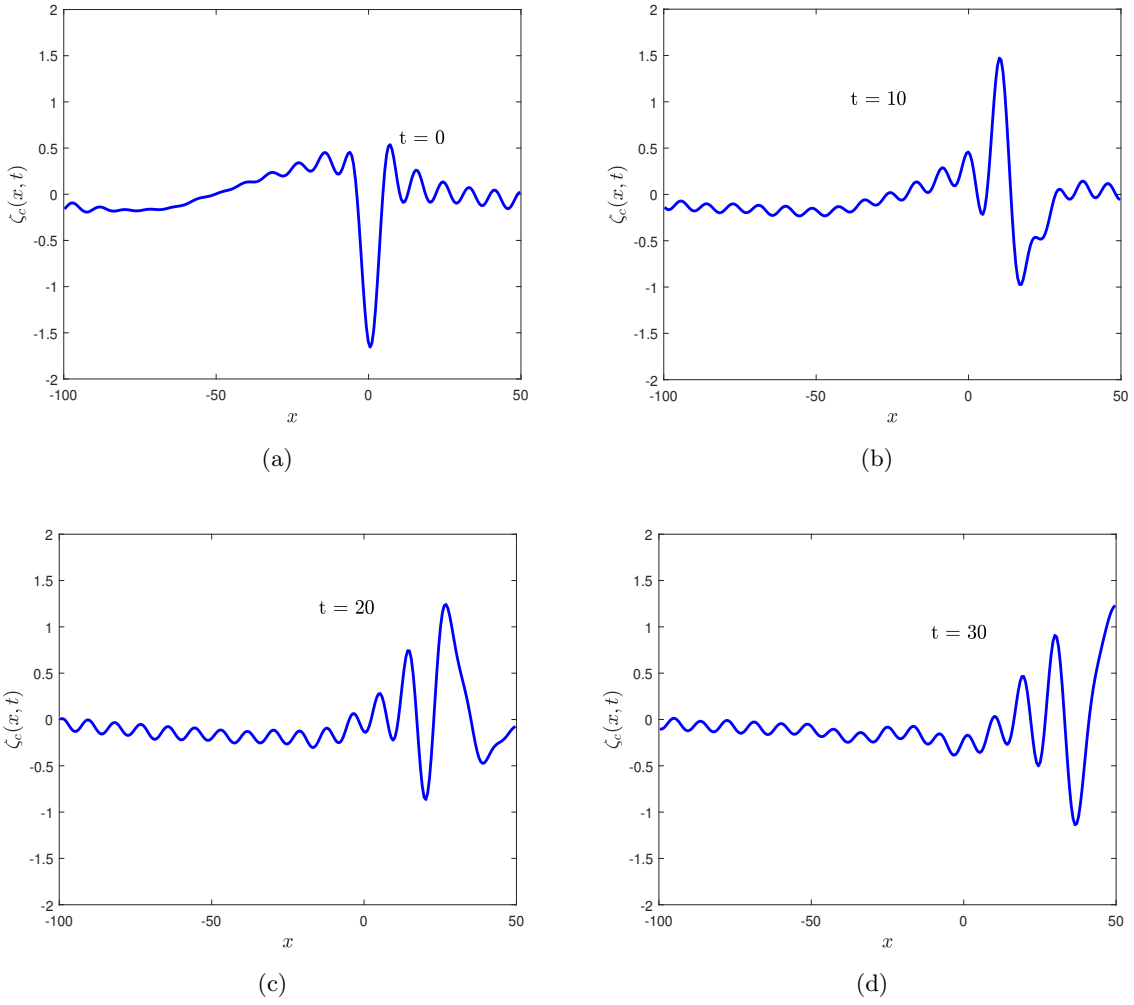

FIGURE 5.17: Variation of interface elevation $\zeta_c(x,t)$ vs x associated with the wavenumber k_{II} in presence of INP device for different time (a) $t = 0$, (b) $t = 10$, (c) $t = 20$, and (d) $t = 30$.

In addition, $\gamma = 1.4$ and $P_a = 1.013 \times 10^5$Pa are symbolized as specific heat ratio of the air and atmospheric air pressure, respectively. Further, in the presence of air compressibility, the expressions for the maximum efficiencies $\eta_{max,j}, \quad j = I, II$ corresponding to the incident wave modes k_I and k_{II} are represented as

$$\eta_{max,j} = \left(\frac{2\tilde{B}_j}{\wedge_{opt} + \tilde{B}_j} \right), \quad \wedge_{opt} = \sqrt{\left(\tilde{A}_j + \frac{\omega V_0}{\gamma p_a} \right)^2 + \tilde{B}_j{}^2}, \quad \text{for} \quad j = I, II. \tag{5.64}$$

Moreover, the non-dimensional form of $\eta_{max,j}, \quad j = I, II$ can be expressed as

$$\eta_{max,j} = \frac{2\nu_j}{\nu_j + \sqrt{\nu_j^2 + \left(\mu_j + \frac{\omega V_0}{\gamma p_a} \frac{\rho_1 g}{\sigma b} \right)^2}}, \quad \text{for} \quad j = I, II. \tag{5.65}$$

Figs. 5.22 and 5.23 illustrate the effect of air compressibility on the efficiency $\eta_{max,j}$ for $j = I, II$

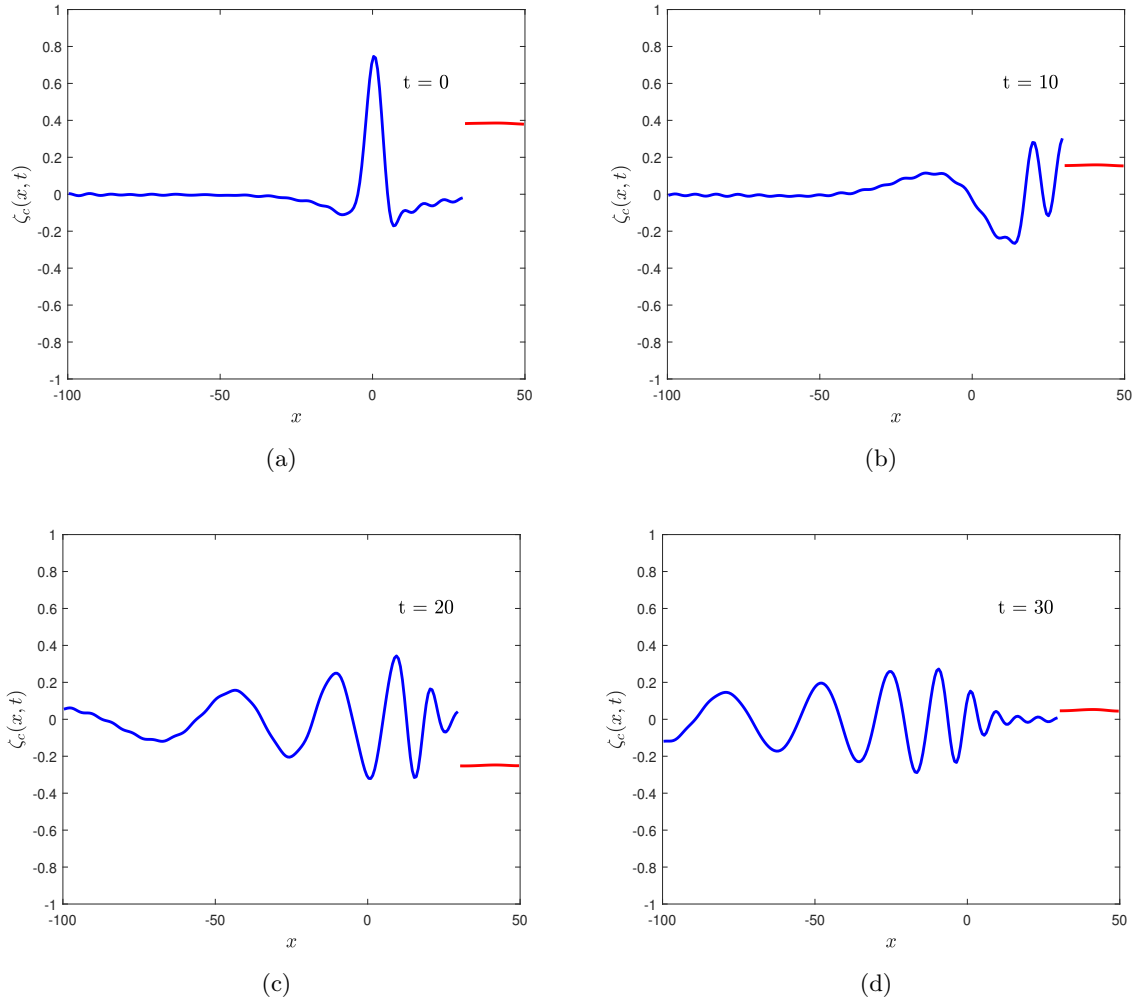

FIGURE 5.18: Variation of free surface elevation $\zeta_c(x,t)$ vs x associated with the wavenumber k_I in presence of IP device for different time (a) $t = 0$, (b) $t = 10$, (c) $t = 20$, and (d) $t = 30$.

for both the INP and IP OWC devices in the SM and IM, respectively. In Figs. 5.22(a) and 5.23(a), it is found that the air compressibility enhances the efficiency $\eta_{max,I}$ associated with the incident wave mode k_I for smaller values of T_0. Whereas, an opposite trend is observed for higher values of T_0. Further, Figs. 5.22(b) and 5.23(b) demonstrate that the efficiency $\eta_{max,II}$ enhances and diminishes alternately as the incident time period T_0 increases. This phenomenon can be explained by Eq. (5.65). It is to be noted that the radiation susceptance parameters μ_j for $j = I, II$ may be positive, negative, or zero depending on the OWC device geometry and the wave frequency ω (see Evans and Porter [5] (Fig. (2)), and Koley and Trivedi [26] (Fig. 7(a)) for details). It is found that when $\mu_j < 0$, the quantity $\left(\mu_j + \frac{\omega V_0}{\gamma p_a}\frac{\rho_1 g}{\sigma b}\right)^2 < \mu_j^2$ for $j = I, II$. Therefore, the efficiency $\eta_{max,j}$ for $j = I, II$ increases. As a result, air compressibility improves the hydrodynamic efficiency of the OWC device. On the other hand, when $\mu_j > 0$, the quantity $\left(\mu_j + \frac{\omega V_0}{\gamma p_a}\frac{\rho_1 g}{\sigma b}\right)^2 > \mu_j^2$ for $j = I, II$, and consequently, the efficiency $\eta_{max,j}$ for

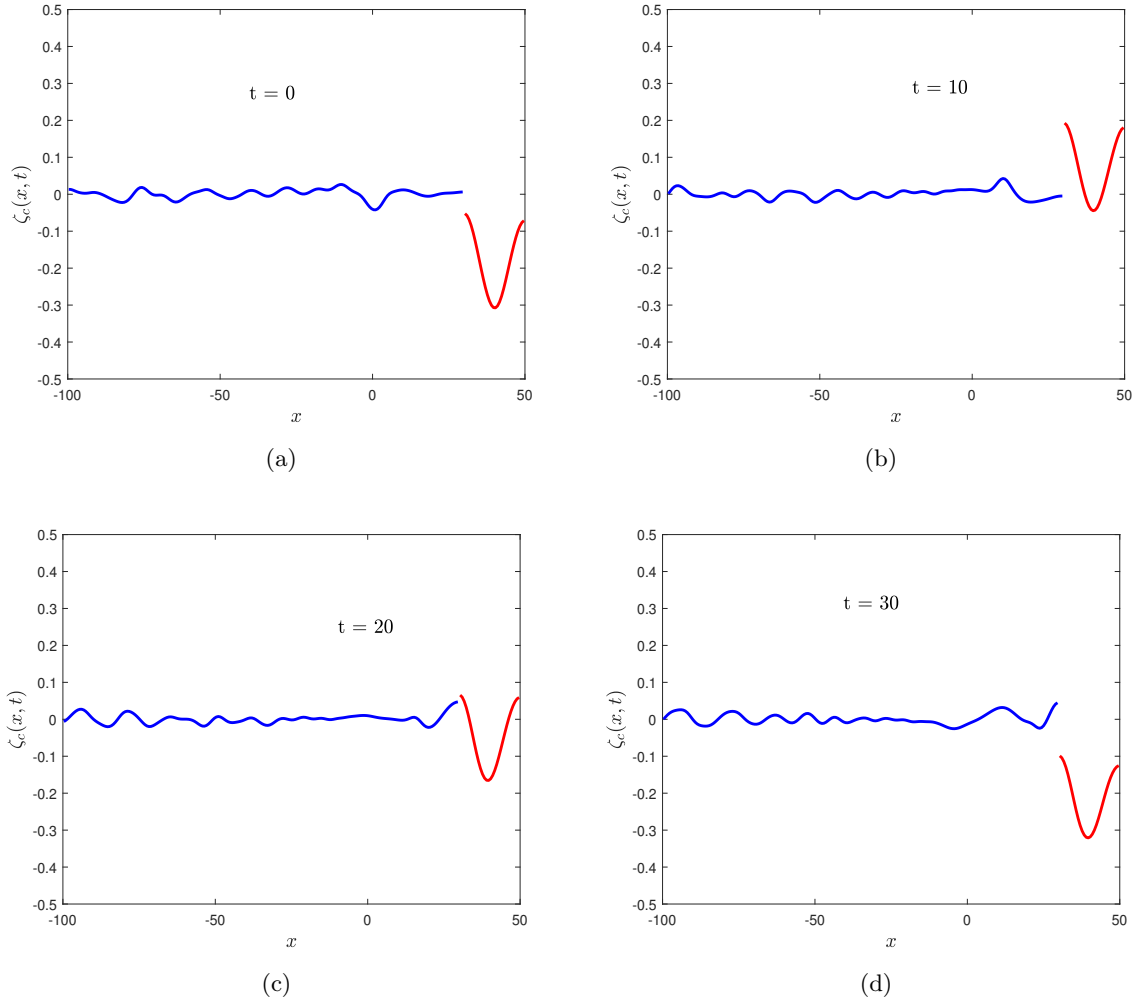

FIGURE 5.19: Variation of free surface elevation $\zeta_c(x,t)$ vs x associated with the wavenumber k_{II} in presence of IP device for different time (a) $t = 0$, (b) $t = 10$, (c) $t = 20$, and (d) $t = 30$.

$j = I, II$ decreases in the presence of air compressibility. Similar observations were reported in Falcão and Henriques [143], and Falcão et al. [142].

5.9 Conclusions

The present study investigates the hydrodynamic performance of two different oscillating water column devices, namely (i) INP device and (ii) IP device placed over the undulated seabed in a two-layer fluid system. The boundary element method is used to solve the associated boundary value problems. Detailed derivations for various parameters related to the performance of the OWC devices, such as the radiation conductance and susceptance coefficients, volume fluxes associated with the scattered potentials, and hydrodynamic efficiencies corresponding to the surface and internal modes, are provided. Further, the free surface and interface elevations are studied in time-domain analysis. The present study leads to the following conclusions:

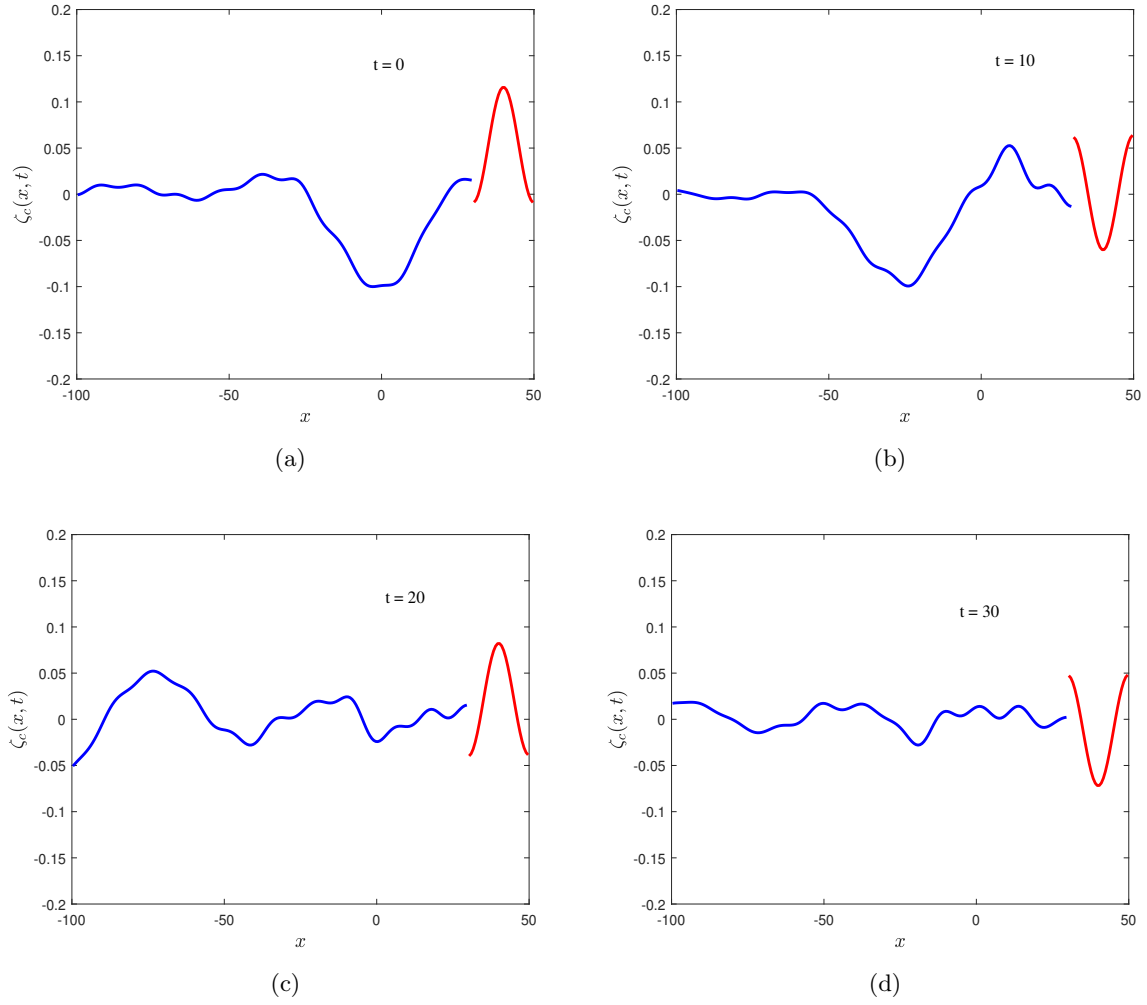

FIGURE 5.20: Variation of interface elevation $\zeta_c(x,t)$ vs x associated with the wavenumber k_I in presence of IP device for different time(a) $t = 0$, (b) $t = 10$, (c) $t = 20$, and (d) $t = 30$.

- For the INP OWC device, the resonance occurs in the efficiency curve $\eta_{max,I}$ due to the variation in chamber length, and the draft of the front wall of the device is similar to the single-layer fluid case. On the other hand, the efficiency $\eta_{max,II}$ varies in a highly oscillatory manner with the variation in incident wavenumber. This highly oscillatory pattern, which occurs due to the exchange of energy between the surface and internal waves, diminishes in the wave regime having higher KH_1 for smaller values of chamber length and for larger front wall draft. Further, resonating interaction between the internal waves with the rippled bottom also plays a major role in the highly resonating pattern of the efficiency $\eta_{max,II}$ curve.

- Moreover, the highly oscillatory pattern in $\eta_{max,II}$ occurs due to the distribution of incoming wave energy associated with the internal wave mode k_{II} to cover a broadband spectrum.

- Due to the multiple resonances and near-resonance interactions of waves with the bottom ripples, the amplitude of resonance in the $\eta_{max,II}$ curve is higher for higher values of

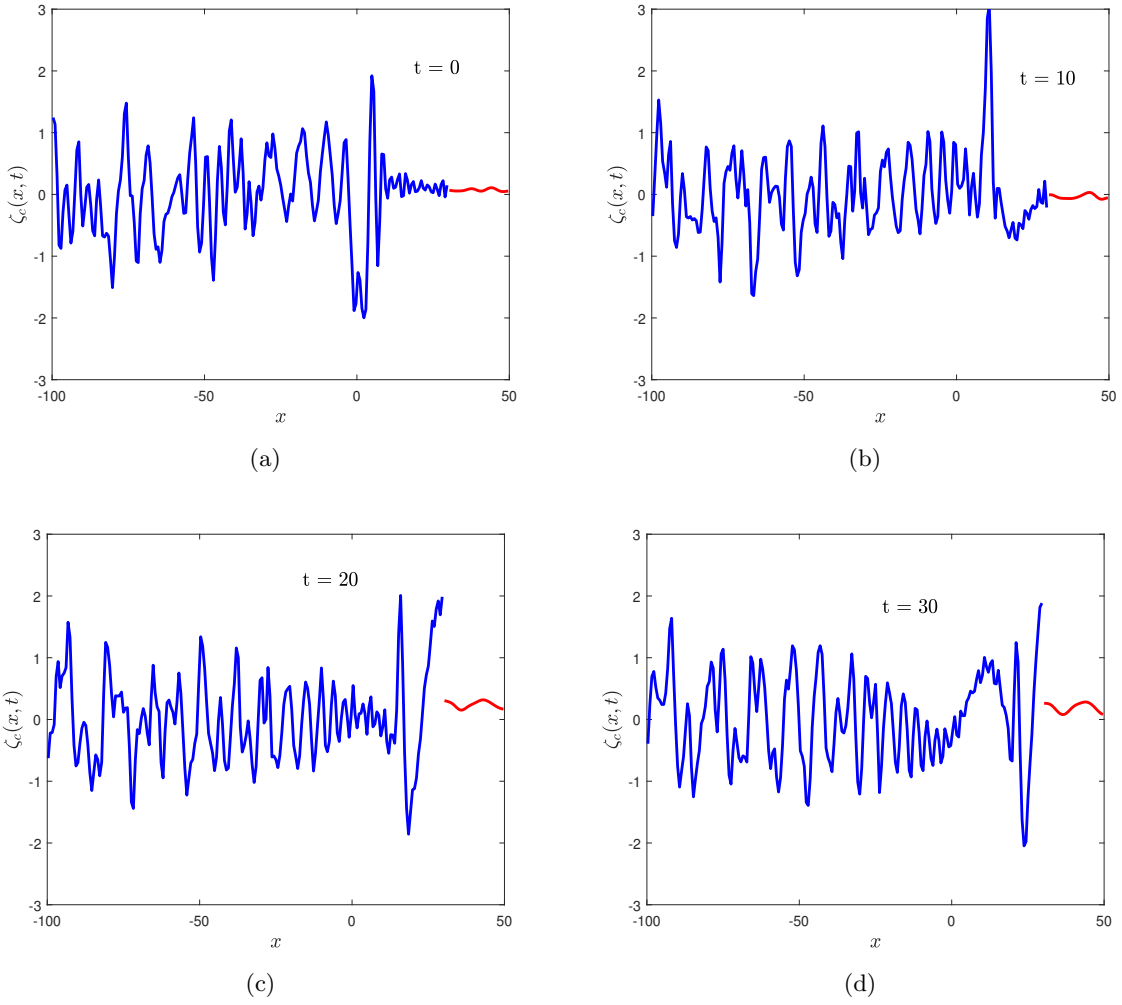

FIGURE 5.21: Variation of interface elevation $\zeta_c(x,t)$ vs x associated with the wavenumber k_{II} in presence of IP device for different time (a) $t = 0$, (b) $t = 10$, (c) $t = 20$, and (d) $t = 30$.

bottom ripple amplitude for certain values of incident wave frequencies.

- For IP OWC devices, the pattern of the efficiency curves $\eta_{max,j}$ (for $j = I, II$) are highly oscillatory in nature in the wave regions having smaller and moderate KH_1 values. The sloshing effect plays a prominent role in this highly oscillatory pattern along with other effects, as mentioned earlier.

- For the INP OWC device, significant variations are observed in the efficiency curve $\eta_{max,II}$ due to the variation in density ratio of the two layers of fluids. A similar pattern is observed for IP OWC devices. However, this oscillatory pattern diminishes for smaller wave numbers KH_1.

- For the INP OWC device, the free surface elevation is higher than interface elevation in the presence of surface wave mode. On the other hand, due to the presence of internal wave

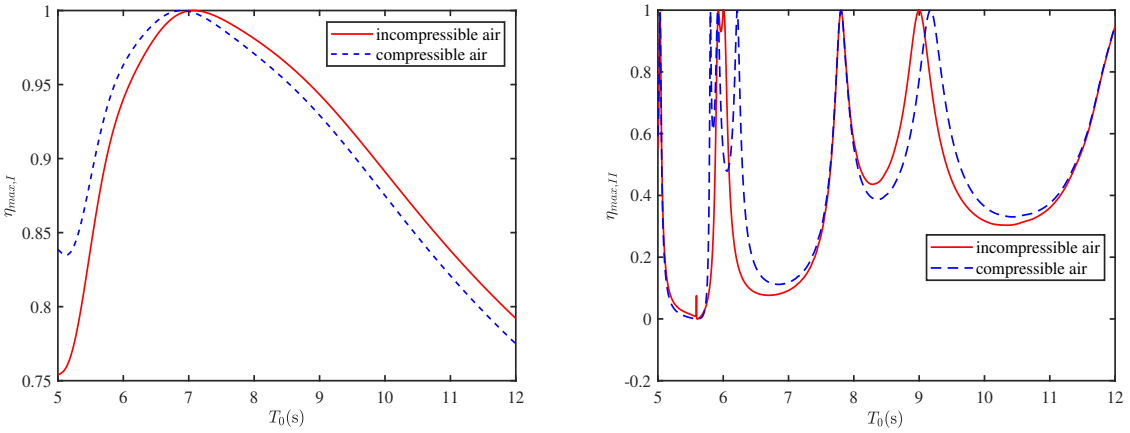

(a) (b)

FIGURE 5.22: Variation of (a) $\eta_{max,I}$, and (b) $\eta_{max,II}$ vs T_0 for INP OWC device without and with air compressibility.

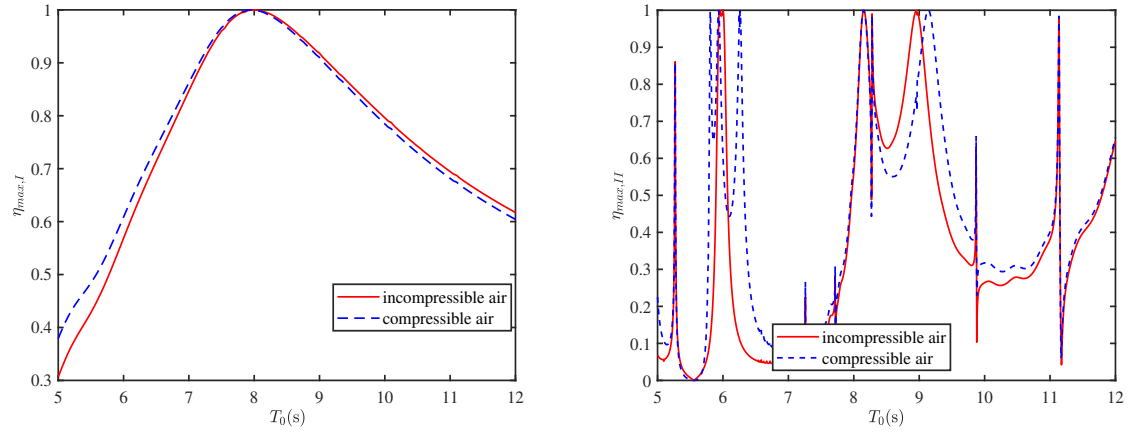

(a) (b)

FIGURE 5.23: Variation of (a) $\eta_{max,I}$, and (b) $\eta_{max,II}$ vs T_0 for IP OWC device without and with air compressibility.

mode, the interface elevation is higher than the free surface elevation. Similar observations are reported for the IP OWC device.

- Air compressibility enhances the efficiency associated with surface mode of the OWC device for shorter incident waves and an opposite trend is observed for longer incident waves. Further, the air compressibility enhances and diminishes the efficiency associated with internal mode alternately as the incident time period increases.

In summary, it is concluded that the hydrodynamic performance of the OWC devices can be enhanced significantly with the appropriate combinations of shape parameters associated with the OWC device and seabed.

Chapter 6

Summary and future work

This chapter summarizes the results and findings obtained in the thesis, the limitations of models used in the present research, and the scope of possible extensions of the present study and future investigations.

6.1 Conclusions

The purpose of this thesis is to develop appropriate numerical tools in order to analyze the working mechanism and hydrodynamic efficiency of the wave energy converter devices such as oscillating water column device and piezoelectric plate wave energy converter devices. Major emphasis is given to investigate the resonating frequencies that occur, which maximizes the power output and, consequently, the efficiency of the devices under the action of regular and irregular incident waves generated in single and two-layer fluid systems. The effect of real seabed topography is considered in most of the problems. Both the frequency and time-domain analysis are carried out. The salient conclusions and contributions of the present study are the following:

In Chapter 1, a detailed literature review and the mathematical background of water wave interaction with OWC and PWEC devices and the associated derivations are provided under the assumption of linear wave-structure interaction theory. In the present thesis, a BEM-based numerical solution technique is adopted to solve a class of physical problems associated with the hydrodynamics of OWC and PWEC devices. The background of constant and linear elements based BEM numerical techniques is reviewed in this chapter.

Chapter 2 deals with the mathematical modeling of the oscillating water column wave energy converter device placed over the undulated seabed. The seabed undulation is finitely extended, and beyond that, the water bed is uniform in nature. Scattering and radiation of the water waves by the oscillating water column are studied in the context of linear water wave theory.

The mathematical problem is studied in the two-dimensional Cartesian coordinate system under the assumptions of small amplitude water wave theory. To solve the associated boundary value problem, a coupled eigenfunction expansion - boundary element method is used. Various important physical parameters, such as the radiation conductance and susceptance coefficients and volume flux associated with the hydrodynamic performance and efficiency of the OWC device are analyzed for a wide range of wave and structural parameters. The convergence of the numerical computations based on the coupled eigenfunction expansion-boundary element method is provided. Further, various resonance mechanisms associated with the shapes and structural configurations of the OWC device are analyzed. Further, two-types of seabed profiles, namely type-I profile (including depression, concave, sloping, and protrusion), and type-II profile (sinusoidally) are considered.

In Chapter 2, the hydrodynamic performance of the OWC device is analyzed in the presence of regular incident waves. However, in real sea conditions, the incident waves are mostly irregular in nature and can be modeled as a superposition of wave components with different frequencies. Therefore, it is very important to analyze the performance and efficiency of the OWC device under irregular/random waves.

In Chapter 3, the performance of breakwater-integrated OWC (oscillating water column) wave energy converter devices is analyzed under the action of unidirectional regular and irregular incident waves. Two different types of OWC devices: (i) type I (LIMPET device having sloping front and rear walls) and (ii) type II (quarter-circle-shaped front wall) OWC devices are considered for the present study. The associated boundary value problem is handled using the boundary element method. Various important physical parameters, such as the radiation conductance and susceptance coefficients and volume flux associated with the hydrodynamic performance and efficiency of the OWC device, are analyzed for a wide range of wave and structural parameters. Detailed derivations of the parameters associated with the performance of the OWC devices under the action of irregular waves are provided. Further, The local wave climate can be modeled using a stationary ergodic process. To analyze the efficiency of the OWC devices in real sea conditions, the Bretschneider Spectrum is taken as the incident wave spectrum along with nine sea states representing the local wave climate at the OWC plant site in Pico, Portugal. The annual-averaged plant efficiencies of the two aforementioned OWC devices are analyzed as a function of chamber length, submergence depth, turbine rotor diameter, and rotational speed of the Wells turbine.

In Chapters 2 and 3, the hydrodynamic performance of the stand-alone OWC device is analyzed. However, the concept of wave energy converters with flexible structures and hybrid multi-energy systems appears to be a new trend in the marine energy industry.

In Chapter 4, the hydrodynamic performance of a hybrid wave energy converter device consisting of a piezoelectric plate and the oscillating water column wave energy converter device placed over

an undulated seabed is investigated. Major emphasis is given to analyze the power extraction of the hybrid wave energy converter device, piezoelectric plate, and the OWC devices for various values of incident wave parameters and shape parameters associated with the hybrid wave energy converter device and undulated seabed. Moreover, the time-domain analysis is carried out by considering the Bretschneider spectrum as the incident wave spectrum for irregular incident waves. A multi-parameter optimization based on the Taguchi method is provided.

In Chapters 2, 3, and 4, the hydrodynamic performance and efficiency of the oscillating water column device and piezoelectric plate are investigated under the action of regular and irregular incident waves generated in a single-layer fluid domain. In some coastal areas, water density is not uniform throughout the water depth due to the (i) mixing of fresh river water with the saline seawater and (ii) solar heating of the upper layer water. As a result, the two-layer fluid model is often used to study the interaction of water waves with coastal structures in estuaries.

In Chapter 5, the hydrodynamic performance of the two types of oscillating water column wave energy converter devices, namely (i) INP (interface non-piercing) OWC device and (ii) IP (interface piercing) OWC device placed over an undulated seabed in a two-layer fluid system are investigated. The boundary element method is used to handle the associated boundary value problems. Major emphasis is given to analyze the efficiency of the OWC devices for various values of incident wave parameters and shape parameters associated with the OWC devices and undulated seabed. Further, the time-domain analysis is provided in which the free surface and interface elevations are demonstrated for different instants of time.

All of the results obtained in Chapters 2-5 are very useful in constructing and designing effective wave energy converter devices, such as oscillating water column devices and piezoelectric plate devices under the action of regular and irregular incident waves in the presence of single and two-layer fluid domains. Furthermore, the numerical tool used here, which is based on the boundary element method, can be extended to analyze a wide range of wave-structure interaction problems that arise in the fields of coastal and offshore engineering, as well as in related branches of mathematical physics. The present solution methodology is robust and can easily handle more complex structural shapes and configurations.

6.2 Major Research Developments and Findings

Chapter 2 illustrates that the resonance occurs for certain values of wave parameters, and the same will increase the hydrodynamic efficiency of the OWC device to unity. These resonances occur for certain suitable combinations of chamber width and the submergence depth of the front wall of the OWC device. This result concludes that with the proper structural design of the OWC device, 100% efficiency can be obtained. Further, the angle of inclination of the

front wall of the device has significant effects on the hydrodynamic efficiency in wave power absorption. A moderate angle of inclination $\theta \approx 45^\circ$ of the front wall can significantly increase the efficiency of the device in the short-wave regime, whereas in the long-wave regime, the angle of inclination $\theta < 15^\circ$ is appropriate. Moreover, the hydrodynamic efficiency of the OWC device significantly depends on the bottom profiles. It is seen that the hydrodynamic efficiency of the OWC device is enhanced for the protrusion-type bed profile in the long-wave regime. However, the depression type of bed profile is appropriate for incident waves having a moderate wavelength. For the sinusoidally varying bottom topography, it is observed that in the long-wave regime, the hydrodynamic efficiency of the device becomes unity for lower values of the wavenumber as the ripple amplitude of the bottom increases. However, a reverse pattern is observed for intermediate values of the wavenumber. A similar result is observed in the short-wave regime with an increase in the number of ripples of the bottom. These observations conclude that with the appropriate structural design of the OWC device and suitable bottom profile can significantly increase the hydrodynamic efficiency of the OWC device.

In Chapter 3, it is observed that for type I OWC device, resonance occurs in the efficiency curve for smaller values of the incident wavenumber with an increase in chamber length and submergence depth. A similar resonance pattern is observed for the type II OWC device with an increase in the radius of the quarter circle and submergence depth of the front wall. Moreover, it is found that the resonances in the horizontal and vertical wave forces acting on the front wall of the OWC devices occur for the same values of the wavenumber. However, the curves of horizontal and vertical wave forces as a function of wavenumber are out-of-phase. The horizontal and vertical wave forces are oscillatory in nature, and the amplitude of oscillation decreases in the short wave regime. It is noticed that for irregular incident waves (spectral density is taken as annual wave spectral density at the OWC plant site Pico, Portugal), the chamber pressure standard deviation decreases with an increase in the turbine damping coefficient. Moreover, the chamber pressure standard deviation increases with an increase in the chamber length and draft of the front wall of the type I OWC device. Similar results are observed for type II OWC device with an increase in radius and draft of the front wall. In addition, the annual-averaged plant efficiency increases with an increase in chamber length and submergence depth of type I OWC device except for significantly higher values of the shape parameters. For type I OWC device, the annual-averaged plant efficiency becomes higher for $0.3 < a/h < 0.6$ and $1.5 < b/h < 2.5$. Similarly, for type II OWC device, the maximum efficiency is achieved for $2.5 < r/h < 3.0$ and $-0.7 < y_0/h < -0.5$. For smaller values of rotor diameter, the annual-averaged plant efficiency decreases with an increase in the rotational speed of the Wells turbine. However, for higher values of the rotor diameter, the efficiency initially increases with an increase in rotational speed and attains a maximum. Hereafter, the efficiency decreases for further increase in the rotational speed of the turbine. In a similar manner, for the lower rotational speed of the turbine, the efficiency decreases with an increase in the rotor diameter, whilst, for higher values of the rotational speed

of the turbine, the efficiency increases with an increase in the rotor diameter. These observations conclude that maximum efficiency can be achieved with appropriate combinations of the turbine rotor diameter and rotational speed.

Chapter 4 demonstrates that the power extraction by the hybrid wave energy converter device consisting of a piezoelectric plate and OWC device is considerably higher than the power extraction by the standalone piezoelectric plate and OWC device for a wider range of incident wave frequencies. Consequently, the present hybrid device is suitable in locations having broadband incident wave spectrum. It is found that due to the occurrences of multiple resonances, the power extraction by the present hybrid wave energy converter device is higher for moderate and larger values of the chamber width in the long and intermediate wave regimes. It is observed that irrespective of the front wall draft, the power extraction by the present hybrid device is higher in the long-wave regime. In contrast, the power extraction decreases with an increase in the front wall draft as the incident wavelength becomes shorter. Similar observations are reported for the standalone OWC devices. It is demonstrated that the power extraction by the present hybrid wave energy converter device is higher for smaller plate lengths and smaller submergence depths of the piezoelectric plate. Similar observations are reported in the power extraction by the standalone piezoelectric plate. Moreover, the ripple amplitude and the number of ripples of the sinusoidally varying seabed significantly influence the power extraction by the hybrid wave energy converter. Similar results are also reported for the standalone OWC devices and piezoelectric plates. In addition, the power extraction by the hybrid wave energy converter device becomes higher when the piezoelectric plate is placed in the closed proximity of the OWC device. The amplitudes of the resonating peaks are higher for a piezoelectric plate having fixed edges, and the number of resonating peaks is more when the seaside edge of the piezoelectric plate is free. It is found that the piezoelectric plate is able to capture the incident wave energy for an extended period of time. Based on the Taguchi method, System 1 is best suited at the locations where the incident wave frequency follows the Bretschneider spectrum in terms of extracting the highest power around the most probable incident wave frequency and associated largest bandwidth. In summary, it is concluded that the hydrodynamic performance of the present hybrid wave energy converter device can be enhanced significantly with the appropriate combinations of shape parameters associated with the OWC device, piezoelectric plate, and undulated seabed.

Chapter 5 highlights that for the INP OWC device, the resonance occurs in the efficiency curve $\eta_{max,I}$ due to the variation in chamber length, and the draft of the front wall of the device is similar to the single-layer fluid case. On the other hand, the efficiency $\eta_{max,II}$ varies in a highly oscillatory manner with the variation in incident wavenumber. This highly oscillatory pattern, which occurs due to the exchange of energy between the surface and internal waves, diminishes in the short wave regime for smaller values of chamber length and for larger front wall draft. Further, resonating interaction between the internal waves with the rippled bottom also plays a

major role in the highly resonating pattern of the efficiency $\eta_{max,II}$ curve. Further, it is also demonstrated that the highly oscillatory pattern in $\eta_{max,II}$ occurs due to the distribution of incoming wave energy associated with the internal wave mode k_{II} to cover a broadband spectrum. In addition, due to the multiple resonances and near-resonance interactions of waves with the bottom ripples, the amplitude of resonance in the $\eta_{max,II}$ curve is higher for higher values of bottom ripple amplitude for certain values of incident wave frequencies. It is observed that for IP OWC devices, the pattern of the efficiency curves $\eta_{max,j}$ (for $j = I, II$) are highly oscillatory in nature in the long and intermediate wave regions. The sloshing effect plays a prominent role in this highly oscillatory pattern, along with other effects, as mentioned earlier. For the INP OWC device, significant variations are observed in the efficiency curve $\eta_{max,II}$ due to the variation in the density ratio of the two layers of fluids. A similar pattern is observed for IP OWC devices. However, this oscillatory pattern diminishes in the short-wave regime. Furthermore, for the INP OWC device, the free surface elevation is higher than the interface elevation in the presence of surface wave mode. On the other hand, due to the presence of internal wave mode, the interface elevation is higher than the free surface elevation. Similar observations are reported for the IP OWC device. In summary, it is concluded that the hydrodynamic performance of the OWC devices can be enhanced significantly with the appropriate combinations of shape parameters associated with the OWC device and seabed. Air compressibility enhances the efficiency associated with the surface mode of the OWC device for shorter incident waves, and an opposite trend is observed for longer incident waves. Further, the air compressibility enhances and diminishes the efficiency associated with internal mode alternately as the incident time period increases.

6.3 Applications

The applications of the present study are the following.

- The qualitative and quantitative results presented in Chapter 2 are very useful in designing and constructing an effective oscillating water column device placed over the undulated seabed. It is to be noted that full-scale experiments to study the performance of OWC devices are very costly and time-consuming. In this regard, often, the numerical results, as presented in Chapter 2, will provide a good background of the outcomes before going into full-scale model tests. This will reduce the number of experiments, and so the associated experimental costs will also be reduced. Further, the numerical simulations also provide a good estimation of the incident wave frequency range to get power output and efficiency from the OWC device.
- The qualitative and quantitative results associated with the turbine parameters and the annual average performance of oscillating water column devices on site-specific locations

are provided in Chapter 3, which are very useful in designing and constructing effective breakwater-integrated oscillating water column devices in real sea environments. The concept of these particular types of breakwater-integrated OWC devices is cost-effective and durable. Further, these types of hybrid structures act as an effective wave barrier in real ocean environments.

- The results associated with the power extraction of a hybrid wave energy converter device consisting of the piezoelectric plate and the oscillating water column device are provided in Chapter 4, which are very useful in designing and constructing wave energy converters with flexible structures and hybrid multi-energy systems. The proposed hybrid device can generate maximum power for a wider range of incident wave frequencies and, therefore, is suitable for locations having broadband incident wave spectrum.

- The qualitative and quantitative results associated with the efficiencies of OWC devices in a two-layer fluid system are given in Chapter 5, which are very useful in designing and constructing OWC wave energy converter devices in a two-layer fluid system. With appropriate shapes, the proposed OWC devices can generate maximum efficiencies in surface and internal wave modes for a wider range of incident wave frequencies.

6.4 Scope of possible extensions for the future work

There are a number of interesting extensions of the present work in a long run as provided in the following

- The problems discussed in the present thesis on water wave interactions with wave energy converter devices are based on the Airy wave theory, which is the simplest first-order small-amplitude wave theory, also known as linear theory. This theory can solve many engineering problems quickly and accurately. In some cases, simple theories can accurately predict wave profiles. However, large waves or waves approaching the shore in shallow water often require higher-order wave theories (non-linear theories) to describe. In this context, the problems discussed in Chapters 2-5 can be extended to the second and higher orders to describe the non-linear hydrodynamics associated with various wave energy converter devices.

- The solution techniques discussed in Chapters 2-5 can be extended to the oblique waves by constructing appropriate Green's function and also using the ray method.

- The problems discussed in the present thesis are solved using the boundary element method and coupled eigenfunction expansion-boundary element method. It can be coupled with

the finite element method to handle the non-homogeneous flexibility and piezoelectric parameters of the piezoelectric plate.

- The solution techniques discussed in Chapters 2-5 are based on the constant and linear boundary element methods. The accuracy of the solutions can be improved further by considering higher-order boundary element methods.
- The present solution techniques can be extended to handle the performance of an array of wave energy converter devices of different configurations present in a wave farm.

References

[1] K. Gunn and C. Stock-Williams, "Quantifying the global wave power resource," *Renewable Energy*, vol. 44, pp. 296–304, 2012.

[2] F. d. O. Antonio, "Wave energy utilization: A review of the technologies," *Renewable and Sustainable Energy Reviews*, vol. 14, no. 3, pp. 899–918, 2010.

[3] A. F. Falcão, A. J. Sarmento, L. M. Gato, and A. Brito-Melo, "The pico owc wave power plant: Its lifetime from conception to closure 1986–2018," *Applied Ocean Research*, vol. 98, p. 102104, 2020.

[4] E. Renzi, "Hydroelectromechanical modelling of a piezoelectric wave energy converter," *Proceedings of the Royal Society A: Mathematical, Physical and Engineering Sciences*, vol. 472, no. 2195, p. 20160715, 2016.

[5] D. Evans and R. Porter, "Hydrodynamic characteristics of an oscillating water column device," *Applied Ocean Research*, vol. 17, no. 3, pp. 155–164, 1995.

[6] D.-Z. Ning, J. Shi, Q.-P. Zou, and B. Teng, "Investigation of hydrodynamic performance of an OWC (oscillating water column) wave energy device using fully nonlinear HOBEM (higher-order boundary element method)," *Energy*, vol. 83, pp. 177–188, 2015.

[7] K. Rezanejad, J. Bhattacharjee, and C. G. Soares, "Stepped sea bottom effects on the efficiency of nearshore oscillating water column device," *Ocean Engineering*, vol. 70, pp. 25–38, 2013.

[8] N. Kannan and D. Vakeesan, "Solar energy for future world:-a review," *Renewable and Sustainable Energy Reviews*, vol. 62, pp. 1092–1105, 2016.

[9] S. Shafiee and E. Topal, "When will fossil fuel reserves be diminished?" *Energy Policy*, vol. 37, no. 1, pp. 181–189, 2009.

[10] H. Mengi-Dinçer, V. Ediger, and Ç. Yesevi, "Evaluating the international renewable energy agency through the lens of social constructivism," *Renewable and Sustainable Energy Reviews*, vol. 152, p. 111705, 2021.

[11] Y. Cheng, W. Du, S. Dai, C. Ji, M. Collu, M. Cocard, L. Cui, Z. Yuan, and A. Incecik, "Hydrodynamic characteristics of a hybrid oscillating water column-oscillating buoy wave energy converter integrated into a π-type floating breakwater," *Renewable and Sustainable Energy Reviews*, vol. 161, p. 112299, 2022.

[12] A. D. Craik, "The origins of water wave theory," *Annu. Rev. Fluid Mech.*, vol. 36, pp. 1–28, 2004.

[13] G. B. Airy, *Tides and Waves*. Encyclopedia Metropolitana, 1845, vol. 5.

[14] G. Stokes, "On the theory of oscillatory waves," *Trans. Camb. Phil. SOC.*, vol. 8, pp. 441–455, 1847.

[15] J. Boussinesq, "Théorie de l'intumescence liquide appelée onde solitaire ou de translation se propageant dans un canal rectangulaire," *CR Acad. Sci. Paris*, vol. 72, no. 755-759, p. 1871, 1871.

[16] H. Lamb, *Hydrodynamics*. Cambridge University Press, Cambridge, 1-8, 1932.

[17] C. C. Mei, *The applied dynamics of ocean surface waves*. World Scientific Publishing Company, Singapore, 1989, vol. 1.

[18] R. G. Dean and R. A. Dalrymple, *Water wave mechanics for engineers and scientists*. World Scientific Publishing Company, Singapore, 1991, vol. 2.

[19] C. M. Linton and P. McIver, *Handbook of mathematical techniques for wave/structure interactions*. Chapman and Hall/CRC, London, 2001.

[20] T. Heath, "A review of oscillating water columns," *Philosophical Transactions of the Royal Society A: Mathematical, Physical and Engineering Sciences*, vol. 370, no. 1959, pp. 235–245, 2012.

[21] Y. Luo, Z. Wang, G. Peng, Y. Xiao, L. Zhai, X. Liu, and Q. Zhang, "Numerical simulation of a heave-only floating OWC (oscillating water column) device," *Energy*, vol. 76, pp. 799–806, 2014.

[22] F. Buriani, "Mathematical modelling of wave–structure interactions with application to wave energy conversion," Ph.D. dissertation, Loughborough University, 2019.

[23] D. V. Evans, "Wave-power absorption by systems of oscillating surface pressure distributions," *Journal of Fluid Mechanics*, vol. 114, pp. 481–499, 1982.

[24] J. Falnes and P. McIver, "Surface wave interactions with systems of oscillating bodies and pressure distributions," *Applied Ocean Research*, vol. 7, no. 4, pp. 225–234, 1985.

[25] T. Kelly, T. Dooley, J. Campbell, and J. V. Ringwood, "Comparison of the Experimental and Numerical Results of Modelling a 32-Oscillating Water Column (OWC), V-shaped Floating Wave Energy Converter," *Energies*, vol. 6, no. 8, pp. 4045–4077, 2013.

[26] S. Koley and K. Trivedi, "Mathematical modeling of oscillating water column wave energy converter devices over the undulated sea bed," *Engineering Analysis with Boundary Elements*, vol. 117, pp. 26–40, 2020.

[27] C. Wang and Y. Zhang, "Wave power extraction analysis for an oscillating water column device with various surging lip-walls," *Ocean Engineering*, vol. 220, p. 108483, 2021.

[28] A. A. M. Rodríguez, R. S. Casarín, and J. M. B. Ilzarbe, "A 3D boundary element method for analysing the hydrodynamic performance of a land-fixed oscillating water column device," *Engineering Analysis with Boundary Elements*, vol. 138, pp. 407–422, 2022.

[29] P. Boccotti, "Caisson breakwaters embodying an OWC with a small opening—part I: Theory," *Ocean Engineering*, vol. 34, no. 5-6, pp. 806–819, 2007.

[30] H. Martins-rivas and C. C. Mei, "Wave power extraction from an oscillating water column along a straight coast," *Ocean Engineering*, vol. 36, no. 6-7, pp. 426–433, 2009.

[31] F. Gouaud, V. Rey, J. Piazzola, and R. Van Hooff, "Experimental study of the hydrodynamic performance of an onshore wave power device in the presence of an underwater mound," *Coastal Engineering*, vol. 57, no. 11-12, pp. 996–1005, 2010.

[32] G. Malara and F. Arena, "Analytical modelling of an U-oscillating water column and performance in random waves," *Renewable Energy*, vol. 60, pp. 116–126, 2013.

[33] T. Vyzikas, S. Deshoulières, M. Barton, O. Giroux, D. Greaves, and D. Simmonds, "Experimental investigation of different geometries of fixed oscillating water column devices," *Renewable Energy*, vol. 104, pp. 248–258, 2017.

[34] G. Malara and F. Arena, "Response of U-Oscillating Water Column arrays: Semi-analytical approach and numerical results," *Renewable Energy*, vol. 138, pp. 1152–1165, 2019.

[35] K. Trivedi, S. Koley, and K. Panduranga, "Performance of an U-shaped Oscillating Water Column Wave Energy Converter Device under Oblique Incident Waves," *Fluids*, vol. 6, no. 4, p. 137, 2021.

[36] R. Mayon, D. Ning, C. Zhang, L. Chen, and R. Wang, "Wave energy capture by an omnidirectional point sink oscillating water column system," *Applied Energy*, vol. 304, p. 117795, 2021.

[37] K. Rezanejad, J. Bhattacharjee, and C. G. Soares, "Analytical and numerical study of dual-chamber oscillating water columns on stepped bottom," *Renewable Energy*, vol. 75, pp. 272–282, 2015.

[38] K. Rezanejad, J. Bhattacharjee, and C. Guedes Soares, "Analytical and numerical study of nearshore multiple oscillating water columns," *Journal of Offshore Mechanics and Arctic Engineering*, vol. 138, no. 2, 2016.

[39] C. Wang, Y. Zhang, and Z. Deng, "Theoretical analysis on hydrodynamic performance for a dual-chamber oscillating water column device with a pitching front lip-wall," *Energy*, vol. 226, p. 120326, 2021.

[40] C. C. Mei, "Resonant reflection of surface water waves by periodic sandbars," *Journal of Fluid Mechanics*, vol. 152, pp. 315–335, 1985.

[41] Y. Luo, J.-R. Nader, P. Cooper, and S.-P. Zhu, "Nonlinear 2uppercaseD analysis of the efficiency of fixed oscillating water column wave energy converters," *Renewable Energy*, vol. 64, pp. 255–265, 2014.

[42] P. R. Teixeira, D. P. Davyt, E. Didier, and R. Ramalhais, "Numerical simulation of an oscillating water column device using a code based on navier–stokes equations," *Energy*, vol. 61, pp. 513–530, 2013.

[43] A. Elhanafi, G. Macfarlane, and D. Ning, "Hydrodynamic performance of single–chamber and dual–chamber offshore–stationary oscillating water column devices using cfd," *Applied Energy*, vol. 228, pp. 82–96, 2018.

[44] C. Wang and Y. Zhang, "Hydrodynamic performance of an offshore oscillating water column device mounted over an immersed horizontal plate: A numerical study," *Energy*, vol. 222, p. 119964, 2021.

[45] P. Mohapatra, K. Vijay, A. Bhattacharyya, and T. Sahoo, "Performance of a shore fixed oscillating water column device for different bottom slopes and front wall drafts: A study based on computational fluid dynamics and biem," *Journal of Offshore Mechanics and Arctic Engineering*, vol. 143, no. 3, 2021.

[46] D.-Z. Ning, R.-Q. Wang, L.-F. Chen, and K. Sun, "Experimental investigation of a land-based dual-chamber owc wave energy converter," *Renewable and Sustainable Energy Reviews*, vol. 105, pp. 48–60, 2019.

[47] E. Gubesch, N. Abdussamie, I. Penesis, and C. Chin, "Maximising the hydrodynamic performance of offshore oscillating water column wave energy converters," *Applied Energy*, vol. 308, p. 118304, 2022.

[48] D. Vicinanza, E. D. Lauro, P. Contestabile, C. Gisonni, J. L. Lara, and I. J. Losada, "Review of innovative harbor breakwaters for wave-energy conversion," *Journal of Waterway, Port, Coastal, and Ocean Engineering*, vol. 145, no. 4, p. 03119001, 2019.

[49] A. F. Falcão and J. C. Henriques, "Oscillating-water-column wave energy converters and air turbines: A review," *Renewable Energy*, vol. 85, pp. 1391–1424, 2016.

[50] M. Mustapa, O. Yaakob, Y. M. Ahmed, C.-K. Rheem, K. Koh, and F. A. Adnan, "Wave energy device and breakwater integration: A review," *Renewable and Sustainable Energy Reviews*, vol. 77, pp. 43–58, 2017.

[51] G. Müller and T. Whittaker, "An investigation of breaking wave pressures on inclined walls," *Ocean Engineering*, vol. 20, no. 4, pp. 349–358, 1993.

[52] G. Müller and T. J. Whittaker, "Visualisation of flow conditions inside a shoreline wave power-station," *Ocean Engineering*, vol. 22, no. 6, pp. 629–641, 1995.

[53] P. Boccotti, "On a new wave energy absorber," *Ocean Engineering*, vol. 30, no. 9, pp. 1191–1200, 2003.

[54] K. Thiruvenkatasamy, S. Neelamani, and M. Sato, "Nonbreaking wave forces on multiresonant oscillating water column wave power caisson breakwater," *Journal of Waterway, Port, Coastal, and Ocean Engineering*, vol. 131, no. 2, pp. 77–84, 2005.

[55] P. Boccotti, P. Filianoti, V. Fiamma, and F. Arena, "Caisson breakwaters embodying an owc with a small opening—part II: A small-scale field experiment," *Ocean Engineering*, vol. 34, no. 5-6, pp. 820–841, 2007.

[56] Y. Liu, H. Shi, Z. Liu, and Z. Ma, "Experiment study on a new designed owc caisson breakwater," in *2011 Asia-Pacific Power and Energy Engineering Conference*. IEEE, 2011, pp. 1–5.

[57] F. M. Strati, G. Malara, and F. Arena, "Performance optimization of a U-oscillating-water-column wave energy harvester," *Renewable Energy*, vol. 99, pp. 1019–1028, 2016.

[58] G. Malara, A. Romolo, V. Fiamma, and F. Arena, "On the modelling of water column oscillations in U-OWC energy harvesters," *Renewable Energy*, vol. 101, pp. 964–972, 2017.

[59] G. Malara, R. Gomes, F. Arena, J. Henriques, L. Gato, and A. Falcão, "The influence of three-dimensional effects on the performance of U-type oscillating water column wave energy harvesters," *Renewable Energy*, vol. 111, pp. 506–522, 2017.

[60] S. J. Ashlin, V. Sundar, and S. Sannasiraj, "Pressures and forces on an oscillating water column–type wave energy caisson breakwater," *Journal of Waterway, Port, Coastal, and Ocean Engineering*, vol. 143, no. 5, p. 04017020, 2017.

[61] P. D. Spanos, F. M. Strati, G. Malara, and F. Arena, "An approach for non-linear stochastic analysis of u-shaped owc wave energy converters," *Probabilistic Engineering Mechanics*, vol. 54, pp. 44–52, 2018.

[62] Y. Goda, *Random seas and design of maritime structures*. World Scientific Publishing Company, Singapore, 2010, vol. 33.

[63] A. De O Falcão and R. Rodrigues, "Stochastic modelling of owc wave power plant performance," *Applied Ocean Research*, vol. 24, no. 2, pp. 59–71, 2002.

[64] C. Josset and A. Clément, "A time-domain numerical simulator for oscillating water column wave power plants," *Renewable Energy*, vol. 32, no. 8, pp. 1379–1402, 2007.

[65] W. Sheng and A. Lewis, "Wave energy conversion of oscillating water column devices including air compressibility," *Journal of Renewable and Sustainable Energy*, vol. 8, no. 5, p. 054501, 2016.

[66] K. Rezanejad, C. G. Soares, I. López, and R. Carballo, "Experimental and numerical investigation of the hydrodynamic performance of an oscillating water column wave energy converter," *Renewable Energy*, vol. 106, pp. 1–16, 2017.

[67] M. L. Jalón and F. Brennan, "Hydrodynamic efficiency versus structural longevity of a fixed OWC wave energy converter," *Ocean Engineering*, vol. 206, p. 107260, 2020.

[68] X. Xie, Q. Wang, and N. Wu, "Potential of a piezoelectric energy harvester from sea waves," *Journal of Sound and Vibration*, vol. 333, no. 5, pp. 1421–1429, 2014.

[69] X. Xie and Q. Wang, "A study on an ocean wave energy harvester made of a composite piezoelectric buoy structure," *Composite Structures*, vol. 178, pp. 447–454, 2017.

[70] K. Zhou, H. Dai, A. Abdelkefi, and Q. Ni, "Theoretical modeling and nonlinear analysis of piezoelectric energy harvesters with different stoppers," *International Journal of Mechanical Sciences*, vol. 166, p. 105233, 2020.

[71] S. Zheng, M. Meylan, X. Zhang, G. Iglesias, and D. Greaves, "Performance of a plate-wave energy converter integrated in a floating breakwater," *IET Renewable Power Generation*, vol. 15, no. 14, pp. 3206–3219, 2021.

[72] V. Vipin and S. Koley, "Mathematical modeling of a submerged piezoelectric wave energy converter device installed over an undulated seabed," *Renewable Energy*, vol. 200, pp. 1382–1392, 2022.

[73] S. Manam and T. Sahoo, "Waves past porous structures in a two-layer fluid," *Journal of Engineering Mathematics*, vol. 52, no. 4, pp. 355–377, 2005.

[74] W. Koo, "Free surface simulation of a two-layer fluid by boundary element method," *International Journal of Naval Architecture and Ocean Engineering*, vol. 2, no. 3, pp. 127–131, 2010.

[75] H. Behera, R. Kaligatla, and T. Sahoo, "Wave trapping by porous barrier in the presence of step type bottom," *Wave Motion*, vol. 57, pp. 219–230, 2015.

[76] S. Das, T. Sahoo, and M. Meylan, "Flexural-gravity wave dynamics in two-layer fluid: blocking and dead water analogue," *Journal of Fluid Mechanics*, vol. 854, pp. 121–145, 2018.

[77] J. R. Cadby and C. Linton, "Three-dimensional water-wave scattering in two-layer fluids," *Journal of Fluid Mechanics*, vol. 423, pp. 155–173, 2000.

[78] C. Linton and M. McIver, "The interaction of waves with horizontal cylinders in two-layer fluids," *Journal of Fluid Mechanics*, vol. 304, pp. 213–229, 1995.

[79] E. Barthélemy, A. Kabbaj, and J. Germain, "Long surface wave scattered by a step in a two-layer fluid," *Fluid Dynamics Research*, vol. 26, no. 4, p. 235, 2000.

[80] C. Linton and J. R. Cadby, "Scattering of oblique waves in a two-layer fluid," *Journal of Fluid Mechanics*, vol. 461, pp. 343–364, 2002.

[81] P. Chamberlain and D. Porter, "Wave scattering in a two-layer fluid of varying depth," *Journal of Fluid Mechanics*, vol. 524, pp. 207–228, 2005.

[82] M. Kashiwagi, I. Ten, and M. Yasunaga, "Hydrodynamics of a body floating in a two-layer fluid of finite depth. part 2. diffraction problem and wave-induced motions," *Journal of Marine Science and Technology*, vol. 11, no. 3, pp. 150–164, 2006.

[83] M.-R. Alam, Y. Liu, and D. K. Yue, "Bragg resonance of waves in a two-layer fluid propagating over bottom ripples. part ii. numerical simulation," *Journal of Fluid Mechanics*, vol. 624, pp. 225–253, 2009.

[84] H. Behera and T. Sahoo, "Gravity wave interaction with porous structures in two-layer fluid," *Journal of Engineering Mathematics*, vol. 87, no. 1, pp. 73–97, 2014.

[85] S. Panda and S. Martha, "Oblique wave scattering by undulating porous bottom in a two-layer fluid: Fourier transform approach," *Geophysical & Astrophysical Fluid Dynamics*, vol. 108, no. 6, pp. 587–614, 2014.

[86] A. Medina-Rodríguez and R. Silva, "Oblique water wave scattering by a trench in a two-layer fluid," *Journal of Engineering Mechanics*, vol. 144, no. 6, 2018.

[87] A. Medina-Rodríguez, Martínez and C. R. Silva, "The effect of an asymmetric submarine trench on the efficiency of an oscillating water column device in a two-layer fluid," *WIT Transactions on Engineering Sciences*, vol. 120, pp. 137–148, 2018.

[88] N. Islam, S. Kundu, and R. Gayen, "Scattering and radiation of water waves by a submerged rigid disc in a two-layer fluid," *Proceedings of the Royal Society A: Mathematical, Physical and Engineering Sciences*, vol. 475, no. 2232, p. 20190331, 2019.

[89] K. K. Barman and S. N. Bora, "Scattering and trapping of water waves by a composite breakwater placed on an elevated bottom in a two-layer fluid flowing over a porous sea-bed," *Applied Ocean Research*, vol. 113, p. 102544, 2021.

[90] B. Bouali and S. Larbi, "Sequential optimization and performance prediction of an oscillating water column wave energy converter," *Ocean Engineering*, vol. 131, pp. 162–173, 2017.

[91] M. Hayati, A. H. Nikseresht, and A. T. Haghighi, "Sequential optimization of the geometrical parameters of an owc device based on the specific wave characteristics," *Renewable Energy*, vol. 161, pp. 386–394, 2020.

[92] Z. He, D. Ning, Y. Gou, and R. Mayon, "Optimization of a wave energy converter square array based on the differential evolution algorithm," *Ocean Engineering*, vol. 262, p. 112189, 2022.

[93] E. Al Shami, X. Wang, R. Zhang, and L. Zuo, "A parameter study and optimization of two body wave energy converters," *Renewable Energy*, vol. 131, pp. 1–13, 2019.

[94] X. Bao, W. Xiao, S. Li, and G. Iglesias, "Parametric study and optimization of a two-body wave energy converter," *IET Renewable Power Generation*, vol. 15, no. 14, pp. 3319–3330, 2021.

[95] C. Patterson, R. Dunsire, and S. Hillier, "Development of wave energy breakwater at siadar, isle of lewis," in *Coasts, marine structures and breakwaters: Adapting to change: Proceedings of the 9th international conference organised by the Institution of Civil Engineers and held in Edinburgh on 16 to 18 September 2009.* Thomas Telford Ltd, 2010, pp. 1–738.

[96] C. Ciria, "Cetmef (2007)-The Rock Manual. the use of rock in hydraulic engineering," *Publicação*, no. C683, 2007.

[97] Y. Yuan, J. Li, and Y. Cheng, "Validity ranges of interfacial wave theories in a two-layer fluid system," *Acta Mechanica Sinica*, vol. 23, no. 6, pp. 597–607, 2007.

[98] S. H. Schot, "Eighty years of sommerfeld's radiation condition," *Historia Mathematica*, vol. 19, no. 4, pp. 385–401, 1992.

[99] G. B. Folland, *Introduction to partial differential equations.* Princeton University Press, Princeton, New Jersey, 2020.

[100] T. Sahoo, *Mathematical techniques for wave interaction with flexible structures.* CRC Press, Boca Raton, 2012.

[101] S. Mohapatra, R. Ghoshal, and T. Sahoo, "Effect of compression on wave diffraction by a floating elastic plate," *Journal of Fluids and Structures*, vol. 36, pp. 124–135, 2013.

[102] R. Weiss, "Product integration for the generalized abel equation," *Mathematics of Computation*, vol. 26, no. 117, pp. 177–190, 1972.

[103] Y. Liu, *Fast multipole boundary element method: theory and applications in engineering.* Cambridge University Press, Cambridge, 2009.

[104] C. A. Brebbia, J. C. F. Telles, and L. C. Wrobel, *Boundary element techniques: theory and applications in engineering.* Springer Science & Business Media, Heidelberg, 2012.

[105] C. C. Mei, *Mathematical analysis in engineering: How to use the basic tools.* Cambridge University Press, Cambridge, 1997.

[106] W. T. Ang, *A beginner's course in boundary element methods.* Universal-Publishers, Boca Raton, 2007.

[107] K. C. Ang, "Introducing the boundary element method with matlab," *International Journal of Mathematical Education in Science and Technology*, vol. 39, no. 4, pp. 505–519, 2008.

[108] P. W. Partridge, C. A. Brebbia *et al.*, *Dual reciprocity boundary element method.* Springer Science & Business Media, Netherlands, 2012.

[109] C. A. Brebbia and J. Dominguez, *Boundary elements: an introductory course.* WIT Press, Boston, 1994.

[110] S. Koley and T. Sahoo, "Wave interaction with a submerged semicircular porous breakwater placed on a porous seabed," *Engineering Analysis with Boundary Elements*, vol. 80, pp. 18–37, 2017.

[111] C. Smith, "Some problems in linear water wave theory," Ph.D. dissertation, University of Bristol, 1983.

[112] J. T. Katsikadelis, *The Boundary Element Method for Engineers and Scientists: Theory and Applications.* Academic Press, London, 2016.

[113] R. Porter and D. Porter, "Water wave scattering by a step of arbitrary profile," *Journal of Fluid Mechanics*, vol. 411, pp. 131–164, 2000.

[114] P. Liu *et al.*, *Advances in coastal and ocean engineering.* World Scientific, Singapore, 1995, vol. 1.

[115] C. D. Wang and M. H. Meylan, "The linear wave response of a floating thin plate on water of variable depth," *Applied Ocean Research*, vol. 24, no. 3, pp. 163–174, 2002.

[116] D.-Z. Ning, R.-Q. Wang, Q.-P. Zou, and B. Teng, "An experimental investigation of hydrodynamics of a fixed owc wave energy converter," *Applied Energy*, vol. 168, pp. 636–648, 2016.

[117] C. Liu, Z. Huang, A. Law Wing Keung, and N. Geng, "A numerical study of wave energy converter in the form of an oscillating water column based on a mixed eulerian-lagrangian formulation," in *ASME 2010 29th International Conference on Ocean, Offshore and Arctic Engineering*. American Society of Mechanical Engineers Digital Collection, 2010, pp. 589–596.

[118] S. Raghunathan, "The wells air turbine for wave energy conversion," *Progress in Aerospace Sciences*, vol. 31, no. 4, pp. 335–386, 1995.

[119] S. Koley, "Integral equation and allied methods for wave interaction with porous and flexible structures," Ph.D. dissertation, IIT, Kharagpur, 2016.

[120] A. A. Medina Rodríguez, J. M. Blanco Ilzarbe, R. Silva Casarín, and U. Izquierdo Ereño, "The influence of the chamber configuration on the hydrodynamic efficiency of oscillating water column devices," *Journal of Marine Science and Engineering*, vol. 8, no. 10, p. 751, 2020.

[121] J. Falnes and A. Kurniawan, *Ocean waves and oscillating systems: linear interactions including wave-energy extraction*. Cambridge University Press, Cambridge, 2020, vol. 8.

[122] K. Ezhilsabareesh, R. Suchithra, and A. Samad, "Performance enhancement of an impulse turbine for owc using grouped grey wolf optimizer based controller," *Ocean Engineering*, vol. 190, p. 106425, 2019.

[123] A. Babarit, *Ocean wave energy conversion*. Elsevier, Oxford, 2018.

[124] S. Koley, "Water wave scattering by floating flexible porous plate over variable bathymetry regions," *Ocean Engineering*, vol. 214, p. 107686, 2020.

[125] K. Trivedi and S. Koley, "Mathematical modeling of breakwater-integrated oscillating water column wave energy converter devices under irregular incident waves," *Renewable Energy*, vol. 178, pp. 403–419, 2021.

[126] F. Buriani and E. Renzi, "Hydrodynamics of a flexible piezoelectric wave energy harvester moored on a breakwater," in *Proceedings of the 12th European Wave and Tidal Energy Conference (EWTEC 2017), Cork, Ireland*, vol. 27, 2017.

[127] M. T. Morris-Thomas, R. J. Irvin, and K. P. Thiagarajan, "An investigation into the hydrodynamic efficiency of an oscillating water column," *Journal of Offshore Mechanics and Arctic Engineering*, vol. 129, no. 4, pp. 273–278, 2007.

[128] Y. Zhang, Q.-P. Zou, and D. Greaves, "Air–water two-phase flow modelling of hydrodynamic performance of an oscillating water column device," *Renewable Energy*, vol. 41, pp. 159–170, 2012.

[129] P. Mohapatra and T. Sahoo, "Hydrodynamic performance analysis of a shore fixed oscillating water column wave energy converter in the presence of bottom variations," *Proceedings of the Institution of Mechanical Engineers, Part M: Journal of Engineering for the Maritime Environment*, vol. 234, no. 1, pp. 37–47, 2020.

[130] Z. Liu, "Experimental and numerical investigation of oscillating water column wave energy convertor," Ph.D. dissertation, Ocean University of China, Qingdao, 2008.

[131] T. Perez and M. Blanke, "Simulation of ship motion in seaway," *Computer Science; Technical Report; The University of Newcastle: Callaghan, Australia*, pp. 1–13, 2002.

[132] E. M. Lewandowski, *The dynamics of marine craft: maneuvering and seakeeping*. World Scientific, Singapore, 2004, vol. 22.

[133] S. Koley, "Wave transmission through multilayered porous breakwater under regular and irregular incident waves," *Engineering Analysis with Boundary Elements*, vol. 108, pp. 393–401, 2019.

[134] D.-Z. Ning, R.-Q. Wang, Y. Gou, M. Zhao, and B. Teng, "Numerical and experimental investigation of wave dynamics on a land-fixed owc device," *Energy*, vol. 115, pp. 326–337, 2016.

[135] P. Kar, S. Koley, and T. Sahoo, "Bragg scattering of long waves by an array of trenches," *Ocean Engineering*, vol. 198, p. 107004, 2020.

[136] A. Sarmento, L. Gato, and A. d. O. Falcao, "Turbine-controlled wave energy absorption by oscillating water column devices," *Ocean Engineering*, vol. 17, no. 5, pp. 481–497, 1990.

[137] A. d. O. Falcão and P. Justino, "OWC wave energy devices with air flow control," *Ocean Engineering*, vol. 26, no. 12, pp. 1275–1295, 1999.

[138] D. R. Noble, S. Draycott, T. A. Davey, and T. Bruce, "Design diagrams for wavelength discrepancy in tank testing with inconsistently scaled intermediate water depth," *International Journal of Marine Energy*, vol. 18, pp. 109–113, 2017.

[139] P. Kar, S. Koley, K. Trivedi, and T. Sahoo, "Bragg scattering of surface gravity waves due to multiple bottom undulations and a semi-infinite floating flexible structure," *Water*, vol. 13, no. 17, p. 2349, 2021.

[140] S. K. Mohanty and M. Sidharth, "Time dependent wave motion in a permeable bed," *Meccanica*, vol. 55, pp. 1481–1497, 2020.

[141] A. J. Sarmento and A. d. O. Falcão, "Wave generation by an oscillating surface-pressure and its application in wave-energy extraction," *Journal of Fluid Mechanics*, vol. 150, pp. 467–485, 1985.

[142] A. F. Falcão, J. C. Henriques, R. P. Gomes, and J. C. Portillo, "Theoretically based correction to model test results of owc wave energy converters to account for air compressibility effect," *Renewable Energy*, vol. 198, pp. 41–50, 2022.

[143] A. F. Falcão and J. C. Henriques, "The spring-like air compressibility effect in oscillating-water-column wave energy converters: Review and analyses," *Renewable and Sustainable Energy Reviews*, vol. 112, pp. 483–498, 2019.

List of Publications

Publication from thesis:

1. S. Koley, and K. Trivedi, "Mathematical modeling of oscillating water column wave energy converter devices over the undulated sea bed," *Engineering Analysis with Boundary Elements* vol. 117, pp. 26-40, 2020. (SCI, IF-3.3), https://doi.org/10.1016/j.enganabound.2020.03.017

2. K. Trivedi, and S. Koley, "Annual mean efficiency of the duct type OWC in regional ocean environments," *Energy Reports*, vol. 8, pp: 346-351, 2022. (SCI, IF-5.2), https://doi.org/10.1016/j.egyr.2022.01.077.

3. K. Trivedi and S. Koley, "Mathematical modeling of breakwater-integrated oscillating water column wave energy converter devices under irregular incident waves," *Renewable Energy*, vol. 178, pp: 403-419, 2021. (SCI, IF-8.7), https://doi.org/10.1016/j.renene.2021.06.075

4. K. Trivedi and S. Koley, "Performance of a hybrid wave energy converter device consisting of a piezoelectric plate and oscillating water column device placed over an undulated seabed," *Applied Energy*, vol. 333, pp: 120627, 2023. (SCI, IF-11.2), https://doi.org/10.1016/j.apenergy.2022.120627

5. K. Trivedi, and S. Koley, "Hydrodynamics of an U-shaped OWC device in a two-layer fluid system," *Energy Reports*, vol. 8, pp: 106-111, 2022. (SCI, IF-5.2), https://doi.org/10.1016/j.egyr.2022.10.250.

6. K. Trivedi and S. Koley, "Mathematical modeling of oscillating water column wave energy converter devices placed over an undulated seabed in a two-layer fluid system," *Renewable Energy*, vol. 333, pp: 119092, 2023. (SCI, IF-8.7), https://doi.org/10.1016/j.apenergy.2022.120627

Conferences

1. K. Trivedi, and S. Koley, "Hydrodynamic Performance of the floating rectangular shaped OWC device in Random Waves Environment", *PACE-an International Congress*, Turkey, 20-23 June, 2021.

2. S. Koley, and K. Trivedi, " Water waves interaction with poroelastic plate floating over undulated bottom topography," *Mathematics of Sea Ice and Ice Sheets* The University of Newcastle, Australia, 9 – 12 November 2020.

3. K. Trivedi, and S. Koley, "Surface gravity waves scattering with floating poroelastic plate over variable bottom topography," *International Webinar on Contemporary Problems on Mechanics and Vibrations (CPMV2021)*, BITS-Pilani, Hyderabad Campus 20-22 May, 2021.

Other publications:

1. K. Trivedi, and S. Koley, "Annual-Averaged Performance of Oscillating Water Column Wave Energy Converter Devices in Real Sea Conditions", *In Advances in Industrial Machines and Mechanisms: Select Proceedings of IPROMM 2020, Springer Singapore*, 541-550, 2021, (SCOPUS).

2. K. Trivedi, and S. Koley, "Performance of an L-shaped Duct Oscillating Water Column Wave Energy Converter Device Under Irregular Incident Waves", *In Advances in Energy Technology: Select Proceedings of EMSME 2020, Springer Singapore*, 719-728, 2022, (SCOPUS).

3. K. Trivedi, and S. Koley, "Motions of a freely floating thick rigid structure over asymmetric trenches," *Structural Integrity and Life* Vol. 21, 2021, (SCOPUS).

4. S. Koley, and K. Trivedi, "Mathematical modeling of Oyster wave energy converter device," *AIP Conference Proceedings*, vol. 2277, No. 1, p. 130014, 2020. (SCOPUS).

5. K. Trivedi, and S. Koley, "Irregular water wave interaction with oscillating water column wave energy converter devices placed over undulated seabed," *AIP Conference Proceedings*, vol. 2357, No. 1, p. 100007, 2022. (SCOPUS).

6. K. Trivedi, and S. Koley, "Performance of an OWC device placed over stepped bottom in random waves environment," *IOP: Journal of Physics conference series* Vol. 1921, No. 1, p. 012121, (SCOPUS).

7. S. Koley, and K. Trivedi, "Performance of an OWC device placed over multi-stepped bottom in random waves environment," *IOP: Journal of Physics conference series* Vol. 1921, No. 1, p. 012129, (SCOPUS).

8. K. Trivedi, and S. Koley, "Hydrodynamic Performance of an OWC Device under the Action of Oblique Incident Waves." *Emerging Trends in Industry 4.0 (ETI 4.0), IEEE*, p 1-5, 2021, (SCOPUS).

9. K. Trivedi, and S. Koley, 'Mathematical modelling of an OWC device mounted over the shoal bottom," *International Power and Renewable Energy Conference (IPRECON), IEEE*, p 1-5, 2021, (SCOPUS).

10. Vipin V., K. Trivedi, and S. Koley, 'Mathematical Modeling of a U-shaped OWC Device over the Slanted Sea Bed." *3rd International Conference on Control Systems, Mathematical Modeling, Automation and Energy Efficiency (SUMMA), IEEE*, p 1022-1026, 2021, (SCOPUS).

11. K. Trivedi, and S. Koley, "Hydroelastic Analysis of Viscoelastic Plate Over the Stepped Bottom," *Fluid Mechanics and Fluid Power, Springer Nature Singapore*, p 367-371, 2021, (SCOPUS).

12. S. Koley, K. Trivedi, and Vipin V., "Hydroelastic analysis of floating long viscoelastic plate in shallow water", *Materials Today: Proceedings*, vol. 49, p 2234-2238, 2021, (SCOPUS).

13. K. Trivedi, and S. Koley, "Modeling the viscoelasticity of floating membrane in water waves", *Materials Today: Proceedings*, vol. 72, p 222-226, 2023, (SCOPUS).

14. K. Trivedi, and S. Koley, "Performance of OWC Device in Random Ocean Waves," *Second International Conference on Electronics and Renewable Systems (ICEARS), IEEE*, p 147-150, 2023, (SCOPUS).

15. K. Trivedi, and S. Koley, "Effect of varying bottom topography on the radiation of water waves by a floating rectangular buoy," *Fluids*, vol. 6(2), p 59, 2021, (SCOPUS).

16. K. Trivedi, S. Koley, and K. Panduranga "Performance of an U-shaped oscillating water column wave energy converter device under oblique incident waves," *Fluids*, vol. 6(4), p 137, 2021, (SCOPUS).

17. K. Trivedi, AR. Ray, PA. Krishnan, S. Koley, and T. Sahoo "Hydrodynamics of an OWC Device in Irregular Incident Waves Using RANS Model," *Fluids*, vol. 8(1), p 27, 2023, (SCOPUS).

Other SCI publications:

1. K. Trivedi, AR. Ray, PA. Krishnan, S. Koley, and T. Sahoo "Hydrodynamics of LIMPET type OWC device under Stokes second-order waves," *Ocean Engineering*, Accepted for publication, (SCI, IF-5.0).

2. A.A.M.Rodríguez, K. Trivedi, S. Koley, I.O. Martinez, E. Mendoza, G.P. Vanegas, R. Silva, "Improved hydrodynamic performance of an OWC device based on a Helmholtz resonator," *Energy*, vol. 273, pp: 127299, 2023. (SCI, IF-9.0), https://doi.org/10.1016/j.energy.2023.127299.

3. S. Koley, K. Panduranga, K. Trivedi, A. AI- Ragum, S. Neelamani, "Numerical and experimental modeling of wave-induced forces on submarine pipeline buried in the soil of different engineering properties," *Ocean Engineering*, vol. 273, pp: 113941, 2023. (SCI, IF-5.0), https://doi.org/10.1016/j.oceaneng.2023.113941.

4. K. Trivedi, and S. Koley, "Hydrodynamic performance of the dual-chamber oscillating water column device placed over the undulated sea bed," *Energy Reports*, vol. 8, pp: 480-486, 2022. (SCI, IF-5.2), https://doi.org/10.1016/j.egyr.2021.11.159.

5. Vipin V., K. Trivedi, and S. Koley, "Performance of a submerged piezoelectric wave energy converter device floating over an undulated seabed," *Energy Reports*, vol. 8, pp: 182-188, 2022. (SCI, IF-5.2), https://doi.org/10.1016/j.egyr.2022.05.165.

6. K. Trivedi, and S. Koley, "Time-domain analysis of quarter-circle shaped oscillating water column device," *Energy Reports*, vol. 8, pp: 431-437, 2022. (SCI, IF-5.2), https://doi.org/10.1016/j.egyr.2022.05.173.

7. Vipin V., K. Trivedi, and S. Koley, "Performance of a submerged piezoelectric wave energy converter device in time domain," *Energy Reports*, vol. 8, pp: 309-314, 2022. (SCI, IF-5.2), https://doi.org/10.1016/j.egyr.2022.10.247.

8. A. Choudhary, K. Trivedi, S. Koley, S.C. Martha, "On the scattering and radiation of water waves by a finite dock floating over a rectangular trench," *Wave Motion*, vol. 8, pp: 309-314, 2022. (SCI, IF-2.4), https://doi.org/10.1016/j.wavemoti.2021.102869.

9. KG. Vijay, S. Koley, K. Trivedi, CS. Nishad, "Hydrodynamic Coefficients of a Floater Near a Partially Reflecting Seawall in the Presence of an Array of Caisson Blocks," *Journal Offshore Mechanics and Arctic Engineering*, vol. 144, pp: 021906 , 2022. (SCI, IF-1.6), https://doi.org/10.1115/1.4052635.

10. P. Kar, S. Koley, K. Trivedi, T. Sahoo, "Bragg scattering of surface gravity waves due to multiple bottom undulations and a semi-infinite floating flexible structure," *Water*, vol. 13(17), pp: 2349, 2021. (SCI, IF-3.4), https://doi.org/10.3390/w13172349.

Biography

Brief Biography of Candidate

Ms. Kshma Trivedi completed her Bachelor of Science from CSGM University, Kanpur, Master of Science from Visvesvaraya National Institute of Technology-Nagpur (VNIT Nagpur), Maharashtra. She has around two years of academic experience in teaching at G. H. Raisoni College of Engineering, Nagpur, and at Kanpur Institute of Technology, Kanpur from 2017-2019. Through INSPIRE Faculty Fellowship Project (DST/INSPIRE/04/2017/002460), she has worked as full-time Ph.D. scholar in the Dept. of Mathematics, Birla Institute of Technology and Science-Pilani, Hyderabad Campus from 2019-2023 under the supervision of Prof. Santanu Koley. She has published 16 SCI, and 17 SCOPUS scientific publications in reputed international journals. She presented her research papers at several national and international conferences held in India and abroad. She has received the CSIR Foreign Travel Grant (TG/12140/23-HRD) to attend and present research papers at ICIAM-2023, Tokyo, Japan, from August 20-25, 2023.

Brief Biography of Supervisor

Prof. Santanu Koley is an Associate Professor in the Department of Mathematics, Birla Institute of Technology and Science-Pilani, Hyderabad Campus. He received his Ph.D. degree from the Indian Institute of Technology Kharagpur in 2016. His main area of research includes Boundary Element Method (Theory & Applications), Mathematical Modeling, Wave Energy Converter Devices, Integral Equations, and Statistical Modeling. He has published 50 SCI papers and 45 SCOPUS papers in the journal of international repute. Prof. Koley has presented several research papers at national and international conferences held in India and abroad. He received a number of prestigious national and international awards like the DST INSPIRE Faculty Award and top cited researcher from EABE, Elsevier, etc. He is currently dealing with two sponsored projects funded by DST, Govt. of India, and SERB, Govt. of India (Core Research Grant). He has received an international travel support Grant from SERB, India, to attend ICIAM 2019 and ICIAM 2023 conferences. Prior to joining BITS-Pilani, Hyderabad Campus, he worked as INSPIRE Faculty at IISER Bhopal - 2018, Assistant Professor at DA-IICT, Gandhinagar - 2017 to 2018, SERB - National Postdoc Fellow at IIT Ropar - 2016 to 2017, and Research Associate at IIT Kharagpur - 2015 to 2016.